About Journal

The University of Sistan and Baluchestan entered into strategic partnership with Iranian Association of Electrical and Electronic Engineers (IAEEE) to publish the **International Journal of Industrial Electronics Control and Optimization (IECO)**. The IECO is a refereed international journal which presents to the international scientific community important results of work in these fields, whether in the form of modeling simulation, analysis, fundamental research, development, application, design or real-time implementation. The scope of IECO is broad, encompassing all aspects of Industrial Electronics, Control and Optimization.

Note: International Journal of Industrial Electronics, Control and Optimization (IECO) has qualified to **ACADEMIC RESEARCH JOURNAL (ELMI-PAJOHESHI)** status certified by the ministry of Science, Research and Technology of Iran (No. 231566/3/18 dated 1396/10/09), and is published by the University of Sistan and Baluchestan through a formal partnership (No. 952/2/1500 dated 1395/11/04) with Iranian Association of Electrical and electronic Engineers (IAEEE) in order to develop scientific and research cooperation.

Aims and Scope

International Journal of Industrial Electronics, Control and Optimization (IECO) is a Peer reviewed journal of advanced and state-of-the-art in the science and engineering of Industrial Electronics, Control and Optimization. Its Scope encompasses the applications of Industrial Electronics, power systems, control, optimization and computational intelligence for the enhancement of industrial and manufacturing system and processes. The scope of the journal include the following:

I. Industrial Electronics

- *Low and high power converters*
- *Renewable energy*
- *Drive control techniques*
- *Techniques for advanced power semiconductor devices*
- *Power quality and utility applications*
- *Communications*
- *Flexible AC Transmission Systems (FACTS)*
- *Control in power electronics*
- *Electromagnetic and thermal performance of electronic power converters*
- *Motion control, robotics, sensors and actuators*
- *Fault detection and diagnosis*
- *Power systems*
- *Factory automation, communication, and computer networks*

II. Control

- *Adaptive control*
- *Control of process systems*
- *Control theory*
- *Data processing*
- *Design of control systems*
- *Hybrid systems*
- *Identification and observation*
- *Intelligent systems*
- *Model-predictive control*
- *Optimal control*
- *Robust control*
- *Fractional order systems*

III. Optimization

- *Ant Colony*
- *Chaos Theory*
- *Evolutionary Computing*
- *Fuzzy Computing*
- *Hybrid Methods*
- *Immunological Computing*
- *Neuro Computing*

- *Particle Swarm*
- *Probabilistic Computing*
- *Rough Sets*
- *Wavelet*

International Journal of Industrial Electronics, Control and Optimization © 2021 IECO
Vol. 4, No. 2, pp. 141-155, April (2021)

An Integrated High Power Self-Equalized Battery Charger Using a Voltage Multiplier and Phase-Shifted Full-Bridge DC-DC Converter for Lithium-Ion Batteries

Mohsen Feizi[1], Reza Beiranvand[2, †], Mahdi Daneshfar[3]

[1,2,3] Faculty of Electrical and Computer Engineering, Tarbiat Modares University, Tehran, Iran

ABSTRACT

Conventional energy storage systems (ESSs) such as super-capacitors and lithium-ion batteries require voltage equalization systems to eliminate voltage imbalances, and bidirectional dc-dc converters to complete the charging process. These separated systems require some sensors, inductors, switches, and transformers. Consequently, the ESSs volumes, prices, and their complexity are dramatically increased by increasing the required series connected batteries count. Here, a self-equalized battery charger is proposed for lithium-ion batteries by combining a voltage multiplier (VM) and a phase-shifted full-bridge (PSFB) dc-dc converter. In the proposed self-equalized battery charger, the voltage multiplier eliminates the voltage imbalances and the PSFB dc-dc converter carries out the charging process. By combining the voltage equalizing and the charging systems into a single system, an integrated converter is obtained which leads to simultaneous charging and equalization operations, power and control sections simplicity, as well as low volume and price. By utilizing the phase-shift control method, zero-voltage-switching (ZVS) operation of power MOSFETs is obtained which leads to high efficiency and low EMI noise. The experimental results for 8 batteries including 48 lithium-ion cells, are in good agreement with the given mathematical analyses and simulation and clearly show the simultaneous charging and voltage equalizing operations, as well.

Article Info

Keywords:
Energy storage system, Equalization, Lithium-Ion batteries, Phase-Shifted full-bridge dc-dc converter, Voltage multiplier, Zero voltage switching (ZVS)

Article History:
Received 2020-07-05
Accepted 2020-09-12

I. INTRODUCTION

Due to high energy storage capability, low self-discharge rate, long lifespan, and no memory effect, lithium-ion batteries are more widely used in low power applications such as laptops and high power systems including electric vehicles (EVs) and hybrid electric vehicles (HEVs) as compared with the convectional batteries. Considering the fact that the voltage value of a single lithium-ion cell, approximately 3.7-4.2 V, is too low, to provide the required power for loads, these cells are connected in series or/and parallel to obtain higher voltages or/and capacities [1]. The ESS consists of two different sections; the battery charger, and the battery management system (BMS). The charger plays an absolutely essential role in the ESS and it needs to have specific features including; high efficiency, low cost, low volume, and high reliability [2-5]. According to the lithium-ion battery charging profile, the battery charger should provide a wide output voltage range [4, 5]. The PSFB dc-dc converter benefits from high power density, high efficiency, and low electromagnetic interference (EMI).

† **Corresponding Author**: beiranvand@modares.ac.ir
Tel:+98-2182884344, Tarbiat Modares University, Faculty of Electrical and Computer Engineering, Tarbiat Modares University, Tehran, Iran

Owing to the aforementioned advantages, the PSFB dc-dc converter is widely used in battery chargers [6-10]. Generally, the dissimilarity between internal resistance, capacity, self-discharge rate, and the environment temperature result in voltage imbalances in series-connected lithium-ion cells[1]. These voltage imbalances are progressively increasing during the discharging/charging intervals. Therefore, some cells may be over-discharged/charged even when the battery pack voltage is withing the safe boundries[10-13]. Consequently, the battery pack capacity is reduced and sometimes an explosion may occur. Thus, for the sake of the batteries and assuring safety, some equalization strategies are crucial to eliminate the voltage imbalances. Due to the aforesaid reasons, battery equalizing has become an important part of the BMS[1].

The equalization topologies are roughly classified into two groups: dissipative and non-dissipative methods [1]. In the dissipative method, the extra energy of over-charged cells is dissipated across some resistors or Zener diodes which decrease the efficiency, and cell capacity but, the equalization speed is relatively high. Besides, there is a considerable number of switches, and gate drivers in the equalizing circuit. Therefore, this method suffers from high cost, and control complexity. In contrast to the previous method, in the non-dissipative method, the additional energy in the over-charged cells is exchanged between cells or between cells and battery pack. As a result, higher efficiency and reliability are achieved. Based on the energy flow direction, the non-dissipative method consists of six major groups including adjacent cell to cell (AC2C), direct cell to cell (DC2C), any cell to any cell (AC2AC), cell to pack (C2P), pack to cell (P2C), and cell to pack to cell (C2P2C). In the AC2C method, the additional energy is transferred between two adjacent cells which may reduce the equalization speed. Moreover, the number of switches and inductors are proportionally increased by increasing the number of series-connected cells. Therefore, this method suffers from control complexity and bulky size [13-17]. In [13] a modified buck-boost converter is used across the two adjacent cells and, the equalization path is controlled by turning the power MOSFETs on and off. [14] proposes a Cuk converter with a fuzzy logic control system, where operation of the employed Cuk converter is similar to the buck-boost converter. In the switched-capacitor converters (SCCs), one switched-capacitor unit is implemented across every two adjacent cells [15]. By switching the complementary MOSFETs across two adjacent cells, the extra energy is transferred between these cells. In the DC2C method, the extra energy can be transferred between different cells in different positions. Consequently, the number of switches is more than twice of the number of cells which results in more control complexity, and larger size [18-21]. In [18] by utilizing a shared multi-secondary windings transformer, energy transportation can be obtained by forming buck-boost and flyback converters. In [19] four power MOSFETs and four diodes connected across each battery. By switching these MOSFETs, the charge transport can be provided for batteries in different paths. [20] proposes an ESS by using an LC resonant tank, where four MOSFETs have been connected across each batter. By turning these switches on and off and operating near the resonant frequency, the DC2C charge equalization is obtained. The additional energy can be exchanged simultaneously among all cells in all positions in the AC2AC method. Although the equalization speed is higher as compared to the AC2C and the DC2C methods, numerous switches, relays, and gate drivers are required [1, 22]. Thus, this method has some drawbacks; high cost, voluminous size, and control complexity, for instance. [1] uses a combination of a boost converter with an LC resonant converter for the voltage equalization. The boost converter is used to regulate the output voltage and the ZCS operation is obtained via the LC resonant converter. By switching the MOSFETs and relays, the equalization paths are obtained in different positions .Operation principle of the given converters in [1] and [22] are the same. In the C2P method, the extra energy is displaced from the over-charged cells to the battery pack [23-27]. A considerable number of switches and transformers are the main drawbacks of this method. Consequently, low efficiency and low modularity are obtained. In [25] the batteries are connected with each other through the multi-secondary windings transformer. The extra energy in batteries is stored in the magnetic core and by switching the MOSFETs it is transferred to the low voltage batteries. Similar to [25] in [26-27], the extra energy is stored in the magnetic core. But, these equalizers employ the flyback converter with one secondary winding transformer. Owing to the transferring energy between the high voltage and low voltage cells by a transformer, the C2P2C method is more efficient and faster than the C2P method [28-31], but it still suffers from a sizeable number of switches and multi windings transformers. The equalization system in [29] is based on a bidirectional flyback dc-dc converter and, therefore, the energy can be transferred either from one battery to another battery or from the pack to the batteries. Also the equalization system in [30-31] consists of two bidirectional dc-dc converters. In [30] the batteries voltages are sensed by one monitoring IC. But, in the [31] this action is done by using a transformer with multi-secondary windings. In these both topologies, the energy is transferred either from one cell to another cell or from the pack to the cells via magnetic cores. In the P2C method, the battery pack provides the required energy for low voltage cells. This method encompasses the full-bridge dc-dc converter [32], multi secondary windings transformer [33], and the VM. The VM based P2C method is also called as integrated converter [13-15, 34-35]. In [32] the required energy for batteries with

low voltages can be achieved from the pack voltage by sensing the batteries voltages and switching the MOSFETs. When one battery has a low voltage value, its bridge MOSFETs are turned-on to get its required energy from the other batteries. In contrast to all of the aforementioned methods, the equalization systems or both charging and equalization sections are integrated into a single system in the integrated method without increasing the number of switches or magnetic components.This feature leads to a simple, small, and competitive. But, all of the previously proposed integrated converters are only applied for low power applications and they have low efficiencies, too This paper proposes a high power self-equalized battery charger by using the PSFB dc-dc converter with a voltage multiplier. By utilizing the proposed converter, both power and control circuits are significantly simplified. Due to the lack of power switches, sensors, and bulky magnetic components in the equalization circuit, both complexity, and cost of the Proposed self-equalized battery charger are significantly reduced.

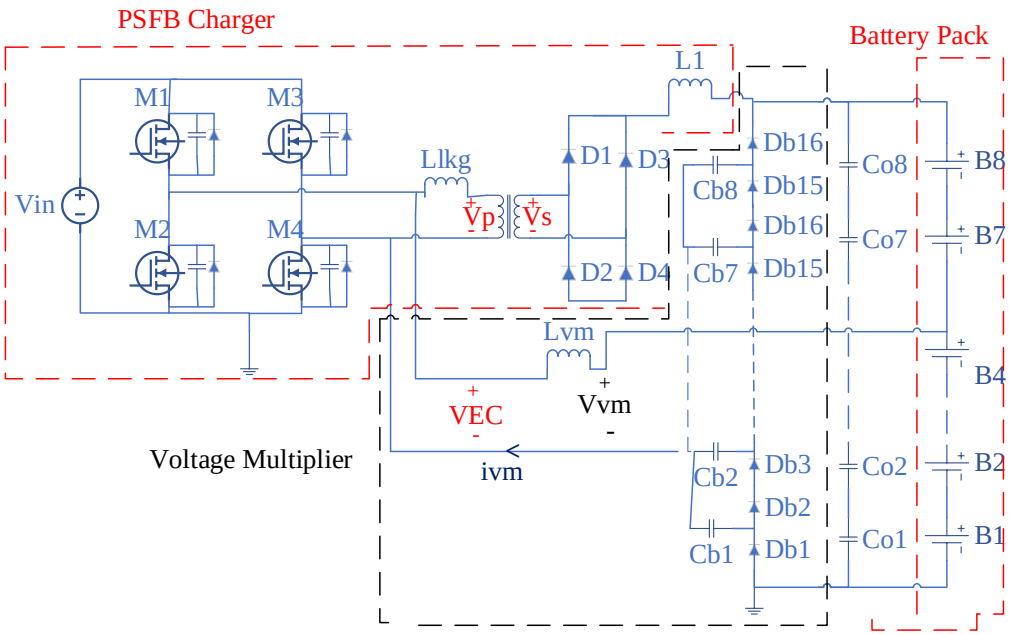

Fig. 1. Proposed self-equalized battery charger for lithium-ion batteries.

By employing the PSFB converter in the charger section, the charger can transfer more power to the battery pack. Moreover, by applying the phase-shift control method, ZVS operation for all of the power MOSFETs is obtained. Thus, the efficiency of the proposed self-equalized battery charger is high and EMI issues are reduced, as well. Also, the switching frequency can be increased to reduce the size of passive components to achieve high power density.

The proposed self-equalized battery charger is introduced in Section II and its major benefits over the traditional equalizers are discussed in Section III. Then, its mathematical analyses and operational principles are explained in Section IV. Finally, the simulation,experimental results, and conclusion and future works are given in Sections V-VII, respectively.

II. Proposed Self-Equalized Battery Charger Configuration

The proposed self-equalized battery charger is shown in Fig .1. By switching power MOSFETs ($M_1 - M_4$) in the charger section, a square voltage waveform is generated across the transformer primary side to adjust the output voltage/current during constant current (CC) and constant voltage (CV) charging intervals, respectively. The current rating of the transformer secondary winding in the current doubler rectifier (CDR) is only half of the load current. Therefore, when the load current is high, the CDR is more efficient than the other rectifiers. Regarding to the CC charging in this project, the CDR is well-suited for this application [6]. By using the phase-shift control strategy in some periods of time each power MOSFETs solely is turned-on. During these periods, the stored energy in the leakage inductance charges and discharges the MOSFETs drain-source capacitors in the other leg. When MOSFET drain-source capacitor is completely discharged completely, its body diode is turned-on. Consequently, the ZVS operation for aforesaid MOSFET is achieved. Therefore, by utilizing the transformer leakage inductance and power MOSFETs drain-source capacitors, the ZVS operation for power MOSFETs is obtained [6-8]. According to Fig. 1, the equalization circuit of the proposed self-equalized battery charger consists of 8 batteries ($B_1 - B_8$), 16 diodes ($D_{b1} - D_{b16}$) in the voltage multiplier, 8 energy-coupling capacitors ($C_{b1} - C_{b8}$), and one equalization inductor (L_{vm}) which limits the equalization current. When an ac input voltage is applied to the voltage multiplier circuit, the

equalization system is activated. As a result, 8 uniform voltages are applied across the batteries. Consequently, all the batteries are properly equalized after some times.

III. Conventional Equalizers Drawbacks in Comparison with the Proposed Self-Equalized Converter

As mentioned earlier, the ESS should have a bidirectional dc-dc converter to charge the batteries and also an equalization system to remove the voltage imbalances across the series-connected batteries. The situation is exacerbated considering that the equalization system should have an equalization circuit and a bidirectional dc-dc converter to eliminate the voltage imbalances completely. Therefore, the ESS suffers from the following drawbacks:

- Numerous MOSFETs

Considering the relatively high cost of the power MOSFETs, the total cost and complexity of the conventional equalizers are high [1], [13-33]. Since the proposed converter does not have power MOSFETs in the equalization circuit, it has lower cost and complexity.

- Magnetic components

In contrast to the conventional equalization circuits [18-22], [29], the proposed integrated converter employs just a small inductor in its equalization circuit. Therefore, the proposed converter benefits from lower cost, lower size and, higher efficiency.

- Lack of the current and the voltage sensors

To detect the batteries voltage and current, some sensors are required in [1], [13-33]. Due to the lack of sensors in the proposed converter, its cost and the control complexity are significantly reduced.

- Control complexity

Traditional ESSs needs separate control systems for both charging and equalization circuits. By using the phase-shift control strategy, and considering lack of power MOSFETs in the proposed equalization circuit, a simple control system is obtained.

A complete comparison between the equalization circuit of the proposed self-equalized battery charger and previously proposed converters is given in Table I that clearly demonstrates the benefits of the proposed battery charger.

IV. Analysis of the Proposed Converter

According to Fig. 1, all of the batteries are simultaneously charged and equalized by utilizing the transformer and the voltage multiplier circuits in the proposed battery charger. The proposed self-equalized battery charger can charger and balance all the batteries during the charging and the discharging intervals. For simplicity, operation of the proposed charger during the charging interval is discussed, here.

A. Simultaneous Charging and Equalization Mechanism

During the CC charging mode, the batteries are charged by I_{CC} and the battery pack voltage is increased from the initial value to V_{CC}. At the same time, the equalization circuit generates the equalization current which charges all the batteries. During the CV charging mode, the battery pack voltage reaches to its maximum value (V_{CV}) and its current is decreased to a preset value. At the same time, the equalization current balances all the series-connected batteries and prevents from any voltage imbalances in the battery pack.

B. Operation of the Converter under the Cells Imbalances Condition

For simplicity and better understanding, the key current and voltage waveforms of the proposed self-equalized battery charger for four batteries are shown in Fig. 2 when B_1 and B_4 have the lowest and highest voltage values, respectively. Besides, the operational modes of the proposed self-equalized charger are depicted just for four batteries which are shown in Fig. 3. However, the simulation and experimental tests are done for 8 batteries, that each of them consists six parallel lithium-ion cells. Based on Fig. 2 and Fig. 3, since in a switching period, i.e. $(t_0 - t_{17})$ the waveforms are the same during $(t_0 - t_9)$ and $(t_9 - t_{17})$ time sub-intervals, only the first sub-interval is analyzed, here. It is noteworthy to mention that, the PSFB dc-dc converter performance in the proposed self-equalized battery charger is roughly similar to the conventional one [6-8]. Therefore, this paper is mainly focused on the equalization circuit analysis.

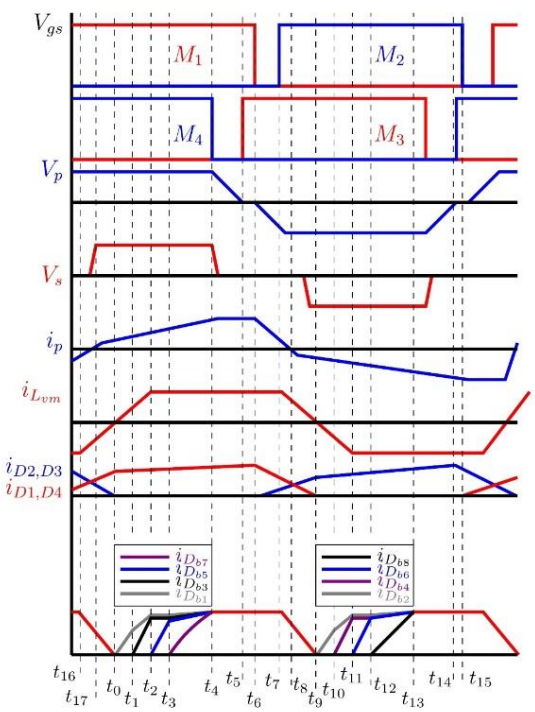

Fig. 2. The key current and voltage waveforms of the proposed battery charger.

Mode 1 $[t_0 - t_1]$: During this state M_1, M_4, D_1, and D_4 are on. Therefore, the battery pack is charged by I_{CC} and its

voltage is being increased. Since B_1 has the lowest voltage value, diode D_{b1} in the equalization circuit is switched on. Consequently, the equalization current charges $B_1 - B_2$, and we can write:

$$\begin{cases} v_{Lvm}(t-t_0) = v_{EC}(t-t_0) - v_{vm}(t-t_0) \\ v_{EC}(t-t_0) = v_p(t-t_0) \\ v_p(t-t_0) = V_{in} \end{cases} \quad (1)$$

Also, by using Equ. (1) and considering volt-balance principle across the equalization inductor

$$\begin{aligned} &< v_{Lvm} >_{T_s} = < v_p >_{T_s} - < v_{vm} >_{T_s} \\ &< v_{vm} >_{T_s} = 0 \end{aligned} \quad (2)$$

Equ. (2) indicates that the $v_{vm}(t)$ has an alternative voltage waveform which is crucial for enabling the equalization circuit. The equalization current can be expressed as follows:

$$i_{vm}(t-t_0) = \frac{V_{T1}}{Z_1}\, e^{-\Upsilon_1(t-t_0)} \sin \omega_{r1}(t-t_0) \quad (3)$$

Also, the diode current can be expressed as below:

$$i_{Db1}(t-t_0) = i_{vm}(t-t_0) \quad (4)$$

The energy-coupling capacitor voltage is given by

$$v_{Cb1}(t-t_0) = \frac{V_{T1}}{Z_1}\,(1 - e^{-\Upsilon_1(t-t_0)} \cos \omega_{r1}(t-t_0)) \quad (5)$$

where

$$\begin{cases} V_{T1} = V_{in} - (V_{B1} + V_{B2} + V_{Cb1t0}) \\ R = R_{vm}\,, \Upsilon_1 = \dfrac{R}{2L_{vm}} \\ Z_1 = \sqrt{\dfrac{L_{vm}}{C_{b1}}}, \omega_{o1} = \dfrac{1}{\sqrt{L_{vm}C_{b1}}}\,, L_{vm} = \sqrt{\omega_{o1}^2 - \Upsilon_1^2} \end{cases} \quad (6)$$

Here, V_{Cb1t0} is the initial value of the $v_{Cb1}(t)$.

During this operational mode, $B_1 - B_4$ and $B_1 - B_2$ are charged by the charging and the equalization currents, respectively. When V_{B1} is large enough, D_{b3} is switched on and this state is finished.

Mode 2 $[t_1 - t_2]$: Fig. 3(b) shows the equivalent circuit of this operational mode. The charger operation is similar to operation mode 1. D_{b3} is switched on in the equalization circuit and, therefore, the equalization current can be expressed as follows:

$$\begin{aligned} i_{vm}(t-t_1) = {} & \frac{V_{T2}\sqrt{2}}{Z_1}\, e^{-\Upsilon_1(t-t_1)} \sin \omega_{r1}(t-t_1) \\ & + \frac{1}{r_D} e^{-\frac{(t-t_1)}{r_D C_{b2}}}\,(V_{Cb1t1} - -V_{B1}) \end{aligned} \quad (7)$$

Also, the energy-coupling capacitors voltages are written

$$\begin{cases} v_{Cb1}(t-t_1) = \dfrac{V_{T2}}{Z_1}(1 - e^{-\Upsilon_1(t)} \cos \omega_{r1}(t-t_1)) \\ v_{Cb2}(t-t_1) = v_{Cb1}(t) + V_{Cb1t1} - V_{Cb2t1} - V_{B1} \end{cases} \quad (8)$$

where,

$$V_{T2} = V_{in} - (V_{B1} + V_{B2} + V_{Cb1t1}) \quad (9)$$

Also, we can write

$$\begin{cases} i_{vm}(t-t_1) = i_{Db1}(t-t_1) + i_{Db3}(t-t_1) \\ i_{Db1}(t-t_1) = \dfrac{V_{T2}}{Z_1\sqrt{2}}\, e^{-\Upsilon_1(t-t_1)} \sin \omega_{r1}(t-t_1) \\ i_{Db3}(t) = i_{Db1}(t) + \dfrac{1}{r_D} e^{-\frac{(t-t_1)}{r_D C_{b2}}}\,(V_{Cb1t1} - V_{Cb2t1} - V_{B1}) \end{cases} \quad (10)$$

When $V_{B1} + V_{B2}$ is large enough, then D_{b5} is switched on and this operation mode is ended.

Mode 3 $[t_2 - t_3]$: The equivalent circuit of this operational state is shown in Fig. 3(c). During this mode, the charger state doesn't change, but D_{b5} is turned on. The equalization current can be expressed as below:

$$\begin{aligned} i_{vm}(t-t_2) = {} & \frac{V_{T3}\sqrt{3}}{Z_1}\, e^{-\Upsilon_1(t-t_2)} \sin \omega_{r1}(t-t_2) + \\ & \frac{1}{r_D} e^{-\frac{(t-t_2)}{r_D C_{b2}}}\,(V_{Cb1t1} - V_{Cb2t1} - V_{B1}) + \\ & \frac{1}{r_D} e^{-\frac{(t-t_2)}{r_D C_{b3}}}\,(V_{Cb2t2} - V_{Cb3t1} - V_{B2}) \end{aligned} \quad (11)$$

Where,

$$V_{T3} = V_{in} - (V_{B1} + V_{B2} + V_{Cb1t2}) \quad (12)$$

The energy-coupling capacitors voltages are given as below:

$$\begin{cases} v_{Cb1}(t-t_2) = \dfrac{V_{T3}}{Z_1}(1 - e^{-\Upsilon_1(t-t_2)} \cos \omega_{r1}(t-t_2)) \\ v_{Cb2}(t) = v_{Cb1}(t-t_2) + V_{Cb1t2} - V_{Cb2t2} - V_{B1} \\ v_{Cb3}(t) = v_{Cb2}(t-t_2) + V_{Cb2t2} - V_{Cb3t2} - V_{B2} \end{cases} \quad (13)$$

Also, we can write:

$$\begin{cases} i_{vm}(t) = i_{Db1}(t-t_2) + i_{Db3}(t-t_2) + i_{Db5}(t-t_2) \\ i_{Db1}(t) = \dfrac{V_{T2}}{Z_1\sqrt{3}}\, e^{-\Upsilon_1(t-t_2)} \sin \omega_{r1}(t-t_2) \\ i_{Db3}(t) = i_{Db1}(t) + \dfrac{1}{r_D} e^{-\frac{(t-t_2)}{r_D C_{b2}}}\,(V_{Cb1t2} - V_{Cb2t2} - V_{B1}) \\ i_{Db5}(t) = i_{Db1}(t) + \dfrac{1}{r_D} e^{-\frac{(t-t_2)}{r_D C_{b3}}}\,(V_{Cb2t2} - V_{Cb3t2} - V_{B2}) \end{cases} \quad (14)$$

When $V_{B1} + V_{B2} + V_{B3}$ is large enough, then D_{b7} is switched on and this operation state ends.

Mode 4 $[t_3 - t_4]$: According to Fig. 3(d), during this operational mode diode D_{b7} in the equalization circuit is turned on and $B_1 - B_3$ are charged by the equalization current through the low side diodes in the equalization network. The equalization current during this state can be expressed as below:

$$\begin{aligned} i_{vm}(t-t_3) = {} & \frac{2V_{T4}}{Z_1}\, e^{-\Upsilon_1(t-t_3)} \sin \omega_{r1}(t-t_3) \\ & + \frac{1}{r_D} e^{-\frac{(t-t_3)}{r_D C_{b2}}}\,(V_{Cb1t1} - V_{Cb2t1} \\ & - V_{B1}) + \\ & \frac{1}{r_D} e^{-\frac{(t-t_3)}{r_D C_{b3}}}\,(V_{Cb2t2} - V_{Cb3t1} - V_{B2}) + \\ & \frac{1}{r_D} e^{-\frac{(t-t_3)}{r_D C_{b4}}}\,(V_{Cb3t3} - V_{Cb4t3} - V_{B3}) \end{aligned} \quad (15)$$

Where,

$$V_{T3} = V_{in} - (V_{B1} + V_{B2} + V_{Cb1t3}) \quad (16)$$

TABLE I

COMPARISON BETWEEN THE PROPOSED SELF-EQUALIZED BATTERY CHARGER AND THE CONVENTIONAL EQUALIZERS

Topology			Charge Capability	Control Complexity	Application	S^{*}	L^{**}	C^{***}	D^{t}	T^{tt}
AC2C	Buck-Boost Converter	[13]	No	Complex	Low Power	2n-2	2n-2	n-1	-	-
	Cuk Converter	[14]				2n-2	2n-2	n	-	-
	Switch-Capacitor Converter	[15]				2n	-	n	-	-
DC2C	Coupled Inductor	[18]	No	Complex	Low Power	2n	-	n	2n	1
	Flying Inductor	[19]				2n+2	-	-	2n+2	-
	Selection Switches	[20]				4n	1	1	3	-
AC2AC		[1]	No	Complex	Low Power	4n+5	2	2	2	-
		[22]				n+2	n	-	n+2	1
C2P	Multi-secondary Windings	[25]	No	Complex	Low Power	n	-	-	1	1
	Flyback Converter	[26]				2n+2	-	-	2n+2	1
C2P2C	Multiple Transformer	[29]	No	Complex	Low Power	2n	-	-	-	2n
	Switched-Transformer	[31]			Medium Power	2n+2	-	2	2	1
P2C	Full-Bridge Converter	[32]	No	Complex	High Power	4n	-	-	-	-
	Integrated Converter	[10]		Simple	Low Power	2	-	n+2	2n	1
		[11]				2	-	n+3	2n	1
		[12]				1	-	n+2	2n+1	1
	Proposed Self-Equalized Battery Charger		Yes	Simple	High Power	4	2	n	2n	1

S^{*}=Switch L^{**}= Inductor C^{***}=Capacitor D^{t}=Diode T^{tt}=Transformer

Also, the energy-coupling capacitors voltage are given as following:

$$\begin{cases} v_{Cb1}(t-t_1) = \dfrac{V_{T3}}{Z_1}\left(1-e^{-\Upsilon_1(t-t_3)}\right)\cos\omega_{r1}(t-t_3) \\ v_{Cb2}(t) = v_{Cb1}(t-t_3) + V_{Cb1t3} - V_{Cb2t3} - V_{B1} \\ v_{Cb3}(t) = v_{Cb1}(t-t_3) + V_{Cb2t1} - V_{Cb3t3} - V_{B2} \\ v_{Cb4}(t) = v_{Cb1}(t-t_3) + V_{Cb3t3} - V_{Cb4t3} - V_{B3} \end{cases} \quad (17)$$

Different components' currents are easily expressed as:

$$\begin{cases} i_{vm}(t-t_3) = i_{Db1}(t) + i_{Db3}(t) + i_{Db5}(t) + i_{Db7}(t) \\ i_{Db1}(t-t_3) = \dfrac{V_{T3}}{2Z_1}\, e^{-\Upsilon_1(t)}\sin\omega_{r1}(t) \\ i_{Db3}(t-t_3) = i_{Db1}(t) + \dfrac{1}{r_D} e^{-\frac{(t)}{r_D C_{b2}}}\left(V_{Cb1t3} - V_{Cb2t3} - V_{B1}\right) \\ i_{Db5}(t-t_3) = i_{Db1}(t) + \dfrac{1}{r_D} e^{-\frac{(t)}{r_D C_{b3}}}\left(V_{Cb2t3} - V_{Cb3t3} - V_{B2}\right) \\ i_{Db7}(t-t_3) = i_{Db1}(t) + \dfrac{1}{r_D} e^{-\frac{(t)}{r_D C_{b4}}}\left(V_{Cb3t2} - V_{Cb4t3} - V_{B3}\right) \end{cases} \quad (18)$$

Modes 5-9 $[t_4 - t_9]$: During these operational modes, the equalization circuit operation is similar to mode 4. But, states of the charger are changed during these operation modes which are roughly the same as in conventional PSFB dc-dc converter. To shorten the discussion, it is not addressed, here.

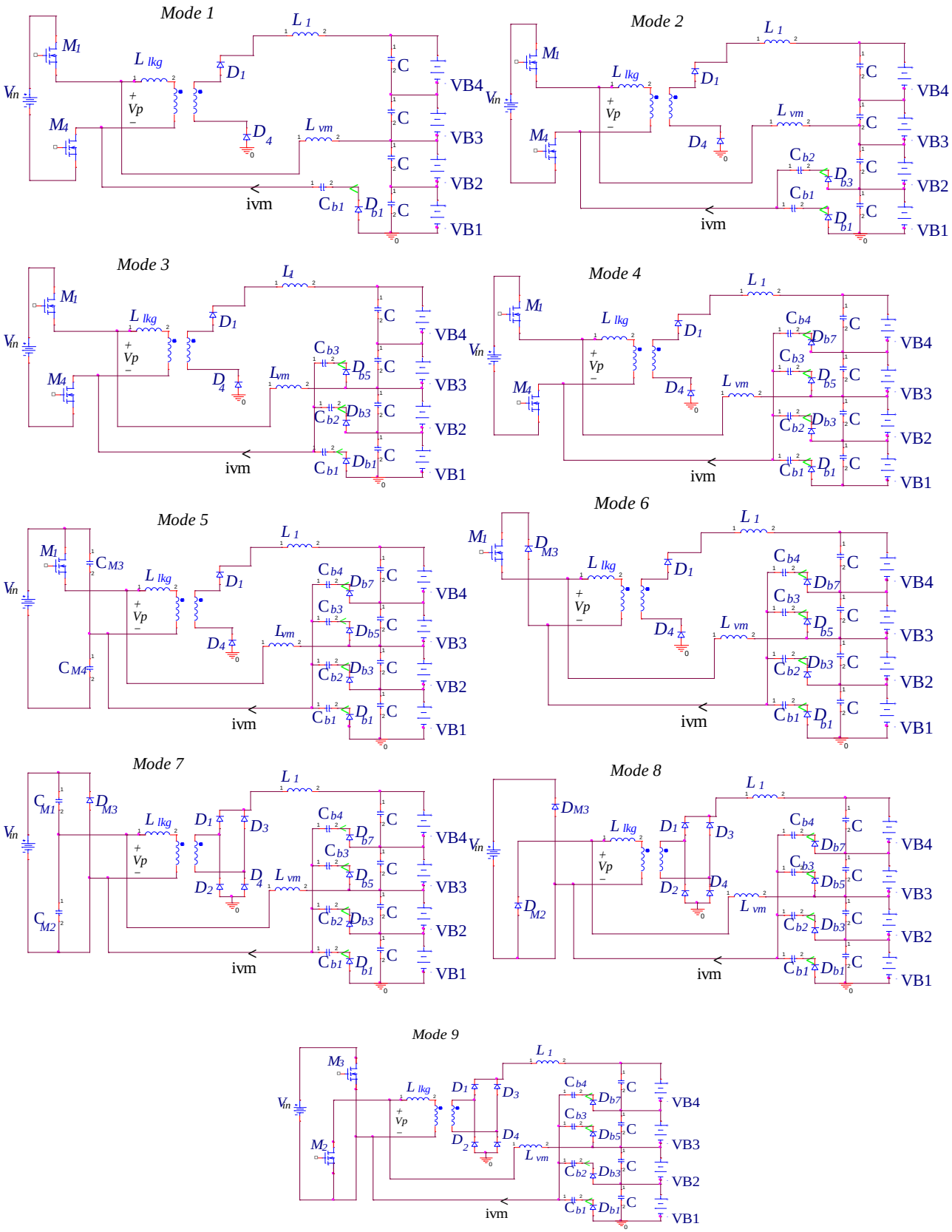

Fig. 3. Operational modes of the proposed self-equalized battery charger.

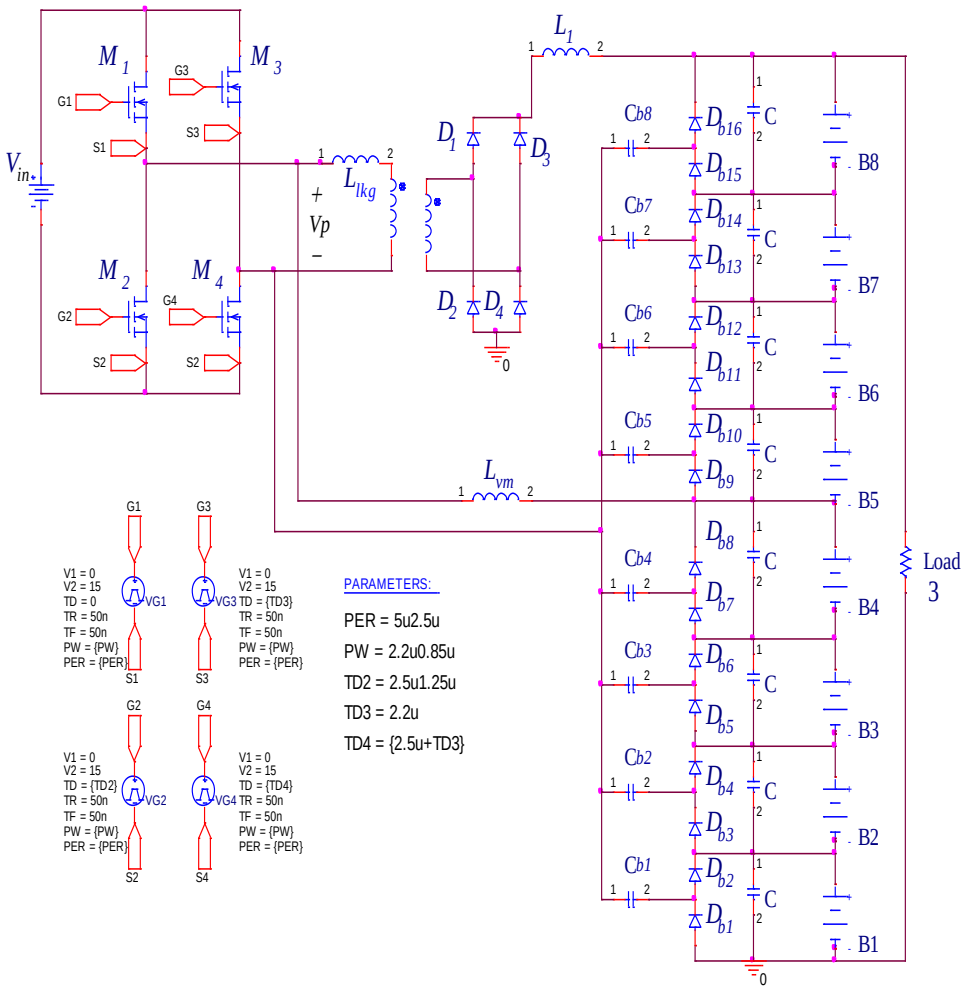

Fig. 4. The simulated circuit of the proposed self-equalized battery charger.

C. *Operation of the Converter under the Cells Balances Condition*

At the time $t = t_b$, when all the batteries equalized, the batteries voltage can be expressed as follow:

$$\begin{cases} V_{Pack} = V_{B1} + V_{B2} + \cdots + V_{B8} \\ V_{B1} = V_{B2} = \cdots = V_{B8} = \dfrac{V_{Pack}}{8} \end{cases} \tag{19}$$

Since the proposed self-equalized battery charger has a symmetrical structure, the energy-coupling capacitors voltages for the i^{th} battery are given by:

$$\begin{cases} v_{Cb(i-1)}(t-t_b) - v_{Cb(i)}(t-t_b) = \dfrac{V_{Pack}}{8} \\ v_{Cb(i-1)}(t-t_b) = -v_{Cb(9-i)}(t-t_b) \\ v_{Cb(i)}(t-t_b) = \dfrac{9-2i}{16} V_{Pack} \end{cases} \tag{20}$$

where $1 \leq i \leq 8$,

D. *Design Considerations*

The main parameters for designing the proposed self-equalized battery charger are listed in Table II. Since the voltage of a single lithium-ion cell is around *3.7- 4.2 V*, for producing *8* uniform voltages, the applied voltage to the equalization circuit must have a square voltage waveform with an amplitude of *3.7 V*. Thus, the equalization inductor is easily identified:

$$L_{vm} = \frac{v_{Lvm} \times D \times T_s}{\Delta I_{Lvm}} = \frac{200 \times 0.4 \times 5}{4} = 110\ \mu H \tag{21}$$

Also, the energy-coupling capacitors are calculated as follow:

$$C_{bi} = \frac{T_s \times D \times \Delta i_c}{\Delta v_{cb}} = \frac{T_s \times D \times i_{Lvm}}{(9-2i) \times \Delta v_{cb}} = 470nF \tag{22}$$

The main transformer secondary side voltage is calculated as follow:

$$V_s = \frac{V_{pack,mim}}{D} = 200V \tag{23}$$

So, the main transformer turns ratio is given by

$$n_1 = \frac{N_s}{N_p} = \frac{\frac{V_{pack,min}}{D}}{V_{in.min}} = 0.26 \quad (24)$$

Also, the output filter inductor value is given by

$$L_1 = \frac{T_s \times V_{B,min} \times D}{2\Delta i_L} = \frac{5\times23\times0.44}{3.6} \approx 15\mu H \quad (25)$$

V. Simulation Results

The performance of the proposed self-equalized battery charger is verified by simulation the converter by using PSpice, as shown in Fig. 4. The key parameters are listed in Table II. Some parameters have been optimized via simulation. The simulation is done for three different conditions including low voltage imbalances, high voltage imbalances, and light load (10 % of nominal load) with the maximum input voltage conditions.

During the first test, the batteries voltages are *2.8, 2.85, 2.9, 2.95, 3, 3.1, 3.15, 3.2* volts, respectively. Fig. 5 verifies the equalization operation of the proposed self-equalized battery charger during this test.

Besides, some diodes currents waveforms in the equalization circuit are shown in Fig. 6. According to this figure, the diode which connects to the battery with the lowest voltage value is turned on before the other diodes to charge and increase its battery voltage. The power MOSFETs currents and voltages waveforms are also shown in Fig. 7. According to the Fig. 7, the ZVS operation for all power MOSFETs is obtained. Therefore, the proposed self-equalized battery charger benefits from high efficiency during the simultaneous charging and equalization operation and high switching frequency is possible to achieve high power density.

TABLE II
The Key Parameters Value of the Proposed Self-Equalized Battery Charger

Description	Symbol	Value
Input Voltage	V_{in}	*200-250 V*
Battery Pack Voltage	V_{pack}	*23-33.6 V*
Constant Current Charging	I_{CC}	*10 A*
Constant Voltage Charging	V_{CV}	*33.6 V*
Switching Frequency	f_{sw}	*200 kHz*
Capacitor Voltage Ripple	ΔV_{Cb}	*1.5 mV*
Output Inductor Current Ripple	ΔI_{L1}	*3.6 A*
Equalizer Inductor	L_{vm}	*110 µH*
Energy-Coupling Capacitors	C_b	*470 nF*
Dead-Time	T_d	*200 ns*
Transformer Turns Ration	n	*0.26*
Batteries	B	*10 mF*
Output Inductor	L_1	*15 µH*

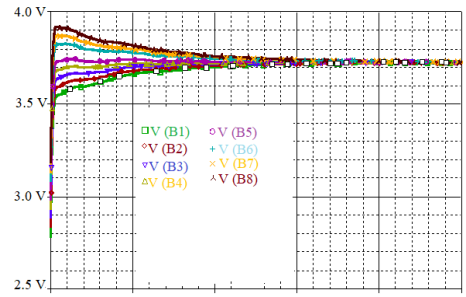

Fig. 5. The resultant batteries voltages of the proposed charger with low voltage imbalances at $V_{in} = 200\,V,\ f_s = 200\,kHz$.

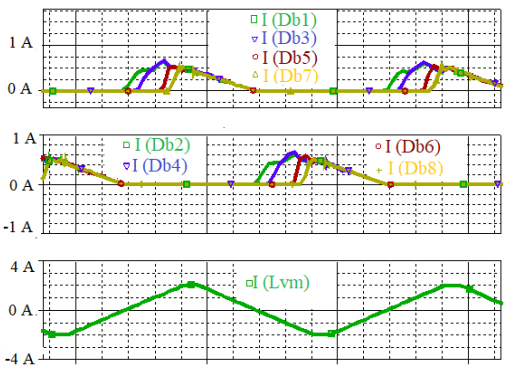

Fig. 6. The key current waveforms of the equalization circuit with low voltage imbalances at $V_{in} = 200\,V$, $f_s = 200\,kHz$.

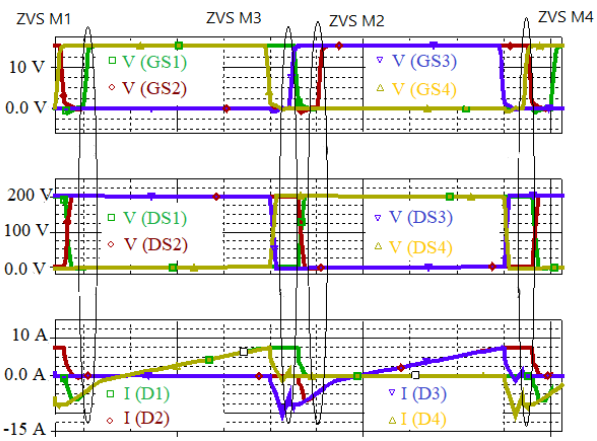

Fig. 7. The voltage and current waveforms of the power MOSFETs in the proposed self-equalized battery charger at $V_{in} = 200\,V, I_{out} = 10\,A,\ f_s = 200\,kHz$.

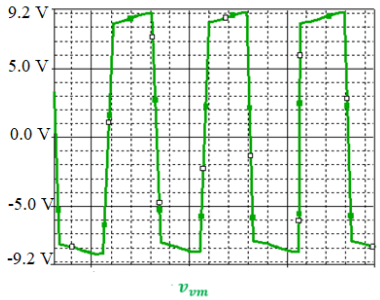

Fig. 8. The applied ac voltage to the VM network under low imbalance condition at $V_{in} = 200\,V$, $f_s = 200\,kHz$.

The applied ac voltage to the VM network is shown in the Fig. 8. According to this figure, the PSFB charger generates the required ac voltage to enable the VM network.

In the second test, the batteries voltages are *1.5, 2, 2.5, 2.8, 2.9, 3, 3.9, 4* volts, respectively. Fig. 9 validates the equalization operation of the proposed self-equalized battery charger under this test. In addition, some equalization circuit diodes currents waveforms are shown in Fig. 10. Based on Fig. 6 and Fig.10, the equalization current is shared between batteries proportional to their voltages. Consequently, the lowest battery with the lowest voltage value receives the maximum portion of the equalization current. Besides, Fig.6 and Fig. 10 indicate that for *n* batteries the amplitude of the equalization current remains constant. This feature results in high reliability and a simple control system without any current sensor.

The applied ac voltage to the VM network under high voltage imbalance condition is shown in the Fig. 11. According to this figure, the PSFB charger generates the required ac voltage to enable the VM network.

In the third case, the ZVS operation of power MOSFETs under the light load condition is tested. The power MOSFETs currents and voltages under this condition are shown in Fig. 12. According to this figure, the ZVS operation for all power MOSFETs is roughly obtained. The measured efficiencies of the proposed self-equalized battery charger under two different conditions in the PSpice software are listed in Table IV.

VI. EXPERIMENTAL RESULTS

In this paper, *48* lithium-ion cells are employed for experimental implementation. 6 lithium-ion cells are connected in parallel to form a battery and 8 batteries are connected in series to form the battery pack. To verify the simulation results, a *300 W* prototype was implemented as shown in Fig. 13. The prototype components and elements are listed in Table III. In this study, the proposed self-equalized battery charger works at a constant switching frequency and a constant duty cycle. Therefore, the proposed

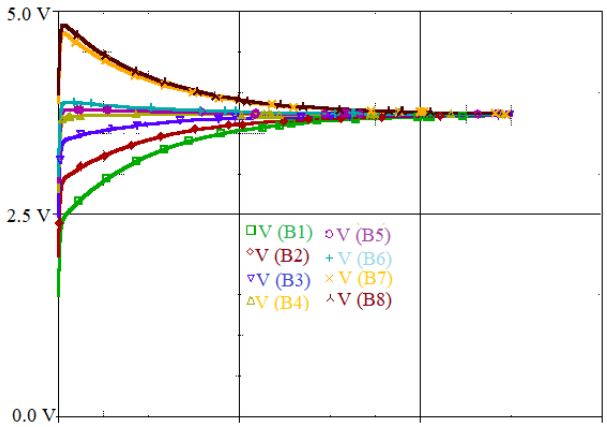

Fig. 9. The resultant batteries voltages of the charger with high voltage imbalances at $V_{in} = 200\,V$, $f_s = 200\,kHz$.

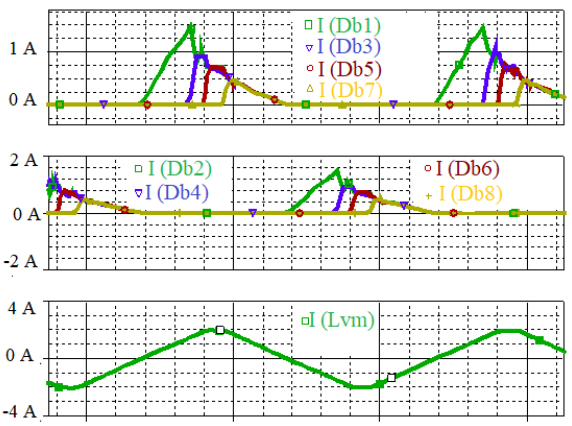

Fig. 10. The key current waveforms of the equalization circuit with high voltage imbalances at $V_{in} = 200\,V$, $f_s = 200\,kHz$.

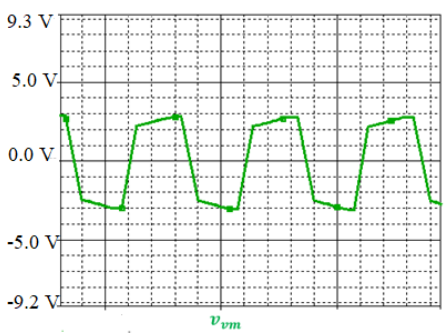

Fig.11. The applied ac voltage to the VM network under high imbalance condition at $V_{in} = 200\,V$, $f_s = 200\,kHz$.

charger benefits from control simplicity. Generally, the equalization current is much smaller than the charging current, consequently, the equalization network power losses are much smaller than the charger circuit losses.

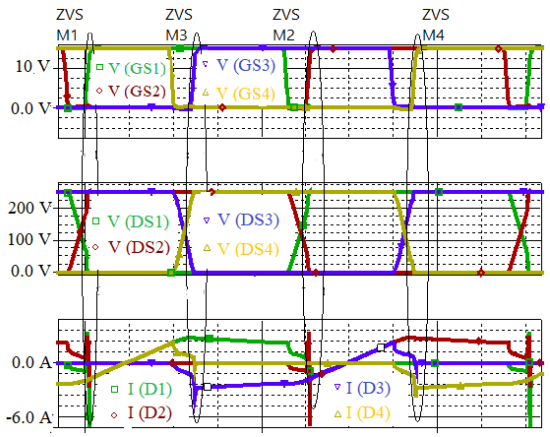

Fig. 12. The voltage and current waveforms of the power MOSFETs in the proposed self-equalized battery charger at $V_{in} = 250\,V, I_{out} = 1\,A,\ \ f_s = 200\,kHz$.

A. Simultaneous equalization and charging test

This test is done under voltage imbalances condition. By using the current probe (PA-677, PINTEK), the equalization current of all batteries are measured. The batteries voltages, $V_{B1} - V_{B4}$, are equal to *2.5, 2.6, 2.7, 2.8, 2.8, 2.9, 2.9, 3*, respectively. During the constant current charging process, the battery pack is charged by the $I_{CC} = 9\,A$ and the battery pack voltage is increased from *22.2 V* to *29.7 V*. During this condition, the voltage imbalances are being removed by the equalization current. During the constant voltage charging process, the charging current is reduced to the pre-set value and the voltage imbalances are reduced to *24 mV*. The equalization current is shown in Fig. 14 and the resultant voltages and the equalization current of some batteries of this test are depicted in Fig. 15.

Considering this fact that the equalization current is much smaller than the charging current, the power losses in the equalization circuit can be neglected. Therefore, the majority of the power is transferred to the battery pack by the charging circuit. The voltage multiplier losses distribution is shown in the Fig. 16. Based on this figure, when the total power in increased the equalization circuit losses are proportionally reduced and they can be neglected. Consequently, the efficiency of the charger circuit is predominant. Fig. 17 and Fig. 18 show the power MOSFETs voltage waveforms under the nominal load with the nominal input voltage, and light load with the maximum input voltage conditions, respectively. According to Fig. 17 and Fig. 18, the ZVS operation of the power MOSFETs is obtained under these conditions. Therefore, the proposed self-equalized battery charger benefits from high efficiency and low EMI noise, as well.

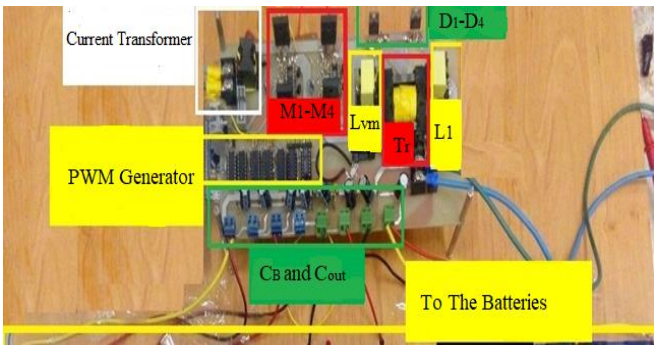

Fig.13. The *300 W* prototype of the proposed self-equalized battery charger for *48* lithium-ion cells.

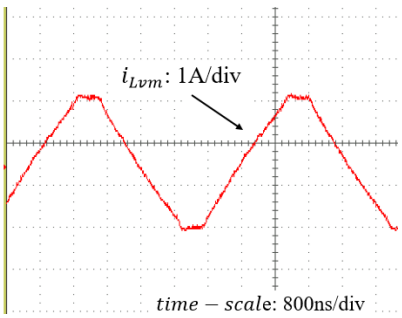

Fig.14. Experimental equalization current at $V_{in} = 200\,V,\ f_s = 200\,kHz$, and $I_{CC} = 9\,A$.

TABLE III
THE COMPONENTS LIST OF THE PROPOSED SELF-EQUALIZED BATTERY CHARGER

Section	Components	Value & Part
Charging Circuit	$M_1 - M_4$	*IRFP460*
	$D_1 - D_4$	*MUR1520G*
	T_r	*ETD29, n = 0.26*
	Output Inductor	*PQ2016,* $L_1 =$ 15 µ*H*
Equalization Circuit	$D_{b1} - D_{b16}$	*SM5820*
	$C_{b1} - C_{b8}$	*Tantalum, 470 nF, 50 V*
	C_B	*470 µF, 50 V*
	L_{vm}	*PQ2020, 110 µH*
Phase-Shifted Modulator	*JK Flip-Flop*	*74HC73*
	RS Flip-Flop	*SN7470*
	Mono Stable	*74HC4538*
	And Gate	*SN74HC04N*
Batteries	---	*INR18650, 2200 mA.h*
Current Probe	---	*PINTEK, PA-677*
Oscilloscope	---	*HANTEK, DSO5102P*
Multi-Meter	---	*SANWA, CD771* *MASTECH, MS8229*

The experimental efficiencies of the proposed self-equalized battery charger for the two aforementioned conditions are listed in Table IV. A comparative study between the

proposed integrated converter experimental results and previous integrated converters experimental results is shown in the Table V. This table demonstrate the effectiveness of the proposed integrated converter over the traditional integrated converters, clearly.

TABLE IV
THE MEASURED EFFICIENCIES OF THE PROPOSED SELF-EQUALIZED BATTERY CHARGER UNDER TWO DIFFERENT CONDITIONS

	Input Voltage	Output Power	Output Current	Efficiency
Simulation	*200 V*	*330 W*	10 A	94 %
	250 V	*33 W*	1 A	87 %
Experimental	*200 V*	*300 W*	10 A	89 %
	250 V	*30 W*	1 A	83 %

TABLE V
COMPARISON BETWEEN EXPERIMENTAL RESULTS OF THE PROPOSED INTEGRATED CONVERTER AND THE PREVIOUS RESEARCHES

Reference	Power	Number of Cells	Charging Capability	Efficiency
[10]	10 W	12	No	At best case 75 %
[11]	3 W	8	No	At best case 70%
[12]	6 W	8	No	At best case 68%
[34]	3 W	3	Yes	At best case 84 %
Proposed Converter	300 W	48	Yes	83-89 %

VII. CONCLUSION AND FUTURE WORKS

In this study, a novel self-equalized battery charger using a voltage multiplier and the PSFB dc-dc converter for lithium-ion batteries is proposed. By utilizing the main transformer and the equalization circuit inductor, the battery pack is charged and its series connected cells are equalized simultaneously by the charging and the equalization currents, respectively. The equalization circuit generates 8 uniform voltages across the batteries and equalizes their voltages. By combining the charging and the equalization circuits, an integrated converter has been obtained which provides some major benefits over the conventional equalizers including the simultaneous charging and equalization operations, control simplicity, high efficiency, low cost, and low size without using power MOSFETs or bulky magnetic components in the equalization circuit. Finally, the theoretical analyses were validated with the simulation and the experimental results for 48 lithium-ion cells.

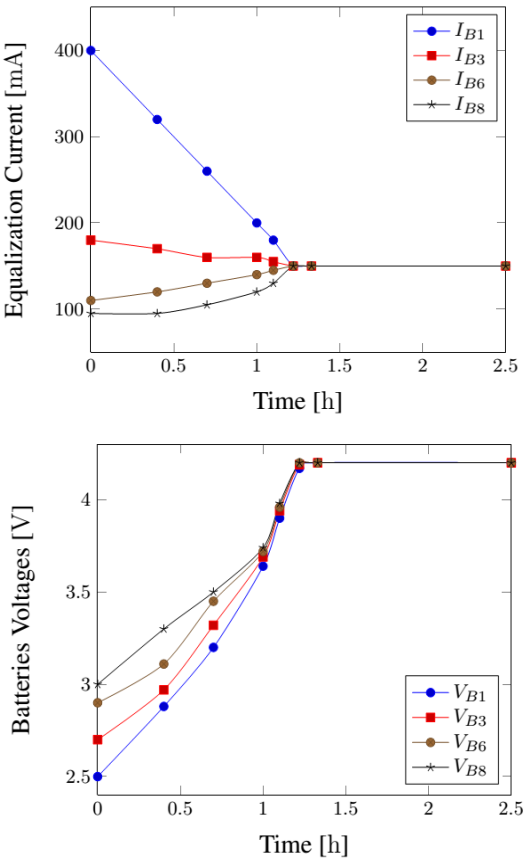

Fig.15. The resultant batteries voltages and the equalization currents in this test.

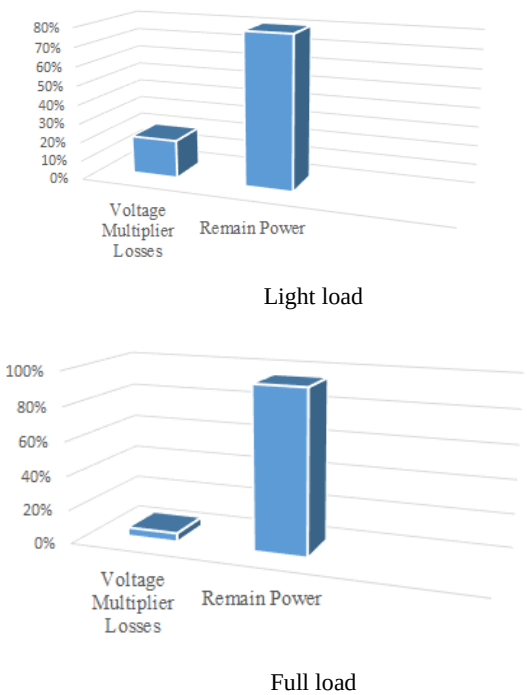

Fig.16. The equalization circuit losses distribution under different load conditions.

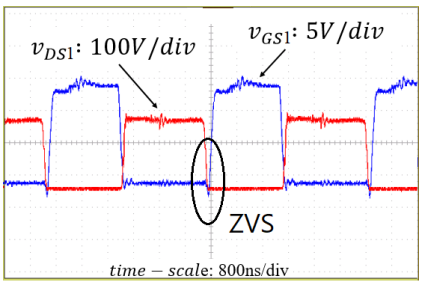

I. M_1

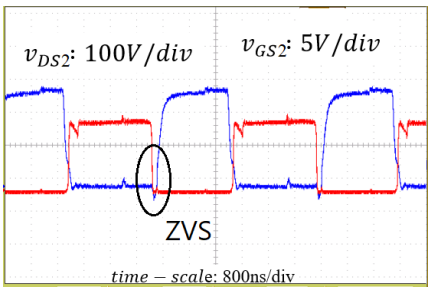

II. M_2

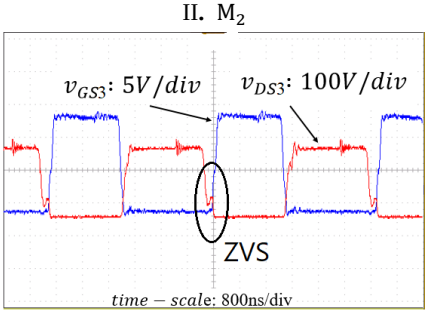

III. M_3

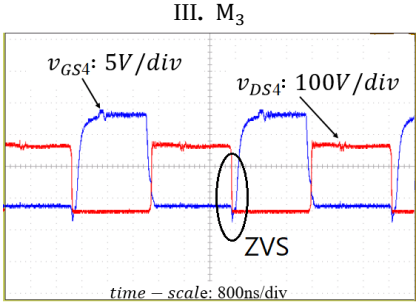

IV. M_4

Fig.17. Different voltage waveforms of the power MOSFETs at $V_{in} = 200\ V, I_{out} = 10\ A,$ and $f_s = 200\ kHz.$

Regarding the abovementioned features and capabilities, some extensions for the near future are increasing the equalization speed by increasing the equalization current without the violation of power conduction losses, burst-mode operation of the converter under full charging conditions, small signal modeling and closed-loop control, and introducing novel voltage multiplier networks with lower components count for voltage balancing of high power EV applications.

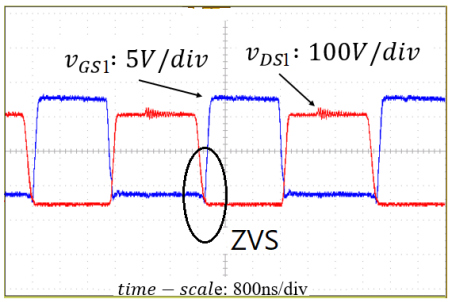

I. M_1

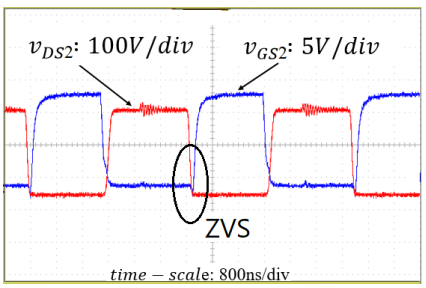

II. M_2

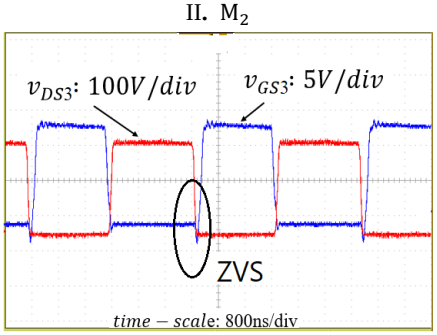

III. M_3

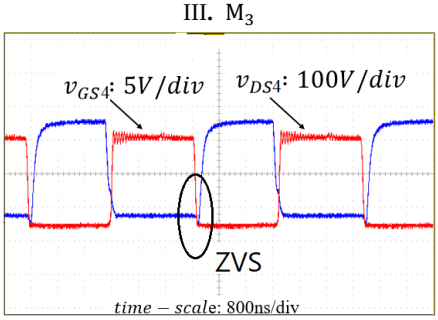

IV. M_4

Fig.18. Different voltage waveforms of the power MOSFETs at $V_{in} = 250\ V, I_{out} = 1\ A,$ and $f_s = 200\ kHz.$

REFERENCES

[1] Shang, Y., Zhang, C., Cui, N., & Guerrero, J. M, "A cell-to-cell battery equalizer with zero-current switching and zero-voltage gap based on quasi-resonant LC converter and boost converter," *IEEE Trans. Power Electron.*, Vol. 30, No. 7, pp. 3731-3747, Aug. 2014

[2] Haghbin, S., Khan, K., Lundmark, S., Alaküla, M., Carlson, O., Leksell, M., & Wallmark, O, "Integrated chargers for EV's and PHEV's: examples and new

solutions," *XIX International Conference on Electrical Machines-ICEM*, pp. 1-6, Sep. 2010

[3] Musavi, F., Craciun, M., Gautam, D. S., Eberle, W., & Dunford, W. G, "An LLC resonant DC–DC converter for wide output voltage range battery charging applications," *IEEE Trans. Power Electron*., Vol. 28, No. 12, pp. 5437-5445, Mar. 2013

[4] Rachid, Aziz, Hassan El Fadil, and Fouad Giri, "Dual stage CC-CV charge method for controlling dc-dc power converter in BEV charger," *IEEE Mediterranean Electrotechnical Conference (MELECON)*, Vol. 2, pp. 74-79, May. 2018

[5] Taheri, Asghar, and Nader Asgari, "Sliding Mode Control of LLC Resonant DC-DC Converter for Wide Output Voltage Range in Battery Charging," *International Journal of Industrial Electronics, Control and Optimization (IECO)*, Vol. 2, No. 2, pp. 127-136, Jan. 2019

[6] Lin, B-R., Kevin Huang, and David Wang, "Analysis and implementation of full-bridge converter with current doubler rectifier," *IEEE Trans. Ind. Electron.*, Vol. 152, No. 5, pp. 1193-1202, Sep. 2005

[7] Zhao, L., Li, H., Wu, X., & Zhang, J, "An improved phase-shifted full-bridge converter with wide-range ZVS and reduced filter requirement," *IEEE Trans. Ind. Electron.*, Vol. 65, No. 3, pp. 2167-2176, Aug. 2017

[8] Lee. Il-Oun, "Hybrid PWM-resonant converter for electric vehicle on-board battery chargers," *IEEE Trans. Power Electron*., Vol. 31, No. 5, pp. 3639-3649, Jul. 2015

[9] Lee, Il-Oun, "Hybrid DC–DC converter with phase-shift or frequency modulation for NEV battery charger," *IEEE Trans. Ind. Electron*., Vol. 63, No. 2, pp. 884-893, Sep. 2015

[10] Uno, Masatoshi, and Akio Kukita, "Double-switch equalizer using parallel-or series-parallel-resonant inverter and voltage multiplier for series-connected Supercapacitors," *IEEE Trans. Power Electron*., Vol. 29, No. 2, pp. 812-828, Apr. 2013

[11] Uno, Masatoshi, and Koji Tanaka, "Double-switch single-transformer cell voltage equalizer using a half-bridge inverter and a voltage multiplier for series-connected Supercapacitors," *IEEE Trans. Veh. Technol*., Vol. 61, No. 9, pp. 3920-3930, Aug. 2012

[12] Uno, Masatoshi, and Akio Kukita, "Single-switch single-transformer cell voltage equalizer based on forward–flyback resonant inverter and voltage multiplier for series-connected energy storage cells," *IEEE Trans. Veh. Technol*., Vol. 63, No. 9, pp. 4232-4247, Mar. 2014

[13] Lee, Y-S., and G-T. Cheng, "Quasi-resonant zero-current-switching bidirectional converter for battery equalization applications," *IEEE Trans. Power Electron*., Vol. 21, No. 5, pp. 1213-1224, Sep. 2006

[14] Lee, Yuang-Shung, and Ming-Wang Cheng, "Intelligent control battery equalization for series connected lithium-ion battery strings," *IEEE Trans. Ind. Electron*., Vol. 52, No. 5, pp. 1297-1307, Sep. 2005

[15] Shang, Y., Cui, N., Duan, B., & Zhang, C, "Analysis and optimization of star-structured switched-capacitor equalizers for series-connected battery strings,". *IEEE Trans. Power Electron*., Vol. 33, No. 11, pp. 9631-9646, Dec. 2017

[16] Hua, C. C., Chuang, C. W., & Fang, Y. H, "Low-cost switched capacitor charge equaliser with cancellation mechanism of alternating current," *IET Power Electronics*, Vol. 9, No. 7, pp. 1454-1461, Jun. 2016

[17] Moghaddam, Ali Farzan, and Alex Van den Bossche, "A Battery Equalization Technique Based on Ćuk Converter Balancing for Lithium Ion Batteries," *International Conference on Modern Circuits and Systems Technologies (MOCAST)*, Vol. 8, pp. 1-4, May. 2019

[18] Park, S. H., Park, K. B., Kim, H. S., Moon, G. W., & Youn, M. J, "Single-magnetic cell-to-cell charge equalization converter with reduced number of transformer windings," *IEEE Trans. Power Electron.*, Vo. 27, No. 6, pp. 2900-2911, Dec. 2011

[19] Yarlagadda, Sriram, Tom T. Hartley, and Iqbal Husain, "A battery management system using an active charge equalization technique based on a DC/DC converter topology," *IEEE Trans. Ind. Applica*, Vol. 49, No. 6, pp. 2720-2729, May. 2013

[20] Yu, Yanqi, Raed Saasaa, Ashraf Ali Khan, and Wilson Eberle, "A Series Resonant Energy Storage Cell Voltage Balancing Circuit," *IEEE J. Emerg Sel. Top. Power Electron*., May. 2019

[21] Chuang, Po-Chun, Yao Ching Hsieh, You-Chun Huang, and Chin-Sien Moo, "Charge-Equalization Circuit with Single Resonant Energy Tank for Series Batteries," *ICIT*, pp. 394-398, 2019

[22] Kim, Moon-Young, Jun-Ho Kim, and Gun-Woo Moon, "Center-cell concentration structure of a cell-to-cell balancing circuit with a reduced number of switches," *IEEE Trans. Power Electron.*, Vol. 29, No. 10, pp. 5285-5297, Nov. 2013

[23] Cai, Chunjian, Junyang Ma, Jianglin Nie, Yupei Wan, Lan Ma, and Zeliang Shu, "A Battery Equalizing Circuit Based on Multi-Winding Transformer," *IEEE Applied Power Electronics Conference and Exposition (APEC)*, pp. 1456-1460, Mar. 2020

[24] Tavakoli, Atrin, Sayed Ali Khajehoddin, and John Salmon, "A Modular Battery Voltage-Balancing System Using a Series-Connected Topology," *IEEE Trans. Power Electron.*, Vol. 35, No. 6, pp. 5952-5964, Oct. 2019

[25] Lim, C. S., Lee, K. J., Ku, N. J., Hyun, D. S., & Kim, R. Y, "A modularized equalization method based on magnetizing energy for a series-connected lithium-ion battery string," *IEEE Trans. Power Electron.*, Vol. 29, No. 4, pp. 1791-1799, Jun. 2013

[26] Imtiaz, A. M., & Khan, F. H, "Time shared flyback converter" based regenerative cell balancing technique for series connected Li-ion battery strings," *IEEE Trans. Power Electron.*, Vol. 28, No. 12, pp. 5960-5975, Apr. 2013

[27] Lou, F., Song, Z., Wei, Y., Zhang, G., Wang, J., & Liang, H, "Design of Liquid Metal Battery Equalization System Based on Bidirectional Flyback Circuit," *IEEE Conference on Energy Conversion (CENCON)*, pp. 59-63, Oct. 2019

[28] Zhan, Huaxia, Xin Xiang, Simon M. Lambert, Volker Pickert, Haimeng Wu, and Xiang Lu, "A cascaded transformer-based equalisation converter for series connected battery cells," Vol. 6, No. 6, 2016

[29] Chang, Y. C., Wang, S. C., Liu, Y. H., & Luo, Y. F, "An Active Fast Equalizer for Series-Connected Batteries with Adaptive Balancing Current Control," *IEEE Transportation Electrification Conference and Expo, Asia-Pacific (ITEC Asia-Pacific)*, pp. 1-5, Jun. 2018

[30] Anno, T., & Koizumi, H, "Double-input bidirectional DC/DC converter using cell-voltage equalizer with flyback transformer," *IEEE Trans. Power Electron.*, Vol. 30, No. 6, pp. 2923-2934, Apr. 2014

[31] Hannan, M. A., Hoque, M. M., Peng, S. E., & Uddin, M. N, "Lithium-ion battery charge equalization algorithm for electric vehicle applications," *IEEE Trans. Ind. Applica.*, Vol. 53, No. 3, pp. 2541-2549, Feb. 2017

[32] Young, C. M., Chu, N. Y., Chen, L. R., Hsiao, Y. C., & Li, C. Z, "A single-phase multilevel inverter with battery balancing," *IEEE Trans. Ind. Electron.*, Vol. 60, No. 5, pp. 1972-1978, Jul. 2012

[33] Einhorn, M., Roessler, W., & Fleig, J, "Improved performance of serially connected Li-ion batteries with active cell balancing in electric vehicles.," *IEEE Trans. Veh. Technol*, Vol. 60, No. 6, pp. 2448-2457, May. 2011

[34] Liu, J., Xu, M., Zeng, J., Wu, J., & Eric, C. K. W, "Modified voltage equaliser based on Cockcroft–Walton voltage multipliers for series-connected Supercapacitors," *IET Electrical Systems in Transportation*, Vol. 8, No. 1, pp. 44-51, May. 2017

[35] M. Uno and K. Yashiro, "Tapped-Inductor-Based Single-Magnetic Bidirectional PWM Converter Integrating Cell Voltage Equalizer for Series-Connected Supercapacitors," *IEEE Trans. Power Electron.*, vol. 35, No. 12, pp. 13157-13171, Dec. 2020

Mohsen Feizi was born in Kurdistan, Iran, in 1995. He received his B.Sc. degree in electrical engineering from the Faculty of Electrical and Mechanical Engineering, Amir Kabir University of Technology, Tehran, Iran, in 2017. He received his M.Sc. degree in Electrical Engineering (Power electronics & Electrical Machinery) from the Faculty of Electrical & Computer Engineering, Tarbiat Modares University, Tehran, Iran, in 2020. His current research interests include electric vehicle battery charger, electric vehicle DC-DC converter (APU), soft switching DC-DC Converters, resonant converters, design and control of power electronic converters.

Reza Beiranvand (SM'08–M'12) received the M.Sc. and Ph.D. degrees in Electrical Engineering (Electronics) from Sharif University of Technology, Tehran, Iran, in 1999 and 2010, respectively. From 2010 to 2012, he was a Postdoctoral Research Fellow with the Electrical Engineering College, Sharif University of Technology, Tehran, Iran. From 1999 to 2007, he was an engineer at R&D centers of PARS-Electric and RADIO SHAHAB MFGs, Tehran, where he was engaged in designing the CRT, LCD, and LED TVs based on the ST and NXP semiconductors, and also on high power factor resonant converters for ballasts and LED applications.
Since 2012, he has been with the Faculty of Electrical and Computer Engineering, Tarbiat Modares University, Tehran, Iran, where he is currently an Assistant Professor and Head of the Power Group and Power Electronics Converters (PEC) research Lab. He was the 2016 IEEE Outstanding reviewer and from 2017-2019 he was the IEEE Consultant in TMU. His current research interests include SMPS, modeling and control of the power electronics converters, resonant converters and soft switching techniques, switched-capacitor converters, electromagnetic devices, and PV-based renewable energy systems.

Mahdi Daneshfar was born in Arak, Iran, in 1992. He received his B.Sc. degree in electrical engineering from the Faculty of Engineering, Arak University, Arak, Iran, in 2015. He received his M.Sc. degree in Electrical Engineering (Power electronics & Electrical Machinery) from the Faculty of Electrical & Computer Engineering, Tarbiat Modares University, Tehran ,Iran, in 2017. His current research interests include high step-up DC-DC converters, soft switching, resonant converters, design and control of power electronic converters.

IECO
This page intentionally left blank.

International Journal of Industrial Electronics, Control and Optimization © 2021 IECO
Vol. 4, No. 2, pp. 157-165, April (2021)

Multi-Channel sEMG-Based Joint Angles Estimation of Lower Limbs Utilizing Bidirectional Recurrent Neural Network

Rohollah Hasanzadeh Fereydooni [1,†], Hassan Siahkali[2], Heidar Ali Shayanfar [3], Amir Hooshang Mazinan [4]

[1,2,3,4] Department of Electrical Engineering, South Tehran Branch, Islamic Azad University, Tehran, Iran.

ABSTRACT

Nowadays, rehabilitative robots, which have received more attention in the field of rehabilitation, can help patients in the rehabilitation training and reduce therapist workload. This paper suggests the use of surface electromyography (sEMG) signals and a bidirectional neural network (BRNN) for the estimation of the joint angles of lower limbs. The input of BRNN is the preprocessed sEMG signals and its outputs are the estimated joint angles of knee, ankle, and hip. In order to prove the usefulness of the BRNN, four normal and healthy subjects and two patients suffering from spinal cord injury (SCI) took part in the experimental tests. The healthy subjects exercised two movement modes including leg extension and treadmill at various loads and speeds, while the SCI subjects conducted only the treadmill exercise. To record useful information, seven leg muscles were used and then the hip, knee, and ankle joint angles were acquired at the same time. The experimental results showed the satisfactory performance of the proposed method in the estimation of joint angles by employing surface electromyography signals for both groups. The proposed estimation method can be used to control the rehabilitation robot of SCI subjects based on sEMG signals.

Article Info

Keywords:
Bidirectional recurrent neural network, Joint angle estimation, Rehabilitation robots, sEMG signals

Article History:
Received 2020-04-11
Accepted 2020-11-11

I. INTRODUCTION

Nowadays, rehabilitative robots, which are increasingly drawing attention in the field of rehabilitation, can help patients in rehabilitation training and reduce therapist workload [1-3]. Presently, rehabilitation robots can be chiefly separated into two types: passive exercise and active exercise. The treadmill used in passive exercises is a traditional limited treatment. The active training has been shown to amend the reorganization of the cortical [4] and to perform better neuro-rehabilitation [5, 6].

During muscle activity, muscle cells generate a weakened electrical potential called sEMG. Surface electrodes sense these sEMG signals [7]. The diagnosis of neurological and neuromuscular problems [8, 9] and application in prosthetic devices such as lower limbs, smart wheelchairs, and prosthetic hands [10–12] can be mentioned as the main application of the sEMG signals. Conventionally, there are three ways to use the sEMG signals. For the first time, they were used as a switch signal to examine the human body in different movement modes [13-16]. By this technique, the amputated member was able to control the prosthetic hand or limb with the help of the remaining muscles [17, 18]. In [14], the sEMG property was extracted by the natural logarithm of root mean square root values, and four motions were classified by a fuzzy C-means clustering method. In [17], a linearized Gaussian hybrid network is proposed to detect EMG patterns for human-assisting manipulator control, and this method shows a high recognition rate for eight different hand movements. Also, the muscle force or torque is estimated by the sEMG signals. In this regard, a

[†]**Corresponding Author**: St_r_hassanzadeh@azad.ac.ir
Tel: +98-12345678,Fax: +98-12345679, Islamic Azad University
Department of Electrical Engineering, South Tehran Branch, Islamic Azad University, Tehran, Iran

number of muscle force models have been developed, such as the Hill muscle model [19] and the Hammerstein muscle model [20]. When a precise relationship is established, sEMG signals show the active patient torque representing the patient's motion intention, and the active training of the rehabilitation robot is frequently controlled by using the sEMG signals. In [21], using sEMG, two methods are proposed for active training of the exoskeleton robots: dynamic human body model and direct force control. The human body force on robots can be computed by the sEMG signals. For the third aspect, the accurate body position is computed by the sEMG signals [22-27]. After finding the relationship between the joint angles and the sEMG signal, an arbitrary feasible posture is tracked in the active training mode by a rehabilitation robot or synthetic device. In [25], a switching regime model is proposed to decode the sEMG activity of 11 muscles to a continuous representation of arm movement in the 3-D space. In [27], a method is proposed to provide volitional control of a knee prosthesis utilizing sEMG signals. The intention of the patient and the set-point angle of the knee joint are computed by sEMG signals. These people can control the artificial hand.

In many approaches, sEMG signals have been used to estimate the joint angles, such as EMG-driven neuromusculoskeletal (NMS) model [28], linear model [29,30], linear switching regime model [31], local approximation, and lazy learning method [32], support vector machine (SVM) method [33], and artificial neural networks (ANN) [34]. They have been suggested for special applications, but there are still difficulties such as accuracy of estimation, real-time and dynamic characteristics, robustness, and uniformity. In [28], dynamic elbow movement is predicted by the NMS model, which requires many physiological parameters. The linear model suggested in [29,30] cannot apparently be used to estimate the real-time joint angle because one of the model parameters (the maximum IEMG signal value) is varying hen hand movements are performed with different efforts. However, in this model, this parameter is set to a constant. In [32], the joint angles of the fingers are estimated by the local approximation and the lazy learning method. The performance of the method was satisfactory for prosthetic hand control, except that a large time delay was shown in the test results, particularly for the movement of the thumb. The effect of finger speed on the joint angle estimation was also disregarded. There are similar problems in [33].

Many papers have used artificial neural networks to estimate joint angles. However, the accuracy of the ANN in estimating the joint angles is not high. The main reasons are that the multilayer perceptron neural network (MLP) is the most common neural network structure in existing studies. The data scale and feature that are two-dimensional data are the input data of MLP, but joint angle estimation is a three-dimensional problem (time, feature, and data scale).

Though sEMG signals have very sophisticated properties, their definite characteristic is that when the human muscle contraction has no variations, their amplitude increases. The process of changing the amplitudes of the sEMG signals consists of useful information to estimate the angles. To increase the accuracy of estimating the joint angles, this paper suggests a bidirectional recurrent neural network to estimate the relation between the joint angles and sEMG signals and develop a nonlinear model. To confirm the effectiveness of the BRNN, four healthy subjects and two SCI patients participated in the experimental tests. Two motions including treadmill training and leg movement at various speeds and loads were performed by the healthy subjects, and the patients only performed treadmill training. The results show that the BRNN can satisfactorily estimate the joint angle using sEMG signals.

II. METHOD AND STRATEGY

A. Data acquisition

In clinics, SCI patients or stroke patients are improved by treadmill exercise and leg extension exercises. In order to acquire experimental data, four healthy subjects (three men, one woman, 28±3 years old, 171±8 cm height) took part in treadmill training and leg extension exercises. Two SCI patients (both males, 42±2 years old, 166±5 cm height) took part in the treadmill exercise only. Fig. 1 shows the acquisition of joint angle information and sEMG signals during the treadmill run by a healthy subject. To record information simultaneously, seven leg muscles including vastus rectus muscle (VR), vastus lateralis muscle (VL), semitendinosus muscle (SM), biceps muscle of thigh (BM), tibialis anterior muscle (TA), extensor pollicis longus (EP), and gastrocnemius muscle (GM) were used and the hip, knee, and ankle joint angles were acquired at the same time. The Biomonitor ME6000 was utilized for the acquisition of the sEMG signal from the muscles. Fig. 2 depicts the raw sEMG signals and joint angles for one healthy subject.

Fig. 1. A healthy participant on the treadmill with sEMG sensors on the leg muscles.

To use sEMG signals in estimating the joint angles, the raw data is to be preprocessed. For this purpose, three following steps are to be executed.

Step1: The 50Hz noise generated by the power supply is filtered and removed in the raw sEMG signals employing a fifth-ordered notch filter.

Step 2: The filtered sEMG signals are rectified.

Step 3: The following equation is used to compute the online moving average (OMA) of the sEMG signals:

$$E(t)=\sqrt{\frac{1}{N}\sum_{i=0}^{N}E(t-i)^2} \quad (1)$$

where N and E (t) denote the number of the segments (N = 200) and the voltage at its sampling point (the rate of the sampling is 2 kHz), respectively.

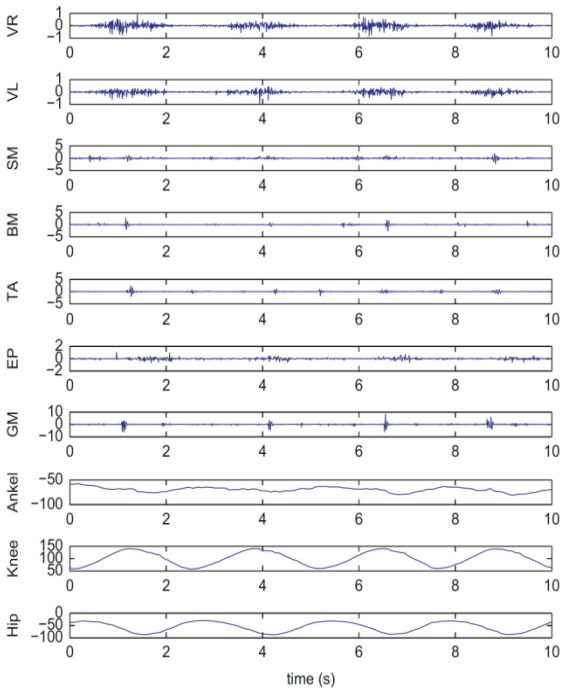

Fig. 2. Raw sEMG data acquired from seven muscles during treadmill exercise.

B. Estimation algorithm of using DRNN

As is seen in Fig. 3, the joint angles are estimated by the preprocessed sEMG signals along with the joint angle that are input signals for training the BRNN. The output of the BRNN is the estimated joint angles. In Fig. 3, the parameters a_j and θ are represented by:

$$\begin{cases}\theta=[\theta_1,...,\theta_i]\\ a_j=[a_{j,1},...,a_{j,i}]\end{cases} \quad (2)$$

where indexes i and j denote the number of acquired data and the number of sEMG channels, respectively.

III. BIDIRECTIONAL RECURRENT NEURAL NETWORK

A. The structure of BRNN

Unlike traditional neural networks, the connection between cells in the hidden layer of the RNN increases, meaning that input data of the hidden layer contains both the original data and the hidden cell state at the former time.

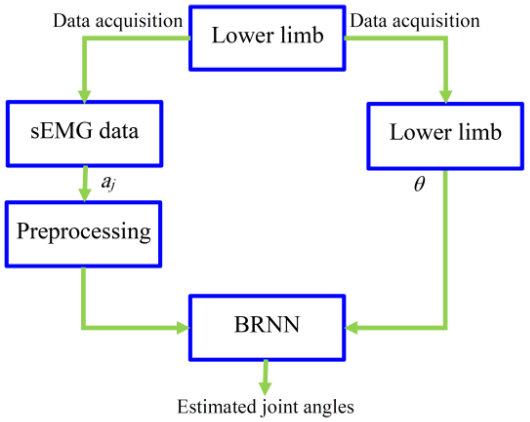

Fig. 3. Estimating the joints angles by the sEMG signal.

Considering an input sequence $x = (x_1, \ldots, x_T)$, an RNN calculates the hidden vector sequence $h = (h_1, \ldots, h_T)$ and output vector sequence $y = (y_1, \ldots, y_T)$ by iterating the following equations from $t = 1$ to T:

$$h_t = \mathrm{H}(W_{xh}x_t + W_{hh}h_{t-1} + b_h) \quad (3)$$

$$y_t = W_{hy}h_t + b_y \quad (4)$$

where W is connection weight matrices (for example, W_{xh} denotes the weight matrix from input to hidden), b is the bias vectors (for example, b_h denotes hidden bias vector), and H denotes the activation function.

H is normally the elementwise utility of the sigmoid function although the long short-term memory (LSTM) architecture, which utilizes purpose-built memory cells to store information, is better in finding and exploiting long-range data. A single LSTM memory cell is drawn in Fig. 4. In this paper, H is represented by the following functions:

$$i_t = \sigma(W_{xi}x_t + W_{hi}h_{t-1} + W_{ci}c_{t-1} + b_i) \quad (5)$$

$$f_t = \sigma(W_{xf}x_t + W_{hf}h_{t-1} + W_{cf}c_{t-1} + b_f) \quad (6)$$

$$c_t = f_t c_{t-1} + i_t \tanh(W_{xc}x_t + W_{hc}h_{t-1} + b_c) \quad (7)$$

$$o_t = \sigma(W_{xo}x_t + W_{ho}h_{t-1} + W_{co}c_t + b_o) \quad (8)$$

$$h_t = o_t \tanh(c_t) \quad (9)$$

where σ is the logistic sigmoid function and i, f, o, and c denote the input gate, forget gate, output gate, and cell activation vectors, respectively.

The connection weight matrices between the cell and gate vectors are diagonal, so the m-th element in each gate vector only accepts input from the m-th element of the cell vector.

One disadvantage of conventional RNN is that they can only utilize the previous data. To overcome this problem, bidirectional RNNs (BRNNs) [35] is used in this paper by processing the information in both directions with two separate hidden layers that are then fed forward to the same output layer.

It is clear from Fig. 5 that a BRNN calculates the forward

hidden sequence $\overrightarrow{h}$, the backward hidden sequence $\overleftarrow{h}$ and the output sequence y by iterating the backward layer from $t = T$ to 1, the forward layer from $t = 1$ to T, and then updating the output layer:

$$\overrightarrow{h}_t = \mathrm{H}\left(W_{x\overrightarrow{h}} x_t + W_{\overrightarrow{h}\overrightarrow{h}} \overrightarrow{h}_{t-1} + b_{\overrightarrow{h}} \right) \tag{10}$$

$$\overleftarrow{h}_t = \mathrm{H}\left(W_{x\overleftarrow{h}} x_t + W_{\overleftarrow{h}\overleftarrow{h}} \overleftarrow{h}_{t-1} + b_{\overleftarrow{h}} \right) \tag{11}$$

$$y_t = W_{\overrightarrow{h}y} \overrightarrow{h}_t + W_{\overleftarrow{h}y} \overleftarrow{h}_t + b_y \tag{12}$$

The bidirectional LSTM, which can access long-range data in both input directions, is constructed by combining BRNN with LSTM [16].

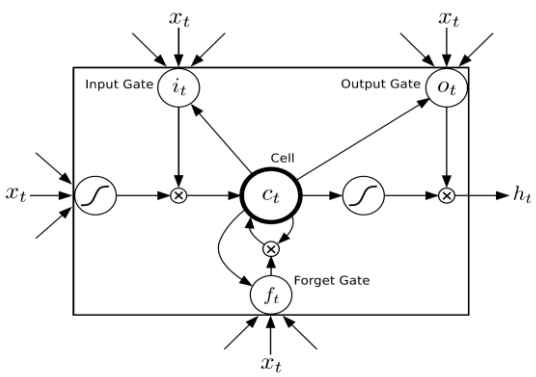

Fig. 4. Long short-term memory cell.

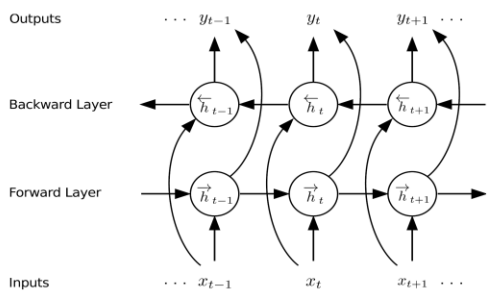

Fig. 5. Bidirectional RNN.

B. *Steps of estimation*

There are four steps in estimating the joint angles using the proposed BRNN:

- Step 1: Build up the BRNN;
- Step 2: Prepare sEMG data;
- Step 3: Train the BRNN. The inputs and outputs of the BRNN are the sEMG signal and the joint angles, respectively. The mean square error selected as the cost function is minimized by the algorithm of backpropagation through time (BPTT) [36].
- Step 4: Verify BRNN. A number of data acquired in step 2 are used to verify the trained BRNN model.

IV. Experimental Results

A. *Results*

Despite the simultaneous recording of sEMG signals from seven muscles, it should be noted that all channels do not contain useful information. It is clear from Fig. 2 that only sEMG of vastus rectus muscle, vastus lateralis muscle, and extensor pollicis longus contain very good dynamic data. Experimentally, the remaining of muscle signals was not utilized. Hence, the number of inputs as well as the complexity of the BRNN can be decreased. For every healthy subject, two BRNNs were created for the treadmill and leg extension exercises. Each input vector of the BRNN has a size of 40 including sEMG signal and the pervious samples. All BRNNs are trained by using back error propagation algorithm with a learning rate of 0.01 and random initial weights in the range of [-0.5; 0.5].

Figs. 6 and 7 depict the estimations of hip, knee, and ankle joint angles of a healthy subject in different conditions. From these figures, the suggested method works better in estimating the hip, knee, and ankle joint angles for fast speed regardless of the load during leg extension exercise. In fact, all four healthy subjects felt it was easier to do the exercise in a quick way that could give them a natural feeling. On the contrary, if they did this relatively slowly, four healthy subjects would feel uncomfortable since they could not control the speed and the slow speed would make them feel no rhythm. Regular and stable signals were generated when the subject had a sense of rhythm.

Similar results are presented in Fig. 7. The accuracy of the joint angles estimation is better in fast speed than in slow speed. From Fig. 7 (b), it is clear that the use of sEMG signals makes a more accurate estimate of the hip joint, knee joint, and ankle joint angles, and the mean angle error was less than 4.8 degrees for all four healthy persons during the treadmill exercise in fast speed with small load. As it is clear in Fig. 7(a) and (c), the estimation of the ankle joint angle is not as satisfactory as the estimation of the joint angles of the knee and hip principally because ankle control is not very natural while exercising at a slow pace. The estimation of the joint angles in fatigue mode (persons felt muscle pain and they did the exercise very hard) is illustrated in Fig. 7(d). Only the knee joint and hip joint angle are shown in this figure because the estimation error of the ankle joint is very large and we deliberately eliminated it. The mean estimation errors of the knee joint angle and the hip joint angle are also big (about 12.781 degrees). This is mainly because when subjects exercise in very fatigue conditions, the leg muscles contract very unstable with trembling of the limbs and in this case, the relationship between the sEMG signals and the angles of the joints becomes much more complicated. For two SCI patients, a BRNN was created for every subject. In Fig. 8, the estimation of the joint angles of the three joints for both subjects is shown, and the results are nearly as

satisfactory as that of the health people. As is seen in Fig. 8, the first subject's ankle joint angle fluctuated to a greater extent during the treadmill exercise because this subject was unable to fully control his legs due to SCI. The second subject performed better in the estimation of the joint angles with a mean error of 2.631 degrees. This should be due to minimal damage to the spinal cord, so the sEMG signals were more stable in this subject than in the other subject.

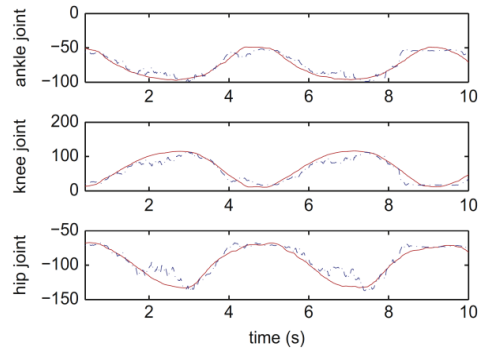

a

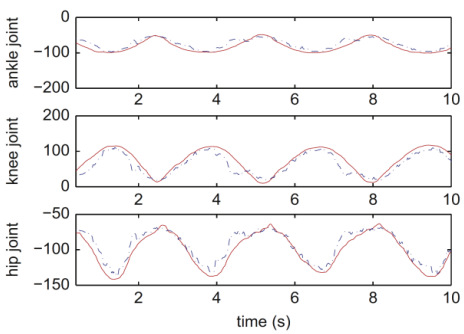

b

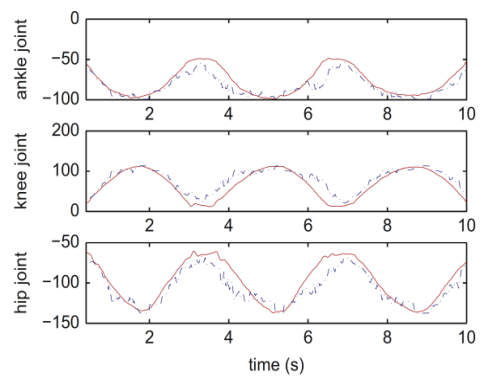

c

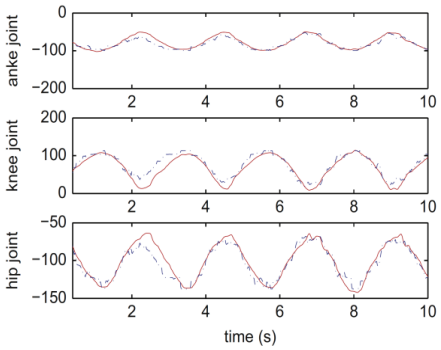

d

Fig. 6. Results obtained from leg extension exercise for a healthy subject. Solid lines (actual angles); dashed lines (estimated angles). (a) Leg extension with slow speed and small load, (b) leg extension with fast peed and small load, (c) leg extension with slow speed and big load, (d) leg extension with fast peed and big load.

Based on the comparison of Figs. 7 and 8, it is obvious that the estimation error of the healthy subjects is bigger than that of the SCI patients. The mean error for the healthy subjects is approximately 8.71 degrees during the leg extension exercise and approximately 5.91 degrees during the treadmill exercise regardless of the results under the fatigue mode, whereas the mean error for the SCI subjects is approximately 4.41 degrees during the treadmill exercise. This is associated with the fact that the movement range of healthy people is bigger than that of the SCI people.

In order to assess the performance of the angle estimation, Pearson's correlation coefficient (PCC) and root mean square error (RMSE) were employed. The PCC and RMSE are computed by:

$$PCC = \frac{\sum \theta_{act,n}\theta_{est,n} - \frac{\sum \theta_{act,n}\sum \theta_{est,n}}{N}}{\sqrt{\left(\sum \theta_{act,n}^2 - \frac{\left(\sum \theta_{act,n}\right)^2}{N}\right)\left(\sum \theta_{est,n}^2 - \frac{\left(\sum \theta_{est,n}\right)^2}{N}\right)}} \quad (13)$$

$$RMSE = \sqrt{\frac{1}{N}\sum_{n=1}^{N}\left(\theta_{act,n} - \theta_{est,n}\right)^2} \quad (14)$$

where $\theta_{act,n}$ and $\theta_{est,n}$ are the measured and estimated angles and N denotes the number of the samples.

Table I provides the values of PCC for four healthy subjects and two SCI patients. The values of RMSE for all cases are given in Table II. All these tests are performed for the leg extension test and hip angle.

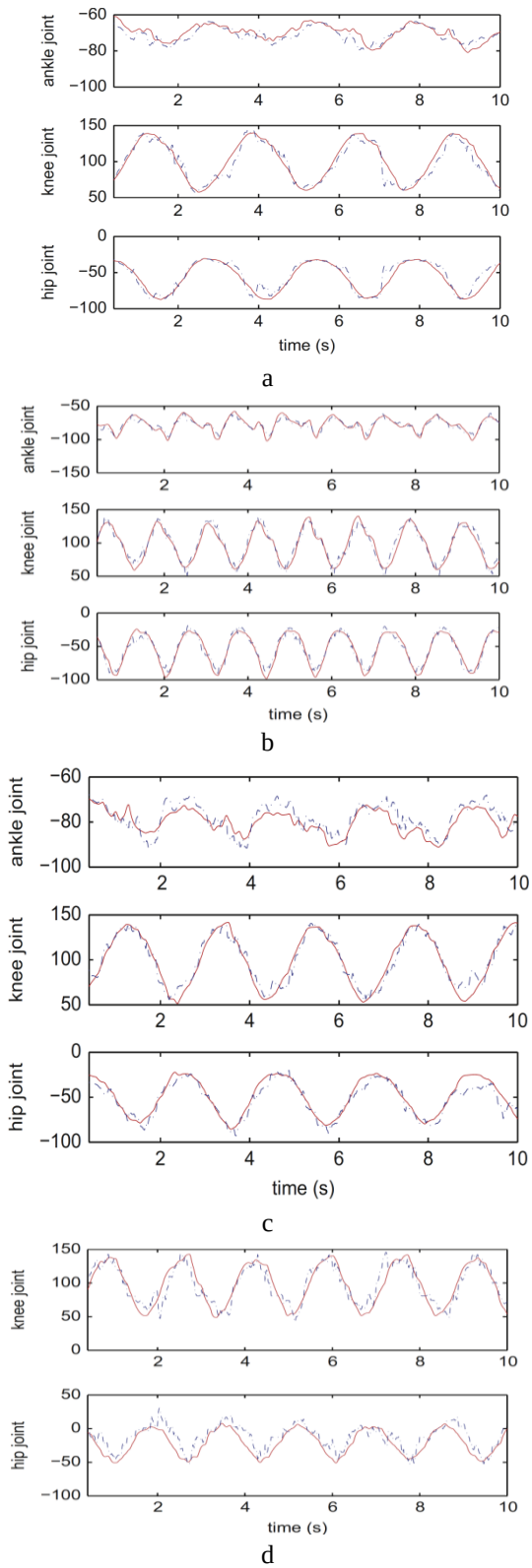

Fig. 7. Results obtained from treadmill exercise for a healthy subject. Solid lines (actual angles); dashed lines (estimated angles). (a) Treadmill exercise with slow speed and small load, (b) treadmill exercise with fast peed and small load, (c) Treadmill exercise with slow speed and big load, (d) treadmill exercise with fatigue.

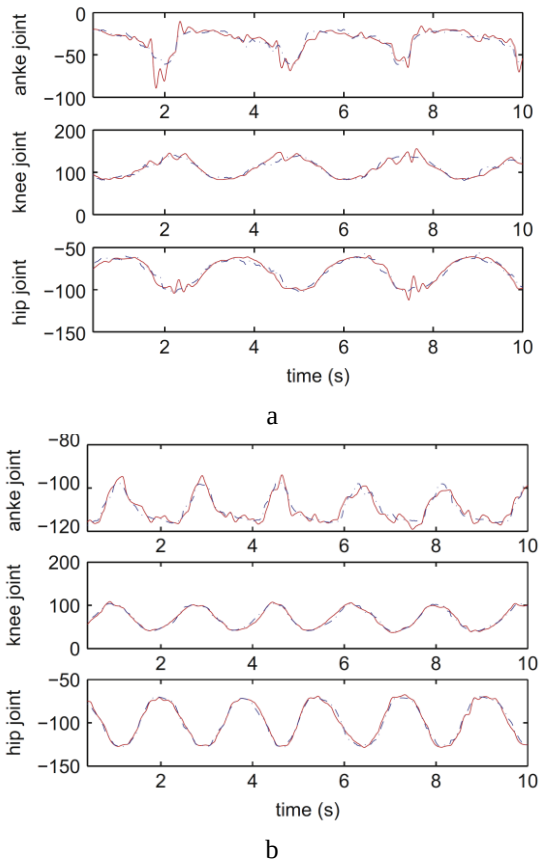

Fig. 8. Results obtained for SCI subjects. Solid lines (actual angles); dashed lines (estimated angles). (a) The first patient, (b) the second patient.

TABLE I
THE VALUES OF PCC FOR HEALTHY SUBJECTS AND SCI PATIENTS.

	Healthy subject				SCI patient	
	S_1	S_2	S_2	S_4	P_1	P_2
Mean	0.968	0.975	0.979	0.985	0.972	0.975
SD	0.013	0.008	0.006	0.003	0.009	0.007
Median	0.970	0.978	0.981	0.986	0.974	0.978
Maximum	0.983	0.984	0.987	0.990	0.981	0.988
Minimum	0.940	0.960	0.969	0.980	0.946	0.963

TABLE II
THE VALUES OF RMSE FOR HEALTHY SUBJECTS AND SCI PATIENTS.

	Healthy subject				SCI patient	
	S_1	S_2	S_2	S_4	P_1	P_2
Mean	9.761	8.882	8.831	8.804	9.865	8.954
SD	1.663	2.138	1.453	1.377	1.754	1.733
Median	10.031	9.329	9.104	8.951	9.430	9.324
Maximum	12.554	10.490	9.802	9.800	10.199	10.086
Minimum	8.780	7.663	7.232	6.895	7.545	7.433

B. Discussion

Based on the results, it can be confirmed that the joint angles of human legs can be satisfactorily estimated by sEMG signals in two modes of treadmill training and leg extension. The estimation of joint angles employing the

BRNN leads to good performance in both spinal patients and healthy people. Compared to traditional angle estimation methods, this approach improves angle estimation precision, characteristics of dynamic and real-time, and robustness. For all healthy people, the average error for leg extension and treadmill exercise are less than 9 degrees and 6 degrees, respectively, while these errors for SCI patients are 5 degrees due to a smaller range of motion. The sampling rate of the sEMG signals is 2 kHz, implying a time delay of 0.5ms. The performance of the proposed method is acceptable despite this time delay. Different speeds and loads are considered in the suggested approach and the results show a robust performance. The smoothness of estimating the joint angles is improved by the suggested method. According to the results, it can be concluded that these signals can be implemented for active training in a better way on the rehabilitation robot for spinal cord and stroke patients.

V. Conclusion

In this study, the sEMG signals are utilized to find a new human–robot interface. A neural network is employed to find the relationship between joint angles and sEMG signals, and practicability of this approach is confirmed by different experiments in healthy people as well as in SCI patients. To develop the nonlinear model, a bidirectional recurrent neural network is proposed. The BRNN is trained by the joint angles and sEMG signals and then used to estimate the joint angles that is usable in controlling rehabilitation robots. There is also a detailed discussion about estimating joint angles under different conditions such as various speeds and loads and in fatigue conditions and the proposed approach shows satisfactory robustness to various situations. Compared with the conventional techniques of estimating joint angles using the sEMG signals, this method improves many features, including the accuracy of the estimation, real-time specification, smoothness, dynamic specification, and robustness.

Appendix

Consider the following candidate Lyapunov function:

$$V(t)=\frac{1}{2}e^{T}(t)e(t) \tag{A.1}$$

where

$$e(t)=y^{*}(t)-y(t) \tag{A.2}$$

and y^{*} is the desired output. The convergence of the system can be `` if:

$$\Delta V(t+1)=V(t+1)-V(t)\le 0 \tag{A.3}$$

By combining (A.1) and (A.3), we have:

$$\Delta V(t+1)=\frac{1}{2}\left[2e(t)+\Delta e(t+1)\right]^{T}\Delta e(t) \tag{A.4}$$

where $\Delta e(t+1)=e(t+1)-e(t)$.

By combining (3), (4) and (A.2), and the use of Taylor series expansion, we can write the linear form of $e(t)$ as follows:

$$e(t+1)=e(t)+\frac{\partial e(t)}{\partial P(t)}\left[\Delta P(t)\right]^{T}+R' \tag{A.5}$$

where $P=[W, b]$, R' is the ignored higher-order terms.

Theorem 1. *Let η be the learning rate of the BRNN. The convergence is ensured if the learning rate satisfies:*

$$0<\eta<\frac{2}{\left(\frac{\partial e(t)}{\partial P(t)}\right)\left(\frac{\partial e(t)}{\partial P(t)}\right)^{T}} \tag{A.6}$$

Therefore, the convergence is ensured and $e(t)\to 0$ as $t\to\infty$.

Proof. (A.4) can be rewritten and simplified as follows:

$$\Delta V(t+1)=\frac{1}{2}e^{T}(t)e(t)\left\|\frac{\partial e(t)}{\partial P(t)}\right\|^{2}\left\{\eta\left\|\frac{\partial e(t)}{\partial P(t)}\right\|^{2}-2\right\} \tag{A.7}$$

If (A.6) is satisfied by the learning rate η, then:

$$\eta\left\|\frac{\partial e(t)}{\partial P(t)}\right\|^{2}-2<0 \tag{A.8}$$

In (A.7), η is positive, $e^{T}(t)e(t)$ and $\left\|\frac{\partial e(t)}{\partial P(t)}\right\|^{2}$ are zero or positive. Hence, by the use of (A.7) and (A.8), we conclude that:

$$\Delta V(t+1)\le 0 \tag{A.9}$$

Thus, the convergence of the BRNN can be ensured by using Lyapunov stability theorem.

References

[1] Yang, T., Gao, X., Gao, R., Dai, F., & Peng, J. (2019). A Novel Activity Recognition System for Alternative Control Strategies of a Lower Limb Rehabilitation Robot. *Applied Sciences*, 9(19), 3986.

[2] Qin, F., Zhao, H., Zhen, S., Sun, H., & Zhang, Y. (2020). Lyapunov Based Robust Control for Tracking Control of Lower Limb Rehabilitation Robot with Uncertainty. *International Journal of Control, Automation and Systems*, 18(1), 76-84.

[3] Wang, A., Hu, N., Yu, J., Liao, W., Zhang, J., Wu, X., & Pei, C. (2019, August). Research on robot control system of lower limb rehabilitation robot based on human gait comfort. *In 2019 International Conference on Advanced Mechatronic Systems (ICAMechS)* (pp. 34-39). IEEE.

[4] M. Lotze, C. Braun, N. Birbaumer, S. Anders, L.G. Cohen, Motor learning elcited by voluntary, *Brain 126* (2003) 866–872.

[5] L.L. Cai, A.J. Fong, C.K. Otoshi, Y. Liang, J.W. Burdick, R.R. Roy, V.R. Edgerton, Implications of assist-as-needed

robotic step training after a complete spinal cord injury on intrinsic strategies of motor learning, *Neuroscience* 26 (4) (2006) 10564–10568.
[6] G. Rosati, P. Gallina, S. Masiero, Design implementation and clinical tests of a wire-based robot for neurorehabilitation, *IEEE Trans. Neural Syst. Rehabil*. Eng. 15 (4) (2007) 560–569.
[7] G. Kamen, D. Gabriel, Essentials of Electromyography, Human Kinetics Publishers, USA, 2009.
[8] M.J. Zwarts, G. Drost, D.F. Stegeman, Recent progress in the diagnostic use of surface EMG for neurological diseases, *J. Electromyogr. Kinesiol*. 10 (5) (2000) 287–291.
[9] S.L. Pullman, D.S. Goodin, A.I. Marquinez, S. Tabbal, M. Rubin, Clinical utility of surface EMG: *report of the therapeutics and technology assessment subcommittee of the American Academy of Neurology*, *Neurology* 55 (2) (2000) 171–177.
[10] C. Cipriani, F. Zaccone, S. micera, M.C. Carrozza, On the shared control of an EMG-controlled prosthetic hand: analysis of user-prosthesis interaction, *IEEE Trans. Robot*. 24 (1) (2008) 170–184.
[11] T.A. Kuiken, G. Li, B.A. Lock, R.D. Lipschutz, L.A. Miller, K.A. Stubblefifield, K.B. Englehart, Targeted muscle reinnervation for real-time myoelectric control of multifunction artifificial arms, *J. Am. Med. Assoc*. 301 (6) (2009) 619–628.
[12] Y. Oonishi, O. Sehoon, Y. Hori, A new control method for power-assisted wheelchair based on the surface myoelectric signal, *IEEE Trans. Ind. Electron*. 57 (9) (2010) 3191–3196.
[13] F. Zhang, P.F. Li, Z.G. hou, X.L. Xie, Y.X. Chen, Q.L. Li, M. Tan, An adaptive RBF neural network control strategy for lower limb rehabilitation robot, *ICIRA 2010* (2010) 417–427.
[14] K. Momen, S. Krishnan, T. Chau, Real-time classifification of forearm electromyographic signals corresponding to user-selected intensional movements for multifunction prosthesis control, *IEEE Trans. Neural Syst. Rehabil. Eng.* 15 (4) (2007) 535–542.
[15] Y.H. Liu, H.P. Huang, C.H. Weng, Recognition of electromyographic signals using cascaded kernel learning machine, *IEEE Trans. Mechatron*. 12 (3) (2007) 253–264.
[16] D. Tkach, H. Huang, T. Kuiken, Study of stability of time-domain features for electromyographic pattern recognition, *J. Neuroeng. Rehabil*. 5 (2010) 7–21.
[17] O. Fukuda, T. Tsuji, M. kaneko, A. Otsuka, A human-assisting manipulator teleoperated by EMG signals and arm motions, *IEEE Trans. Robot. Autom*. 19 (2) (2003) 210–222.
[18] S. Yu, M.H. Fisher, A. Wolczowski, G.D. Bell, D.J. Burn, R.X. Gao, Towards an EMG-controled prosthetic using a 3-D electromagnetic positioning system, *IEEE Trans. Instrum. Meas.* 56 (1) (2007) 178–186.
[19] N.A. Shrirao, N.P. Reddy, D.R. Kosuri, Neural network committees for finger joint angle estimation from surface EMG signals, *Biomed. Eng. OnLine* 8 (2) (2009) 1–11.
[20] A.V. Hill, The heat of shortening and the dynamic constants of muscle, *Proc. R. Soc. Lond. B 126* (1938) 136–195.
[21] C. Fleischer, A. Wege, K. Kondak, G. Hommel, Application of EMG signals for controlling exoskeleton robots, Biomed. Tech. 51 (5) (2006) 314–319.
[22] C.A.M. Doorenbosch, J. Harlaar, Accuracy of a practicable EMG to force model for knee muscles, *Neurosci. Lett.* 368 (1) (2004) 78–81.
[23] G.L. David, F.B. Thor, An EMG-driven musculoskeletal model to estimate muscle forces and knee joint moments in vivo, *J. Biomech.* 36 (2003) 765–776.
[24] Q. Shao, N.B. Daniel, K. Manal, S.B. Thomas, An EMG-driven model to estimate muscle forces and joint moments in stroke patients, *Comput. Biol. Med*. 39 (12) (2009) 1083–1088.
[25] P.K. Artemiadis, K.J. Kyriakopoulos, A switching regime model for the EMG-based control of a robot arm, *IEEE Trans. Syst. Man Cybern. Part B: Cybern.* 41 (1) (2011) 53–63.
[26] P.K. Artemiadis, K.J. Kyriakopoulos, EMG-based position and force estimates in coupled human-robot systems: towards EMG-controlled exoskeletons, *Springer Tracts Adv. Robot.* 54 (2009) 241–250.
[27] K.H. Ha, H.A. Varol, M. Goldfarb, Volitional control of a prosthetic knee using surface electromyography, *IEEE Trans. Biomed. Eng*. 58 (1) (2011) 144–151.
[28] K.K. Koo Terry, F.T. Mak Arthur, Feasibility of using EMG driven neuromusculoskeletal model for prediction of dynamic movement of the elbow, *J. Electromyogr. Kinesiol.* 15 (2005) 12–26.
[29] Y. Masahiro, M. Masahiko, T. Kazuyo, Real time hand motion estimation using EMG signals with support vector machines, *in: SICE-ICASE International Joint Conference*, 2006, pp. 593–598.
[30] Y. Masahiro, M. Masahiko, T. Kazuyo, Hand pose estimation using EMG signals, *in: IEEE International Conference on EMBS*, 2007, pp. 4830–4833.
[31] N.P. Reddy, V. Gupta, Toward direct biocontrol using surface EMG signals: control of fifinger and wrist joint models, *Med. Eng. Phys.* 29 (2007) 398–403.
[32] A. Christian, C. Cipriani, M. Controzzi, M.C. Carrozza, G. Lundborg, B. Rose´n, F. Sebelius, Using EMG for real-time prediction of joint angles to control a prosthetic hand equipped with a sensory feedback system, *J. Med. Biol. Eng.* 30 (6) (2010) 399–406.
[33] J. Shi, Y. Zheng, Z. Yan, SVM for estimation of wrist angle from sonomyography and sEMG signals, *in: IEEE International Conference on EMBS*, 2007, pp. 4806–4809.
[34] K.J. Hunt, M. Munih, N.deN. Donaldson, F.M.D. Barr, Investigation of the hammerstein hypothesis in the modeling of electrically stimulated muscle, *IEEE Trans. Biomed. Eng.* 45 (8) (1998) 998–1009.
[35] M. Schuster and K. K. Paliwal, "Bidirectional Recurrent Neural Networks," *IEEE Transactions on Signal Processing*, vol. 45, pp. 2673–2681, 1997.
[36] Farahani, Mohsen. "A multi-objective power system stabilizer." *IEEE Transactions on Power Systems* 28.3 (2012): 2700-2707.

Rohollah Hasanzadeh Fereydooni received his B.Sc. degree in Robotic Engineering at the Shahrood University of Technology, Iran in 2011 and his M.Sc. degree in Mechatronic Engineering at South Tehran Branch, Islamic Azad University, Tehran, Iran in 2014. He is now a Ph.D. candidate in Control Engineering at South Tehran Branch, Islamic Azad University. His research interests include rehabilitation robots, robotics, and intelligent systems.
E-mail: st_r_hassanzadeh@azad.ac.ir (Corresponding author).

Hassan Siahkali was born in Tehran, Iran. He received his B.S. degree in Electronics Engineering at Tabriz University, Tabriz, Iran, in 1993, and his M.S. and Ph.D. degrees in Electrical Engineering at the Amir Kabir University of Technology and Sharif University of Technology, Tehran, Iran, in 1996 and 2010, respectively. From 1999 to 2006, he was with Niroo Research Institute, Tehran, Iran. From 2006 to 2012, he worked as the manager of Energy and System Studies Center at the MONENCO Consulting Engineer Company, Tehran, Iran. In 2006, he joined Islamic Azad University –South Tehran Branch as an assistant professor in Engineering Faculty. His current research interests include power system operation and planning, electricity markets, and power system quality.

Heidar Ali Shayanfar was born in Zabol, Iran, on March 11, 1951. He received his B.S. and M.S.E. degrees in Electrical Engineering in 1973 and 1979 and his Ph.D. degree in Electrical Engineering at Michigan State University, U.S.A., in 1981. Currently, he is a full professor at the Electrical Engineering Department of Iran University of Science & Technology (lUST), Tehran, Iran. His research interests are the application of artificial intelligence to power system control design, dynamic load modeling, power system observability studies, voltage collapse, applications of facts devices in power systems, and restructured power systems.

Amir Hooshang Mazinan received his Ph.D. degree in Control Engineering in 2009. He is currently an associate professor and the director of Control Engineering Department at IAU South Tehran Branch starting from 2009. His research interests include intelligent systems, model-based predictive control, over-actuated space systems modeling and control, time frequency representation, filter banks, wavelet theory, and image-video processing.

IECO

This page intentionally left blank.

International Journal of Industrial Electronics, Control and Optimization © 2021 IECO
Vol. 4, No. 2, pp. 167-179, April (2021)

PWM Control Methods Based on Mathematical Equations for Z-Source Inverters

Taher Ahmadzadeh [1], Ebrahim Babaei [2, †], Mehran Sabahi [3], Taher Abedinzadeh [4]

[1, 4] Department of Electrical Engineering, Shabestar Branch, Islamic Azad University, Shabestar, Iran
[2, 3] Faculty of Electrical and Computer Engineering, University of Tabriz, Tabriz, Iran

ABSTRACT

In power converters, the total harmonic distortion (THD) can be decreased by using two strategies which are filtering and controlling methods. The filtering strategy is indeed costly because of using hardware devices (such as capacitors and inductors). A suitable strategy to control the modern power converters without using the hardware devices is the pulse width modulation (PWM) technique. In this paper, three new PWM control methods based on mathematical equations for various Z-source inverters (ZSIs) are proposed. Controlling the duty cycles of switches is the basic idea of these methods to control the output voltage. The proposed control methods are analyzed under the circumstances of constant input and balanced output voltage (CIBOV) and ripple input and balanced output voltage (RIBOV). The advantages of the proposed methods are control of voltage, current and harmonic distortion. Other advantages of these methods are lower value for THD and elimination of low-order harmonics. The correct operation of the proposed PWM techniques is proved by using the simulation results.

Article Info

Keywords:
Pulse width modulation (PWM), Quasi-Z-source inverter (qZSI), Shoot-through (ST) state, Total harmonic distortion (THD).

Article History:
Received 2020-06-01
Accepted 2020-10-14

I. INTRODUCTION

The dc-ac converters (or inverters) are suitable topologies for medium-power and high-power applications. Hence, these converters have a main role in the industry and urban lifestyle [1]-[4]. Up to now, various topologies of inverters have been presented such as inverters based on voltage source (VSIs), current source (CSIs), and impedance source (ZSIs). Each one of them has its own limitations that should be considered in switching states [4]-[8]. The inverter topologies based on the Z-source network have the capability of voltage boost by shoot-through (ST) states. Moreover, they are suitable for applications such as photovoltaic, fuel cell, motor drive, and wind turbine [7]-[10].

In a power converter, power losses can be lower by reducing the value of total harmonic distortion (THD). To achieve this aim, a suitable topology or control method can be employed. Moreover, filtering and controlling strategies can decrease the THD and eliminate low-order harmonics [1]-[3]. The filtering technique needs some hardware devices (such as capacitor and inductor). To decrease the size and cost of the filter, the higher switching frequency can be profitable which causes more switching losses. Hence, that's better to focus on control methods [1], [2], [11].

In the ac output of an inverter, the magnitude, frequency, and phase can be controlled by an appropriate control method. The pulse width modulation (PWM) techniques have the capability to control the switching states, and in comparison with other strategies can cause a decrease in low-order harmonics [1]-[3], [11]. UP to now, several PWM techniques for inverter based on Z-source topology have been introduced. The main purpose of them is a simple implementation, high voltage gain, low device stress, less commutation per switching cycle, and low harmonics and THD [12]-[18].

Three basic techniques are the simple boost control (SBC), maximum boost control (MBC), and maximum constant

†Corresponding Author: e-babaei@tabrizu.ac.ir
Tel: +98- 41-33393763, Fax: +98- 41-33300819, University of Tabriz
Faculty of Electrical and Computer Engineering, University of Tabriz, Tabriz, Iran

boost control (MCBC) [12]. In order to control the ST duty cycle (D_{sh}) in the SBC method, a triangular carrier wave is compared to two straight lines. But, in MBC and MCBC strategies, the ST states generate from the comparison of two envelope curves with the triangular carrier waveform. The ST time per switching cycle is constant for SBC and MCBC. But, it is variable for MCB. The MBC technique has a higher voltage boost factor and lower voltage stress across the devices in comparison with the two others. However, it has the drawbacks of low-frequency ripples on the Z-source network. In order to reduce the volume and cost of the LC network, the elimination of low-frequency current ripples is needed which is achieved by a constant ST duty cycle [12].

Other various solutions have been introduced in [13]-[15] to reduce the inductor current ripple for the ZSI topologies. In [13], a switching technique for the ZSI has been presented. This strategy has used the unequal ST time intervals to reduce the inductor current ripple. This method compared to the conventional method with equal ST time intervals can reduce the inductor current ripple by 27.8% without increasing the number of switching states. Also, to reduce this problem, [14] has employed the advanced bus clamping switching sequences as titled ABC4-MCB control method. This method in comparison with the ZSVM6-MCB strategy, for the equal average switching frequency, reduces the maximum instantaneous inductor current ripple around by 34%. In this technique, the reduction percentage of the inductor current ripple is constant over the entire range of the ST time interval (0-0.48). In [15], the current ripple of ZSI has been firstly analyzed. Moreover, a comparison between ZSI and VSI has been given in terms of current ripples. At last, a variable dc-link voltage and switching frequency method has been employed to reduce the conduction and switching losses without increasing the predicted peak current ripple.

Ref. [16] has introduced a dual switching frequency modulation algorithm for ZSI and qZSI to combine high-frequency PWM with low-frequency singular PWM which causes a reduction in the converter size as it operates at the high switching frequency.

In [17], several new control methods for single-phase ZSIs have been presented. Also, a comparison among them has been given. Moreover, an optimized closed-loop control scheme has been designed to eliminate more harmonic. These techniques in comparison with conventional boost control strategies have a simple algorithm, more flexible voltage gain, and lower harmonics.

In [18], an improved sinusoidal PWM (SPWM) method for the one-phase and multi-phases approaches of the quasi ZSIs (qZSIs) has been introduced. The main aim of this strategy is that a similar control signal at per time interval can be generated by the controller because one of the switches is turned on and the other one is turned off. Also, the switching state of another MOSFET can be produced by a NOT gate. In this paper, the related mathematical analysis of qZSI has been also provided and the controller is designed based on these calculations.

In [1] and [2], several PWM control methods for conventional VSI have been introduced. The basic idea of them is to control the duty cycles of the switches in such a way that a load sees a controllable average voltage. Inspired by [1] and [2], three new PWM control methods based on mathematical equations for various single-phase Z-source topologies have been proposed in this paper. Significantly, the proposed methods have been analyzed for a conventional single-phase qZSI. The main advantage of the proposed methods is based on the mathematical foundation. In other words, the proposed methods include some mathematical equations in which each one of them has a controllable capability. Other benefits of proposed methods are lower value for THD and elimination of low-order harmonics. This paper is categorized as follows. In section II, a brief review of the conventional single-phase qZSI topology is performed. In section III, the operating principle of three proposed PWM control methods with related equations is presented. Since the proposed methods can also generate the desired output voltage from a regulated and unregulated input voltage. So, in this section, these methods are analyzed under situations of CIBOV (constant input and balanced output voltage) and RIBOV (ripple input and balanced output voltage). Section IV provides a comparison between the proposed methods and other methods. The simulation results given in section V prove the correct operation of the proposed methods.

II. Conventional Quasi-Z-Source Inverter (QZSI)

Fig. 1 shows the conventional single-phase qZSI topology [19]. This inverter has two modes such as shoot-through (ST) and non-shoot-through (non-ST) switching states. The equivalent circuits of qZSI are shown in Fig. 2. Considering Fig. 2(a), in the ST switching state (T_{sh} time interval), the switches are turned on, whereas, the diode of D is turned off. In this mode, the following equations can be obtained:

$$v_{L1,sh} = V_{dc} + V_{C2} \quad , \quad v_{L2,sh} = V_{C1} \quad , \quad v_{o,sh} = 0 \qquad (1)$$

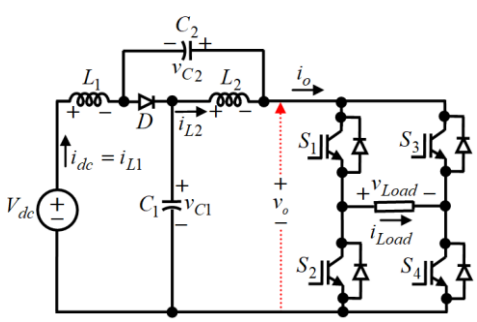

Fig. 1. Conventional single-phase qZSI topology [19].

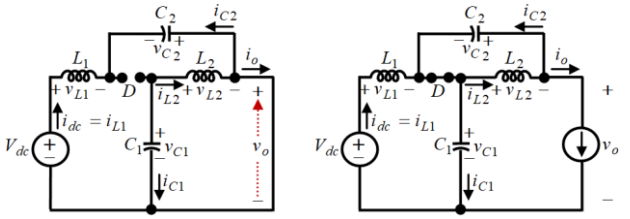

Fig. 2. Circuits of qZSI; (a) ST state, (b) non-ST state.

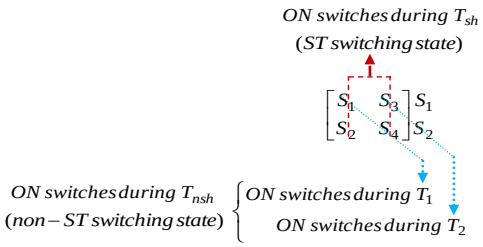

Fig. 3. First proposed control method.

where v_{L1} and v_{L2} are the voltages across the L_1 and L_2 inductors, V_{C1} and V_{C2} are the voltages across the C_1 and C_2 capacitors, and V_{dc} and v_o are the input and dc-link voltages of the inverter, respectively.

According to Fig. 2(b), in the non-ST switching state (T_{nsh} time interval), the diode of D is turned on, whereas, the switches have different states of turning on. In this mode, the following equations can be written:

$$v_{L1,nsh} = V_{dc} - V_{C1}\,,\quad v_{L2,nsh} = -V_{C2}\,,\quad v_{o,nsh} = V_{C1} + V_{C2} \tag{2}$$

In steady-state, the average voltages across C_1 and C_2 capacitors (V_{C1} and V_{C2}) for all times can be calculated as follows [10], [19]:

$$V_{C1} = \frac{1-D_{sh}}{1-2D_{sh}}V_{dc}\,,\qquad V_{C2} = \frac{D_{sh}}{1-2D_{sh}}V_{dc} \tag{3}$$

where D_{sh} is the duty cycle of the ST switching state, which can be defined as follows:

$$D_{sh} = \frac{T_{sh}}{T_s} = 1 - M \tag{4}$$

where M is the modulation index of the inverter.

From Equs. (2) and (3), the maximum voltage across the dc-link ($v_{o,\max}$) is equal to [10], [19]:

$$v_{o,\max} = BV_{dc} = \frac{1}{1-2D_{sh}}V_{dc} \tag{5}$$

where B is the boost factor of the qZSI.

By substituting Equ. (4) into Equ. (5), we have:

$$M = \frac{1}{2}\left(1 + \frac{V_{dc}}{v_{o,\max}}\right) \tag{6}$$

Assuming a purely resistive load (R_L), the average current through the dc-link ($I_{o,av}$) for all times is equal to:

$$I_{o,av} = \frac{1-D_{sh}}{R_L}V_{o,\max} \tag{7}$$

III. Proposed Mathematical PWM Control Methods for Single-Phase ZSIs

The various PWM strategies have been introduced to control the Z-source topologies [12]-[18]. The PWM strategies presented in [1] and [2] are based on mathematical equations. But, these PWM control methods have been designed for the inverter topologies based on voltage-source. Hence, in the inverter topologies based on the Z-source network, the ST switching state should be added to these control methods. In this paper, by using the concepts of PWM control methods presented in [1] and [2], three new PWM control methods based on mathematical equations are proposed for various single-phase Z-source topologies. The main purpose of these methods is to control the ST duty cycle (D_{sh}) through which a load can be able to see a controllable average voltage. In the mathematical proposed control methods, the sampling time (T_s) is divided into two time intervals as T_{sh} and T_{nsh} for the Z-source inverters, which can be written as follows:

$$T_s = T_{sh} + T_{nsh} \tag{8}$$

where T_{sh} and T_{nsh} are the ST and non-ST switching states, respectively, which considering Equ. (6) can be obtained as follows:

$$T_{sh} = D_{sh}T_s = (1-M)T_s = \frac{T_s}{2}\left(1 - \frac{v_{dc}(t)}{v_{o,\max}(t)}\right) \tag{9}$$

$$T_{nsh} = (1-D_{sh})T_s = MT_s = \frac{T_s}{2}\left(1 + \frac{v_{dc}(t)}{v_{o,\max}(t)}\right) \tag{10}$$

Considering Equs. (8) and (10), the non-ST switching state (time interval of T_{nsh}) is also divided into two-time intervals such as T_1 and T_2 , which can be written as follows:

$$T_{nsh} = T_1 + T_2\ ;\ D_{sh}T_s \le T_i \le (1-D_{sh})T\ \ for\ i = 1,2 \tag{11}$$

It is noticeable that the proposed strategy is based on a matrix of the switches (S), which can be defined as follows:

$$S = \begin{bmatrix} S_1 & S_3 \\ S_2 & S_4 \end{bmatrix}_{2\times 2} \tag{12}$$

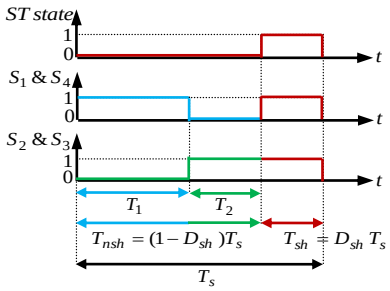

Fig. 4. Control signals of the first proposed PWM control method.

A. First Proposed Control Method

In the first proposed control method, the sequence of turning on and off for the switches is shown in Fig. 3. In the non-ST switching state (time interval of T_{nsh}), when the switches of S_1 and S_4 are turned on for the time interval of T_1, the switches of S_2 and S_3 should be turned off for this time and vice versa for the time interval of T_2. To generates the ST switching state (time interval of T_{sh}), the S_1 to S_4 switches are turned on. When the switching frequency of inverter (f_s) in comparison with the output frequency of inverter (f_L) has been selected big enough ($f_s >> f_L$), the average voltage across the output load (v_{Load}) can be obtained as follows [1]:

$$v_{Load}(t)=\frac{1}{T_{nsh}}(T_1-T_2)v_{o,nsh}=\frac{1}{T_{nsh}}(T_1-T_2)v_{o,\max}(t) \qquad (13)$$

From Equs. (11) and (13), the values of T_1 and T_2 are equal to:

$$T_1=\frac{T_{nsh}}{2}\left(1+\frac{v_{Load}(t)}{v_{o,\max}(t)}\right) \quad for \quad T_{sh}\le T_1\le T_{nsh} \qquad (14)$$

$$T_2=\frac{T_{nsh}}{2}\left(1-\frac{v_{Load}(t)}{v_{o,\max}(t)}\right) \quad for \quad T_{sh}\le T_2\le T_{nsh} \qquad (15)$$

Fig. 4 shows the first proposed control signals for the switches of single-phase inverter based on the Z-source network. The first control method can be analyzed under two conditions as follows:

1) Achieved Results for Constant Input and Balanced Output Voltage (CIBOV): In this case, the dc input voltage has the constant value, smooth and without the ripple, which can be defined as follows:

$$v_{dc}(t)=V_{dc} \qquad (16)$$

In the CIBOV case, the voltage of output load (v_{Load}) is considered as follows:

$$v_{Load}(t)=V_{o,\max}\sin\omega_L t \qquad (17)$$

where $V_{o,\max}$ and ω_L are the maximum and angular speed of the output load voltage, respectively.

By substituting Equs. (16) and (17) into Equs. (14) and (15), the values of T_1 and T_2 are equal to:

$$T_1=\frac{(1-D_{sh})T_s}{2}(1+\sin\omega_L t)=\frac{M}{2f_s}(1+\sin\omega_L t) \qquad (18)$$

$$T_2=\frac{(1-D_{sh})T_s}{2}(1-\sin\omega_L t)=\frac{M}{2f_s}(1-\sin\omega_L t) \qquad (19)$$

In this case, the current through the RL output load (i_{Load}) is equal to:

$$i_{Load}(t)=I_{o,\max}\sin(\omega_L t+\phi_L) \qquad (20)$$

where $I_{o,\max}$ is the maximum current through the RL output load and ϕ_L is the phase difference between the voltage and current of RL output load, which can be calculated as follows:

$$I_{o,\max}=\frac{V_{o,\max}}{\sqrt{R_L^2+(L_L\omega_L)^2}} \quad , \quad \phi_{Load}=\tan^{-1}\left(\frac{L_L\omega_L}{R_L}\right) \qquad (21)$$

From Equ. (13), the relation between dc-link and output currents for the time interval of T_{nsh} can be calculated as follows [1]:

$$i_{o,nsh}(t)=\frac{1}{T_{nsh}}(T_1-T_2)\,i_{Load}(t) \qquad (22)$$

Considering Equs. (18) to (22), in the non-ST switching state, the instantaneous current of dc-link ($i_{o,nsh}(t)$) is equal to:

$$i_{o,nsh}(t)=\frac{I_{o,\max}}{2}[\cos\phi_L-\cos(2\omega_L t+\phi_L)] \qquad (23)$$

2) Achieved Results for Ripple Input and Balanced Output Voltage (RIBOV): In this case, the dc input voltage has variable value, not smooth and with ripple, which can be defined as follows:

$$v_{dc}(t)=V_{dc}+V_r\sin\omega_r t \qquad \forall t:\ v_{dc}(t)>0 \qquad (24)$$

By substituting Equ. (24) into Equs. (14) and (15), the values of T_1 and T_2 are equal to:

$$T_1=\frac{(1-D_{sh})T_s}{2}\left(1+\frac{V_{o,\max}\sin\omega_L t}{V_{o,\max}+V_r\sin\omega_r t}\right)=\frac{M}{2f_s}\left(1+\frac{V_{o,\max}\sin\omega_L t}{V_{o,\max}+V_r\sin\omega_r t}\right) \qquad (25)$$

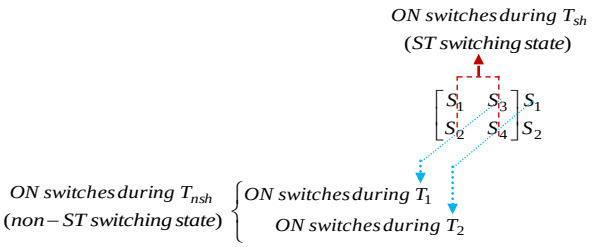

Fig. 5. Second proposed control method.

$$T_2 = \frac{(1-D_{sh})T_s}{2}\left(1-\frac{V_{o,\max}\sin\omega_L t}{V_{o,\max}+V_r\sin\omega_r t}\right) = \frac{M}{2f_s}\left(1-\frac{V_{o,\max}\sin\omega_L t}{V_{o,\max}+V_r\sin\omega_r t}\right) \quad (26)$$

B. Second Proposed Control Method

In the second proposed control method, the sequence of turning on and off for the switches is shown in Fig. 5. In this method for the time interval of T_{nsh}, the switches of S_2 and S_3 are turned on and the switches of S_1 and S_4 are turned off for the time interval of T_1, and vice versa for the time interval of T_2. The time interval of T_{sh} is similar to the first proposed method.

Considering $f_s >> f_L$, the average voltage across the output load (v_{Load}) is equal to:

$$v_{Load}(t) = \frac{1}{T_{nsh}}(-T_1+T_2)v_{o,nsh} = \frac{1}{T_{nsh}}(-T_1+T_2)v_{o,\max}(t) \quad (27)$$

From Equs. (11) And (27), the values of T_1 and T_2 are equal to:

$$T_1 = \frac{T_{nsh}}{2}\left(1-\frac{v_{Load}(t)}{v_{o,\max}(t)}\right) \quad for \quad T_{sh} \le T_1 \le T_{nsh} \quad (28)$$

$$T_2 = \frac{T_{nsh}}{2}\left(1+\frac{v_{Load}(t)}{v_{o,\max}(t)}\right) \quad for \quad T_{sh} \le T_2 \le T_{nsh} \quad (29)$$

The second proposed control signals for the switches of single-phase Z-source inverter are shown in Fig. 6. This control method can be analyzed under two conditions as follows:

1) Achieved Results for Constant Input and Balanced Output Voltage (CIBOV): In this case, by placing Equs. (16) And (17) into Equs. (28) And (29), the values of T_1 and T_2 are equal to:

$$T_1 = \frac{(1-D_{sh})T_s}{2}(1-\sin\omega_L t) = \frac{M}{2f_s}(1-\sin\omega_L t) \quad (30)$$

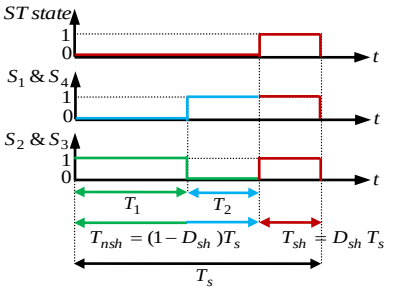

Fig. 6. Control signals of the second proposed PWM control method.

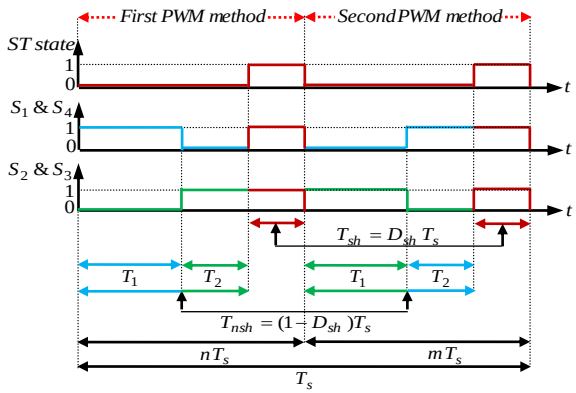

Fig. 7. Control signals of the third proposed PWM control method.

$$T_2 = \frac{(1-D_{sh})T_s}{2}(1+\sin\omega_L t) = \frac{M}{2f_s}(1+\sin\omega_L t) \quad (31)$$

2) Achieved Results for Ripple Input and Balanced Output Voltage (RIBOV): In this case, by placing Equs. (17) And (24) into Equs. (28) And (29), the values of T_1 and T_2 are equal to:

$$T_1 = \frac{(1-D_{sh})T_s}{2}\left(1-\frac{V_{o,\max}\sin\omega_L t}{V_{o,\max}+V_r\sin\omega_r t}\right) = \frac{M}{2f_s}\left(1-\frac{V_{o,\max}\sin\omega_L t}{V_{o,\max}+V_r\sin\omega_r t}\right) \quad (32)$$

$$T_2 = \frac{(1-D_{sh})T_s}{2}\left(1+\frac{V_{o,\max}\sin\omega_L t}{V_{o,\max}+V_r\sin\omega_r t}\right) = \frac{M}{2f_s}\left(1+\frac{V_{o,\max}\sin\omega_L t}{V_{o,\max}+V_r\sin\omega_r t}\right) \quad (33)$$

C. Third Proposed Control Method

By combining both the first and second proposed PWM methods, the third control method is proposed. In this method, a sampling time period is divided into two sections such as n and m, which are shown in Fig. 7. The third proposed

control signals for the switches of single-phase Z-source inverter are shown in Fig. 7.

According to Equs. (13) And (27), the average voltage across the output load (v_{Load}) can be obtained as follows:

$$v_{Load}(t)=\left[\frac{n}{T_{nsh}}(T_1-T_2)+\frac{m}{T_{nsh}}(-T_1+T_2)\right]v_{o,\max}(t) \qquad (34)$$

IV. Comparison

Various PWM control methods have been introduced for the ZSI topologies. But overall they can be classified into carrier-based PWM strategies [12]-[18]. In this technique, the control signals for switch gates generate from the comparison of linear or curve reference waves with the triangular carrier waveform. Hence, the pulse widths of signal gates can be equal or unequal which causes the values of the ST duty cycle will respectively be constant or variable [9], [12].

Three fundamental and most important PWM control methods are related to the simple boost control (SBC), maximum boost control (MBC), and maximum constant boost control (MCBC) [9], [12]. Table I and Figs. 8 and 9 present a comparison between the three techniques of SBC, MBC, and MCBC. Considering Table I and Figs. 8 and 9, the SBC method is used to control of D_{sh} (ST duty cycle) in which the ST time per switching cycle is kept constant. Hence, the boost factor will be a constant value. Under these conditions, the dc inductor current and capacitor voltage, which are associated with the output frequency, will have no ripples. In this strategy, the value of D_{sh} is decreased with the increase of M, which causes relatively high voltage stress across the devices. In the MBC method, the ST time per switching cycle is variable. MBC in comparison with SBC not only reduces the voltage stress across the devices for the same modulation index but also increases the voltage boost factor and inverter voltage gain. However, it has the drawbacks of low-frequency ripples on the Z-source network. So that the inductor current ripple becomes significant when the output frequency is low, and a large inductor is required. In order to reduce the volume and cost of the LC network, the elimination of low-frequency current ripple is needed by using a constant ST duty cycle. At the same time, a higher voltage boost and lower voltage stress for any given modulation index are simultaneously demanded. The MCBC method is introduced to achieve the above aims [9], [12].

Proposed control methods not only can be achieved all the benefits of SBC, MBC, and MCBC but also they have a number of unique advantages that are listed below:

- The most important advantage of the proposed control methods is having a mathematical basis.

TABLE I
Comparison of SBC, MBC, and MCBC Strategies.

PWM method	ST duty cycle	Voltage boost factor	Inverter voltage gain	Devices voltage stress
	$D_{sh}=\frac{T_{sh}}{T}$	$B=\frac{1}{1-2D_{sh}}$	$G=M\times B$	V_s/V_{dc} versus G
SBC	$1-M$	$\frac{1}{2M-1}$	$\frac{M}{2M-1}$	$2G-1$
MBC	$\frac{2\pi-3\sqrt{3}M}{2\pi}$	$\frac{\pi}{3\sqrt{3}M-\pi}$	$\frac{\pi M}{3\sqrt{3}M-\pi}$	$\frac{3\sqrt{3}G-M}{\pi}$
MCBC	$1-\frac{\sqrt{3}M}{2}$	$\frac{1}{\sqrt{3}M-1}$	$\frac{M}{\sqrt{3}M-1}$	$\sqrt{3}G-1$

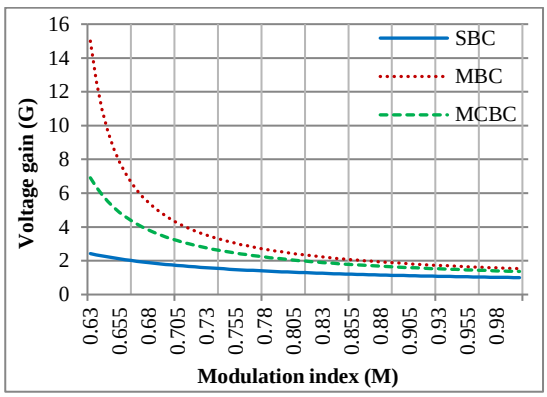

Fig. 8. Comparison of voltage gain versus modulation index.

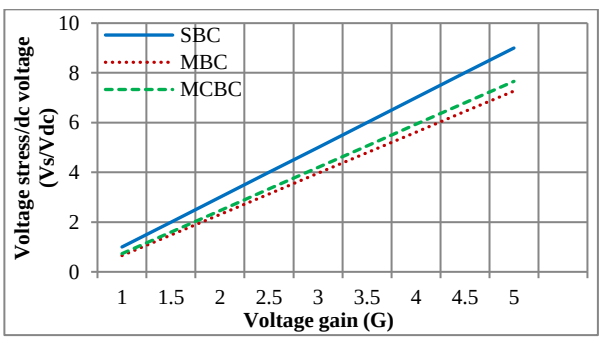

Fig. 9. Comparison of normalized devices voltage stress versus voltage gain.

- Considering Equs. (4) to (6), the used relationship between D_{sh} and M is related to the SBC method. Hence, all obtained results for the proposed methods will be under this technique. However, due to the capability of the proposed methods, the D_{sh} and M relationship related to the MBC or MCBC methods can be used instead of the SBC.
- The switching states of the SBC, MBC, and MCBC are generated by comparing two straight lines or two curves with a triangle carrier waveform each of which had its own advantages and disadvantages. But the proposed control methods have used a series of mathematical

equations for generating the switching states which can overcome their disadvantages (such as higher harmonics and THD).

- According to Fig. 7 ($nT_s + mT_s = T_s$ or $n+m=1$), the n or m can be used to control the one parameter of the inverter. Thus, in the third proposed technique, not only the voltage and current can be controlled but also it can control (or eliminate) the extra parameters such as harmonic and THD without any hardware elements.

V. Simulation Results and Discussion

In this paper, the proposed PWM methods are implemented for qZSI topology. To prove the correct performance of the proposed PWM control methods under CIBOV and RIBOV conditions, the achieved results of the simulation are used. Moreover, in the same condition, a comparison is done between proposed and SBC methods in terms of harmonics, THD, and dynamic response. Table II shows the used parameters for the simulations.

A. *Check the Correct Operation of the Proposed Control Methods*

Figs. 10 to 15 show the simulation results of the proposed PWM control methods for single-phase qZSI under CIBOV and RIBOV operations. According to Table II, the input voltage source and the maximum amplitude of RL output load voltage are equal to $V_{dc} = 50V$ and $V_{o,\max} = 250V$, respectively. That means the boost factor of the inverter is equal to $B = 5$. Simulation Results for Single-Phase qZSI under three proposed control methods can be analyzed as follows:

1) Obtained Results for the First Control Method: Figs. 10 and 11 show the simulation results for the first proposed PWM control method under CIBOV and RIBOV operations, respectively. From Equs. (6) and (4), the modulation index and duty cycle should be $M = 0.6$ and $D_{sh} = 0.4$, respectively. From Equs. (1) and (2), the obtained voltages across the dc-link of qZSI for ST and non-ST states are $v_{o,sh} = 0V$ and $v_{o,nsh} = 250V$, respectively, which are shown in Figs. 10(b) and 11(a). The voltage and current of RL output load under CIBOV and RIBOV operations are shown in Figs. 10(d, e) and 11(c, d), respectively.

2) Obtained Results for the Second Control Method: Figs. 12 and 13 show the simulation results for the second proposed PWM control method under CIBOV and RIBOV operations, respectively. From Equs. (1) and (2), the obtained voltages across the dc-link of qZSI for ST and non-ST states should be $v_{o,sh} = 0V$ and $v_{o,nsh} = 250V$, respectively, which are shown in Figs. 12(b) and 13(a). The voltage and current of RL output load under CIBOV and RIBOV operations are shown in Figs. 12(d, e) and 13(c, d), respectively.

3) Obtained Results for the Third Control Method: Figs. 14 and 15 show the simulation results for the third proposed PWM control method under CIBOV and RIBOV operations, respectively. Figs. 14(b) and 15(a) show the obtained voltages across the dc-link for ST and non-ST states, respectively. Figs. 14(d, e) and 15(c, d) show the voltage and current of RL output load under CIBOV and RIBOV operations, respectively.

As a result, considering the obtained theoretical and simulation results, the simulation results shown in Figs. 10 to 15 are similar to the theoretical analysis, which proves the suitable performance of the proposed PWM control methods.

TABLE II
USED PARAMETERS FOR THE SIMULATION.

Quantity	Symbol	Value
Input voltage source	V_{dc}	$50V$
Maximum output voltage	$V_{o,\max}$	$250V$
Z-source network	$C_1 = C_2$	$2mF$
	$L_1 = L_2$	$0.5mH$
Output load values	R_L	40Ω
	L_L	$5mH$
	f_L	$50Hz$
Switching frequency	f_s	$20kHz$

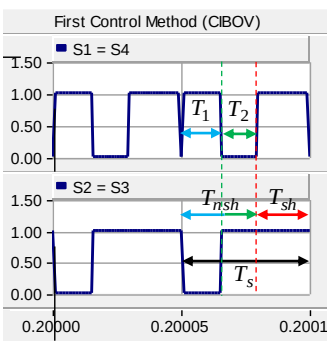

(a)

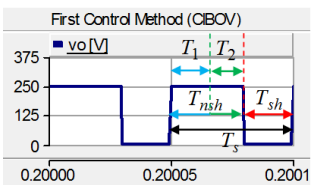

(b)

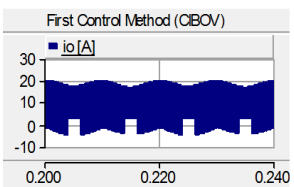

(c)

Fig. 10. continued

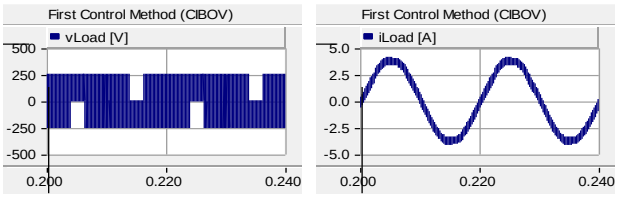

(d) (e)

Fig. 10. Simulation results for the first proposed PWM control method under CIBOV operation; (a) gate pulses of switches, (b) voltage of dc-link, (c) current of dc-link, (d) voltage of RL output load, (e) current of RL output load.

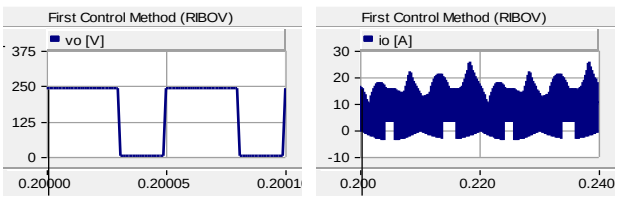

(a) (b)

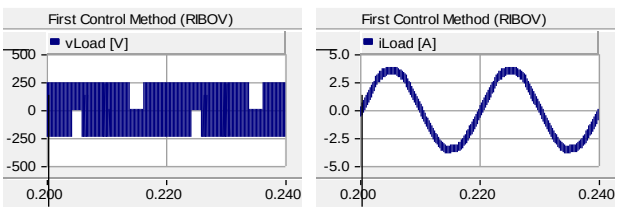

(c) (d)

Fig. 11. Simulation results for the first proposed PWM control method under RIBOV operation; (a) dc-link voltage, (b) current of dc-link, (c) voltage of RL output load, (d) current of RL output load.

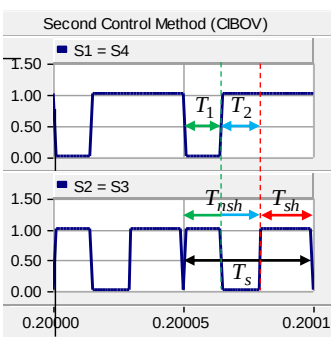

(a)

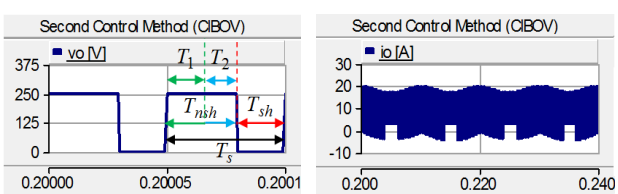

(b) (c)

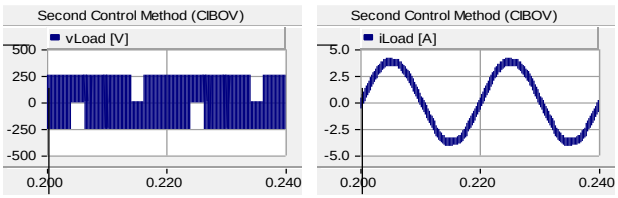

(d) (e)

Fig. 12. Simulation results for the second proposed PWM control method under CIBOV operation; (a) gate pulses of switches, (b) voltage of dc-link, (c) current of dc-link, (d) voltage of RL output load, (e) current of RL output load.

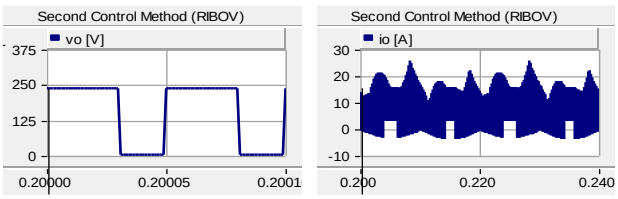

(a) (b)

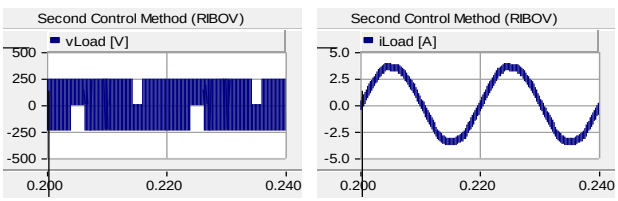

(c) (d)

Fig. 13. Simulation results for the second proposed PWM control method under RIBOV operation; (a) dc-link voltage, (b) current of dc-link, (c) voltage of RL output load, (d) current of RL output load.

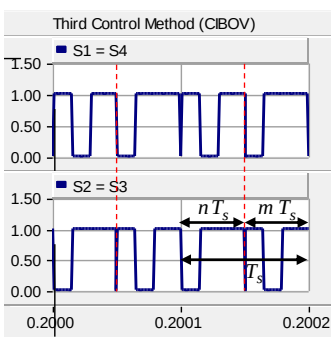

(a)

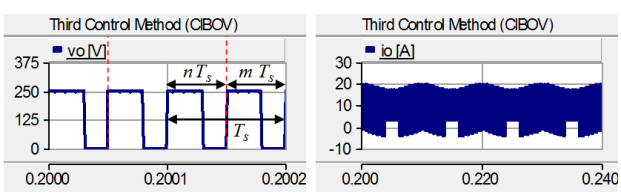

(b) (c)

Fig. 14. continued

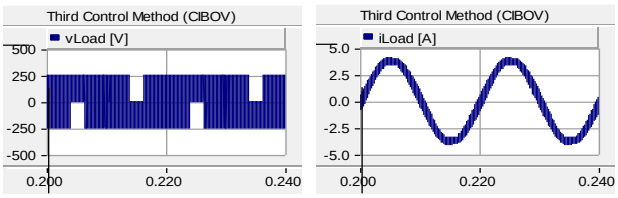

(d) (e)

Fig. 14. Simulation results for the third proposed PWM control method under CIBOV operation; (a) gate pulses of switches, (b) voltage of dc-link, (c) current of dc-link, (d) voltage of *RL* output load, (e) current of *RL* output load.

B. Harmonic and THD Analysis

The harmonic spectrums and THD results of output voltage and current for the proposed and SBC control methods under different operational conditions are illustrated in Figs. 16 to 19. In CIBOV and RIBOV cases, the harmonics components of the proposed methods are less than the SBC method (Figs. 16 and 18). Also, the THD of the output voltage for the proposed methods is less than the SBC method (Figs. 17 and 19). The THD of the output current for the first and second proposed methods is almost equal to the SBC method. But, it has a lower value for the third proposed method. In addition, the reduction of harmonics and THD values for the third proposed strategy is more in comparison with the first and second proposed methods (Figs. 17 and 19).

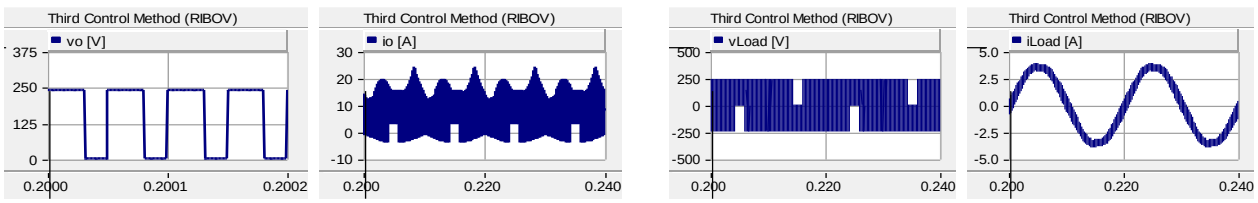

(a) (b) (c) (d)

Fig. 15. Simulation results for the third proposed PWM control method under RIBOV operation; (a) dc-link voltage, (b) current of dc-link, (c) voltage of *RL* output load, (d) current of *RL* output load.

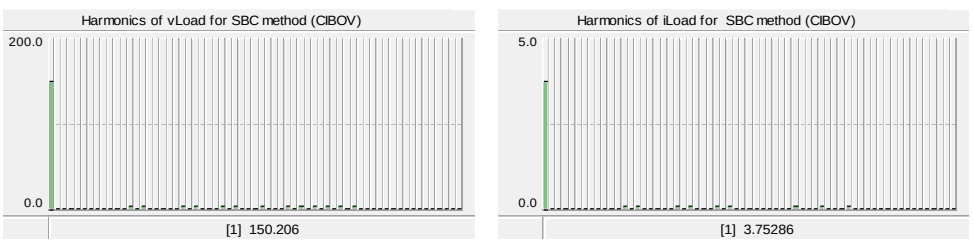

(a)

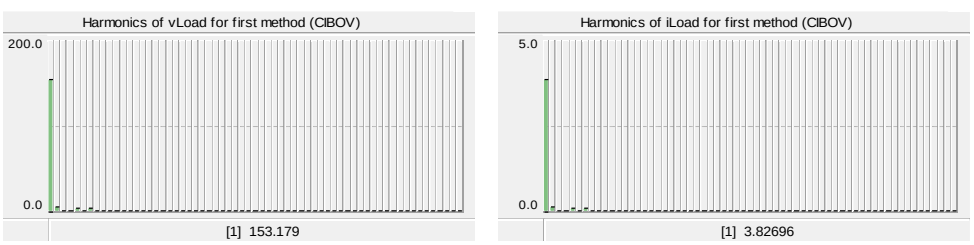

(b)

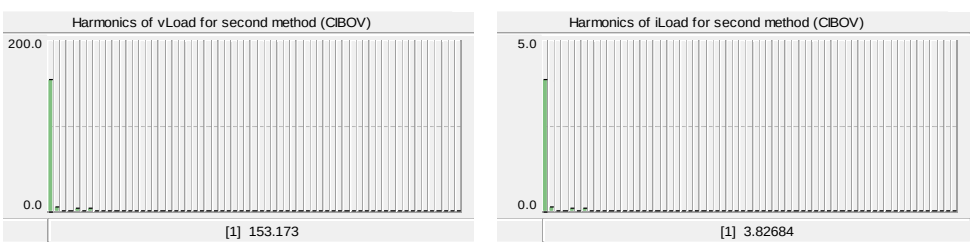

(c)

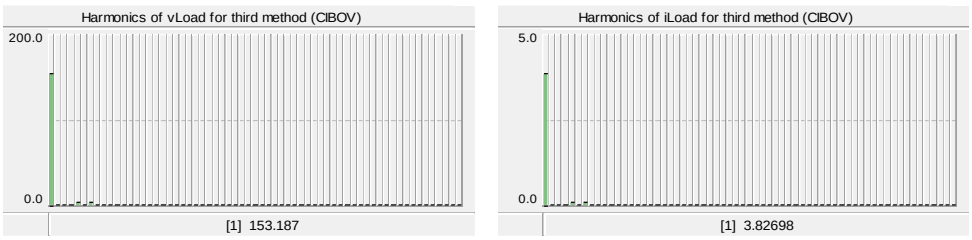

(d)

Fig. 16. Harmonic spectrums under CIBOV operation; (a) SBC method, (b) first proposed method, (c) second proposed method, (d) third proposed method.

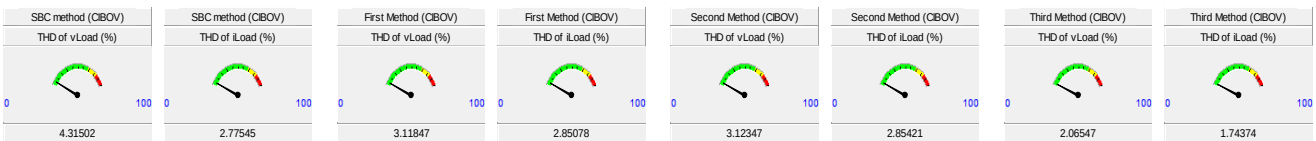

(a) (b) (c) (d)

Fig. 17. THD analysis under CIBOV operation; (a) SBC method, (b) first proposed method, (c) second proposed method, (d) third proposed method.

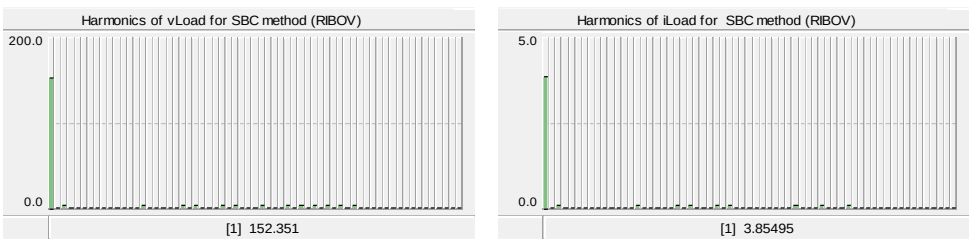

(a)

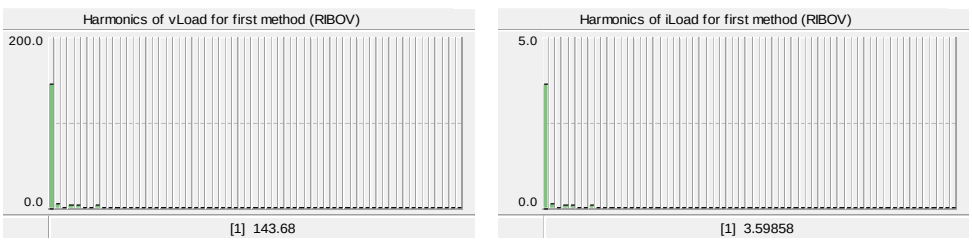

(b)

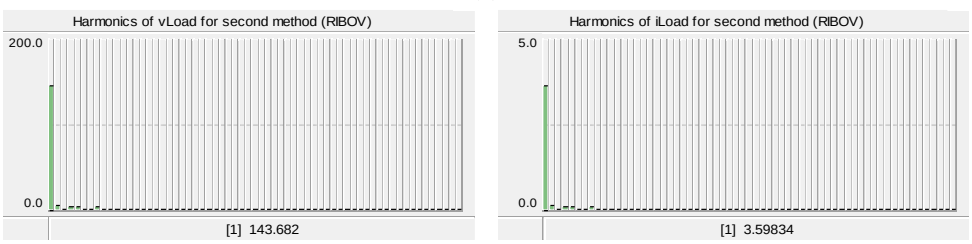

(c)

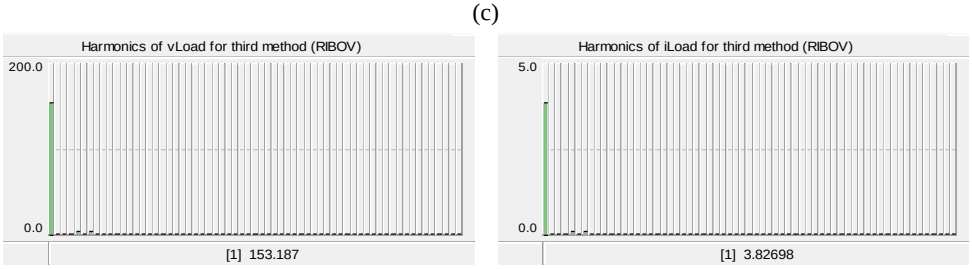

(d)

Fig. 18. Harmonic spectrums under RIBOV operation; (a) SBC method, (b) first proposed method, (c) second proposed method, (d) third proposed method.

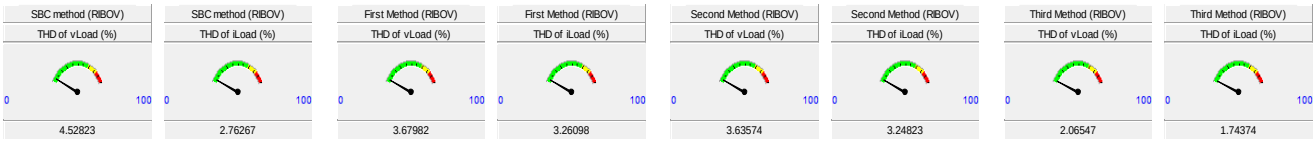

(a) (b) (c) (d)

Fig. 19. THD analysis under RIBOV operation; (a) SBC method, (b) first proposed method, (c) second proposed method, (d) third proposed method.

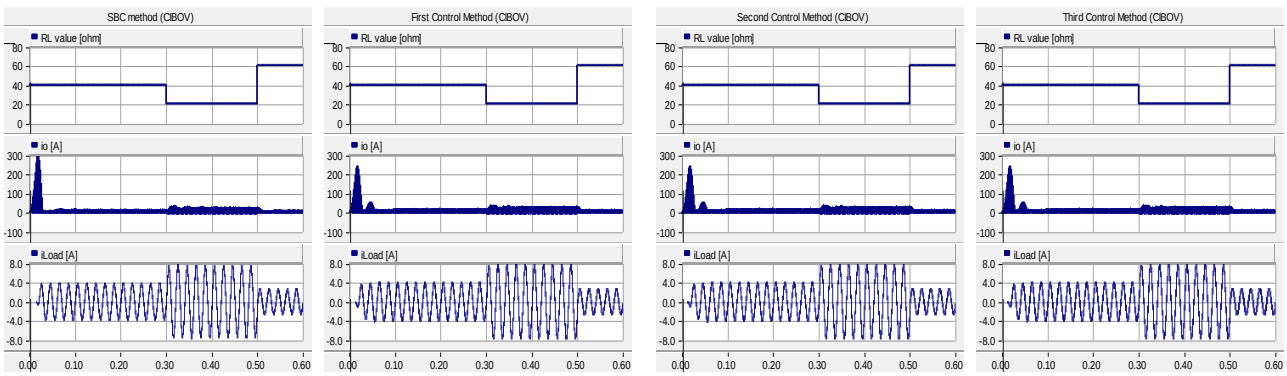

(a) (b) (c) (d)

Fig. 20. Dynamic response evaluation under CIBOV operation; (a) SBC method, (b) first proposed method, (c) second proposed method, (d) third proposed method.

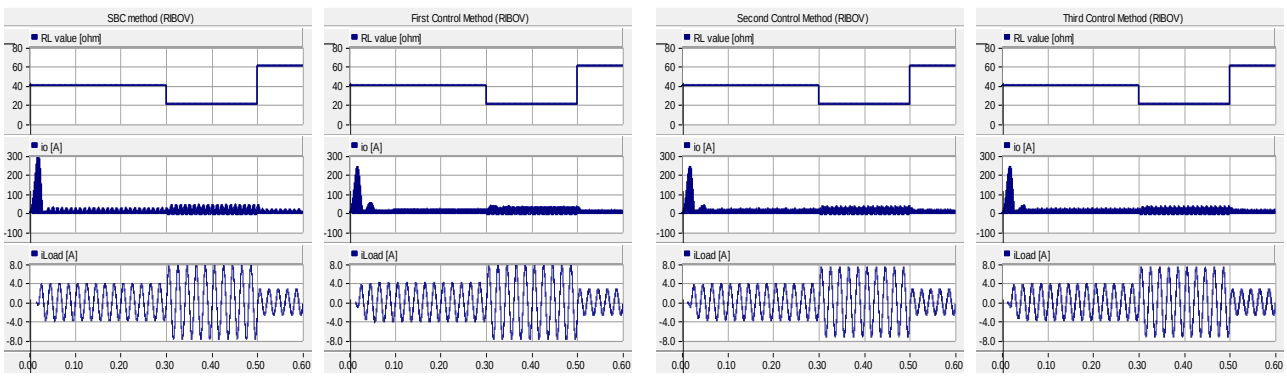

(a) (b) (c) (d)

Fig. 21. Dynamic response evaluation under RIBOV operation; (a) SBC method, (b) first proposed method, (c) second proposed method, (d) third proposed method.

C. Dynamic Response Evaluation

In order to dynamic change evaluation in the output of qZSI, the output resistance value (R_L) will be changed among 20, 40, and 60 ohms. During this evaluation, the output inductor value has a constant value ($L_L = 5\,mH$). Figs. 20 and 21 show dynamic change evaluation in the qZSI output by using the proposed and SBC control techniques under CIBOV and RIBOV operations. For different values of output resistance (R_L), the simulation results shown in Figs. 20 and 21 demonstrate the appropriate operating of dynamic changes in the qZSI output for proposed methods under CIBOV and RIBOV operations. Also, the output current in the proposed strategies has a lower amplitude in the transient mode in comparison with the SBC method.

VI. CONCLUSION

The design of a suitable control method for the inverters can be an effective solution to the elimination of low order harmonics, the lower value for THD, and decreasing the size and cost of the filter. Hence, in this paper, three new PWM control methods based on mathematical equations were proposed for controlling the various single-phase ZSIs. The proposed methods can also be extended to the various three-phase Z-source topologies. Regardless of whether the input voltage is constant or variable, the proposed PWM techniques can produce a desired balanced and unbalanced

voltage at the output of the inverter. The proposed methods were analyzed under different circumstances (CIBOV and RIBOV), which the worthiness of them was confirmed by obtained simulation results in PSCAD software.

REFERENCES

[1] E. Babaei, "A new pulse with modulation technique for inverters," *Arabian Journal for Science and Engineering*, Vol. 39, No. 8, pp. 6235-6247, Aug. 2014.

[2] E. Babaei and M. Sabahi, "Development of pulse with modulation technique for controlling invrters under balanced and unbalanced operations," *Arabian Journal for Science and Engineering*, Vol. 39, No. 4, pp. 2941-2951, Apr. 2013.

[3] S. Xiao, T. Shi, X. Li, Z. Wang, and C. Xia, "Single-current-sensor control for PMSM driven by quasi-Z-source inverter," *IEEE Trans. Power Electron.*, Vol. 34, No.7, pp. 7013-7024, Jul. 2019.

[4] N. Vosoughi, S. H. Hosseini, and Mehran Sabahi, "A new transformer-less five-level grid-tied inverter for photovoltaic applications," *IEEE Trans. Energy Convers.*, Vol. 35, No.1, pp. 106-118, Mar. 2020.

[5] X. Guo, N. Wang, J. Zhang, B. Wang, and M.K. Nguyen, "A novel transformerless current source inverter for leakage current reduction," IEEE Access, Vol. 7, pp. 50681-50690, Apr. 2019.

[6] T. Ahmadzadeh, E. Babaei, M. Sabahi, and T. Abedinzadeh, "An improved transformerless grid-connected PV system with related control strategy to reduce leakage current, extract maximum power point and control power," *Iranian Journal of Electrical and Electronic Engineering (IJEEE)*, Vol. 16, No.4, pp. 513-523, Dec. 2020.

[7] A. Karbalaei and M. Mardaneh, "Improved symmetric switched-inductor/capacitor quasi Z-source inverter with ability uplifted-boost," *International Journal of Industrial Electronics, Control and Optimization (IECO)*, Vol. 3, No. 1, pp. 47-58, Jan. 2020.

[8] A. Karbalaei and M. Mardaneh, "Improved symmetric switched-inductor/capacitor quasi Z-source inverter with ability uplifted-boost," *International Journal of Industrial Electronics, Control and Optimization (IECO)*, Vol. 3, No. 1, pp. 47-58, Jan. 2020.

[9] E. Babaei and T. Ahmadzadeh, "A new structure of buck-boost Z-source converter based on Z-H converter," *Journal of Operation and Automation in Power Engineering (JOAPE)*, Vol. 4, No. 2, pp. 25-39, Dec. 2016.

[10] T. Ahmadzadeh and E. Babaei, "Improved quasi-Z-source based three-Phase three-Level neutral point clamped inverter," in *Proc. PEDSTC*, pp. 99-103, 2018.

[11] T. Ahmadzadeh, E. Babaei, and M. Sabahi, "Modified PWM control method for neutral point clamped ultilevel inverters," in *Proc. ECTICON*, pp. 765-768, 2017.

[12] M. Shen, J. wang, A. Joseph, F. Z. peng, L. M. Tolbert, and D. J. Adams "Constant Boost Control of the Z-Source Inverter to Minimize Current Ripple and Voltage Stress," *IEEE Trans. Ind. Appl.*, Vol. 42, No.3, pp. 770-778, May/Jun. 2006.

[13] R. Iijima, T. Isobe, and H. Tadano, "Optimized short-through time distribution for inductor current ripple reduction in Z-source inverters using space-vector modulation," *IEEE Trans. Ind. Appl.*, Vol. 55, No. 3, pp. 2922-2930, May/Jun. 2019.

[14] S. Singh and S. Sonar , "A new SVPWM technique to reduce the inductor current ripple of three-phase Z-source inverter," *IEEE Trans. Ind. Electron.*, Vol. 67, No. 5, pp. 3540-3550, May. 2020.

[15] D. Shuai and Z. Qianfa, "Analysis and control of current ripples of Z-source inverters," *IEEE Access*, Vol. 8, pp. 41220-41228, Feb. 2020.

[16] M. Mohammadi, J.S. Moghani, and J. Milimonfared, "A novel dual switching frequency modulation for Z-source and quasi-Z-source inverters," *IEEE Trans. Ind. Electron.*, Vol. 65, No. 6, pp. 5167-5176, Jun. 2018.

[17] W. Xu, M. Liu, J. Liu, K.W. Chan, and K.W.E. Cheng, "A series of new control methods for single-phase Z-source inverters and the optimized operation," *IEEE Access*, Vol. 7, pp. 113786-113800, Aug. 2019.

[18] L. Hang, U. Subramaniam, G. Bayrak, H. Moayedi, D. Ghaderi, and M.R. Minaz, "Influence of a proposed switching method on reliability and total harmonic distortion of the quasi Z-source inverters," *IEEE Access*, Vol. 8, pp. 33088-33100, Feb. 2020.

[19] M. K. Nguyen, Y. C. Lim, and S. J. Park, "A comparison between single-phase quasi-Z-source and quasi-switched boost inverters," *IEEE Trans. Ind. Electron.*, Vol. 62, No. 10, pp. 6336-6344, Oct. 2015.

Taher Ahmadzadeh was born in Tabriz, Iran in 1986. He received his A.Sc. degree in Electronic Engineering from Islamic Azad University, Ahar Branch, Ahar, Iran, in 2006, his B.Sc. degree in Electronic Engineering from Islamic Azad University, Tabriz Branch, Tabriz, Iran, in 2009, and his M.Sc. degree in Electrical Engineering from the Aras International Campus, University of Tabriz, Tabriz, Iran, in 2014. He is currently working towards his Ph.D. degree in Electrical Engineering from the Department of Engineering, Shabestar Branch, Islamic Azad University, Shabestar, Iran. His current research interests include the analysis and control of power electronic converters and their applications.

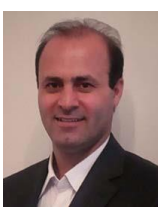

Ebrahim Babaei was born in Ahar, Iran, in 1970. He received his B.Sc. degree in Electronic Engineering and his M.Sc. degree in Electrical Engineering from the Department of Engineering, University of Tabriz, Tabriz, Iran, in 1992 and 2001, respectively, graduating with first-class honors. He received his Ph.D. degree in Electrical Engineering from the Department of Electrical and Computer Engineering, University of Tabriz, in 2007. In 2004, he joined the Faculty of Electrical and Computer Engineering, University of Tabriz. He was an assistant professor from 2007 to 2011, an associate professor from 2011 to 2015 and has been a professor since 2015. He is the author of more than 300 journal and conference papers. He also holds 17 patents in the area of power electronics. His current research interests include the analysis and control of power electronic converters and their applications, dynamic power system, power system transients. Prof. Babaei has been the Editor-in-Chief of the Journal of Electrical Engineering of the University of Tabriz, since 2013. He is also currently an Associate Editor of the IEEE TRANSACTIONS ON

INDUSTRIAL ELECTRONICS. He is a Guest Editor for a special issue on “Recent Advances in Multilevel Inverters and their Applications” in the IEEE Transactions on Industrial Electronics. In 2013, he was the recipient of the Best Researcher Award from the University of Tabriz. Prof. Babaei has been included in the Top One Percent of the World’s Scientists and Academics according to Thomson Reuters' list in 2015.

Mehran Sabahi was born in Tabriz, Iran, in 1968. He received his B.Sc. degree in Electronic Engineering from the University of Tabriz, his M.Sc. degree in Electrical Engineering from Tehran University, Tehran, Iran, and his Ph.D. degree in Electrical Engineering from the University of Tabriz, in 1991, 1994, and 2009, respectively. In 2009, he joined the faculty of electrical and computer engineering at the University of Tabriz where he has been an associate professor since 2015. His current research interests include power electronic converters and renewable energy systems.

Taher Abedinzadeh was born in Khoy, Iran, in 1983. He received his B.Sc. degree in Electrical Engineering from Iran University of Science and Technology, Tehran, Iran, in 2005, his M.Sc. degree in Electrical Engineering from the Sharif University of Technology, Tehran, Iran, in 2007, and his Ph.D. degree in Electrical Engineering from Islamic Azad University, Science and Research Branch, Tehran, Iran, in 2014. He is a Faculty Member of Islamic Azad University-Shabestar Branch, Shabestar, Iran. His current research interests include power systems, smart grids, and renewable energies.

IECO

This page intentionally left blank.

International Journal of Industrial Electronics, Control and Optimization © 2021 IECO
Vol. 4, No. 2, pp. 181-190, April (2021)

RF Source Localization Using Obstacles Map and Reflections

Saeid Haidari [1,†], Hadi Moradi [2], Seyyed.M.M.Dehghan [3]

[1] Faculty of Engineering, University of Zabol, Iran.
[2] School of Electrical and Computer Engineering, University of Tehran, Iran.
[2] Intelligent Systems Research Institute, SKKU, South Korea.
[3] Malek-Ashtar University of Technology, Tehran.

ABSTRACT

This paper proposes radio frequency (RF) source localization in a non-line of sight condition using the map of obstacles. Received signal strength indicator (RSSI) and angle of arrival (AOA) measurements are observations obtained from the signal received on the unmanned aerial vehicles (UAV). In the proposed approach, AOA is used to determine the obstacle on the map from which the reflection has happened. Then, RSSI information is used to determine the location of the RF source. In the basic version of the approach, the RF source is located by triangulation. In the advanced approach, the reflection angle is also estimated to improve the localization accuracy. The estimation is done using the particle filter approach. In addition, it is shown analytically that the maximum localization error for the advanced approach is bounded, but the relative formation of the reflectors with respect to each other can increase the localization error for the basic approach.

Article Info

Keywords:
Obstacle Map, Particle filter, Reflection, RF source Localization, RSSI, UAV.

Article History:
Received 2020-10-28
Accepted 2021-02-02

I. INTRODUCTION

Cellphones can be used as RF sources to localize their users in different applications, especially in search and rescue missions over a large area. In some projects such as ARVA [1] and WISCOM [2], RF source localization in disastrous situations has been developed for search and rescue purposes in which the typical localization method based on BTS towers cannot be used. Moreover, in large open areas where network coverage is not available, such as a desert, RF source localization can be used for search and rescue missions. Using UAVs in outdoor search and rescue missions are very popular due to their maneuverability and fast coverage of the areas. UAVs can localize an RF source using RSSI [3], TOA [4], Time Difference Of Arrival (TDOA) [5], and Angle Of Arrival (AoA) measurements [6]. Hybrid methods have also been proposed, e.g., a combination of RSSI and AOA [7] and TDOA/FDOA measurements [8]. RF source localization is affected by different types of signal propagation including Line Of Sight (LOS) and Non-Line Of Sight (NLOS) propagations. Localization based on LOS signals, which is not usual in typical environments, is straightforward and already solved. In some conditions, LOS and NLOS signals happen at the same time. There are approaches proposed to mitigate the NLOS effect on localization [9-11]. Also, some approaches are proposed to consider the LOS and NLOS effects within a single model [12]. In a research paper on localization in the indoor environment using reflection and scattered signal, it is assumed that a LOS signal is also available in addition to a multipath signal. The locations of reflectors and scatters are determined using PSO as a searching algorithm [13]. If the signal path between an RF source and a receiver is blocked by an obstacle, the signal is received by the NLOS propagation.

For localization in the NLOS condition the fingerprinting approach can be used. In this approach, a database of received signals is required. It should be created using experimental data or propagation model in which each possible location of the RF source corresponds to a unique receiving signal pattern. This

[†]Corresponding Author: s.heidari@uoz.ac.ir
Tel: +98-32222023, University of Zabol
Faculty of Engineering, University of Zabol, Zabol, Iran.

approach is usually used in indoor applications [14-15]. For outdoor fingerprinting-based localization, a large database should be created [16]. This approach is not applicable for large outdoor localization as it is very time consuming and sometimes impossible to provide the required database.

RF source localization based on the NLOS propagation models has been investigated in the past few years. Dehghan et al. used the diffraction model for the knife-edge obstacles to localize an RF source and corresponding obstacle simultaneously. The diffraction model depends on the height of the obstacle that is located between the RF source and the receiver and on the distances of the obstacle from the RF source and the receiver [17]. Also, Song et al. have used a reflection-based propagation model, TOA-AOA, and the map of urban environments for localization in which the orientation of the buildings as reflectors are vertical to each other [18]. There is an approach that uses TOA/AOA measurements and a reflection model in a scenario in which a transmitter with a known location is used for self-localization of a receiver [19], but it is not applicable for target localization in a search and rescue scenario. In another research, TDOA/AOA-based RF source localization is performed using a reflection model in the NLOS condition. An expectation maximization algorithm is used to optimize the nonlinear localization equations. The accuracy of localization depends on the initial value of the parameters of the optimization including the reflection parameters [20].

In some new works, the localization is performed using reconfigurable intelligent surfaces (RISs) that can change the propagation environment for the reflection. The application includes robots and automated vehicles for the localization and communication system. The parameters of propagation in the RISs can be controlled by a microcontroller using feedback. RISs can be mounted on the wall of the building [21-22].

In another paper, AOA, angle of departure (AOD), and relative time of flight (rTOF) are used for localization. Multipath triangulation for localization of target by using AODs of multipath signals has become possible in which antenna array is required at the target side, but implementation is impossible for localizing a target in search and rescue operation [23].

These approaches employ time-based localization that needs time synchronization between the RF source and the receivers using dedicated devices. In addition, they are developed for urban environments and their assumptions are not suitable for large outdoor areas. In another work, the authors used fully reflected RSSI and AOA measurements for RF source localization by employing an RSSI reflection model. For localization, two steps are used. In the first step, parameters of reflection are obtained and in the second step, location of the RF source is estimated, using the reflection parameters [24-25]. Using RSSI measurement for localization is common due to its easiness of use and the availability of cheap sensors [26].

The presence of obstacles is a challenge in the robotic field research, such as obstacle avoidance [27]. Previously detected obstacles may be used as an aid in navigation. In this paper to improve the RF source localization, RSSI/AOA in a fully NLOS condition is used for localization based on the map of the obstacles and a reflection model. In the studied condition, the obstacles as reflectors have unknown directions as shown in Fig.1. In the first step of the proposed algorithm, the AOA of the signal and the map of the environment are used to determine the location of the reflection point on the map. The proposed approach has two versions. In its basic version, the RSSI and AOA measurements and the map are used for localization. In this case, three reflections are required for localization. In the advanced approach, the estimation of the reflection angle from the RSSI samples is also used. This version needs two reflections for localization and exhibits higher accuracy of localization than the basic one.

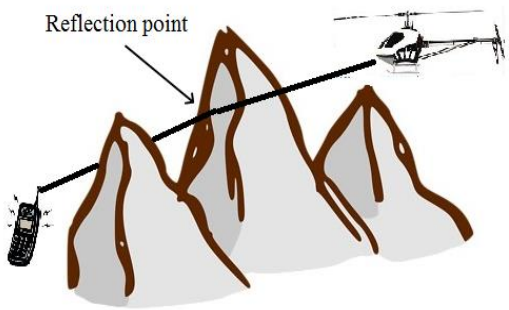

Fig.1. An illustration of the localization of an RF source using reflected signal in the outdoor environment.

The Bayes filter is the technique commonly used for localization in UAV and AUV and robotic field [28]. So, to estimate the RF source location, a particle filter is used because of the nonlinearity of the estimation equation and the motion of the UAV. Afterward, it is analytically shown that using the basic version may lead to a large localization error but using the advanced version has a bounded error.

In the next section, NLOS propagation from the reflector is explained. Then, the proposed approach for map-based localization is described, and the uncertainty of the localization for both versions is calculated. Finally, the simulation results show that the localization with the advanced approach has small uncertainty in comparison to the basic one.

II. REFLECTION PROPAGATION

RF signals propagate in the LOS or NLOS manner. The NLOS signals can be propagated by diffraction, reflection, and/or scattering mechanisms [26]. For a reflected signal, the strength of the signal depends on the path length between the receiver and the RF source. It also depends on the reflection coefficient magnitude, which is between 0 and 1. If it is equal to 1, the signal is reflected without any attenuation. If it is zero,

the signal is absorbed. Path loss in dB for a reflection can be modeled by Equ.(1) [29]:

$$Path\ Loss = 20\log\left(4\pi/\lambda\right) + 20\log(d) - 20\log(|\Gamma(\theta)|) \quad (1)$$

in which λ is the signal's wavelength, d is the path length between the RF source, the receiver, and θ is the reflection angle, $20\log(|\Gamma(\theta)|)$ is the reflection coefficient loss in dB, and $|\Gamma(\theta)|$ is the reflection coefficient magnitude, which is a function of the reflection angle. For a large reflection angle, the effect of roughness surface on the reflected signal is high and the reflection coefficient magnitude has a small amount. The reflection coefficient magnitude for two different frequencies including GSM frequencies and two different polarizations of the signal are shown in Fig. 2.

Generally, shadowing, which is a Gaussian random variable, is added to the path loss with standard deviation (SD) 2.2 to7.7 dB to show the unmolded part of the signal [30].

III. THE PROPOSED APPROACH

It is assumed that there is no LOS path between the RF source and the UAV. Thus, the signal is received using the reflection propagation mechanism. Furthermore, the problem is solved in 2D, and the effect of the UAV altitude is neglected because of the large distance between the UAV and the RF source in comparison with their altitude difference. Moreover, it is assumed that the reflected signals are based on a single bounce and the signals with two or more bounces are weak enough to be neglected. In the proposed approach, RSSI and AOA observations are used for localization.

The path loss of a reflected RF signal depends on the distance between the RF source and the reflector (d_{est}), the reflection angle (θ), and the distance between the reflector and the receiver (d_{obs}) as illustrated in Fig. 3.

In the first step of the proposed approach, the UAV moves in the direction of the received signal and starts to gather RSSI observations periodically. In this scenario, the angle of reflection is constant and the path length between the RF source and the UAV, i.e. $d_{obs} + d_{est}$ which is d in Eq. (2),

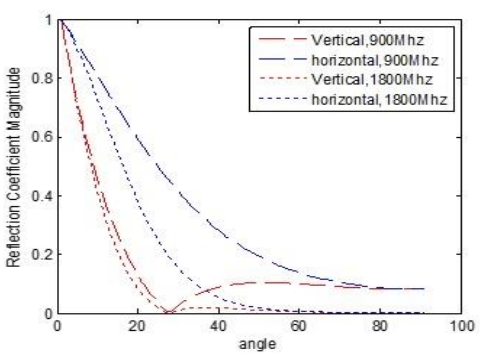

Fig. 2 The magnitudes of the reflection coefficients for a dry ground's surface with 4 cm SD of roughness [29].

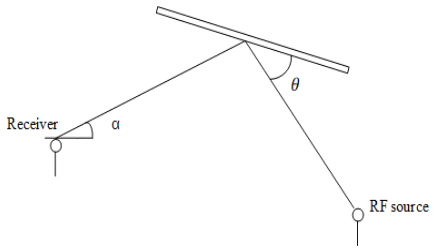

Fig.3. Reflected signal in 2D is illustrated by the RF source location and the reflector and receiver location

$$dPath\ Loss = 20\log\left(4\pi/\lambda\right) + 20\log(d) - 20\log(|\Gamma|) - 20\,log\left(4\pi/\lambda\right) - 20\log(d + \Delta d) + 20\log(|\Gamma|) = 20\log(\frac{d}{d+\Delta d}) \quad (2)$$

can be estimated using the differential RSSI samples based on Eq. (2).

in which Δd is a constant distance step size between two consecutive waypoints in which the UAV takes observations. In the reflection-based RF source localization, the location and/or direction of the reflector are also unknown. As shown in Fig. 4, the loci of the possible locations of the RF source are circles. For each possible location of the reflector in the direction of the signal bearing, a circle can be considered as the locus of the RF source. It is shown in Fig. 4 that the intersection of these circles does not determine a unique location for the RF source even if two or more reflections are used. Consequently, more information is needed to obtain a unique location for the RF source in addition to the path length and the AoA of each reflection. In other words, the localization will not lead to a unique RF source location using the estimated path length and the angle of arrival even for different reflected signals.

In Subsection *A*, more information including the location of the reflector extracted from the obstacle map is used for

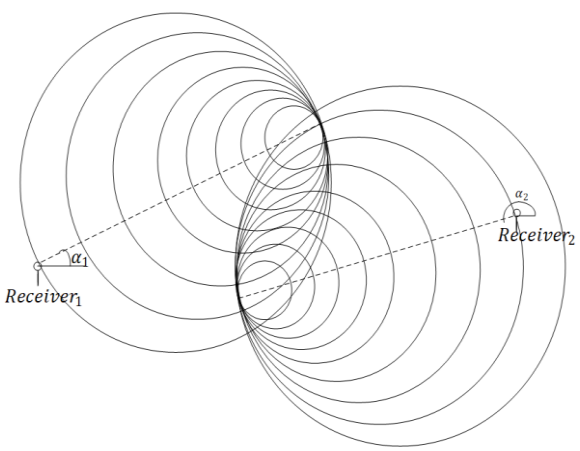

Fig.4. For two reflections, possible location of the RF source is a common area for the RF source locations.

localization. By this approach, the RF source location will be estimated uniquely.

A. Localization using map

Localization using the map of the obstacles and RSSI/AOA observations can lead to a unique location for the RF source. The intersection of the line of bearing with the obstacles map determines the location of the reflector. It should be noted that the orientation of the obstacles on the map are unknown because they are a natural obstacle (irregular terrain).

By using the reflector location, which is determined on the map, and the estimated reflection path length from RSSI samples, a circle is constructed as the RF source locus. In our basic version, the location of the RF source is estimated using the intersection of the three loci circles as shown in Fig. 5. It should be mentioned that the AOA of the signal has an error. This error leads to uncertainty in the reflection point detection. But the error is not large if the AOA is accurate.

It should be mentioned that the reflectors have roughness and the reflected signal with a large reflection angle has weak strength and it can be neglected. As such, localization using two reflections with a small reflection angle is also rendered possible.

To improve the map-based localization, the advanced approach is proposed, and Eq. (1) is used in which $|\Gamma|$ depends on the reflection angle. So, RSSI observation for a reflected signal is a function of the reflection angle in addition to the path length between the RF source and the receiver. As shown in Fig. 6, for a reflection angle (θ_1), there are two possible reflector orientations, so the RF source can be localized using two reflected signals and the estimated path length between the RF source and the receiver and the reflection angle (Fig. 6). The estimation of the RF source location in 2D Cartesian space is performed using particle filter due to the nonlinearity and complications of Eq. (1).

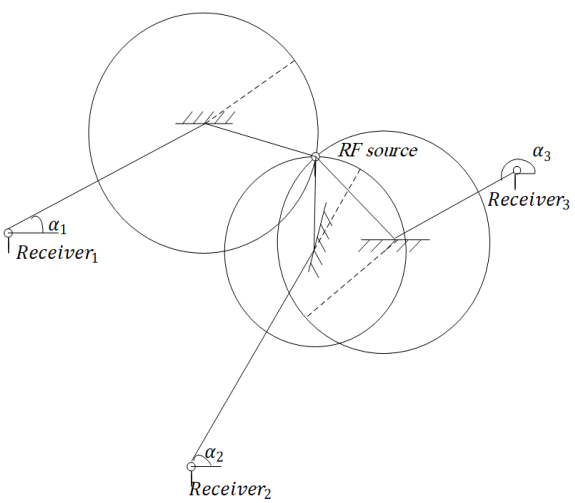

Fig.5. The localization of an RF source with the map and three reflections

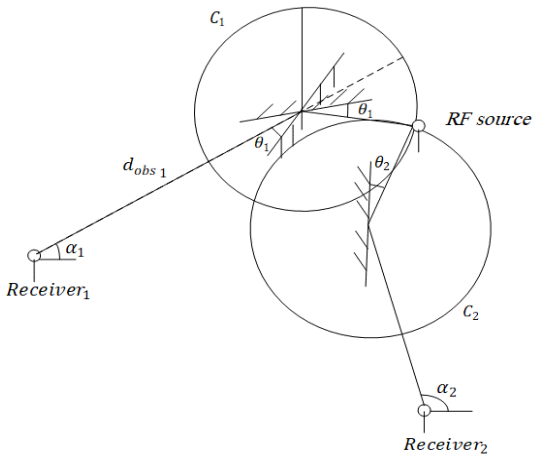

Fig.6. The localization with two reflections using map and reflection angle

1)Particle filter development for the map-based localization

As previously mentioned, the particle filter approach is used as the estimator for the RF source localization due to the nonlinearity of the reflection coefficient in the path loss equation. Particles include the location of the RF source in the Cartesian coordinate, i.e.,$(x^{[i]}, y^{[i]})$.

$$X^{[i]}(t) =< x^{[i]}, y^{[i]} > \quad (3)$$

The steps of the particle filter are presented below.

Particle initialization:

The elements of the particles, i.e. x and y, are uniformly distributed over the possible range, based on the geographical information of the search area.

Prediction of the next state:

The parameters of the particle are the locations of the RF source which are time invariant. It is assumed that the motion model of the UAV is accurate enough and the particles do not change in the prediction phase. The particles are augmented with a low SD in the perdition step to prevent the incorrect convergence of the filter.

Updating particles weight:

The observation model is determined with the path loss equation (Equ. (1)) which is used to update the particles' weight. Considering the known transmitted power, the path loss can be measured using the power received by the UAV. Based on this description, the observation model can be shown by Equ.(4):

$$p\left(Z(t)\middle|X^{[i]}(t)\right) = p(PL_{msr}(t)| < x^{[i]}(t), y^{[i]}(t) >) = p(PL_{msr}(t)|PL_{cal}^{[i]}(t)) \quad (4)$$

in which $PL_{msr}(t)$ is the measured path loss and $PL_{cal}^{[i]}(t)$ is the path loss that is calculated based on the location of each particle. For each particle, $PL_{cal}^{[i]}(t)$ is calculated using Equ.

(5).

$$PL_{cal_1}^{[i]}(t) = 20\,log\left(4\pi/\lambda\right) - 20log\,\Gamma(\theta) + 20log(d_{obs_1} + \sqrt{(x^{[i]}(t) - x_{obs_1})^2 + (y^{[i]}(t) - y_{obs_1})^2}) \quad (5)$$

in which x_{obs_1} and y_{obs_1} are the elements of the location of the first obstacle as the first reflector, which is obtained from the map, d_{obs_1} is the distance between the obstacle and the receiver, which is known, and θ is the reflection angle, which can be obtained based on the locations of the RF source, the receiver, and the reflector. It is calculated using Equ. (6).

$$\begin{aligned} a&=\sqrt{((x^{[i]}(t) - x_{obs_1})^2 + \left(y^{[i]}(t) - y_{obs_1}\right)^2} \\ b&=\sqrt{((x^{[i]}(t) - x_{r_1})^2 + \left(y^{[i]}(t) - y_{r_1}\right)^2} \\ \theta &= 90 - 0.5{*}cos^{-1}\left(\frac{{d_{obs_1}}^2 + a^2 - b^2}{2*a*d_{obs1}}\right) \end{aligned} \quad (6)$$

in which (x_r, y_r) is the location of the UAV which is known considering an accurate navigation system. It is assumed that the path loss has Gaussian distribution, so Equ. (7) is used to update the particles' weights.

$$w_t^{[i]}{}_1 = \frac{1}{\sigma_{sh} * \sqrt{2\pi}} e^{-\frac{\left(PL_{msr_1}(t) - PL_{cal_1}^{[i]}(t)\right)^2}{2{\sigma_{sh}}^2}} \quad (7)$$

Because two reflections are required for localization using the advanced approach, the particles' weights are updated using the weights of the measurements for two reflections (Equ. (8)).

$$w_t^{[i]} = w_t^{[i]}{}_1 * w_t^{[i]}{}_2 \quad (8)$$

Resampling:

The number of effective particles is named N_{eff}. When N_{eff} is smaller than a threshold, resampling is performed. Equ. (9) is used to obtain N_{eff} in which $\widetilde{\omega}^{[i]}$ is the normalized weight of the particle i. After resampling, the particles weight will be 1/N.

$$N_{eff} = \frac{1}{\sum_{i=1}^{N}(\widetilde{\omega}^{[i]})^2} \quad (9)$$

B. Analytical calculation of the RF source location uncertainty

The uncertainty of the RF source location depends on the geometry of the problem, the location of the reflector, and the variance of the observation noise. The location of the RF source can be obtained using the parameters of the reflection path loss including d and θ. These parameters have uncertainty around the true values due to the observation uncertainty and the presence of noise. If the observations have a bounded error, then the variance of these parameters is bounded too. To show the effectiveness of the approach, the uncertainty of the location is calculated based on the variance of the parameters of the path loss (Equ. (10)) [31].

$$VAR(x_{RF}) = \sum_i \left(\frac{\partial(x_{RF})}{\partial(parameter_i)}\right)^2 VAR(parameter_i) \quad (10)$$

$$VAR(y_{RF}) = \sum_i \left(\frac{\partial(y_{RF})}{\partial(parameter_i)}\right)^2 VAR(parameter_i)$$

1)Localization uncertainty of the basic version

In the basic version of the map-based localization, the path length between the RF source and the receiver, i.e. d, is the only parameter of the path. With this parameter and using the map, three reflections are required for localization. The intersection of three circles is the RF source location. The equations of the three circles are shown in Equ. (11) in which (x_{obs}, y_{obs}) and $(x_{obs'}, y_{obs'})$ and $(x_{obs''}, y_{obs''})$ are the location of the reflectors.

$$\begin{aligned} &(x_{RF} - x_{obs})^2 + (y_{RF} - y_{obs})^2 = (d - d_{obs})^2 \\ &(x_{RF} - x_{obs'})^2 + (y_{RF} - y_{obs'})^2 = (d' - d_{obs'})^2 \\ &(x_{RF} - x_{obs''})^2 + (y_{RF} - y_{obs''})^2 = (d'' - d_{obs''})^2 \end{aligned} \quad (11)$$

Thus, the trilateration method is used to the RF source location and the above nonlinear equations are converted to linear ones as follows:

$$\begin{aligned} y_{RF} &= a_1 x_{RF} + b_1 \\ y_{RF} &= a_2 x_{RF} + b_2 \\ a_1 &= \frac{x_{obs} - x_{obs'}}{y_{obs'} - y_{obs}} \\ a_2 &= \frac{x_{obs'} - x_{obs''}}{y_{obs''} - y_{obs'}} \end{aligned} \quad (12)$$

Eq. (12) shows two independent line equations that are obtained by differentiating the circles equations mentioned in Eq. (11). The intersection of the lines is shown by Equ. (13):

$$\begin{aligned} x_{RF} &= \left(\frac{b_1 - b_2}{a_2 - a_1}\right) \\ y_{RF} &= a_2\left(\frac{b_1 - b_2}{a_2 - a_1}\right) + b_2 \end{aligned} \quad (13)$$

Without the loss of generality, it is assumed that only one of the lines has uncertainty which is caused by the effect of the uncertainty of d on the path loss. To calculate the uncertainty of the localization, the derivative of the RF source location to this parameter is obtained by using the chain rule. Based on this description, the MSE of the location is obtained by using Equ. (14):

$$MSE|_{[x\,y]} = VAR(x_{RF}) + VAR(y_{RF}) = \frac{(d - d_{obs})^2}{(y_{obs'} - y_{obs})^2}\left[\left(\frac{1}{a_2 - a_1}\right)^2 + \left(\frac{a_2}{a_2 - a_1}\right)^2\right] VAR(d) \quad (14)$$

It is obvious that the MSE of the RF source location depends on the slope of the lines which are shown by a_1 and a_2. If these slopes are equal, then the error will be very large.

The derivative-based optimization of the MSE function, which is demonstrated by Equ. (15), leads to $a_2 = -1/a_1$. This means that if the second line is vertical to the first one, then the uncertainty of localization will be minimal. The minimum value of the MSE is calculated by Equ. (15).

$$\min(MSE|_{[x\,y]}) = \frac{(d-d_{obs})^2}{(y_{obs'}-y_{obs})^2}\frac{1}{1+a_1{}^2}VAR(d) = \left(\frac{d-d_{obs}}{d_{reflectors}}\right)^2 VAR(d) \quad (15)$$

in which $d_{reflectors}$ is the distance between two centers of the locus circles that are determined by the reflector locations. When the reflectors are close to each other, the minimum of the uncertainty of the RF source location will be large even if $VAR(d)$ has a bounded value.

2)Localization uncertainty of the advanced version

In the advanced version of the map-based localization, the RF source localization is performed using the path loss parameters and AOA as Equ. (16).

$$x_{RF} = d_{obs}cos(\alpha) + (d-d_{obs})cos(\alpha-2\theta) + x_r$$
$$y_{RF} = d_{obs}sin(\alpha) + (d-d_{obs})sin(\alpha-2\theta) + y_r \quad (16)$$

in which it is assumed that the error of the parameters has a known variance. The derivatives of Equ. (16) with respect to the parameters of the path loss, i.e. d and θ, are shown in Equ. (17).

$$\frac{\partial x_{RF}}{\partial d} = \cos(\alpha-2\theta)$$
$$\frac{\partial y_{RF}}{\partial d} = \sin(\alpha-2\theta)$$
$$\frac{\partial x_{RF}}{\partial \theta} = 2(d-d_{obs})\sin(\alpha-2\theta) \quad (17)$$
$$\frac{\partial y_{RF}}{\partial \theta} = -2(d-d_{obs})\cos(\alpha-2\theta)$$

The uncertainty of the RF source location, which is caused by the variance of the distance, can be calculated using Equ. (18):

$$MSE|_{[x\,y]}(d) = VAR(x_{RF}) + VAR(y_{RF}) = VAR(d) \quad (18)$$

Equ. (18) shows that the uncertainty of the localization is equal to the error of d. Also, it shows that the geometric relation of the reflectors has no effect on the uncertainty of the localization.

The error of the RF source location caused by $VAR(\theta)$ is calculated using Equ. (19).

$$MSE|_{[x\,y]}(\theta) = VAR(x_{RF}) + VAR(y_{RF}) = 4(d-d_{obs})^2 VAR(\theta) \quad (19)$$

In this equation, it is shown that the uncertainty of the RF source location, which is caused by the reflection angle uncertainty, depends on the distance between the obstacle and the RF source. If $VAR(\theta)$ has a bounded value, the uncertainty of the RF source localization will be bounded. It should be mentioned that the above calculation is done for one reflection. If two or more reflections are used for the localization, the localization uncertainty will be equal or lower than the above-calculated value. In other words, the summation of the uncertainties calculated by Eq. (18) and (19) is the maximum uncertainty of the localization by the advanced approach, which is a bounded error.

The above calculation shows that the maximum uncertainty of the RF source localization by the advanced approach is bounded if the errors of its parameters are bounded, but the minimum localization error of the basic approach for a bounded error of the path loss parameters can be large when the reflectors are near each other.

IV. SIMULATION AND RESULTS

In the simulations, it is assumed that the obstacles map is available. Also, the locations of the reflectors are previously determined using this map and the AOA of the received signals. After receiving the first reflected signal, the UAV moves in the direction of the signal and takes several RSSI samples. Furthermore, the reflection surface is considered large enough to use the mentioned propagation equation and the reflector's material is assumed to be dry soil. Finally, only horizontal polarization is used for localization.

In the first simulations, for the localization using the basic version, it is assumed that three reflections are determined as shown in Fig.7. The RF source is localized, using the map, considering three reflections, and employing a least-square estimator. For each configuration, different SDs of the noise are applied in which the main part of the noise is shadowing. In each simulation, it is assumed that the location of the obstacle or reflector has no error or there is a 400-meter SD error caused by the map or AOA error. Monte-Carlo simulation is run with an average of 100 consecutive runs whose results are presented in Table.I.

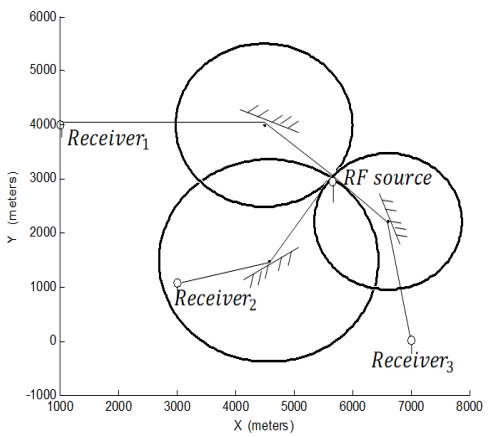

Fig.7. Localization using the basic approach in the first configuration of the reflectors

TABLE. I. RMSE OF THE LOCALIZATION OF THE BASIC APPROACH FOR THE FIRST CONFIGURATION

	SD of Noise(dB)				
	1	2	3	4	5
RMSE in meter (obstacles locations do not have errors)	153	302	483	679	764
RMSE in meter (obstacles locations have errors)	450	489	539	689	881

In the second simulation, the third reflector is considered closer to the second reflector as shown in Fig. 8. The results are presented in Table II.

TABLE. II. RMSE OF THE LOCALIZATION OF THE BASIC APPROACH FOR THE SECOND CONFIGURATION

	SD of Noise(dB)				
	1	2	3	4	5
RMSE in meter (obstacles locations do not have error)	174	364	560	784	855
RMSE in meter (obstacles locations have error)	503	579	893	899	932

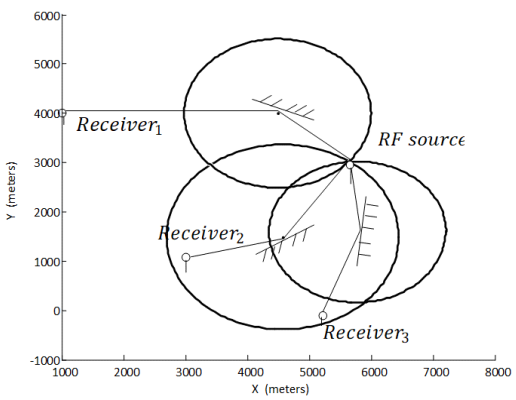

Fig. 8. Localization using the basic approach in the second configuration of the reflectors.

In the third simulation configuration, the third reflector is close to the second reflector in Fig. 9. The results of the localization are presented in Table III.

TABLE. III. RMSE OF LOCALIZATION OF THE BASIC APPROACH FOR THE THIRD CONFIGURATION

	SD of Noise(dB)				
	1	2	3	4	5
RMSE in meter (obstacles locations do not have errors)	209	513	857	922	1150
RMSE in meter (obstacles locations have errors)	694	679	807	1151	1099

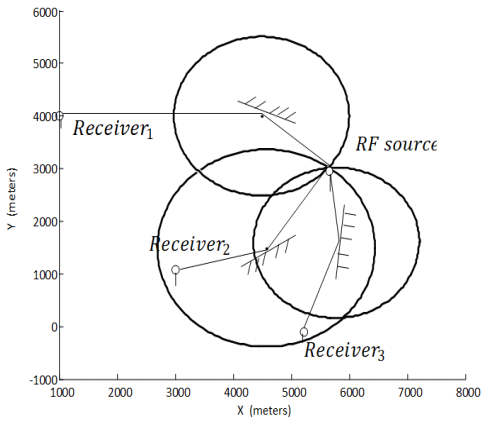

Fig.9. Localization using the basic approach in the third configuration of the reflectors

The above simulations show that if one of the reflectors is close to the other one, the localization error will be large. In the second set of simulations, the advanced approach for the localization with the map is evaluated. The localization is done by using two reflections as shown in Fig. 10. A particle filter is used for localization. In these simulations, 500 particles are used to achieve enough estimation accuracy. The Monte-Carlo simulation is done using an average of 100 consecutive runs. The results are presented in Table IV.

TABLE. IV. RMSE OF LOCALIZATION USING THE ADVANCED APPROACH

	SD of Noise(dB)				
	1	2	3	4	5
RMSE in meter (obstacles location does not have errors)	89	107	130	175	213
RMSE in meter (obstacles location has errors)	420	483	554	602	637

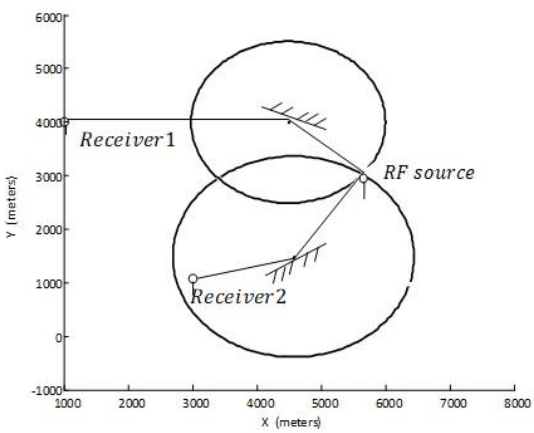

Fig.10. Configuration of the two reflectors for the localization using the advanced approach

The above simulation shows that the error of the localization, using the advanced approach, is low when the location of the reflector has a low error. If the location of the obstacle has a large error, the error of the RF source localization will be noticeable though it will be still lower in comparison to that of the basic version.

Using the advanced approach for one reflection results in two possible locations of the RF source, the error for localization with one reflection in the final simulation is obtained. It is assumed that the localization area is bounded to one of the possible RF source locations for one reflection. This is possible when the orientation of the obstacle is determined without enough accuracy. This simulation shows the maximum error of the localization using the advanced approach when the noise variance has a known amount in Table V.

TABLE V. RMSE OF LOCALIZATION USING THE ADVANCED APPROACH AND ONE REFLECTOR

	SD of Noise(dB)				
	1	2	3	4	5
RMSE in meter (obstacles location does not have errors)	271	287	294	343	382
RMSE in meter(obstacles location has errors)	462	465	515	607	655

The above simulations show that map-based localization has a lower error in all configurations when the advanced approach is used and the noise has bounded variance. In contrast, the basic approach could have a large error in some configurations because of the geometric relation of the reflectors.

The advanced approach is compared with the proposed approach below for localization in [25] in which two reflections are needed and the RSSI and AOA are the observations similar to the advanced approach. The approach proposed in [25] is simulated in the scenario that is shown in Fig. 10. In this approach, a fingerprinting is created using the reflection propagation equation and it is used to estimate the reflection parameter, i.e., the reflection angle and path length between the RF source and the receiver. Then, the RF source localization is done by placing the estimated parameter in the linear equation of possible locations of the RF source and solving this equation. Table.VI presents the results of the simulation using this approach. In this table the errors of the parameters estimation are also presented which are obtained in the step one of the approach.

TABLE VI. RMSE OF THE PARAMETERS ESTIMATION BASED ON THE RSSI OBSERVATION AND LOCALIZATION OF THE RF SOURCE USING THE PROPOSED APPROACH IN [25]

SD of Noise(dB)	RMSE of θ (deg.)	RMSE of d in meter	RMSE of localization(meters)
1	1.98	391	489
2	2.53	447	545
3	3.77	583	623
4	4.03	653	722
5	4.69	731	810

In Table.VII, RMSE of localization for the proposed approach in this paper and the proposed approach in [25] is compared. It is shown that the localization accuracy of the advanced approach when obstacles location has no error or has error, is more than the basic approach in the best configuration of the obstacle and the proposed approach in [25] (with out map) for different SD's of noise.

TABLE .VII. RMSE OF LOCALIZATION FOR THE PROPOSED APPROACH IN [25], THE ADVANCED APPROACH AND THE BASIC APPROACH.

SD of Noise(dB)	approach in [25] (meter)	basic approach (meter)	basic approach (meter) (obstacle location has error)	Advanced approach (meter)	advanced approach (meter) (obstacles location has error)
1	489	153	450	89	420
2	545	302	489	107	483
3	623	483	539	130	554
4	722	679	689	175	602
5	810	764	881	213	637

V. CONCLUSION AND FUTURE WORKS

This paper analyzes the localization in the NLOS condition using a map of the obstacles in a large outdoor environment. The RSSI and AOA observations are used and two approaches are proposed for localization. In the basic approach, RSSI is used for range estimation and localization is performed using three reflections. To improve the localization in the advanced approach, the reflection angle and two reflections are used. It is shown in the simulation and analytical calculation that the localization with the advanced approach has a lower error in comparison to the basic approach for different configurations of the reflectors.

In future works, an approach can be proposed to obtain the optimal reflector on the map for improving localization. In addition, the RF source beacons can be used to obtain the obstacle map, and localization can be done using the estimated map. Also, an optimal UAV path should be determined for

taking the RSSI sample and improving localization. In the NLOS condition, the diffracted signal may also be available. Using the map in the NLOS condition can be extended for reflected and diffracted signals simultaneously.

VI. REFERENCES

[1] S. Zorn, M. Gardill R. Rose, A. Goetz, and R. Weigel Alexander Koelpin, "A Smart Jamming System for UMTS/WCDMA Cellular Phone Networks for Search and Rescue Applications," *2012 IEEE MTT-S International Microwave Symposium Digest*, pp. 1-3, 2012.

[2] M. Berioli, J. M. Chaves, N. Courville, P. Boutry, J. Fondere, H. Skinnemoen, H. Tork, M. Werner and M. Weinlich, "WISECOM: A rapidly deployable satellite backhauling system for emergency situations," *International Journal of Satellite Communications and Networking, Special Issue on Emergency Telecommunications via Satellites*, Volume 29, Issue 5, pp. 419–440, 2011.

[3] S. Ferreira, G. Carvalho, F. Ferreira, J. Sousa," Assessing the capacity of man-portable UAVs for network access point localization, using RSSI link data," *In 2014 International Conference on Unmanned Aircraft Systems (ICUAS)*, IEEE, pp. 355-364.2014,

[4] Z. Ma, K.C. Ho, " TOA localization in the presence of random sensor position errors," *In 2011 IEEE International Conference on Acoustics, Speech and Signal Processing (ICASSP)*, IEEE, pp. 2468-2471, 2011.

[5] M. Yang, D. R. Jackson, J. Chen, Z. Xiong & J. T. Williams, "A TDOA localization method for nonline-of-sight scenarios," *IEEE Transactions on Antennas and Propagation*, vol.67, issue. 4, 2666-2676, 2019.

[6] J.R. Jiang , C.M. Lin , F.Y. Lin and S.T. Huang, "ALRD: AoA localization with RSSI differences of directional antennas for wireless sensor networks," *International Journal of Distributed Sensor Networks*, vol. 9, issue.3, p.52,2012.

[7] S.Tomic, M. Beko, R. Dinis, "Distributed algorithm for target localization in wireless sensor network using RSS and AoA measurement", *Pervasive and Mobile Computing*, vol.37, pp. 63-77, pp. 63-77, 2017.

[8] S.K. Han, W.S. Ra, J.B. Park, "TDOA/FDOA based target tracking with imperfect position and velocity data of distributed moving sensors", *International Journal of Control, Automation and Systems*, vol.15, issue.3, pp 1155–1166, 2017.

[9] S. Venkatraman and J. Caffery, " H. -R. You," Location using LOS range estimation in NLOS environments," *In Vehicular Technology Conference. IEEE 55th Vehicular Technology Conference. VTC Spring 2002 (Cat. No. 02CH37367)*, vol.2, pp 856 – 860, 2002.

[10] P. Closas, C. Fernández-Prades, and J. A. Fernández-Rubio, "A Bayesian approach to multipath mitigation in GNSS receivers," *IEEE J. Sel. Topics Signal Process*, vol. 3, isuee. 4, pp. 695–706, Aug. 2009.

[11] M. Gholami, and R.W. Brennan, "Comparing two clustering-based techniques to track mobile nodes in industrial wireless sensor networks," *Journal of Systems Science and Systems Engineering*, vol.25, no.2, pp.177-209. 2016.

[12] X. Zhang, Y. Sun, and J. Xiao, "A novel radio source search algorithm using force field vectors and received signal strengths," *International Journal of Mechatronics and Automation*, vol.3, isuue.1, pp.25-35, 2013.

[13] Z. Li, Z. Tian, Z. Wang, and Z. Zhang, "Multipath-assisted Indoor Localization Using a Single Receiver," *IEEE Sensors Journal*, vol.21, issue.1, pp. 692 – 705, 2020.

[14] S. He, S.H. Gary Chan, "Wi-Fi Fingerprint-base Indoor Positioning: Recent Advanced and Comparisons," *IEEE Communication Survey & Touturials*, vol.18 ,pp.466-490, 2015.

[15] E. Kupershtein, M. Wax, and I. Cohen, "Single-site emitter localization via multipath fingerprinting," *IEEE Trans. Signal Process*, vol.61, issue.1, pp. 10–21, Jan. 2013.

[16] D. Zimmermann, J. Baumann, A. Layh, F. Landstorfer, R. Hoppe and G. Wolfle, "Database Correlation for Positioning of Mobile Terminals in Cellular Networks using Wave Propagation Models," *IEEE Vehicular Technology Conference*, pp 4682 – 4686, Fall. 2004.

[17] S. M. M. Dehghan, S. Haidari and H. Mordi, "Toward aerial simultaneous target localization and obstacle estimation using RSSI observations," *3rd RSI International Conference on Robotics and Mechatronics (ICROM), Tehran*, pp.517 – 522, 2015.

[18] H. B. Song, H. G. Wang, K. Hong, and L. Wang, " A novel source localization scheme based on unitary esprit and city electronic maps in urban environment," *Progress In Electromagnetics Research*, pp.243-262, 2009.

[19] C. Gentner, T. Jost, W. Wang, S. Zhang, A. Dammann, and U.C. Fiebig, "Multipath Assisted Positioning with Simultaneous Localization and Mapping," *IEEE Transaction on Wireless Communication*, vol. 15, issue.9 , 2016.

[20] W. Xu, F.Quitin, M. Leng, W.P.Tay and S. G. Razul,"Distributed Localization of a RF target in NLOS Environments," *IEEE Journal on Selected Areas in Communications*, pp.1317 – 1330, 2015.

[21] J. He, H. Wymeersch, T. Sanguanpuak, O. Silvén, and M. Juntti, "Adaptive beamforming design for mmwave RIS-aided joint localization and communication," *IEEE Wireless Communications and Networking Conference Workshops IEEE. Korea*, pp. 1-6, 2020

[22] T. Ma, Y. Xiao, X. Lei, W. Xiong, and Y. Ding, "Indoor Localization with Reconfigurable Intelligent Surface," *IEEE Communications Letters*, PP.1-6, 2020.

[23] E. Soltanaghaei, A. Kalyanarnman, and K. Whitehouse, "Multipath triangulation: decimeter-level WiFi localization and orientation with a single unaided receiver," *in Proceedings of ACM MobiSys*, 2018.

[24] S. Haidari, H. Moradi, M.Shahabadi, S.M. M. Dehghan, "RF source Localization using Reflection Model in NLOS Condition,"*In 4rd RSI International Conference on Robotics and Mechatronics (ICROM)*, Tehran, 2016.

[25] S. Haidari, H. Moradi, M. Shahabadi, S.M. M. Dehghan, "A reflection-based rf source localization algorithm," *International Journal of Robotics and Automation*, vol.34, issue.3, 2019.

[26] R. Zekavat and R. M. Buehrer, H*and book of position location,Wiley* IEEE Press , 2011.

[27] F. Sabahi, "Robot Action Space of Tractable Subsumption Architecture," *International Journal of Industrial Electronics, Control and Optimization*, vol.2, issue.4, pp.297-304, 2019.

[28] R.P. França, G.A. Pimentel, and A.T.Salton, "Parametric and Nonparametric Bayesian Filters for Autonomous Underwater Vehicle Localization," *Journal of Control, Automation and Electrical Systems*, vol.31, issue 1, pp.40-

51, 2020.
[29] H. Budiarto, K. Korihata, k. Haneda and J. Takada, "Experimental study of non-specular wave scattering from building surface roughness for the mobile propagation modeling,"*IEICE transaction Communications*, vol.87, issue.4, pp.958-966, 2004.
[30] D.Tassetto, E.H. Fazli and M. Werner, " A novel hybrid algorithm for passive localization of victims in emergency situations," *IEEE 4th Advanced Satellite Mobile Systems*, pp. 320–327, 2008.
[31] D. M. Hamby,"A review of techniques for parameter sensitivity analysis of environmental models," *environmental Monitoring and Assessment, Volume 32*, Issue 2, pp 135-154, September 1994.

Saeid Haidari received his B.Sc. in Electrical Engineering from Nikbakht University, Iran in 2003 and M.Sc. in Control Engineering from University of Kerman, Iran in 2007, and Ph.D. degrees in robotic and AI from University of Tehran. Currently he is an assistant professor at university of Zabol, Iran. His research interests include autonomous aerospace systems, aerial robotics, RF source localization, complex and Multi-agent systems, evolutionary computation, UAVs cooperation.

Hadi Moradi is an associate professor at the Electrical and Computer Engineering Department of the University of Tehran. He is also a member of Control and Intelligent Processing Center of Excellence. He received his BSc in Electrical Engineering from the University of Tehran and his MS and PhD degrees in Computer Engineering (Robotics), respectively, in 1994 and 1999 from the University of Southern California. Before joining the Tehran University in 2008, he spent several years in industry as a research scientist. He joined USC at 2000 as a faculty at the Computer Science Department. In 2004, he spent two years at the Intelligent Systems Research Center at Sungkyunkwan University, in South Korea till 2006. His current research interests include motion planning, manipulation, service robotics, educational robotics, and intelligent tutoring system, especially game-based teaching.

S.M. Mehdi Dehghan received his B.Sc. in Electrical and Computer Engineering, M.Sc. in Artificial Intelligence and Robotics, and Ph.D. in Control, respectively, in 1999, 2002, and 2015 from the University of Tehran. His research interests include autonomous aerospace systems, aerial robotics, navigation, complex and Multi-agent systems, UAVs cooperation, SLAM of RF sources and attitude determination and control. He is now an assistant professor at the Department of Control Engineering at the Malek-Ashtar University of Technology.active and hybrid filters, the application of power electronics in renewable energy systems and electrified railway systems, reactive power control, harmonics, and power quality compensation systems such as SVC, UPQC, FACTS devices.

International Journal of Industrial Electronics, Control and Optimization © 2021 IECO
Vol. 4, No. 2, pp. 191-210, April (2021)

Multi-Objective ORPD Considering Different Load Models for Active Distribution Networks

Saman Hosseini-Hemati[1], Shahram Karimi [2], Gholam Hossein Sheisi [3,†]

[1,2,3] Electrical Engineering Department, Engineering Faculty, Razi University, Kermanshah, Iran.

ABSTRACT

Secure and economical operation of distribution networks needs the management of reactive power resources. Optimal Reactive Power Dispatch (ORPD) optimally manages the reactive power scheduling of generators and distribution generations, as well as the Reactive Power Compensation (RPC) devices. This paper investigates the effect of load models on the multi-objective ORPD problem in active distribution networks. Moreover, a modified Grey Wolf Optimizer (GWO), called Civilized GWO (CGWO), is introduced in this paper to solve the ORPD problem. The proposed strategy, including multi-objective function, various load models, DG's reactive power, RPCs, and the introduced CGWO, is tested on standard IEEE 33- and 69-bus distribution systems. The results indicate that the load models have a significant impact on the cost function amount. Moreover, the performance of the proposed algorithm is evaluated using ten standard benchmark functions. The optimization results demonstrate the robustness of the introduced optimization algorithm and its capability in finding better solutions than the Particle Swarm Optimization (PSO), Exchange Market Algorithm (EMA), and the original GWO.

Article Info

Keywords:
Civilized Grey Wolf Optimizer, Load Modeling, Multi-Objective Optimization, Optimal Reactive Power Dispatch.

Article History:
Received 2020-04-05
Accepted 2020-11-11

ABBREVIATION

ABC	Artificial Bee Colony
ACOPF	AC Optimal Power Flow
ALC	Aging Leader and Challengers
ALO	Ant Lion Optimizer
BSO	Backtracking Search Optimizer
CBA	Chaotic Bat Algorithm
CGWO	Civilized Grey Wolf Optimizer
CKHA	Chaotic Krill Herd Algorithm
CLPSO	Comprehensive Learning Particle Swarm Optimization
COM	Commercial
CPSMOEA	Classification and Pareto domination based Multi-Objective Evolutionary Algorithm
CP	Constant Power
DAMOPSO	Dynamically Adaptive Multi-Objective Particle Swarm Optimization
DE	Differential Evolution
DG	Distributed Generation
DMSDE	Dynamic Multi-group Self-adaptive Differential Evolution
DS	Distribution System
DSA	Differential Search Algorithm
EMA	Exchange Market Algorithm
FAHCLPSO	Fuzzy Adaptive Heterogeneous Comprehensive-Learning Particle Swarm Optimization
FF	Firefly
GBTLBO	Gaussian Barebones Teaching-Learning Based Optimization
GWO	Grey Wolf Optimizer
GSA	Gravitational Search Algorithm
HSA	Harmony Search Algorithm
HTSSA	Hybrid Tabu Search-Simulated Annealing
ICA	Imperialist Competitive Algorithm
IND	Industrial
IPM	Interior Point Method
ISFSOA	Improved Stochastic Fractal Search Optimization Algorithm
IWO	Invasive Weed Optimization

[†]**Corresponding Author**: shahramkarimi@razi.ac.ir
Tel: +98-8334277605, Fax: +98-8334277605, Razi University
Electrical Engineering Department, Engineering Faculty, Razi University, Kermanshah, Iran

MO	Multi-Objective
MOEA	Multiple Evolutionary Algorithms
MTLA-DDE	Modified Teaching Learning Algorithm and Double Differential Evolution
NA	Not Available
NLP	Nonlinear Programing
OGSA	Opposition-based Gravitational Search Algorithm
OGWO	Opposition-based Grey Wolf Optimizer
OPF	Optimal Power Flow
ORPD	Optimal Reactive Power Dispatch
PLoss	Power Loss
PSO	Particle Swarm Optimization
QP	Quadratic Programing
RES	Residential
RPC	Reactive Power Compensation
SARGA	Self-Adaptive Real Coded Genetic Algorithm
SDP	Semidefinite Programming
SDR2	Semidefinite Programming Relaxation
SO	Single-Objective
SOA	Seeker Optimization Algorithm
SPMGSO	Strength Pareto Multigroup Search Optimizer
Std.	Standard Deviation
TS	Transmission System
TVD	Total Voltage Deviation
VSI	Voltage Stability Index
WOA	Whale Optimization Algorithm

NOMENCLATURE

f_{loss}	Active power losses
G_k	Conductance of kth branch which connects bus i and bus j
V_i	Voltage magnitude of ith bus
θ_{ij}	Voltage phase between bus i and bus j
N_{bra}	Number of branches
$f_{\Delta V}$	Total voltage deviation
V_i^*	Desired voltage magnitude at bus i
f_{RPC}	Cost of RPC devices
C_{CAP}	Cost coefficient of RPC
Q_{Cs}	Actual capacity of sth RPC
N_Q	Number of RPC devices
P_{Gi}	Active power output of generator i
Q_{Gi}	Reactive power output of generator i
P_{DGi}	Active power output of DG at bus i
Q_{DGi}	Reactive power output of DG at bus i
P_{Li}	Active power demand at bus i
Q_{Li}	Reactive power demand at bus i
Q_{Ci}	Reactive power of RPC at bus i
B_k	Susceptance of the kth branch
N_{bus}	Number of buses
N_G	Number of generators
N_{DG}	Number of DG sources
N_T	Number of tap setting transformer branches
T	Tap setting
S_l	Branch loading of lth line
P_{Li0}	Active power demand at bus i for a specified operating point
Q_{Li0}	Reactive power demand at bus i for a specified operating point
α	A parameter of load model related to active power
β	A parameter of load model related to reactive power
$ObjFunc$	Objective function
$\vec{X}$	Position vector of a wolf
$\vec{A}$	Random value in a specified interval
$\vec{C}$	Random value in a specified interval
rand	Random value in a specified interval
max	Maximum
max	Minimum
$\text{Iteration}_{\max}$	Maximum iteration
N	Number of grey wolves
N_s	Number of societies
D_{is}	Distance between ith wolf and sth beta
C_α	Importance coefficient related to alpha wolf
C_β	Importance coefficient related to beta wolf
C_δ	Importance coefficient related to delta wolf
t	Iteration

I. INTRODUCTION

The expansion of power systems in large geographic areas to supply the loads has led to an unreasonable increase in electrical losses. Although these losses cannot completely be eliminated, they can be limited to an acceptable value. This affects the whole system operation, decreases the voltage drops, and yields different economic and environmental benefits [1–3].

ORPD is a sub-problem of the OPF that aims to minimize the total power losses through finding an optimal setting of the control variables and satisfying operational constraints. The independent variables are generator voltage, transformer tap setting, and reactive power output of RPC devices (such as capacitor banks [4]).

Furthermore, DGs have drawn special attention all over the world [5]. Generally, these devices are installed in distribution networks [6]. However, a high DG's penetration may lead to an overvoltage due to reverse power flow [7]. So, ORPD can be applied to optimize the active power losses and prevent voltage violations by managing reactive power resources.

Different optimization algorithms have been applied to the ORPD problem. Conventional approaches such as the gradient method, NLP, QP, IPM [8,9], and the Lagrangian method [10] have been proposed to optimize RPD in the power grids. Since this problem is non-differential, nonlinear, multi-modal, and non-convex, most algorithms find local optimums and need excessive numerical iterations [11].

The advent of heuristic optimization algorithms has provided alternative powerful approaches for solving the ORPD problem. In [2], WOA-based ORPD has been proposed to reduce electrical losses. Reference [12] has

presented an ABC algorithm to optimize the power losses in which the penalty method is used to satisfy the inequality constraints. A similar work considering three objectives including voltage deviation and stability in addition to power loss is proposed in [13]. Reference [14] separately optimized the same objectives for TSs using CBA. In [15], GSA has been introduced to find the best settings of independent variables of ORPD through the Newtonian laws. An OGSA has been introduced in [11] to improve the voltage stability of the power system in addition to minimizing transmission loss. GBTLBO algorithm and its modified version have been presented in [16]. GWO algorithm has been suggested in [17] to handle the ORPD problem. Reference [18] has applied the OGWO to the mentioned issue. The work presented in [19] has reported CKHA that is based on the concept of chaos theory to enhance the computational speed and improve the convergence profile of ORPD. Improved versions of DE, namely quasi-oppositional DE and multi-objective DE have respectively been used in [20,21] to solve both the single- and multi-objective ORPD problems. Reference [22] solved the problem based on the EMA by modeling the behavior of the stock market under diverse market conditions. In [23], the ORPD and some single- and multi-objective problems have been solved by DSA. Another paper reported the application of HSA in optimizing some objectives such as power losses, bus voltages, and voltage stability [24]. Zhou et al. in [25] introduced SPMGSO for a multi-objective ORPD problem. In [26], an optimal setting of the problem's control variables has been found by BSO to minimize the total line losses. Reference [27] proposed ALO, which is based on the antlion's hunting behavior in nature to escape the local minima. Reference [28] introduced conic relaxation (a tight SDP and SDR2) of the ORPD based on the convex relaxations of the ACOPF problem. A similar relaxation has been proposed in [29]. In [30] the ISFSOA has been used to optimize three objectives separately. The reviewed studies are some examples of heuristic optimization algorithms used for this challenging problem.

A new category of methods known as hybrid optimization algorithms has widely been applied to ORPD problems. A combination of ABC and DE techniques as a hybrid optimization algorithm has been reported in [31] to overcome the disadvantage of requiring a large population size of DE and strengthen the global search ability of ABC. Reference [32] has offered a hybrid modified TLBO and double DE algorithm to handle ORPD. Other hybrid approaches, such as HTSSA [33] and ABC-FF algorithm [34], have been addressed to find the optimal solution to the ORPD problem. Reference [35] reported a candidate pool of different algorithms such as genetic algorithm, PSO, DE, and adaptive metropolis search to form adaptive MOEA for multi-objective ORPD problems. A combination of PSO and ALC has been introduced by Singh in [36] for solving ORPD. Reference [37] proposed CPSMOEA, which has two steps including optimization and decision stages for solving multi-objective ORPD problems.

Due to the integration of reactive power generation of DGs as control variables, a multi-objective ORPD problem has been established. This problem aims to decrease the total power loss, reduce voltage deviation, and minimize the total capacity of RPC devices. In [6], the DAMOPSO technique has been introduced for the ORPD problem in distribution systems. Reference [38] has proposed an organizational multi-agent system based on Holonic structure for optimal dispatch of reactive power in smart grids.

A taxonomy of the reviewed approaches in terms of objectives, optimization frameworks, case studies, considered DGs, penalty terms, etc. is shown in Table I. According to this table, four objectives including the total PLoss, TVD, VSI, and RPCs were optimized with/without DGs so that in all of these researches, PLoss is considered as the main objective function. Some approaches consider the penalty function to satisfy the violated constraints such as PQ buses voltage. Also, the listed papers are classified based on SO and MO, different analyzed case studies, publication year, and publisher. As can be seen, the main differences of these papers are in the solving algorithms, considered objective functions, and kind of the case study systems (transmission or distribution). For instance, in [36] PLoss and TVD have been considered separately as objective functions for solving the ORPD problem by the ALC-PSO approach on IEEE 30, 57, and 118-bus transmission test systems without considering DG. As another example, in [39] ADMM algorithm has been proposed for the ORPD problem in distribution systems (69, 123, and 1066-bus) in which DG units are considered.

As one can see in Table I, most of the studies have just analyzed the ORPD for transmission systems. However, due to the importance of integration of distribution systems and DGs, some research, like [6,38,39,46–48], has focused on the ORPD in distribution networks. Nevertheless, among the reviewed papers for distribution grids, [6,38,39] have only considered the reactive power of DGs as the main control variable. Moreover, [6,38,39,46–48] have not considered different load models such as IND, RES, or COM.

This work responds to the following needs of the ORPD problems:

- Proposing a powerful optimization algorithm: In this paper, a modified GWO, called CGWO, is proposed to solve the ORPD problem in active distribution networks. The suggested algorithm is based on a population of wolves, so it has greater exploration than mathematical approaches that are based on a single solution. Thus, there are multiple candidates that can share their information to suddenly jump and search the promised parts of the solution space according to behavior and social life of grey wolves more extensively; moreover,

they help other candidate wolves avoid local minima. The proposed CGWO is a swarm intelligence method, which means that it can memorize the search space information at each course of iteration while evolutionary methods such as GA and DE discard the obtained data of the former generations. Also, compared to the mentioned techniques, the CGWO has fewer operators and can easily be implemented. The entire hunting process with all of the existing wolves (solutions) reflects a random search one without derivative operations. The proposed CGWO is more robust than other analyzed algorithms. Its robustness is evaluated based on mean and standard deviation. Moreover, it can always search for global or near-global solutions.

- Considering real models of distribution network loads: Different load types have significant effects on the power system studies including the ORPD problem. Their impacts are usually applied by the mathematical representation of approximate relationships between active/reactive power and voltage magnitude. Our work covers the effects of different load types (such as CP, IND, RES, and COM loads) on the multi-objective ORPD problem.
- Considering impact of the outputs of DGs and RPCs on the ORPD: This paper aims to simultaneously consider DG and RPC outputs and various load models to make a new version of the ORPD problem according to the real-world active distribution networks that has not been considered so far.
- Considering various objectives: In this paper, a single-objective function is suggested that simultaneously handles different objectives including total power losses, voltage deviation, and RPC costs. In fact, using an efficient method, three described objectives are converted into a single objective function.

The main contributions of this paper can be highlighted as:

- Introducing a new and powerful CGWO algorithm for ORPD problems in active distribution networks.
- Introducing a multi-objective function to simultaneously optimize line losses, voltage deviation, and RPC cost.
- Proposing a new definition of ORPD in active distribution networks.
- Integrating various load models to the ORPD problem and analyzing their effects on this kind of problem.
- Considering DG's reactive power output as a control variable.

The rest of the paper is organized as follows: Section II presents the ORPD formulation. In Section III, the CGWO structure is addressed. Simulation results on two distribution case studies are discussed in Section IV. The conclusion is presented in Section V.

TABLE I
TAXONOMY OF THE PROPOSED APPROACHES FOR ORPD PROBLEM

Ref	Approach	Objective Functions				Optimization	Case Study	Year & Publisher	Main Findings/Advantages/Disadvantages
		PLoss	TVD	VSI	RPC				
[49]	DE	•				SO	14-30-118 (TS)	2008-Elsevier	The penalty method has been applied for all inequality constraints. It fails to provide a meaningful solution with lower power losses for large scale transmission networks.
[24]	HSA	•	•	•		SO	30-57 (TS)	2011-Elsevier	It optimized three objectives separately and changing some constraints lead to bad solutions.
[12]	ABC	•				SO	30-118 (TS)	2012-Elsevier	This paper is based on the penalty method and in comparison to DE, PSO, and IPM, it can find solutions with better power losses.
[15]	GSA	•	•			MO	30-57-118 (TS)	2012-IET	This work uses of a constant term to convert a multi-objective problem into a single-objective one.
[31]	DE-ABC	•				SO	14-30-57 (TS)	2013-Elsevier	The findings confirm that this method is slightly better than DE and ABC.
[25]	SPMGSO	•	•	•		SO	30-162 (TS)	2014-IEEE	The optimization algorithm has many parameters and all objectives have separately been optimized.
[6]	DAMOPSO	•	•		•	MO	33 (DS)	2014-Elsevier	This paper could not provide an operating point optimizing all objectives considering DGs of distribution grid.
[11]	OGSA	•	•	•		SO	30-57-118 (TS)	2014-Elsevier	The reported approach is competitive in small bi-objective problems and greatly superior in high dimensional ones.
[35]	MOEA	•	•			MO	30 (TS)	2014-Wiley	The proposed method is a penalty based-bi-objective optimization algorithm which is based on evolutionary method.
[16]	GBTLBO	•				SO	14-30 (TS)	2015-Elsevier	This work only optimized the power losses applying the penalty factors for voltage and reactive power constraints. It covers insufficiencies of TLBO.
[17]	GWO	•				SO	30-118 (TS)	2015-Elsevier	It only optimized the transmission losses and outperforms six techniques.

Table .1 Continued

[19]	CKHA	•	•	•	SO	30-57 (TS)	2015-IET	This method needs two additional adjustable parameters to outperform 12 other algorithms and shows fast convergence behaviour than original KHA.
[36]	ALC-PSO	•	•		SO	30-57-118 (TS)	2015-Elsevier	Due to the single-objective characteristic of the reported algorithm, it can only optimize two objectives separately.
[39]	ADMM	•			SO	69-123-1066 (DS)	2016-IEEE	This work converts the nonconvex ORPD problem applying DG's output to a convex one. The reported method has not been validated by comparing with other new techniques.
[26]	BSO	•			SO	14-30-57 (TS)	2016-IEEE	All inequality constraints have been met by the penalty method. The introduced algorithm needs two operators. The simulation results do not show significant improvement in objective function.
[33]	HTSSA	•	•		SO	30 (TS)	2016-Elsevier	It combines the main search strategies of TS and SA algorithms. The results indicate that considering penalty terms can increase the run time.
[20]	QODE	•	•	•	MO	30-57-118 (TS)	2016-Elsevier	It applies a constant term to convert the multi-objective problem into a single-objective one. Compare to DE, it needs more time to find the solution.
[23]	DSA	•	•	•	SO	30-57 (TS)	2016-Springer	This method slowly convergences and most of the reported solutions is same as those searched by other techniques.
[22]	EMA	•	•	•	SO	30-118 (TS)	2016-Elsevier	This technique needs two market risk factors with four parameters which should always be adjusted to find the best solution. This method is a penalty based-single-objective optimization
[2]	WOA	•			SO	14-30 (TS)	2017-Elsevier	It is a penalty based method and the simulation results show that the WOA outperforms other algorithms such as ABC, GSA, and PSO.
[27]	ALO	•		•	SO	30-118-300 (TS)	2017-Elsevier	Convergence behaviour of the reported algorithm is very similar to ABC. This paper optimized different objectives separately considering penalty function.
[34]	ABC-FF	•	•		SO	14-39 (TS)	2018-Elsevier	The reported solutions confirm that combination of two algorithms with many parameters does not form a powerful optimization technique.
[18]	OGWO	•			SO	14-30-57 (TS)	2018-Wiley	It only minimized the power losses and outperforms seven techniques and quickly convergence to optimal solution.
[28]	SDR2	•			SO	3375 (TS)	2019-IEEE	It applied a tight semidefinite programming relaxation to the ORPD problem and used convex relaxations of AC power flow.
[29]	-	•			SO	30-118(TS)	2019-IEEE	It only optimized the transmission losses and outperforms some techniques.
[30]	ISFSOA	•	•	•	SO	30 (TS)	2019-UAD	It considered three objectives. But, it separately optimized them.
[13]	ABC	•	•	•	SO	30-57 (TS)	2020-Elsevier	It is not so fast for large systems and used of the penalty function to satisfy inequality constraints.
[37]	CPSMOEA	•	•		MO	30-118 (TS)	2020-IEEE	It applied a two-stage algorithm to solve the multi-objective ORPD problem.
[14]	CBA	•	•	•	SO	14-39-57-118-300 (TS)	2020-IEEE	Three objectives were optimized separately. It used of the penalty function to satisfy inequality constraints.

II. ORPD PROBLEM FORMULATION

This paper considers three objective functions, including active power losses, the sum of the voltage deviations, and the total capacity of RPC devices. These objective functions are optimized for different load models and considering the operational constraints.

A. Objectives

1) Minimization of Active Power Losses

Minimizing the active power losses f_{loss} in the network is one of the main objectives of the ORPD and can be defined as:

$$f_{loss} = \sum_{k=1}^{N_{bra}} G_k\left[V_i^2 + V_j^2 - V_i V_j \cos\theta_{ij}\right] \quad (1)$$

2) Minimization of Total Voltage Deviation

Minimization of total voltage deviation as (2) can improve the voltage profile and enhance the security level

of the network.

$$f_{\Delta V} = \sum_{i=1}^{N_{bus}} (V_i - V_i^*)^2 \quad (2)$$

where V_i^* is usually set to 1.00 pu.

3) Minimization of RPC Cost

In addition to optimizing the power losses and voltage deviation, the ORPD problem aims to reduce the cost of RPC devices [6]. This cost (f_{RPC}) depends on the total capacity of RPC devices so that a lower cost means a lower capacity of them. Cost minimization of RPC devices can be presented as follows:

$$f_{RPC} = \sum_{s=1}^{N_Q} C_{CAPs} |Q_{Cs}| \quad (3)$$

If C_{CAP}=1, (3) becomes a function of the total capacity of RPC devices.

B. Constraints

1) Equality Constraints

The power balance equations represent a set of equality constraints considering DG and RPC outputs as follows:

$$P_{Gi} + P_{DGi} - P_{Li} - V_i \sum_{j=1}^{N_{bus}} V_j \left(G_k \cos\theta_{ij} + B_k \sin\theta_{ij}\right) = 0 \quad (4)$$

$$Q_{Gi} + Q_{DGi} + Q_{Ci} - Q_{Li} - V_i \sum_{j=1}^{N_{bus}} V_j \left(G_k \sin\theta_{ij} + B_k \cos\theta_{ij}\right) = 0 \quad (5)$$

2) Inequality Constraints

Inequality constraints for control and state variables can be listed as below:

- Inequality constraints on control variables: Generally, these constraints consist of limitations on the terminal voltage of generators (6), the reactive power output of the RPC devices (7), and DGs (8), and tap setting of transformers (9).

$$V_{gi}^{min} \le V_{gi} \le V_{gi}^{max}, \quad i = 1,2,\dots,N_G \quad (6)$$

$$Q_{Ci}^{min} \le Q_{Ci} \le Q_{Ci}^{max}, \quad i = 1,2,\dots,N_G \quad (7)$$

$$Q_{DGi}^{min} \le Q_{DGi} \le Q_{DGi}^{max}, \quad i = 1,2,\dots,N_{DG} \quad (8)$$

$$T_i^{min} \le T_i \le T_i^{max}, \quad i = 1,2,\dots,N_T \quad (9)$$

- Inequality constraints on dependent variables: The voltage level at each bus should be limited as follows:

$$V_i^{min} \le V_i \le V_i^{max}, \quad i = 1,2,\dots,N_{bus} \quad (10)$$

Other inequality constraints are the line thermal capacity and reactive power output of the generators, which can be expressed by:

$$S_l^{min} \le S_l \le S_l^{max}, \quad l = 1,2,\dots,N_{bra} \quad (11)$$

$$Q_{gi}^{min} \le Q_{gi} \le Q_{gi}^{max}, \quad i = 1,2,\dots,N_G \quad (12)$$

C. Load Modeling

Voltage-dependent load models can be stated as below:

$$P_{Li} = P_{Li0} V_i^{\alpha} \quad (13)$$

$$Q_{Li} = Q_{Li0} V_i^{\beta} \quad (14)$$

In this work, practical voltage-dependent load models (i.e., industrial, residential, and commercial loads) are considered in addition to the constant power model. According to [50], the values of α and β for different load types are illustrated in Table II.

TABLE II
DIFFERENT LOAD MODELS [50]

Load model	α	β
CP	0.00	0.00
IND	0.18	6.00
RES	0.92	4.04
COM	1.51	3.40

D. ORPD as an Optimization Problem

The ORPD problem provides optimum values of control variables by minimizing a pre-specified objective function with respect to the operational constraints of the system. The ORPD problem can mathematically be formulated as follows:

$$\begin{cases} \min\ ObjFunc \\ \text{subject to } (4) - (12) \text{ considering } (13) \text{ and } (14) \end{cases} \quad (15)$$

In this paper, using the method presented in [51], three objectives described as (1)-(3) are converted into a single objective function as follows:

$$ObjFunc = f_{loss}\left(1 + s_{\Delta V} \times \frac{f_{\Delta V}}{\sum_{i=1}^{N_{bus}} P_{Li}} + s_{RPC} \times \frac{f_{RPC}}{\sum_{i=1}^{N_{bus}} P_{Li}}\right) \quad (16)$$

Where $s_{\Delta V}$ and s_{RPC} are equal to 0 or 1. If $s_{\Delta V} = 1$, then $f_{\Delta V}$ is considered as a part of the objective function; otherwise, $f_{\Delta V}$ is not one of the objectives. The same statement is valid for RPC devices.

III. PROPOSED OPTIMIZATION ALGORITHM

A. Brief GWO Formulation

Social Hierarchy: GWO algorithm was first proposed in [52]. There are four types of wolves affected by a social hierarchy as shown in Fig. 1. The leader wolf is called

alpha or dominant wolf. He/he decides about all things (hunting, sleeping, etc.) and his/her decisions are mostly dictated to the group. At the next level, beta or subordinate wolf helps alpha type make a better decision or do other activities related to the pack. He/she commands the other lower-type wolves but only respects the alpha type and plays the advisor role to the dominant wolf. The lowest level in the wolf hierarchy is omegas. They are non-dominant wolves and always have to surrender to all the other dominant ones. Since omegas are at the bottom of the social chain, they are allowed to eat as the last wolves. The third level is delta. In fact, if a wolf is not an alpha, beta, or omega, he/she is a delta wolf. He/she has to respect the alpha and beta types while commanding the omegas.

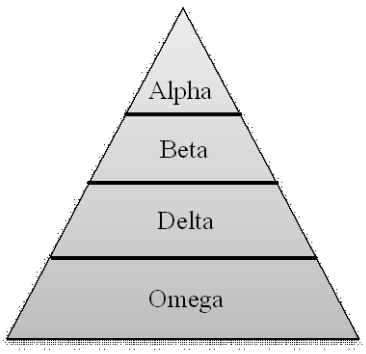

Fig. 1. Grey wolves hierarchy [52]

Designation of Superior Wolves: Among N solutions, the first three best ones are selected as alpha, beta, and delta wolves. Other solutions are omega wolves. The optimization process (procedure of hunting) is guided by alpha, beta, and delta because they have better knowledge about the potential position of prey.

Encircling Prey and Hunting: During hunting, wolves encircle the prey. The model of the encircling behavior of grey wolves is [52]:

$$\vec{X}(t+1) = \frac{\vec{X}_1 + \vec{X}_2 + \vec{X}_3}{3} \tag{17}$$

where

$$\vec{X}_1 = \vec{X}_\alpha - \vec{A}_1 \cdot \vec{D}_\alpha; \qquad \vec{D}_\alpha = \left|\vec{C}_1 \cdot \vec{X}_\alpha - \vec{X}\right|;$$

$$\vec{X}_2 = \vec{X}_\beta - \vec{A}_2 \cdot \vec{D}_\beta; \qquad \vec{D}_\beta = \left|\vec{C}_2 \cdot \vec{X}_\beta - \vec{X}\right|;$$

$$\vec{X}_3 = \vec{X}_\delta - \vec{A}_3 \cdot \vec{D}_\delta; \qquad \vec{D}_\delta = \left|\vec{C}_3 \cdot \vec{X}_\delta - \vec{X}\right|;$$

$$\vec{A}_1 = 2\vec{a} \cdot \mathrm{rand}_{\alpha 1} - \vec{a}; \qquad \vec{C}_1 = 2 \cdot \mathrm{rand}_{\alpha 2};$$

$$\vec{A}_2 = 2\vec{a} \cdot \mathrm{rand}_{\beta 1} - \vec{a}; \qquad \vec{C}_2 = 2 \cdot \mathrm{rand}_{\beta 2};$$

$$\vec{A}_3 = 2\vec{a} \cdot \mathrm{rand}_{\delta 1} - \vec{a}; \qquad \vec{C}_3 = 2 \cdot \mathrm{rand}_{\delta 2};$$

and where $\vec{X}_\alpha$, $\vec{X}_\beta$, and $\vec{X}_\delta$ denote the position of alpha, beta, and delta, respectively, $\vec{A}$ contains random values in interval $[-2\vec{a},\ 2\vec{a}]$ to mathematically model approaching the prey and attacking it, where attacking the prey is modeled by $\vec{a}$; $\vec{C}$ is a random value in interval [0, 2] and models the effects of barriers for approaching the prey in nature, and rand represents a random number in interval [0, 1].

Searching prey (Exploration): As mathematically described, the position of the alpha, beta, and delta wolves affects the other grey wolves. They firstly diverge from the hunt and each other to find the prey and then converge to attack it. $\vec{A}$ Mathematically indicates the divergence so that $|\vec{A}| > 1$ forces the search agents to diverge from the hunt and hopefully explore a better solution and also emphasizes the exploration power of GWO to globally search.

Attacking Prey (Exploitation): Hunting is terminated by attacking the prey. Approaching the target is mathematically modeled by linearly decreasing the value of $\vec{a}$ from 2 to 0 as below:

$$\vec{a} = 2 - \frac{2t}{\mathrm{Iteration}_{\max}} \tag{18}$$

As another part of exploitation, $|\vec{A}| < 1$ means that the next position of a grey wolf is between its current position and the prey position. In other words, it obliges the grey wolves to attack the prey. It is worth to mention that $\vec{a}$ can also affect exploration power by forcing $|\vec{A}| > 1$ as already described.

B. Formulation of the Introduced CGWO

1) CGWO Concept

Suppose that there are N grey wolves as N potential solutions. The best solution among all wolves is considered as the alpha wolf. He/she is the leader. In order to form different societies, N_s groups of wolves are considered as N_s societies. Each society has its own leader; in other words, the next best N_s solutions (among $(N-1)$ ones) are considered as N_s beta wolves (leader of each society). Betas respect the leader (i.e., alpha) and help him/her make a better decision; moreover, they can only command the other lower-level wolves in their society. In addition to betas, there are N_s delta wolves; but they are not necessarily the next best N_s solutions among the remaining $(N-N_s-1)$ ones. Accordingly, the distance between each remaining wolf and N_s betas should be determined. A wolf belongs to the society s if the distance between him/her and sth beta is minimum. The best solution (except its beta) is selected as delta wolf. Therefore, each society has its own delta and each delta only follows his/her beta and commands the other wolves in the beta's society. The rest of the wolves (i.e., $(N-2N_s-1)$ solutions) are members of societies. The concept of CGWO is illustrated in Fig. 2.

The main steps are:

Step 1. Determine the number of societies, N_s.

Step 2. Calculate $ObjFunc$ for all wolves and sort them from the best to the worst solutions.

Step 3. Select the best wolf as alpha.

Step 4. Select the next best N_s solutions as betas.

Step 5. Calculate the distance between the rest of the wolves and all betas as follows:

$$D_{is} = \|X_i(t), X_s(t)\|_2, \quad i \in \{(N - N_s - 1)\text{remained wolves}\}, \quad s \in \{N_s \text{ beta wolves}\} \tag{19}$$

Since D_{is} represents the distance between ith wolf and sth beta, so the ith wolf belongs to the sth society if D_{is} is minimum.

Step 6. Select the next best wolf in each society as the delta.

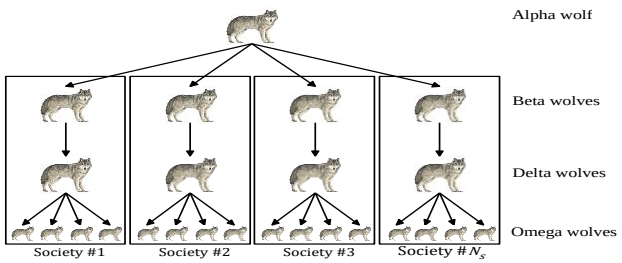

Fig. 2. Concept of CGWO

2) Modification of Hunting Model

In the original GWO, as presented in (17), there is a constant weighting factor (equal to ≈0.33) to model the effect of alpha, beta, and delta for X_1, X_2, and X_3, respectively. In order to give CGWO more random behavior throughout optimization and increase the effect of betas in societies, the following equation is proposed to modify (17) as (20).

$$\vec{X}(t+1) = C_\alpha \times \text{rand} \times \vec{X}_1 + C_\beta \times \text{rand} \times \vec{X}_2 + C_\delta \times \text{rand} \times \vec{X}_3 \tag{20}$$

where C_α, C_β, and C_δ show the importance of alpha, beta, and delta wolves in societies. Based on our experiments, choosing $C_\beta > C_\alpha$ provides a better solution because, in each society, beta is the leader, not alpha. Additionally, because, in each society, beta represents a better wolf than delta, so $C_\beta > C_\delta$.

C. CGWO Algorithm

The main steps of the introduced CGWO algorithm are presented in Fig. 3 and can be stated as follows:

Initialization Step. Initialize the number of grey wolves, societies, a, A, C, C_α, C_β, C_δ, and $\text{Iteration}_{\max}$. Then, set $t = 0$.

Iteration Step. Set $t = t + 1$.

Load Flow Step. Get the results of (4) and (5) considering different load models (applying (13) and (14)). These represent the load flow equations considering DG and RPC outputs as well as various demand types. These equations as the main equality constraints are satisfied by the power flow program.

Civilization Step. Run six steps presented in subsection III.B.1 (i.e., Step 1-6) to set/update societies and determine alpha, beta, delta, and then omega wolves. It is important to note that due to the evaluation of $ObjFunc$ in each iteration, the designation of wolves (i.e., alpha, beta, and delta wolves) may be changed.

Update Position Step. Use (20) to update the positions of grey wolves.

Boundaries Step. Check that the variables are within their pre-specified limits. Apply boundaries (Eq. (6)-(12)) if limits are violated; This can be investigated for X_i as:

$$X_i = X_i * F(ubt + lbt) + X_i^{max} * ubt + X_i^{min} * lbt \tag{21}$$

where ubt, lbt and F are defined as below:

$$ubt = \begin{cases} 1 & if\ X_i > X_i^{max} \\ 0 & if\ X_i \le X_i^{max} \end{cases} \tag{22}$$

$$lbt = \begin{cases} 1 & if\ X_i < X_i^{min} \\ 0 & if\ X_i \ge X_i^{min} \end{cases} \tag{23}$$

$$F(ul) = \begin{cases} 1 & if\ ul \ge 1 \\ 0 & if\ ul < 1 \end{cases} \tag{24}$$

Otherwise, go to **Criterion Step**.

Criterion Step. If $t = \text{Iteration}_{\max}$, then go to the **Results Step**; otherwise, go to the **Iteration Step**.

Results Step. Print the results of alpha.

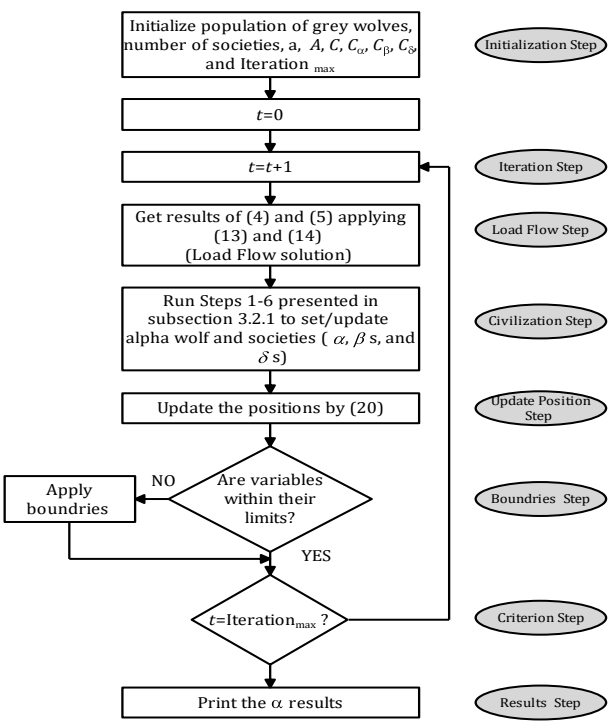

Fig. 3. CGWO algorithm

IV. SIMULATION RESULTS

The proposed strategy is investigated on two distribution systems including the IEEE 33-bus and 69-bus networks and also ten benchmark functions in Appendix A. The suggested strategy has been developed in MATLAB software and the best obtained results, as well as the mean and standard deviation over 20 runs, are compared with other programmed algorithms such as GWO, PSO, and EMA [53]. To aim this purpose, different case studies based on the objectives presented in (1)-(3) investigating (15) and (16) are considered as:

Case 1– Optimization of three objectives including f_{loss}, $f_{\Delta V}$, and f_{RPC} ($s_{\Delta V} = 1$ and $s_{RPC} = 1$).

Case 2– Optimization of two objectives including f_{loss} and $f_{\Delta V}$ ($s_{\Delta V} = 1$ and $s_{RPC} = 0$).

Case 3– Optimization of two objectives including f_{loss} and f_{RPC} ($s_{\Delta V} = 0$ and $s_{RPC} = 1$).

In this paper, in addition to the above cases, four different load models, according to Table II, are also considered. The parameters of CGWO are illustrated in Table III. It should be noted that regarding the radial structure and high R/X ratios of test systems, the power flow method is backward-forward power flow. By using this method, power losses for each branch and voltage magnitudes for each bus node are determined. The forward/backward sweep for the solution of distribution network load flow is utilized to investigate the power loss, line current, and voltage at each bus. This paper uses the power flow results of MATPOWER [54].

TABLE III
CGWO PARAMETERS

Parameter	value
Number of grey wolves (N)	20
Number of societies (N_s)	4
Maximum iteration ($\text{Iteration}_{\max}$)	50
Importance coefficient of alpha wolf (C_α)	0.3
Importance coefficient of beta wolves (C_β)	0.6
Importance coefficient of delta wolves (C_δ)	0.1

A. IEEE 33-bus Distribution System

The first test network is IEEE 33-bus radial system with a total load of $3.72 + j2.30$ MVA. Data of 32 branches and 32 loads are given in [55]. Based on [6], as depicted in Fig. 4, two DGs and two capacitors as RPC devices are installed in this system according to Table IV.

1) Total power losses and voltage deviation before optimization

Before optimization, the total power losses and voltage deviation for three operation conditions under different load types are as Table V. In the first operation condition (denoted with I in Table V), the test network is considered without DGs and capacitors. In the second operation condition (denoted with II in Table V), it is supposed that the capacitors are connected to the test network and the DGs are not exploited. Finally, in the third operation condition (denoted with III in Table V), it is assumed that the DGs are connected to the test network and the capacitors are disconnected.

TABLE VI
DATA OF DGS AND RPC DEVICES [6] – IEEE 33-BUS SYSTEM

RPC/DG	Installed at node	Parameter	value
C_1	6	$Q_{C1,\min}$ (kVAR)	0
		$Q_{C1,\max}$ (kVAR)	600
C_2	31	$Q_{C2,\min}$ (kVAR)	0
		$Q_{C2,\max}$ (kVAR)	1050
DG_1	2	P_{DG1} (kW)	1000
		$Q_{DG1,\min}$ (kVAR)	-100
		$Q_{DG1,\max}$ (kVAR)	500
DG_2	13	P_{DG2} (kW)	1000
		$Q_{DG2,\min}$ (kVAR)	-100
		$Q_{DG2,\max}$ (kVAR)	500

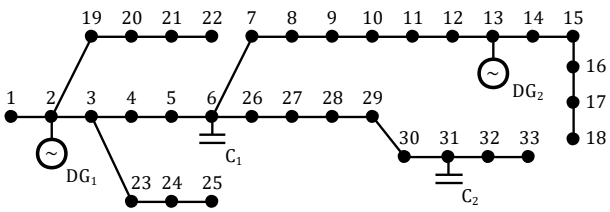

Fig. 4. Modified IEEE 33-bus distribution network

TABLE V
SYSTEM CONDITION UNDER DIFFERENT LOAD MODELS BEFORE OPTIMIZATION – IEEE 33-BUS SYSTEM

Parameter	Condition	Load model			
		CP	IND	COM	RES
Total real power loss (f_{loss} in MW)	I	0.2027	0.1617	0.1550	0.1594
	II	0.1425	0.1409	0.1264	0.1323
	III	0.1348	0.1037	0.1073	0.1072
Total voltage deviation ($f_{\Delta V}$ in pu)	I	0.1171	0.0914	0.0883	0.0909
	II	0.0614	0.0494	0.0476	0.0490
	III	0.0485	0.0369	0.0364	0.0373

I: Without DGs and RPCs; II: Without DGs; III: Without RPCs.

2) Optimization results for CP load model

The optimization results are presented in Table VI for the CP model considering different objectives as Cases 1-3. This table shows that the CGWO proposes a better and more robust solution than GWO, PSO, EMA, and DAMOPSO algorithms for all cases. In Case 1, three objective functions, f_{loss}, $f_{\Delta V}$ and f_{RPC}, are considered as a multi-objective function. In Case 2 and Case 3, f_{RPC} and $f_{\Delta V}$ are not considered in the multi-objective function, respectively.

a) Case 1

Based on Table VI, in Case 1, the proposed CGWO finds an operating point with $f_{loss} = 0.0689$ MW, $f_{\Delta V} =$

0.0148 pu, and $f_{RPC} = 0.7646$ MVAR. In this condition, the objective function is 0.0833 MW. It is clear that the total power losses searched by CGWO are improved by about 3%–33% compared to other presented algorithms. Moreover, the voltage deviation is reduced at least by 1% up to 58% in comparison with other optimization techniques and the base case. In this case, it is important to note that DAMOPSO shows different solutions (Pareto ones) in which minimum values of f_{loss}, $f_{\Delta V}$ and f_{RPC} are not simultaneously searched, while our proposed CGWO and $ObjFunc$ (as (16)) are powerful enough to find the best operating point simultaneously. Results of Case 1 in Table VI show that the best operating point found by EMA is close to that searched by GWO. But, the robust results indicate that GWO has a better mean and standard deviation than EMA.

b) Case 2

In Case 2, the suggested technique outperforms other algorithms and improves f_{loss} and $f_{\Delta V}$ (main objectives) by 2%–16% and 18%–22%, respectively compared to the other methods due to finding $f_{loss} = 0.0675$ MW and $f_{\Delta V} = 0.0141$ pu. Although, in this case, f_{RPC} is not taken as a part of $ObjFunc$, and CGWO reduces it by 14% (average-in comparison with other algorithms). In this case, the value of the objective function is 0.0677 MW. Like Case 1, the results of EMA and GWO are approximately the same in power losses, voltage deviation, and objective function. But, PSO and DAMOPSO propose two quite far operating points. The robust results in terms of mean and standard deviation indicate that the introduced algorithm can provide better solutions than the other presented techniques.

c) Case 3

In the final case, CGWO introduces the best solution ($ObjFunc$ is 0.0830 MW) in terms of the minimum line losses (0.0699 MW) and RPC capacity (0.6931 MVAR). In Case 3, although it is not necessary to optimize $f_{\Delta V}$, the proposed method shows a lower $f_{\Delta V}$ (on average, 12% better than GWO, EMA, PSO, and DAMOPSO). The best, mean, and standard deviation of CGWO clearly demonstrate that it can always converge to a better operating point than the other analyzed algorithms. Moreover, EMA and GWO find similar solutions. In comparison with CGWO, PSO and DAMOPSO converge to bad operating points due to their higher power loss, bigger voltage deviation, and the use of more reactive power.

The optimal settings of control variables for Cases 1-3 are depicted in Figs. 5(a)-(c), respectively. It can be seen that all variables are within their limits and CGWO proposes the full usage of DGs in Cases 1 and 3 and almost does not offer the use of C_1 in the same cases. The position of operating points in the objective space found by CGWO is compared with GWO (as better solution among GWO, EMA, and PSO) and Pareto solutions obtained by DAMOPSO in Fig. 6.

TABLE VI
OPTIMIZATION RESULTS OF IEEE 33-BUS SYSTEM – CP MODEL

Cases	Technique	f_{loss} (MW)	$f_{\Delta V}$ (pu)	f_{RPC} (MVAR)	$ObjFunc$ (MW)		
					Best	Mean	Std.
Without optimization (with only DGs)		0.1348	0.0485	0.0000	-	-	-
1	DAMOPSO[a] [6]	0.0799	0.0162	1.6500	NA	NA	NA
		0.0806	0.0149	1.6500	NA	NA	NA
		0.1016	0.0345	0.3000	NA	NA	NA
	PSO	0.0709	0.0172	0.7758	0.0860	8.61E-2	4.08E-5
	EMA	0.0708	0.0171	0.7750	0.0859	8.61E-1	3.66E-6
	GWO	0.0708	0.0171	0.7800	0.0857	8.58E-2	3.56E-6
	CGWO	0.0689	0.0148	0.7646	0.0833	8.33E-2	3.43E-6
2	DAMOPSO [6]	0.0800	0.0180	1.5000	NA	NA	NA
	PSO	0.0691	0.0181	1.0086	0.0694	6.97E-3	4.16E-6
	EMA	0.0687	0.0172	0.9897	0.0690	6.92E-2	2.79E-5
	GWO	0.0686	0.0170	0.9996	0.0689	6.90E-3	3.05E-6
	CGWO	0.0675	0.0141	0.9455	0.0677	6.77E-2	2.90E-6
3	DAMOPSO [6]	0.0795	0.0182	1.5000	NA	NA	NA
	PSO	0.0713	0.0183	0.8204	0.0871	8.73 E-2	4.20 E-7
	EMA	0.0709	0.0177	0.7420	0.0851	8.52 E-3	2.98 E-6
	GWO	0.0708	0.0175	0.7500	0.0850	8.50 E-2	2.88 E-5
	CGWO	0.0699	0.0159	0.6931	0.0830	8.30 E-2	1.43 E-6

a For Case 1, [6] has proposed different solutions and three of them (based on minimum f_{loss}, $f_{\Delta V}$, and f_{RPC}) are presented here.

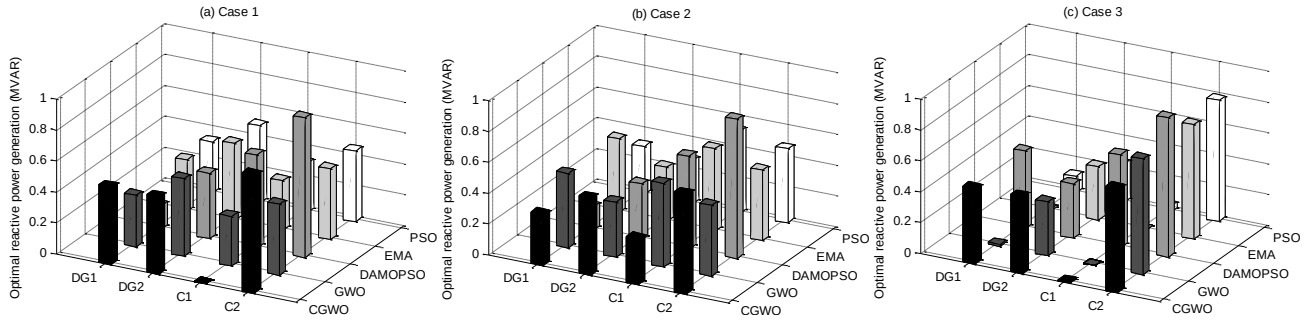

Fig. 5. OPTIMAL OUTPUTS OF DGS AND RPC DEVICES IN IEEE 33-BUS SYSTEM – CP MODEL

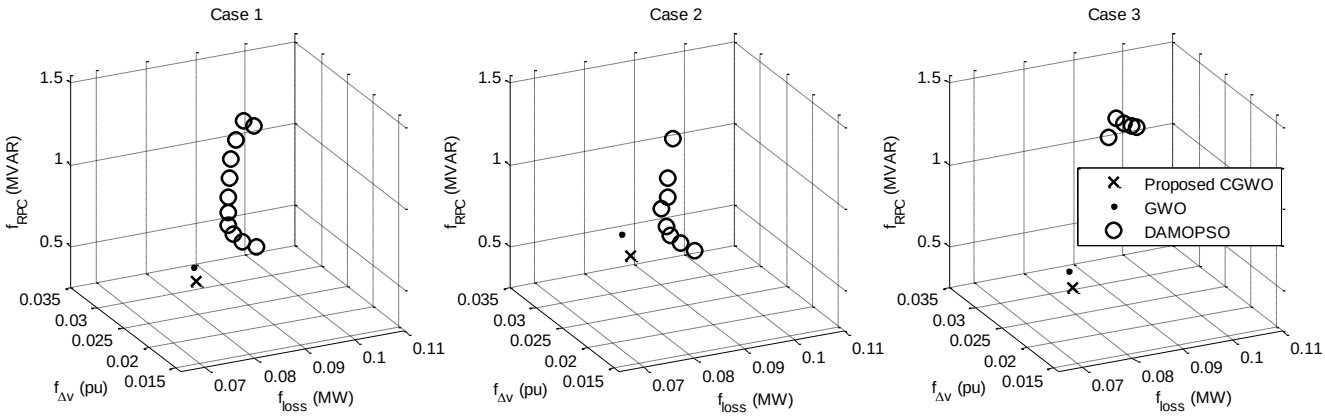

Fig. 6. COMPARISON OF DIFFERENT METHODS BASED ON THE FOUND OPERATING POINTS – IEEE 33-BUS SYSTEM – CP MODEL

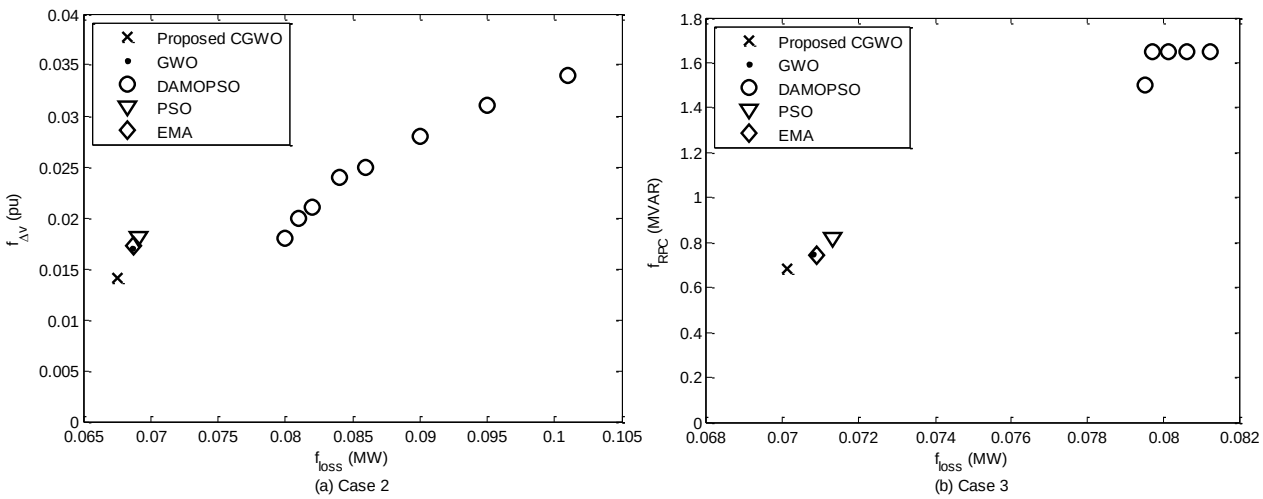

Fig. 7. COMPARISON OF DIFFERENT METHODS BASED ON THE FOUND OPERATING POINTS FOR CASES 2 AND 3 – IEEE 33-BUS SYSTEM – CP MODEL

The results of CGWO demonstrate the best operating point to optimize the distribution system based on the ORPD. This implies that there is a solution that can satisfy all objectives to be minimum simultaneously (less than [6]).

Figs. 7(a) and (b) compare the objectives in the objective space for Cases 2 and 3, respectively. Although the total RPC capacity is in conflict with the line loss, the CGWO can find a better solution than other algorithms. The voltage profiles of different cases based on the CGWO results are shown in Fig. 8. This figure demonstrates that the voltage magnitude of all nodes is improved. Accordingly, the proposed technique offers the best voltage profiles, but the relationship between the power losses and voltage deviation is complex (according to (2) and Fig. 7(a)).

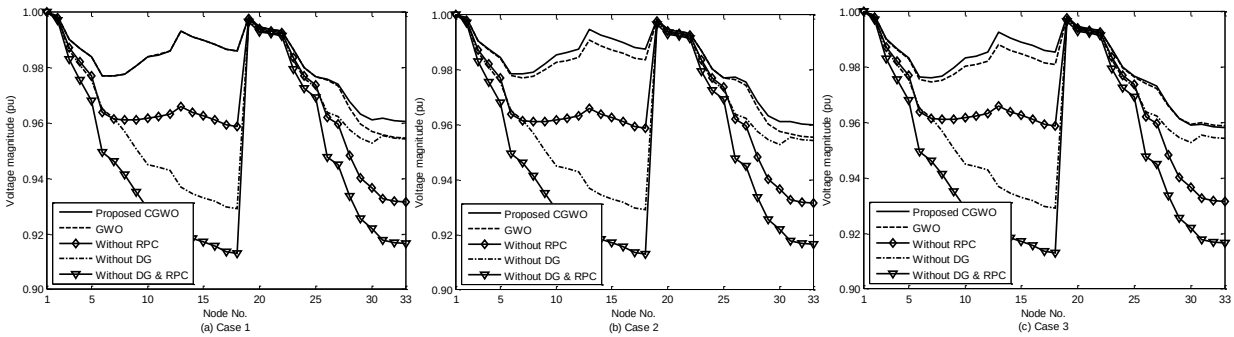

Fig. 8. VOLTAGE PROFILE OF IEEE 33-BUS SYSTEM BASED ON THE CGWO RESULTS

3) Optimization results for IND, COM, and RES load model

Here, only Case 3 is applied to the ORPD problem because investigating $f_{\Delta V}$ as a part of the $ObjFun$ leads to $V_i \to 1$ for $i = 1, 2, \dots, N_{bus}$. Based on (13) and (14), IND, COM, and RES demands (both actively and reactively) converging to the CP model. This means that α and β are not so important in optimization.

The best, mean, and standard deviation of results are presented in Table VII. From this table, it can be seen that the proposed CGWO is robust and can search a better operating point. The $ObjFun$s for IND, RES, and COM types are 0.0759, 0.0748, and 0.0732 MW, respectively. The results obtained by the CGWO algorithm clearly demonstrate that, compared to the best solution of the other reported algorithms, the total power losses are leastwise improved by 6%, 4%, and 4% for IND, RES, and COM loads, respectively. The total RPC capacity as the second part of the $ObjFun$ is also reduced at least by 11% for all load types. As Case 3 for CP load, the proposed approach shows an about 17% reduction in $f_{\Delta V}$ compared to GWO as a better solution among the other techniques. In accordance to Table VIII, it is interesting to note that if the results of the CP model, i.e., its optimal reactive power injections by DGs and RPCs, are considered for other load types, they lead to an increase in the objective functions of IND, RES, and COM by 2.5%, 1.5%, and 1.4%, respectively (in comparison with optimal results of these models). The control variables obtained in optimization by the proposed CGWO are reported in Table IX. The optimal reactive power generation by all DGs and RPC devices are illustrated in Fig. 9.

Fig. 10 shows the relationship between different objectives and various load types. In fact, it illustrates the interesting effect of different load types on the total power losses and RPC capacities (two main objectives) as well as the total voltage deviation. In other words, this shows the relationships between $\{f_{loss}, f_{RPC}, \text{ and } f_{\Delta V}\}$ and $\{\alpha \text{ and } \beta\}$. According to Fig. 10(a), the total active power losses, as per the main objective, are reduced by increasing the factor α. Fig. 10(b) indicates that the COM and CP models lead to the lowest and highest voltage deviation, respectively. In fact, COMs' bus voltages are closer to the desired magnitude, $V^* = 1$ pu and therefore the minimum value of $f_{\Delta V}$ occurs at this load condition. Finally, Fig. 10(c) shows that the lowest reactive power injection by RPC devices is obtained for the IND model, which has the highest value of β. Among different load types, CP reflects the worst condition in terms of the total power losses, RPCs, and the voltage deviation.

TABLE VII
OPTIMIZATION RESULTS OF IEEE 33-BUS SYSTEM – CASE 3 – DIFFERENT LOAD MODELS

Load model	Technique	f_{loss} (MW)	$f_{\Delta V}$ (pu)	f_{RPC} (MVAR)	$ObjFunc$ (MW)		
					Best	Mean	Std.
IND	PSO	0.0715	0.0213	0.5152	0.0816	8.18E-3	3.89E-5
	EMA	0.0710	0.0206	0.5350	0.0813	8.15E-2	4.11E-6
	GWO	0.0704	0.0201	0.5308	0.0805	8.07E-1	3.98E-6
	CGWO	0.0673	0.0158	0.4771	0.0759	7.59E-5	4.61E-8
RES	PSO	0.0680	0.0188	0.6146	0.0796	7.97E-2	3.02E-5
	EMA	0.0675	0.0189	0.6077	0.0788	7.90E-3	2.36E-3
	GWO	0.0663	0.0171	0.5950	0.0772	7.73E-2	4.11E-5
	CGWO	0.0648	0.0147	0.5677	0.0748	7.48E-2	2.67E-6
COM	PSO	0.0662	0.0181	0.6794	0.0787	7.81E-1	3.79E-4
	EMA	0.0651	0.0176	0.5965	0.0760	7.61E-3	3.31E-5
	GWO	0.0650	0.0175	0.6059	0.0759	7.61E-2	3.15E-7
	CGWO	0.0636	0.0146	0.5491	0.0732	7.33E-2	2.97E-6

TABLE VIII
OBJECTIVE FUNCTION EVALUATION FOR IND, RES, AND COM LOADS USING THE OPTIMAL RESULTS OF CP COMPARED TO THE OBTAINED RESULTS FOR EACH TYPE RESPECTIVELY – IEEE 33-BUS SYSTEM

Load model	$ObjFunc$ (MW) using X_{CP}	$ObjFunc$ (MW) using $X_{Load\ types}$
IND	0.0778	0.0759
RES	0.0759	0.0748
COM	0.0742	0.0732

TABLE IX
CONTROL VARIABLES OF IEEE 33-BUS SYSTEM BY CGWO– DIFFERENT LOAD MODELS

Load Model	Q_{DG1} (pu)	Q_{DG2} (pu)	Q_{C1} (pu)	Q_{C2} (pu)	$ObjFunc$ (MW)
CP (Case 1)	0.50000	0.50000	0.00031	0.76429	0.0833
CP (Case 2)	0.33313	0.50000	0.29752	0.64793	0.0677
CP (Case 3)	0.49173	0.50000	0.00819	0.67649	0.0831
IND	0.50000	0.46607	0.00053	0.47658	0.0759
RES	0.46887	0.47505	0.01174	0.55592	0.0748
COM	0.50000	0.47550	0.00000	0.54910	0.0733

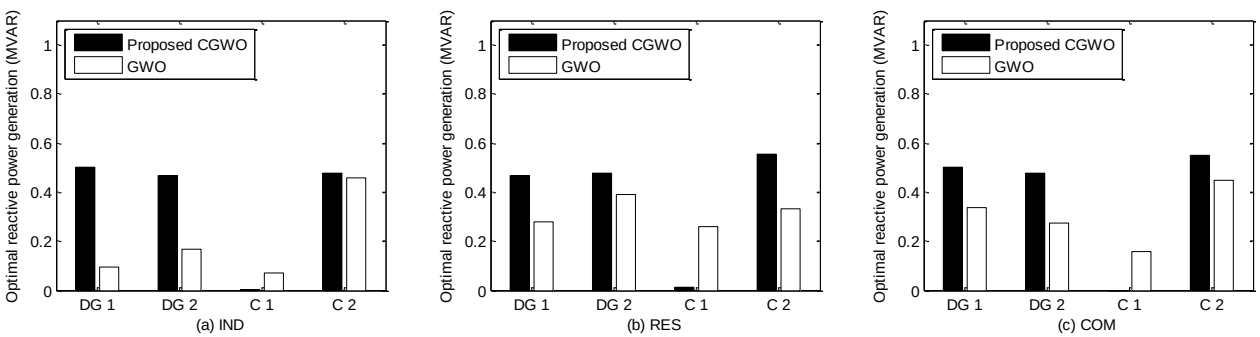

Fig. 9. Optimal outputs of DGs and RPC devices in IEEE 33-bus system – Case 3 – Different load models

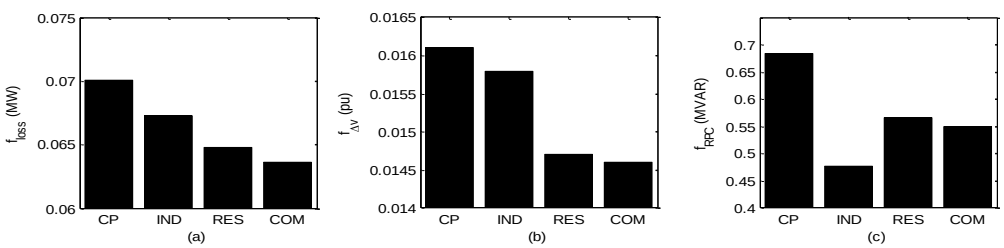

Fig. 10. Relationships between $\{f_{loss},\ f_{RPC}$, and $f_{\Delta V}\}$ and {CP, IND, RES, and COM} in IEEE 33-bus system by CGWO – Case 3

B. IEEE 69-bus Distribution System

The IEEE 69-bus distribution network is a larger-scale system, which was used as the second case study to verify the wide application of the proposed method. Its detailed data are taken from [55] and its single line diagram is shown in Fig. 11. In this network, there are two DGs and three RPC devices (based on [6]) and their capacities and sits are presented in Table X.

1) Total power losses and voltage deviation before optimization

Similar to the previous network, the total power loss and the total voltage deviation in base conditions (without ORPD) of the 69-bus network under different load models are listed in Table XI. In condition I, the studied network is considered without the presence of the DGs and capacitors. In condition II, three capacitors are considered to be connected to candidate buses. In this condition, it is supposed that the DG units are disconnected. In the final operation condition, the test system is analyzed with two DG units connected to buses 17 and 63, but all capacitors are overlooked according to condition III.

2) Optimization Results

The results of ORPD based on the GWO, PSO, EMA, and the proposed CGWO for optimizing Case 3 (as the previous network) are tabulated in Table XII. As can be seen, the suggested optimization strategy is robust and shows high performance in improving total power losses and total RPC capacity. This table clearly shows that the total power losses obtained by CGWO are improved by 4%, 4%, 5%, and 5% compared to the best solution of other

methods for CP, IND, RES, and COM models, respectively. This means that in comparison with the base case (without optimization-only with DGs), CGWO can significantly reduce f_{loss} by 41% (on average) for all load types. Moreover, the RPC capacity as the second part of the objective function is reduced by 3%, 5%, 4%, and 5% versus the best reported solution of the other methods for the mentioned models, respectively. The values of the objective function obtained by CGWO are 0.0880, 0.0799, 0.0765, and 0.0720 MW, which show a 5% improvement versus the traditional GWO. From the obtained results in Table XIII, it can be found that if the optimal reactive power injections by DGs and RPCs related to CP type are considered for IND, RES, and COM load models, their objective functions are increased by 2.16% (in comparison with optimal results of these models).

Fig. 12 compares the operating points for various load models obtained by CGWO (solid shapes) and GWO as the best method among the other analyzed algorithm (hollow shapes). It is clear that the proposed CGWO results outperform the GWO ones.

The optimal outputs related to DGs and RPCs searched by all the analyzed algorithms for various load models are depicted in Fig. 13. This figure shows that in all load models except for the RES one, CGWO sets DG_1 output to its maximum value. Additionally, the reactive generation of C_2 is negligible, while, for example, GWO uses about 5% (on average) of its capacity. However, CGWO for CP, RES, and COM demands utilizes 35% of C_3, while GWO uses less than 29% (unlike C_2). As can be seen in Fig. 13 and Table X, the newly introduced algorithm has a high capability to find more suitable control variables than other techniques for all load models; this leads to lower power losses and RPC cost, better voltage deviation, and considerably lower objective function. Finally, Table XIV demonstrates the optimal control variables obtained by the CGWO approach for this network. This table clearly shows that all independent variables related to reactive power injections by DGs and RPCs are within their pre-specified limits.

Fig. 14 illustrates the relationships between $\{f_{loss}, f_{RPC}, \text{and } f_{\Delta V}\}$ and {CP, IND, RES, and COM}. The total power losses show exponential decay behavior by increasing α in Fig. 14(a). As it can be seen in Fig. 14(c), the RPC cost has a similar behavior (unlike the 33-bus system). Injecting more reactive power by RPCs in IND load than RES load leads to a lower $f_{\Delta V}$ (Fig. 14(b)). In addition, in this network, the COM type makes the studied network to have lower power losses, RPC cost, and better voltage deviation. This condition leads to a minimum bus voltage better than the other models as shown in Fig. 15. It is observed that the highest f_{loss}, f_{RPC}, $f_{\Delta V}$, and minimum voltage magnitude are obtained from the CP load model.

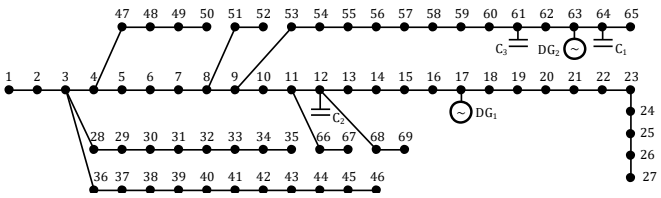

Fig. 11. Modified IEEE 69-bus distribution network

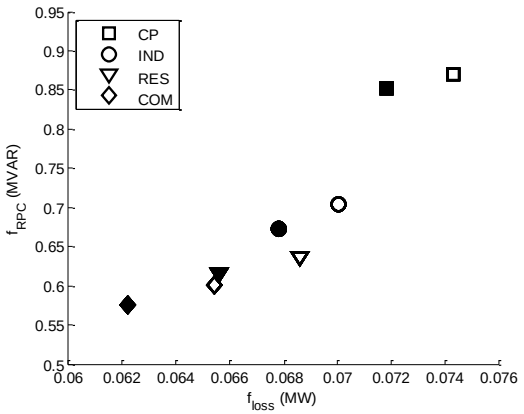

Fig. 12. Comparing the found operating points by different methods – IEEE 69-bus system – Solid and hollow shapes are respectively for CGWO and GWO – Case 3

TABLE X
DATA OF DGS AND RPC DEVICES [6] – IEEE 69-BUS SYSTEM

RPC/DG	Installed at node	Parameter	value
C_1	64	$Q_{C1,\min}$ (kVAR)	0
		$Q_{C1,\max}$ (kVAR)	900
C_2	12	$Q_{C2,\min}$ (kVAR)	0
		$Q_{C2,\max}$ (kVAR)	1500
C_3	61	$Q_{C3,\min}$ (kVAR)	0
		$Q_{C3,\max}$ (kVAR)	1500
DG_1	17	P_{DG1} (kW)	296
		$Q_{DG1,\min}$ (kVAR)	0
		$Q_{DG1,\max}$ (kVAR)	250
DG_2	63	P_{DG2} (kW)	500
		$Q_{DG2,\min}$ (kVAR)	0
			156

TABLE XI
SYSTEM CONDITION UNDER DIFFERENT LOAD MODELS BEFORE OPTIMIZATION – IEEE 69-BUS SYSTEM

Parameter	Condition	Load model			
		CP	IND	RES	COM
Total real power loss (f_{loss} in MW)	I	0.2250	0.1750	0.1708	0.1650
	II	0.2276	0.2568	0.2383	0.2289
	III	0.1413	0.1043	0.1060	0.1045
Total voltage deviation ($f_{\Delta V}$ in pu)	I	0.0993	0.0813	0.0788	0.0756
	II	0.0286	0.0243	0.0235	0.0225
	III	0.0523	0.0423	0.0413	0.0397

I: Without DGs and RPCs; II: Without DGs; III Without RPCs.

TABLE XII
OPTIMIZATION RESULTS OF IEEE 69-BUS SYSTEM – CASE 3 – DIFFERENT LOAD MODELS

Load model	Technique	f_{loss} (MW)	$f_{\Delta V}$ (pu)	f_{RPC} (MVAR)	$ObjFunc$ (MW)		
					Best	Mean	Std.
CP	PSO	0.0756	0.0315	0.8807	0.0932	9.34E-2	3.45E-6
	EMA	0.0746	0.0311	0.8623	0.0915	9.17E-2	4.32E-5
	GWO	0.0743	0.0310	0.8702	0.0914	9.14E-3	2.93E-7
	CGWO	0.0718	0.0289	0.8521	0.0880	8.80E-2	2.89E-6
IND	PSO	0.0702	0.0285	0.7427	0.0840	8.41E-3	4.02E-6
	EMA	0.0701	0.0284	0.7010	0.0831	8.32E-2	3.51E-8
	GWO	0.0700	0.0283	0.7047	0.0831	8.32E-2	3.10E-3
	CGWO	0.0678	0.0261	0.6733	0.0799	7.99E-3	2.73E-6
RES	PSO	0.0694	0.0294	0.6631	0.0819	8.20E-2	2.97E-9
	EMA	0.0683	0.0286	0.6448	0.0803	8.05E-2	4.81E-6
	GWO	0.0686	0.0287	0.6367	0.0804	8.05E-1	2.93E-5
	CGWO	0.0656	0.0272	0.6153	0.0765	7.66E-2	2.80E-6
COM	PSO	0.0675	0.0279	0.6498	0.0794	7.96E-3	3.89E-7
	EMA	0.0652	0.0268	0.6240	0.0762	7.63E-2	2.56E-4
	GWO	0.0654	0.0268	0.6010	0.0760	7.61E-3	3.38E-6
	CGWO	0.0622	0.0256	0.5750	0.0720	7.21E-2	3.09E-6

TABLE XIII
OBJECTIVE FUNCTION EVALUATION FOR IND, RES, AND COM LOADS USING THE OPTIMAL RESULTS OF CP COMPARED TO THE OBTAINED RESULTS FOR EACH TYPE RESPECTIVELY – IEEE 69-BUS SYSTEM

Load model	$ObjFunc$ (MW) using X_{CP}	$ObjFunc$ (MW) using $X_{Load\ types}$
IND	0.0826	0.0799
RES	0.0786	0.0765
COM	0.0724	0.0720

TABLE XIV
CONTROL VARIABLES OF IEEE 69-BUS SYSTEM BY CGWO– DIFFERENT LOAD MODELS-CASE 3

Load Model	Q_{DG1} (pu)	Q_{DG2} (pu)	Q_{C1} (pu)	Q_{C2} (pu)	Q_{C3} (pu)	$ObjFunc$ (MW)
CP	0.25000	0.15600	0.27901	0.00046	0.57265	0.0880
IND	0.25000	0.15600	0.11830	0.00150	0.55352	0.0799
RES	0.16570	0.15600	0.04782	0.00097	0.56653	0.0765
COM	0.25000	0.15600	0.15440	0.00067	0.41993	0.0720

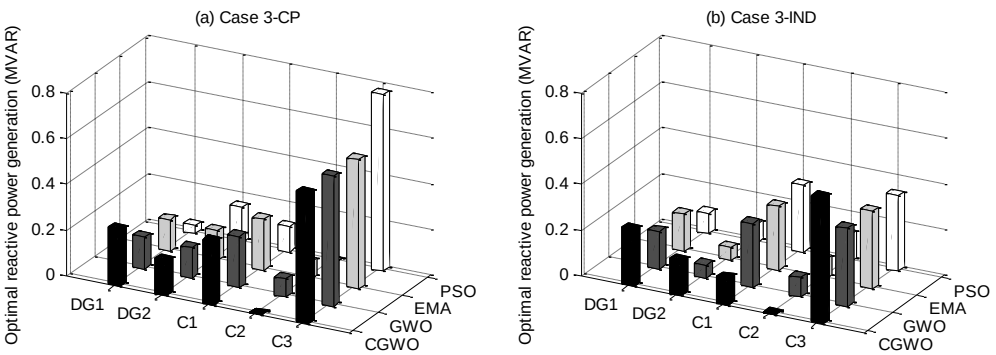

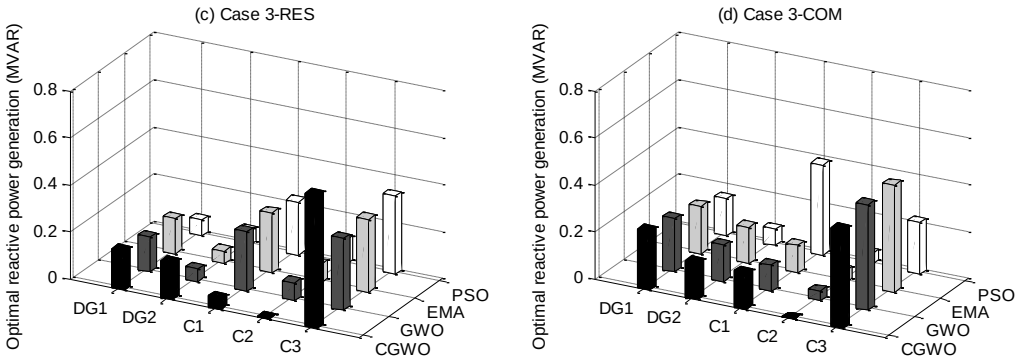

Fig. 13. Optimal outputs of DGs and RPC devices in IEEE 69-bus system – Case 3

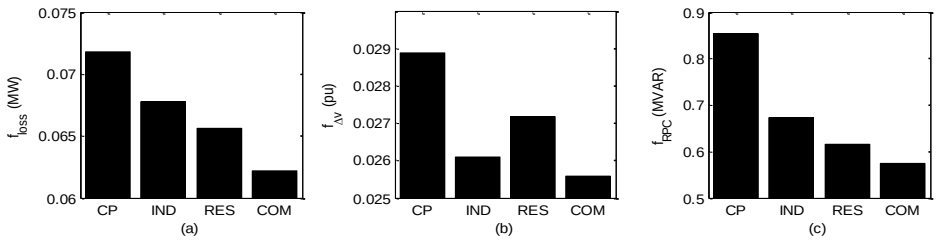

Fig. 14. Relationships between $\{f_{loss},\ f_{RPC}$, and $f_{\Delta V}\}$ and {CP, IND, RES, and COM} in IEEE 69-bus system by CGWO – Case 3

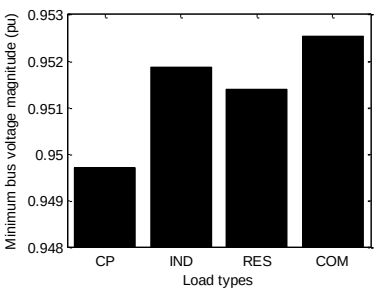

Fig. 15. Minimum bus voltages of different load models by CGWO – IEEE 69-bus system

V. CONCLUSION

This paper proposed a CGWO as a powerful optimization technique for solving the ORPD problem. In the CGWO, the best wolf is selected as alpha and each society has its own beta and gamma. Based on the social hierarchy of grey wolves, beta wolves respect and help alpha and can only command the other lower-level wolves (gamma and omega) in their society. In addition, a new version of the ORPD was introduced for distribution networks considering different load models, including CP, IND, COM, and RES types. Furthermore, for this optimization problem, a novel objective function was suggested that investigates different objectives such as total power losses, voltage deviation, and RPC cost. The proposed technique was tested on two standard distribution systems including IEEE 33- and 69-bus distribution grids considering DGs and RPC devices. The results indicated that:

- The proposed CGWO can solve high-complex ORPD problems in distribution systems considering different load models.
- The CGWO can search a better operating point (in terms of line losses, RPC capacity, and voltage deviation) than other presented methods for all load types.
- It is robust, meaning that it can always find a better $ObjFunc$ for different distribution systems (in comparison with different analyzed techniques) while meeting all constraints.
- The performance of the proposed $ObjFunc$ is more efficient than the Pareto solution. In fact, it properly converts a multi-objective ORPD problem into a single-objective one.
- The lowest power losses are related to the COM load, while the CP leads to the highest line losses.
- The CP and COM types lead to the lowest and highest minimum bus voltages, respectively. This means that COM reflects a better voltage profile than the other types.
- The worst voltage deviations are related to the COM model.
- The behavior of IND and RES load models is between CP and COM load models.

APPENDIX A

The effectiveness of the proposed CGWO in solving standard optimization problems is verified by ten benchmark functions as Table AI. The optimum value of all listed functions is 0. The proposed CGWO was run over 20 times on each standard function and its parameters are =

30, $N_s = 4$, $\text{Iteration}_{\max} = 1000$, $C_\alpha = 0.3$, $C_\beta = 0.6$, and $C_\delta = 0.1$. The optimization results of CGWO, GWO [52], EMA, and PSO [52] in terms of average and standard deviation are presented in Table AII. As it is obvious, the CGWO outperforms the other methods and results in high local minima avoidance. This shows the superior ability of the proposed hunting model and civilization and also emphasizes the balance between exploitation and exploration power.

TABLE AI
BENCHMARK FUNCTIONS

No.	Name	Formulation	Dimension	Range	$f_{\min}$
1	Sphere	$f_1(x) = \sum_{i=1}^{n} x_i^2$	30	[-100, 100]	0
2	Step function	$f_2(x) = \sum_{i=1}^{n} ([x_i + 0.5])^2$	30	[-100, 100]	0
3	Quartic	$f_3(x) = \sum_{i=1}^{n} i x_i^4 + \text{rand}[0,1)$	30	[-1.28, 1.28]	0
4	Schwefel's 1.2	$f_4(x) = \sum_{i=1}^{n} \left(\sum_{j=1}^{i} x_j \right)^2$	30	[-100, 100]	0
5	Schwefel's 2.21	$f_5(x) = \max_i \{\lvert x_i \rvert, 1 \le i \le n\}$	30	[-100, 100]	0
6	Schwefel's 2.22	$f_6(x) = \sum_{i=1}^{n} \lvert x_i \rvert + \prod_{i=1}^{n} \lvert x_i \rvert$	30	[-10, 10]	0
7	Ackley	$f_7(x) = -20 \exp\left(-0.2 \sqrt{\frac{1}{n} \sum_{i=1}^{n} x_i^2} \right) - \exp\left(\frac{1}{n} \sum_{i=1}^{n} \cos(2\pi x_i) \right) + 20 + e$	30	[-32, 32]	0
8	Griewank	$f_8(x) = \frac{1}{4000} \sum_{i=1}^{n} x_i^2 - \prod_{i=1}^{n} \cos\left(\frac{x_i}{\sqrt{i}} \right) + 1$	30	[-600, 600]	0
9	Penalized function 1	$f_9(x) = \frac{\pi}{n} \left\{ 10 \sin(\pi y_1) + \sum_{i=1}^{n-1} (y_i - 1)^2 [1 + 10 \sin^2(\pi y_{i+1})] + (y_n - 1)^2 \right\} + \sum_{i=1}^{n} u(x_i, 10, 100, 4)$, $y_i = 1 + \frac{x_i + 1}{4}$, $u(x_i, a, k, m) = \begin{cases} k(x_i - a)^m & x_i > a \\ 0 & -a < x_i < a \\ k(-x_i - a)^m & x_i < -a \end{cases}$	30	[-50, 50]	0
10	Penalized function 2	$f_{10}(x) = 0.1 \left\{ \sin^2(3\pi x_i) + \sum_{i=1}^{n} (x_i - 1)^2 [1 + \sin^2(3\pi x_{i+1})] + (x_n - 1)^2 [1 + \sin^2(3\pi x_n)] \right\} + \sum_{i=1}^{n} u(x_i, 5, 100, 4)$	30	[-50, 50]	0

TABLE AII
OPTIMIZATION RESULTS OF BENCHMARK FUNCTIONS

Method		Function									
		f_1	f_2	f_3	f_4	f_5	f_6	f_7	f_8	f_9	f_{10}
PSO [52]	Avg	1.360E-04	1.02E-04	1.228E-01	7.012E+1	1.086E+1	4.214E-02	2.76E-01	6.917E-03	6.917E-03	6.675E-03
	Std	2.020E-04	8.28E-05	4.495E-02	2.211E+1	3.170E-01	4.542E-02	5.09E-01	2.63E-02	2.630E-02	8.907E-03
EMA	Avg	6.382E-25	0	3.717E-02	5.716	1.017E-02	2.335E-13	1.180E-01	1.079E-02	1.077	5.943E-03
	Std	1.433E-24	0	1.036E-02	2.904	7.401E-03	3.854E-13	3.682E-01	1.493E-02	1.466	4.213E-03
GWO [52]	Avg	6.59E-28	8.165E-01	2.213E-03	3.29E-06	5.61E-07	7.18E-17	1.06E-13	4.485E-03	5.343E-02	6.544E-01
	Std	6.34E-05	1.26E-04	1.002E-01	7.914E+1	1.315	2.901E-02	7.783E-02	6.659E-03	2.073E-02	4.474E-03
CGWO	Avg	6.544E-36	0	1.517E-03	2.565E-09	7.365E-08	2.677E-21	5.524E-14	1.395E-03	2.490E-06	3.971E-05
	Std	6.177E-36	0	7.264E-04	5.957E-09	7.177E-08	1.990E-21	7.207E-15	3.411E-03	1.017E-06	1.060E-05

APPENDIX B

In this section, the values of some parameters of the CGWO algorithm including the number of grey wolves, societies, and maximum iteration are experimented and their influence on the performance of the proposed technique is analyzed to determine their optimal settings. To evaluate the effect of these parameters on the final solution, only the results of Case 1 of IEEE 33-bus distribution network considering the CP model are presented here. So, several runs with different parameter values were carried out. The results depicted in Fig. B indicated that:

Number of society: According to Fig. B(a), this parameter varied in the range of 1–7 to study the effect of N_s on the $ObjFunc$. It is clear that the optimum choice for this parameter is $N_s = 4$. Increasing the number of society ($N_s \geq 5$) can slightly improve the final solution.

Number of grey wolves: Based on Fig. B(b), the best choice is $N = 20$ and more wolves can reduce the objective function by less than 0.1%.

Number of iteration: Fig. B(c) indicates that $\text{Iteration}_{\max} > 50$ cannot help the algorithm find better $ObjFunc$.

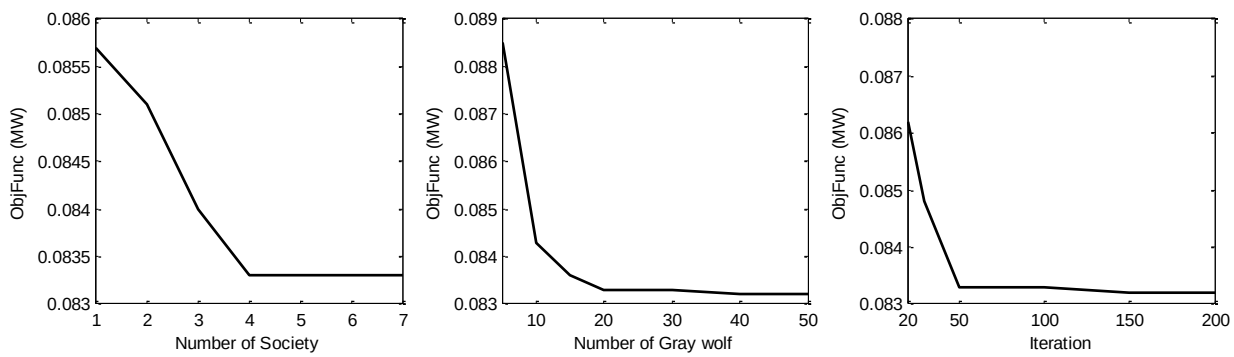

Fig. B. Effect of the CGWO parameters on the objective function – IEEE 33-bus – Case 1 – CP model

REFERENCES

[1] Shefaei A, Vahid-Pakdel MJ, Mohammadi-ivatloo B. "Application of a hybrid evolutionary algorithm on reactive power compensation problem of distribution network". *Comput Electr Eng* 2018;72:125–136.

[2] OualidMedani K ben, Sayah S, Bekrar A. "Whale optimization algorithm based optimal reactive power dispatch: A case study of the Algerian power system". *Electr Power Syst Res* 2017:In Press.

[3] Atwa YM, El-Saadany EF, Salama MMA, Seethapathy R. "Optimal renewable resources mix for distribution system energy loss minimization". *IEEE Trans Power Syst* 2010;25:360–370.

[4] Dixit M, Kundu P, Jariwala HR. "Optimal integration of shunt capacitor banks in distribution networks for assessment of techno-economic asset". *Comput Electr Eng* 2018;71:331–345.

[5] Barati H, Shahsavari M. "Simultaneous optimal placement and sizing of distributed generation resources and shunt capacitors in radial distribution systems using crow search algorithm". *Int J Ind Electron Control*

Optim 2018;1:27–40.

[6] Cheng S, Chen M-Y. "Multi-objective reactive power optimization strategy for distribution system with penetration of distributed generation". *Int J Electr Power Energy Syst* 2014;62:221–228.

[7] Wang Y, Zhang P, Li W, Xiao W, Abdollahi A. "Online overvoltage prevention control of photovoltaic generators in microgrids". *IEEE Trans Smart Grid* 2012;3:2071–2078.

[8] Granville S. "Optimal reactive dispatch through interior point methods". *IEEE Trans Power Syst* 1994;9:136–146.

[9] Quintana VH, Santos-Nieto M. "Reactive-power dispatch by successive quadratic programming". *IEEE Trans Energy Convers* 1989;4:425–435.

[10] Granada M, Rider MJ, Mantovani JRS, Shahidehpour M. "A decentralized approach for optimal reactive power dispatch using a Lagrangian decomposition method". *Electr Power Syst Res* 2012;89:148–156.

[11] Shaw B, Mukherjee V, Ghoshal SP. "Solution of reactive power dispatch of power systems by an opposition-based gravitational search algorithm". *Int J Electr Power Energy Syst* 2014;55:29–40.

[12] Ayan K, Kılıç U. "Artificial bee colony algorithm solution for optimal reactive power flow". *Appl Soft Comput* 2012;12:1477–1482.

[13] Ettappan M, Vimala V, Ramesh S, Kesavan VT. "Optimal reactive power dispatch for real power loss minimization and voltage stability enhancement using Artificial Bee Colony Algorithm". *Microprocess Microsyst* 2020;76.

[14] Mugemanyi S, Qu Z, Rugema FX, Dong Y, Bananeza C, Wang L. "Optimal reactive power dispatch using chaotic bat algorithm". *IEEE Access* 2020;8:65830–65867.

[15] Duman S, Sonmez Y, Guvenc U, Yorukeren N. "Optimal reactive power dispatch using a gravitational search algorithm". *IET Gener Transm Distrib* 2012;6:563–576.

[16] Ghasemi M, Taghizadeh M, Ghavidel S, Aghaei J, Abbasian A. "Solving optimal reactive power dispatch problem using a novel teaching–learning-based optimization algorithm". *Eng Appl Artif Intell* 2015;39:100–108.

[17] Sulaiman MH, Mustaffa Z, Mohamed MR, Aliman O. "Using the gray wolf optimizer for solving optimal reactive power dispatch problem". *Appl Soft Comput* 2015;32:286–292.

[18] Raj S, Bhattacharyya B. "Reactive power planning by opposition-based grey wolf optimization method". *Int Trans Electr Energy Syst* 2018;28:1–29.

[19] Mukherjee A, Mukherjee V. "Solution of optimal reactive power dispatch by chaotic krill herd algorithm". *IET Gener Transm Distrib* 2015;9:2351–2362.

[20] Basu M. "Quasi-oppositional differential evolution for optimal reactive power dispatch". *Int J Electr Power Energy Syst* 2016;78:29–40.

[21] Basu M. "Multi-objective optimal reactive power dispatch using multi-objective differential evolution". *Int J Electr Power Energy Syst* 2016;82:213–224.

[22] Rajan A, Malakar T. "Exchange market algorithm based optimum reactive power dispatch". *Appl Soft Comput* 2016;43:320–336.

[23] Abaci K, Yamaçli V. "Optimal reactive-power dispatch using differential search algorithm". *Electr Eng* 2017;99:213–225.

[24] Khazali AH, Kalantar M. "Optimal reactive power dispatch based on harmony search algorithm". *Int J Electr Power Energy Syst* 2011;33:684–692.

[25] Zhou B, Chan KW, Yu T, Wei H, Tang J. "Strength pareto multigroup search optimizer for multiobjective optimal reactive power dispatch". *IEEE Trans Ind Informatics* 2014;10:1012–1022.

[26] Shaheen AM, El-Sehiemy RA, Farrag SM. "Integrated strategies of backtracking search optimizer for solving reactive power dispatch problem". *IEEE Syst J* 2018;12:424–433.

[27] Mouassa S, Bouktir T, Salhi A. "Ant lion optimizer for solving optimal reactive power dispatch problem in power systems". *Eng Sci Technol an Int J* 2017;20:885–895.

[28] Bingane C, Anjos MF, Digabel SL. "Tight-and-cheap conic relaxation for the optimal reactive power dispatch problem". *IEEE Trans Power Syst* 2019;Early Acce.

[29] Davoodi E, Babaei E, Mohammadi-ivatloo B, Rasouli M. "A novel fast semidefinite programming-based approach for optimal reactive power dispatch". *IEEE Trans Ind Informatics* 2019;Early Acce.

[30] Tran HV, Pham TV, Pham LH, Le NT, Nguyen TT. "Finding optimal reactive power dispatch solutions by using a novel improved stochastic fractal search optimization algorithm". *TELKOMNIKA* 2019;17:2517–2526.

[31] Li Y, Wang Y, Li B. "A hybrid artificial bee colony assisted differential evolution algorithm for optimal reactive power flow". *Int J Electr Power Energy Syst* 2013;52:25–33.

[32] Ghasemi M, Ghanbarian MM, Ghavidel S, Rahmani S, Moghaddam EM. "Modified teaching learning algorithm and double differential evolution algorithm for optimal reactive power dispatch problem: A comparative study". *Inf Sci (Ny)* 2014;278:231–249.

[33] Lenin K, Reddy BR, Suryakalavathi M. "Hybrid Tabu search-simulated annealing method to solve optimal reactive power problem". *Int J Electr Power Energy Syst* 2016;82:87–91.

[34] Shareef SKM, Rao RS. "Optimal reactive power dispatch under unbalanced conditions using hybrid swarm intelligence". *Comput Electr Eng* 2018;69:183–193.

[35] Hongxin L, Yinhong L, Jinfu C. "Adaptive multiple evolutionary algorithms search for multi-objective optimal reactive power dispatch". *Int Trans Electr Energy Syst* 2014;24:780–795.

[36] Singh RP, Mukherjee V, Ghoshal SP. "Optimal reactive power dispatch by particle swarm optimization with an aging leader and challengers". *Appl Soft Comput* 2015;29:298–309.

[37] Zhang M, Li Y. "Multi-objective optimal reactive power dispatch of power systems by combining classification-based multi-objective evolutionary algorithm and integrated decision making". *IEEE Access* 2020;8:38198–38209.

[38] Ansari J, Gholami A, Kazemi A. "Holonic structure: a state-of-the-art control architecture based on multi-agent systems for optimal reactive power dispatch in smart grids". *IET Gener Transm Distrib* 2015;9:1922–1934.

[39] Zheng W, Wu W, Zhang B, Sun H, Liu Y. "A fully distributed reactive power optimization and control

method for active distribution networks". *IEEE Trans Smart Grid* 2016;7:1021–1033.
[40] Naderi E, Narimani H, Fathi M, Narimani MR. "A novel fuzzy adaptive configuration of particle swarm optimization to solve large-scale optimal reactive power dispatch". *Appl Soft Comput* 2017;53:441–456.
[41] Ghasemi M, Ghavidel S, Ghanbarian MM, Habibi A. "A new hybrid algorithm for optimal reactive power dispatch problem with discrete and continuous control variables". *Appl Soft Comput* 2014;22:126–140.
[42] Chen G, Liu L, Zhang Z, Huang S. "Optimal reactive power dispatch by improved GSA-based algorithm with the novel strategies to handle constraints". *Appl Soft Comput* 2017;50:58–70.
[43] Jangir P, Parmar SA, Trivedi IN, Bhesdadiya RH. "A novel hybrid Particle Swarm Optimizer with multi verse optimizer for global numerical optimization and Optimal Reactive Power Dispatch problem". *Eng Sci Technol an Int J* 2017;20:570–586.
[44] Mehdinejad M, Mohammadi-Ivatloo B, Dadashzadeh-Bonab R, Zare K. "Solution of optimal reactive power dispatch of power systems using hybrid particle swarm optimization and imperialist competitive algorithms". *Int J Electr Power Energy Syst* 2016;83:104–116.
[45] Srivastava L, Singh H. "Hybrid multi-swarm particle swarm optimisation based multi-objective reactive power dispatch". *IET Gener Transm Distrib* 2015;9:727–739.
[46] Zhang J, Liu N, Lu X, Wu M. "Two-layer reactive power optimal dispatching model for high-voltage distribution network and application". *IEEE PES Asia-Pacific Power Energy Eng. Conf., Brisbane, Australia*: 2015, p. 1–5.
[47] Zhou H, Guo J, Zhou R, Gu K, Qian L. "Interior point method based reactive power optimization of active distribution network". *China Int. Conf. Electr. Distrib. (CICED 2016)*, 2016, p. 1–6.
[48] Sheng W, Liu K, Pei H, Li Y, Jia D, Diao Y. "A fast reactive power optimization in distribution network based on large random matrix theory and data analysis". *Appl Sci* 2016;6:1–19.
[49] Varadarajan M, Swarup KS. "Differential evolution approach for optimal reactive power dispatch". *Appl Soft Comput* 2008;8:1549–1561.
[50] Singh D, Singh D, Verma KS. "Multiobjective optimization for DG planning with load models". *IEEE Trans Power Syst* 2009;24:427–436.
[51] Bhattacharya A, Roy PK. "Solution of multi-objective optimal power flow using gravitational search algorithm". *IET Gener Transm Distrib* 2012;6:751–763.
[52] Mirjalili S, Mirjalili SM, Lewis A. "Grey wolf optimizer". *Adv Eng Softw* 2014;69:46–61.
[53] Ghorbani N, Babaei E. "Exchange market algorithm". *Appl Soft Comput* 2014;19:177–187.
[54] MATPOWER package 2019. https://matpower.org/.
[55] Baran ME, Wu FF. "Network reconfiguration in distribution systems for loss reduction and load balancing". *IEEE Trans Power Deliv* 1989;4:1401–1407.

Saman Hosseini-Hemati was born in Kermanshah, Iran. He received his B.S. degree in Electrical Engineering from Islamic Azad University, Ardabil, Iran, in 2008, and his M.S. degree in Electrical Engineering from Islamic Azad University, Saveh, Iran, in 2010. In 2014, he joined Islamic Azad University, Kermanshah branch as an Instructor at department of the Electrical Engineering. His current research interests include planning and operation of Active Distribution Networks (ADN), Optimal Reactive Power Dispatch (ORPD), Optimization Algorithms, CHP operation, and renewable energy resources.

Shahram Karimi was born in Kermanshah, Iran, in 1972. He received the B.S. degree in Electrical Engineering from University of Tabriz, Tabriz, Iran, in 1995, his M.S. degree in Electrical Engineering from Sharif University of Technology, Tehran, Iran, in 1997, and his Ph.D. degree in Electrical Engineering from Henri Poincaré Université, Nancy, France, in 2008, all in Electrical Engineering. He is currently an Assistant Professor at department of the Electrical Engineering, Razi University, Kermanshah, Iran. His research interests include microgrid voltage and frequency control, active power filters, power quality, FACTS Devices and fault tolerant converters.

Gholam Hossein Sheisi was born in Tehran, Iran. He received his B.S. degree in Electrical Engineering from Tennessee State University, Tennessee, USA, in 1979 and his M.S. and Ph.D. degrees in Electrical Engineering from Missouri State University, Missouri, USA, in 1982 and 1985, respectively. In 1991 he joined Razi University as an Assistant Professor at department of the Electrical Engineering. His current research interests include Unit Commitment, Planning and Operation of Electrical Networks, Optimization and renewable energy sources.

International Journal of Industrial Electronics, Control and Optimization © 2021 IECO
Vol. 4, No. 2, pp. 211-220 , April (2021)

Soft Sensor Development for Monitoring ASTM-D86 Index: Effect of Feed Flow Rate Change

Bahareh Bidar[1,†], Mir Mohammad Khalilipour[2], Farhad Shahraki[3], Jafar Sadeghi[4]

[1,2,3,4] Center for Process Integration and Control, Department of Chemical Engineering, University of Sistan and Baluchestan, Zahedan, Iran

ABSTRACT

Changes in a crude oil flow rate to an atmospheric distillation unit can influence the quality of the products. This paper presents a modification method for a soft sensing model, including an update term, which makes it compatible with industrial variations. A modified soft sensing structure is adopted using the lookup table (LUT) method where steady-state soft sensing models are performed. The steady-state soft sensing models are proposed based on the local instrumental variable (LIV) technique for an industrial atmospheric distillation unit (ADU) at Shiraz refinery, Iran. The LIV-based soft sensors use tray temperature measurements to monitor the ASTM-D86 index of side products for a nominal flow rate (60,000bbl/day). The lookup tables have been developed based on the difference between the predicted values of the ASTM-D86 index and the corresponding simulation values to make update terms in different feed flow rates. The results present improvement in the predictions of LIV-based soft sensors, as well as acceptable control performance in feed flow rate variations. The comparison of soft sensing results with/without the lookup tables demonstrates that the proposed update term helps to predict product quality more precisely and is suitable for advanced monitoring scheme due to no complexity and low computational time.

Article Info

Keywords:
ASTM-D86 Index, Crude distillation column, Data-driven soft sensor, Local instrumental variable (LIV), Lookup table method

Article History:
Received 2020-05-16
Accepted 2020-11-28

I. INTRODUCTION

Crude distillation units (CDUs) are considered the principal process in oil refineries. The atmospheric distillation column (ADU) is the heart of a CDU and the most fundamental step in the refining process. The primary purpose of an ADU is to separate crude oil into its components (or distillation cuts, distillation fractions) including naphtha, kerosene, gas oil, etc. for further processing by other units. Crude oil is a complex blend of hundreds of hydrocarbons that makes it difficult to determine its product quality with distillation fractions. Typically, petroleum product quality is specified by ASTM standard methods. ASTM-D86 is the standard test method used to experimentally measure the batch distillation curve of a petroleum product at atmospheric pressure [1, 2].

The online monitoring of temperature, pressure, and flow rate is simply done by using available hardware sensors. However, online monitoring of product qualities is only possible by installing online sensors, which are very complex, hard-to-maintain, and expensive. One of the challenging issues in the quality monitoring or controlling of ADUs is the unavailability of suitable hardware sensors for online measuring of the ASTM index. The procedure of laboratory measurements for the ASTM analysis is also ponderous and time-consuming, so it is not practical to measure this quality more than once in a shift (e.g., 8 hours) or up to twice in 24 hours [3-5].

Since accurate and reliable measurements are required for control purposes, the lack of online measurement of product

[†]Corresponding Author: b.bidar@eng.usb.ac.ir
Tel: +98-54-3113-2813, Fax: +98-54-3344-7092, Center for process Integration and Control, Department of Chemical Engineering, University of Sistan and Baluchestan, Zahedan, Iran.

quality can be complemented by soft sensing methods. A soft sensor is a mathematical model that is used instead of a physical sensor when a physical sensor cannot be placed due to several reasons like non-availability of a sensor, economic constraints, placement constraints, etc. In the control theory field, these soft sensors are known as observers. If a system is observable, it is possible to fully reconstruct the system states that are used in the control structure from its output measurements using state observers. In the measurement and monitoring field, soft sensors are also known as observers if the relationships describe the process mechanistically [6, 7]. They have been successfully adopted in several applications to provide accurate and reliable estimates without requiring further expenditure on hardware sensors or laboratory measurements [8, 9].

There are two different approaches to design soft sensors: model-driven and data-driven. Model-driven soft sensors are based on prior knowledge of the system and use first-principle models to estimate the desired variables. Data-driven soft sensors use models that are based on available data of the system and extremely interesting in the process industries as they can quickly be developed without the need for insights into the complex mechanisms of industrial units. They describe the real process dynamics of complex processes more realistically [10-12]. Typical data-driven techniques to estimate the process variables include partial least squares (PLS) [13-15], principal component analysis (PCA) [16-18], artificial neural networks (ANN) [19-21], neuro-fuzzy system (NFS) [22-25], support vector regression (SVR) [26-28], and their modifications [29-32].

The state-dependent parameter (SDP) modeling approach is an identification and modeling technique that was introduced by Peter C. Young and co-workers [33] and first adopted for soft sensor development by Gharehbaghi and Sadeghi [34] and Bidar et al. [35]. The modeling approach is based on the data-based mechanistic (DBM) modeling philosophy. In the DBM philosophy, the non-stationary and nonlinear aspects of the system are reflected by varying parameter models, whether parameters are varying with time or state variables of the system. The identification procedure is based on a stochastic state-space formulation, which uses a recursive Kalman filter (KF), fixed interval smoothing (FIS), and iterative back-fitting algorithms [36].

Furthermore, the SDP modeling approach outperforms other traditional data-driven methods like PCR, PLS, ANN, SVR, and so on, due to its remarkable capability to describe the behavior of non-linear systems. As a result, SDP-based soft sensors have shown successful applications for the estimation of process variables. However, nonparametric methods like SDP suffer from the use of the back-fitting algorithm because the functionality of each SDP affects the estimation of the other SDPs, which produces other problems associated with the back-fitting algorithm.

To deal with this issue, Bidar et al. [37] proposed a novel SDP method by local instrumental variable (LIV). The LIV approach uses polynomial modeling combined with instrumental variable (IV) concepts to introduce the simultaneous estimation method of SDPs. The proposed method was applied to predict 95%ASTM-D86 of side products in a simulated ADU based on tray temperature measurements. LIV-based soft sensors were developed based on steady-state simulation data of an industrial ADU at a nominal feed flow rate of 60,000 bbl/day. The optimal performance was achieved with the help of LIV-based soft sensors in closed-loop control of the simulated process around the nominal flow rate.

However, in real crude distillation processes, the feed flow rate is variable due to operational and feed availability constraints. The persistence of such variations in the feed flow rate can raise serious challenges in the control of the process. Due to the highly nonlinear and ill-conditioned characteristics of ADU, LIV-based soft sensors have been trained with steady-state data at constant capacity while feed flow rate variations have a significant impact on the reliability of their estimates. The weakness of the proposed soft sensing model is to ignore the feed flow rate variation. Therefore, feed flow rate data like tray temperature measurements need to be properly incorporated into the soft sensing model. The slow and complex dynamic of ADU makes it difficult to gather dynamic data in different feed flow rates.

The objective of the present paper is to modify the LIV-based soft sensor model including an update term, which makes it compatible with industrial variations. An update term allows information about the feed flow rates to be included in the soft sensing model and improves their estimates. In other words, the flow rate-based corrector is proposed to develop a high-quality soft sensing model with good generalization abilities.

The lookup table (LUT) method is implemented to make update terms, which is based on ASTM-D86 differences (e.g. the difference between the outputs of LIV-based soft sensors and corresponding simulation values) obtained in different feed flow rates. The linear interpolation method is used to determine difference data for interpolated values. The difference data are augmented to the prediction values of soft sensors to maintain the 95%ASTM-D86 indexes at setpoint levels. As lookup table can produce a quick interpolation platform to link with soft sensing models, it can be easily combined with different soft sensing algorithms, including the effect of changes in influencing process variables.

The paper is organized as follows. Section II provides a brief overview of the SDP/LIV technique and then presents the modification by lookup table method. In this section, the issues of problem description (Section II.A), LIV-based soft

sensor modeling (Section II.B), feed flow rate analysis (Section II.C), and lookup table method (Section II.D) are described in detail. Successful implementation results of the modified LIV-based soft sensors are provided and discussed in Section III. The paper is concluded in Section IV.

II. MODIFIED LIV-BASED SOFT SENSOR MODELING METHOD

A. Problem description

Fig. 1 shows the flowsheet of the ADU considered in this paper including a crude tower, top condenser, two pumparounds, and three side strippers. The column has 43 trays and three main products including naphtha, kerosene, and gas oil, which are taken from three side strippers, and the atmospheric residue is sent to the vacuum distillation unit (VDU) for further processing. Further information about the case study is available in [38, 39].

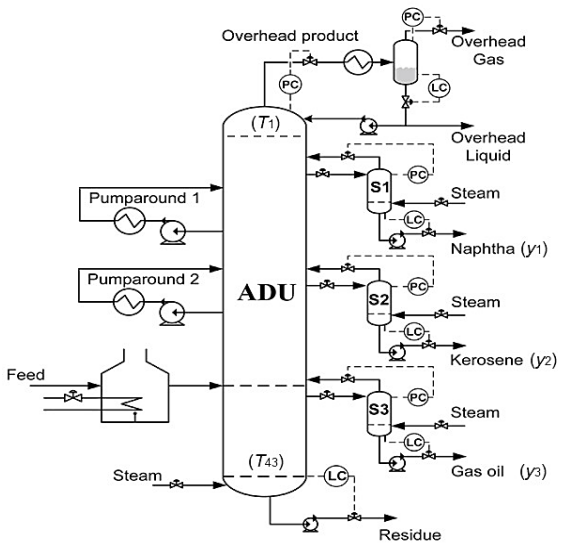

Fig. 1. The flowsheet of the atmospheric distillation column (ADU) [38].

The steady and dynamic simulations of the ADU were performed using the Aspen plus and Aspen dynamics, respectively. As is shown in [37], soft sensors were developed based on the LIV modeling approach to the continuous prediction of the 95%ASTM-D86 index of side products. Therefore, temperature measurements (e.g., T_1–T_{43}) inside the ADU and 95%ASTM-D86 index of naphtha (y_1), kerosene (y_2), and gas oil (y_3) were chosen as the input and output variables, respectively, and were initially used to identify soft sensing structures. Most informative temperatures were selected based on both correlation analysis and backward elimination method. The selected temperatures (three tray temperatures for each quality variable) and the corresponding output variables (y_1, y_2, and y_3) are given in Table I.

The LIV-based soft sensors were applied to the Aspen dynamic model of the ADU using MATLAB-Function blocks in Simulink while the proportional-integral plus (PIP) control structure was implemented. PIP is directly derived from Non-Minimum State Space (NMSS) form, which is essential for the True Digital Control (TDC) design. The PIP is considered as an extension to Proportional Integral (PI) and Proportional Integral Derivative (PID) control, but with additional feedback and input compensators introduced by the NMSS State Variable Feedback (SVF) control law. Since PIP control is a sequel to SVF control design, it can be utilized in any state space design method [38, 40].

TABLE I. SELECTED TEMPERATURES AND OUTPUT VARIABLES OF LIV-BASED SOFT SENSORS [37]

Product quality/ Output variable	Setpoint of output variable (°F)	Input variables
95%ASTM-D86 of naphtha (y_1)	385.7	T_4, T_{14} ,T_{28}
95%ASTM-D86 of kerosene (y_2)	502.3	T_{20}, T_{21}, T_{43}
95%ASTM-D86 of gas oil (y_3)	623	T_{32}, T_{34}, T_{43}

Fig. 2 shows the location of the LIV-based soft sensors of the PIP controller and its application to the distillation column. The LIV-based soft sensors were developed at the nominal feed flow rate of 60,000 bbl/day. The detailed prediction results are presented in [37]. As the LIV-based soft sensors have been developed at a constant capacity, feed flow rate variations have a significant impact on the accuracy and reliability of the estimates. Therefore, the prediction performance of LIV-based soft sensors gets reduced. Accordingly, the feed flow rate analysis is discussed in Section II.C.

B. LIV-based soft sensor modeling

The soft sensing model between temperature measurements (secondary variables) and each 95%ASTM-D86 index (primary variable) was identified based on SDP/LIV modeling in the following form [37]:

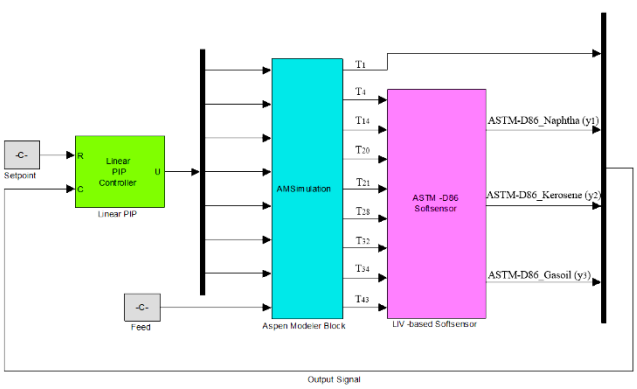

Fig. 2. The LIV-based soft sensors and PIP controller in MATLAB-Simulink [37]

$$\begin{cases} y_t = \sum_{i=1}^{n} a_{i,t} \cdot z_{i,t} + e_t \\ a_{i,t} = a_i\left(x_{1,i,t}, x_{2,i,t}, \ldots, x_{ns_i,i,t}\right) \end{cases}, \quad \forall t, \ e_t = N\left(0, \sigma^2\right) \tag{1}$$

in which y_t is the model output, n is the number of SDPs/regressors, $z_{i,t}$ is the i^{th} regressor, and $a_i(.)$ is the SDP that is a function of the i^{th} correspondent states ($x_{j,i,t}$, $j = 1,2,\ldots,ns_i$). In the case where $a_{i,t}$ is not state-dependent, $ns_i = 0$. e_t is a zero-mean white Gaussian distributed unknown noise with variance σ^2 . In local polynomial modeling combined with the IV concepts, the functionality of each SDP from its corresponding states is defined by a local polynomial in the state variable space, where the parameters of these polynomials are locally estimated by the implementation of IV method. Therefore, $a_{i,t}$ can be defined as,

$$a_{i,t} = \mathbf{S}_{i,t}\mathbf{A}_{i,t} \quad i = 1,2,\ldots,n \tag{2}$$

where $\mathbf{A}_{i,t}$ is the vector of locally constant parameters of the polynomial demonstrating $a_{i,t}$ and $\mathbf{S}_{i,t}$ can be written as,

$$\mathbf{S}_{i,t} = \mathbf{S}_{0,i,t} \otimes \mathbf{S}_{1,i,t} \otimes \mathbf{S}_{2,i,t} \otimes \cdots \otimes \mathbf{S}_{ns_i,i,t} \quad , \quad i = 1,2,\ldots,n \tag{3}$$

and,

$$\mathbf{S}_{j,i,t} = \begin{bmatrix} 1 & x_{j,i,t} & x_{j,i,t}^2 & \cdots & x_{j,i,t}^{q_{j,i}} \end{bmatrix} \quad j = 0,1,2,\ldots,ns_i \tag{4}$$

where $\otimes$ is the Kronecker tensor product symbol and $q_{j,i}$ is the order of polynomial describing $a_{i,t}$ with respect to $x_{j,i,t}$ such that $q_{0,i} = 0$. The number of parameters in $\mathbf{A}_{i,t}$ is obtained by $p_i = \prod_{j=0}^{ns_i}\left(1 + q_{j,i}\right)$. All members of $\mathbf{A}_{i,t}$ are state-dependent functions of $x_{j,i,t}$. Substituting Eq. (2) in Eq. (1) yields the model in vector form as,

$$y_t = \mathbf{z}_t\mathbf{A}_t + e_t \tag{5}$$

where $\mathbf{z}_t$ is the new vector of regressors and $\mathbf{A}_t$ is the vector of the parameters of local polynomials describing each state-dependent parameter. To identify the soft sensing model in the form of Eq. (1), the simulated datasets of input and output variables were established using the Monte Carlo method via linking the MATLAB-Simulink to Aspen dynamic model. The simulated data for building soft sensing models were obtained under the following conditions. The random signals of bounded and varying amplitude (within ±20ºF of the steady-state setpoints as given in Table I) with a nominal feed flow rate of 60,000 bbl/day were introduced as quality variations of side products during simulations. The simulation was performed as long as the steady-state operating condition was achieved (about 20 hr) to obtain the corresponding temperature profile (T_1–T_{43}). It assumes that there are no changes in pressure and tray efficiencies of the column.

A total of 1000 steady-state random data samples were collected and divided into the training dataset (500 samples) and testing dataset (500 samples). All representative temperatures were considered as states in one parameter and the corresponding regressor was chosen as one. In the online implementation of models, the temperatures were sensed and transferred to LIV-based soft sensors and the predicted outputs were taken and used in the PIP controller (see Fig. 2). The SDP method is a well-known modeling method, which was introduced into the field of soft sensing, so readers can refer to our previous papers [35, 37, 41] for more details on the SDP/LIV algorithm.

C. Feed flow rate analysis

Monitoring of control variable is shown that product quality can be affected by feed flow rate variations. Therefore, using only inferential temperature measurements cannot guarantee the desired value of setpoints because the tray temperatures do not correspond exactly to the product quality. Based on the process expert's knowledge, the acceptable operating range for the feed flow rate of the simulated ADU is from 50,000 to 65,000 bbl/day. To investigate the effect of feed flow rate, three simulation runs are conducted by changing the feed flow rate from 60,000 bbl/day to 50,000, 55,000, and 65,000 bbl/day. The input or feed flow rate signal of the ADU model is represented by a Ramp function. During each simulation run, the Ramp block slope and start time are set at ±3360 bbl/hr and 0.5 hr, respectively. The total simulation time is set at 20 hr as is required to reach a steady-state.

The PIP control structure and its parameters are the same as the nominal case (e.g., the feed flow rate of 60,000 bbl/day). The setpoints of the PIP controller are considered similar to the nominal values of 95%ASTM-D86, which are listed in Table I. After the system reached the steady-state condition, the results of product quality obtained by the Aspen IQ inferential quality software package and the LIV-based soft sensors are recorded. Aspen IQ is a built-in inferential sensor in the Aspen technology package, which

makes online implementation and remote monitoring. The 95%ASTM-D86 values produced by Aspen IQ are considered as the "real" values. In each steady-state level, the difference between LIV-based soft sensor and Aspen IQ values or the difference data indicates system deviation from actual conditions.

The data of different flow rates can be efficiently utilized to consider the feed flow disturbances, which can be used to make update terms. An update term allows information about the feed flow rate variations to be included in the soft sensor system to improve the resulting estimates. Accordingly, in the next step, the lookup table method is proposed to develop a flow rate-based corrector using an update term to compensate for varying crude oil flow rates.

D. Lookup table method

Many Simulink models rely upon discrete-valued functions for which the function values are defined as lookup tables. Such discrete-valued functions arise in applications for which no known closed-form algebraic definition exists. The one-dimensional lookup table (1-D) computes an approximated function that the function can be approximated by either a single continuous function or possibly a small number of disjoint continuous functions. Most lookup table blocks have the following interpolation methods available: flat (constant), linear, and cubic spline. Function values are defined as the lookup table between input value (breakpoint) and output value (table data), with an interpolation function used to evaluate intermediate values in the table data [42]. The 1-D lookup table model can be formulated as follows:

$$\Delta y = f(x) \tag{6}$$

In this case, there is one independent variable of feed flow rate (x) and one dependent variable of difference data (Δy), which makes the input-output pair. The first stage of a lookup table operation involves determining input values. The breakpoints of the lookup tables are considered at four levels of feed flow rate including 50,000, 55,000, 60,000, and 65,000 bbl/day, while the table data is different for each byproduct. The second stage involves generating table data that correspond to the supplied breakpoints. The table data can be prepared using the following steps:

1) The dynamic model runs at a flow rate of 60,000 bbl/day (nominal case), and $y_{predicted}$ and $y_{AspenIQ}$ are obtained through LIV-based soft sensors and Aspen IQ, respectively. $y_{predicted}$ and $y_{AspenIQ}$ are considered as 95%ASTM-D86 index of byproducts.
2) The dynamic model runs by varying the feed flow rate from 60,000 bbl/day to 50,000, 55,000, and 65,000 bbl/day, and after the steady-state is achieved, $y_{predicted}$ and $y_{AspenIQ}$ are recorded for each run.
3) Calculate the difference data (Δy) between $y_{predicted}$ and $y_{AspenIQ}$ of each run, which is determined by

   Δy = LIV-based soft sensor value $\left(y_{predicted}\right)$

   - Aspen IQ value $\left(y_{AspenIQ}\right)$

   for all product qualities.

The resulting data are tabulated and finally, the 1-D lookup table is formed with these data and when used in the dynamic model, it will give the update term for any feed flow rate level. Appropriate difference values for any given flow rate level are found by comparing the input flow rate to table data. If the inputs match the values of the flow rate level specified in breakpoint data sets, the block outputs the corresponding values. However, if the inputs fail to match values in the breakpoint data sets, the block performs interpolation between input-output pairs to determine an appropriate output value. In the block parameter dialog box, it can be specified how to compute the output in this situation. Then, the output value must be combined with the predicted values of the LIV-based soft sensor to achieve satisfied prediction performance.

III. Results and Discussion

To investigate the prediction performance of LIV-based soft sensors, a steady-state simulation of the nominal case (e.g., the feed flow rate of 60,000 bbl/day) was performed. The predicted results of the proposed soft sensors for the 95%ASTM-D86 index of three byproducts were compared with the Aspen IQ results through Fig. 3. y_1, y_2, and y_3 are the 95%ASTM-D86 index of naphtha, kerosene, and gas oil, respectively. It can be observed that the predicted quality of all byproducts is close enough to corresponding Aspen IQ values. It should be noticed that the difference between the LIV-based soft sensor and Aspen IQ results is slightly increased from the top product (naphtha) to the bottom product (gas oil) of the column. The difference data for 95%ASTM-D86 of naphtha, kerosene, and gas oil is 0.02% (0.07ºF), 0.04% (0.27ºF) and 0.06% (0.33ºF), respectively. However, in this case, the maximum difference in the 95%ASTM-D86 index is lower than 0.5ºF when the steady-state condition is reached. The reason for this increase in the difference between predicted results is that the complex conditions and internal interaction of the column affect the main variables in the top-down crude oil distillation column

[43]. The aforementioned reasons make the model response more accurate and simpler for naphtha rather than kerosene, and gas oil.

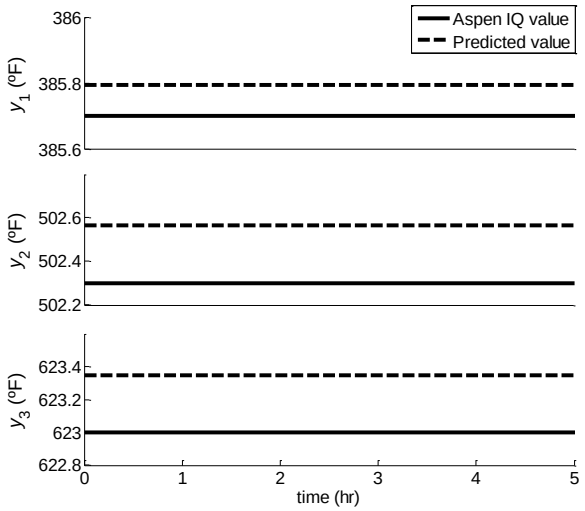

Fig. 3. The steady-state results of LIV-based soft sensors in the PIP control structure at a feed flow rate of 60,000 bbl/day

To investigate the prediction performance of the LIV-based soft sensors against feed flow rate variations, three simulation runs are conducted in the range of acceptable feed flow rate values. The change in feed flow rate from 60,000 bbl/day to 50,000 and 55,000 bbl/day and from 60,000 bbl/day to 65,000 bbl/day is continuously imposed through the Ramp function with the slope of -3360 bbl/hr and +3360 bbl/hr, respectively. While the simulation is run to reach a lower level of flow rates, e.g., a feed flow rate of 50,000 bbl/day, the steady-state parameters from the previous run with a higher flow rate level (e.g., a flow rate of 55,000 bbl/day) are used to initiate new simulation run. Table II shows the results of the LIV-based soft sensors and Aspen IQ, as well as the difference data (Δy) at each crude oil feed flow rate.

The difference data for each byproduct as depicted in Fig. 4 show significant variations when the feed flow rate change is imposed. It can be concluded that Δy values change with both feed flow rate and byproduct type. Fig. 4 shows that there is an almost linear relationship between the difference data and feed flow rate. However, the difference data is increased from the top-down column; in other flow rate levels, the gap between the difference data is also increased from naphtha to gas oil.

TABLE II. THE DIFFERENCE BETWEEN THE PREDICTED VALUES OF THE LIV-BASED SOFT SENSOR AND THE ASPEN IQ VALUES AT DIFFERENT FEED FLOW RATES

Feed flow rate (bbl/day)	Product	$y_{AspenIQ}$ (°F)	$y_{predicted}$ (°F)	Δy (°F)
50,000	Naphtha	385.6978	384.8201	-0.8777
	Kerosene	502.2982	508.7777	6.4795
	Gas oil	622.9988	631.3546	8.3558
55,000	Naphtha	385.6993	385.1145	-0.5848
	Kerosene	502.2996	505.6467	3.3471
	Gas oil	623.0001	627.8317	4.8316
60,000	Naphtha	385.6999	385.7936	0.0937
	Kerosene	502.3000	502.5650	0.265
	Gas oil	623.0000	623.3477	0.3477
65,000	Naphtha	385.7009	386.4092	0.7083
	Kerosene	502.3001	499.4574	-2.8427
	Gas oil	623.0000	614.8229	-8.1771

*Differences are calculated as $\Delta y = y_{predicted} - y_{AspenIQ}$

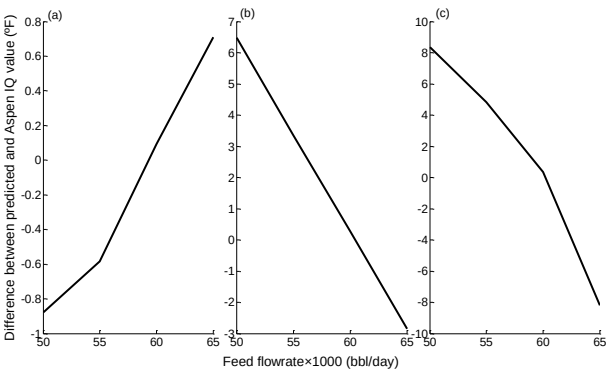

Fig. 4. The difference between the predicted and Aspen IQ values of (a) naphtha, (b) kerosene, and (c) gas oil against feed flow rate variations

In other words, Δy values for naphtha are lower than that for kerosene and gas oil at each flow rate level. The main reason behind this behavior is that the proposed soft sensor models have been developed based on steady-state data at a nominal flow rate of 60,000 bbl/day. Therefore, feed flow rate variations can directly affect the column performance and consequently reduce the prediction performance of the soft sensing system.

An accurate soft sensing system should be able to keep up with the desired product qualities while respecting the process under the variations in the flow rate of the crude oil feed. Accordingly, the lookup table method discussed previously in Section II.D is adopted to solve this issue. The Simulink model of the system is shown in Fig. 5, which includes the modified LIV-based soft sensor with LUT providing the input signal of the PIP control structure.

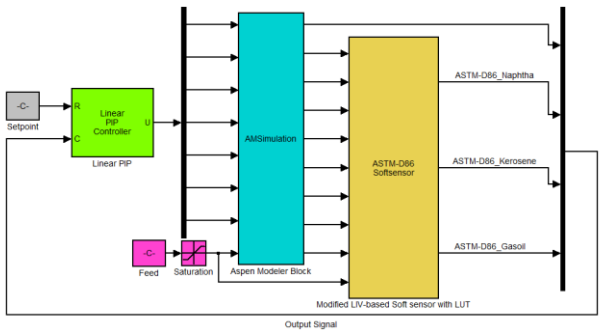

Fig. 5. Modified LIV-based soft sensor with LUT and PIP control structure in MATLAB-Simulink

Lookup table models are constructed individually for each byproduct, as shown in Fig. 6, which includes LUTs along with LIV-based soft sensors. For example, the input values of naphtha LUT are given by [50,000: 55,000: 60,000: 65,000], and the table data are difference values of [-0.8777: -0.5848: 0.0937: 0.7083] as given in Table II.

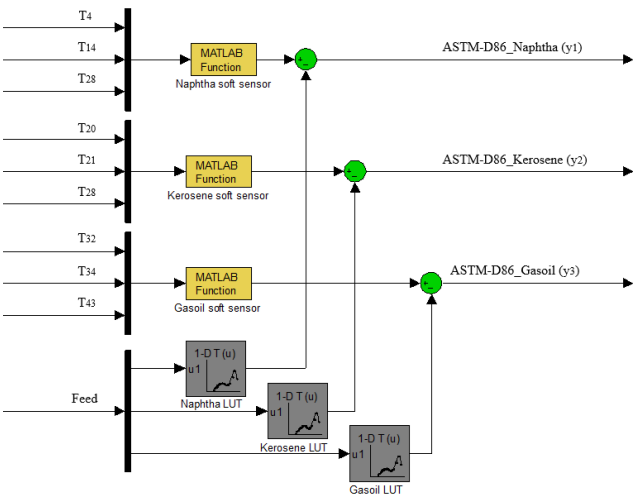

Fig. 6. Lookup table models in soft sensing structure

The kerosene and gas oil LUTs also contain a set of entries as shown in Table II. The linear interpolation method is used to determine the difference data for interpolated values. The modified structure shown in Fig. 6 includes three 1-D lookup tables for each byproduct where the outputs provide Δy values to the corresponding soft sensor for the prediction of product quality. The difference data are augmented to the prediction values of soft sensors to maintain the 95%ASTM-D86 index at the setpoint level. The ease of use in the proposed method can be justified by the fact that the lookup table is a standard library block in Simulink-MATLAB.

The modified Simulink model is run for the nominal case (e.g., a feed flow rate of 60,000 bbl/day) and the results are plotted in Fig. 7. The 95%ASTM-D86 of the various products satisfy the Aspen IQ values with no error. Therefore, LIV-based soft sensors provide good tracking as the error of their prediction is bounded for a bounded disturbance and the prediction converges to the actual quality value. The maximum prediction error for naphtha, kerosene, and gas oil soft sensors are 8.9336×10^{-5}, 2.6160×10^{-6}, and 1.3652×10^{-5}, respectively. The results of the modified soft sensor well match Aspen IQ values and hence the difference is practically zero after reaching the steady-state condition.

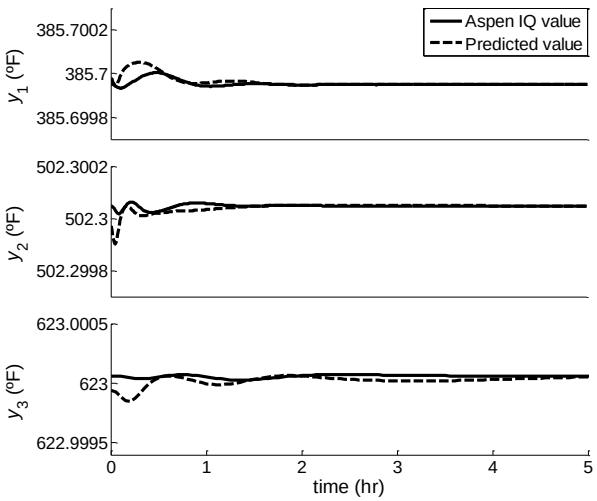

Fig. 7. The steady-state results of the modified LIV-based soft sensors in the PIP control structure at a feed flow rate of 60,000 bbl/day

The modified soft sensor is also tested to verify the prediction results through the simulation of two cases: (1) decreasing the feed flow rate from 60,000 bbl/day to 55,000 bbl/day, and (2) increasing the feed flow rate from 60,000 bbl/day to 65,000 bbl/day. The soft sensing models in both cases are the same. The Simulink models are run by applying a ramp signal of the feed flow rate to the system, whose prediction results are shown in Figs. 8 and 9.

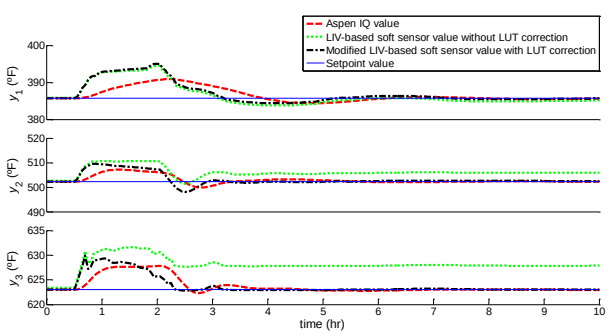

Fig. 8. The prediction results of the LIV-based soft sensor and Aspen IQ with/without LUT against a feed flow rate change from 60,000 bbl/day to 55000 bbl/day (case 1)

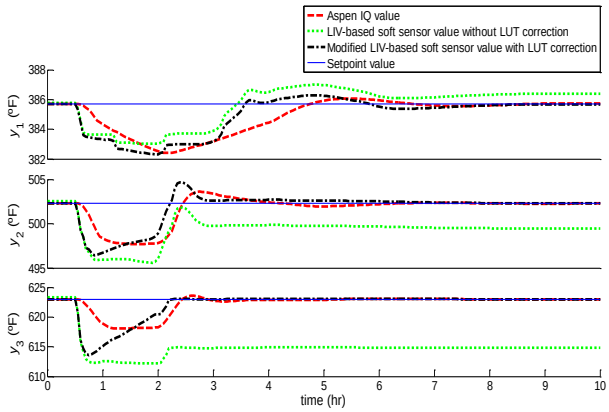

Fig. 9. The prediction results of the LIV-based soft sensor and Aspen IQ with/without LUT against a feed flow rate change from 60,000 bbl/day to 65000 bbl/day (case 2)

In Figs. 8 and 9, the results given by the modified soft sensor are compared to Aspen IQ values and also the results of LIV-based soft sensors without LUTs in each case. It can be seen that both increase and decrease trend were observed in the product qualities within 4 hours, indicating the system instability during the feed flow rate variations. In other words, flow rate level variations cause a transition period in sensing product qualities. However, the modified soft sensor provides good tracking in both cases. Figs. 8 and 9 indicate that the LIV-based soft sensors without LUTs do not provide a reliable estimate and fail to precisely match setpoint values even when the system reaches the steady-state condition. There is a significant difference between LIV-based soft sensors without LUT and Aspen IQ values, especially for kerosene and gas oil.

However, after applying the LUTs, the new difference values (Δy) are practically zero for naphtha, kerosene, and gas oil, which means that the predicted values are well-matched to Aspen IQ as well as setpoint values in both cases. Accordingly, the prediction results of modified LIV-based soft sensors are more reliable than LIV-based soft sensors. It is obvious that the modified model has the capability to operate efficiently within the feed flow rate range of 55,000-65,000 bbl/day.

The efficiency of the proposed method is its low computational complexity and processing time since the lookup tables are pre-calculated and stored in a MATLAB data file as a part of the simulation initialization phase or even stored in hardware in application platforms. The lookup table is an array that replaces runtime computation with a simpler array indexing operation. Moreover, the common method of reducing computational complexity in engineering applications is to use lookup tables [44]. The advantage of using the lookup table is that it is not time-consuming. As can be identified from Figs. 8 and 9, there is no delay in the prediction results of modified LIV-based soft sensors compared with Aspen IQ values.

IV. CONCLUSION

The modification of LIV-based soft sensor models for online monitoring of 95%ASTM-D86 index in the atmospheric distillation unit (ADU) has been addressed by incorporating the lookup table (LUT) method. The proposed LIV-based soft sensors were developed based on tray temperature measurement at a nominal feed flow rate of 60,000 bbl/day and applied to the Aspen dynamic model of the ADU using MATLAB-Simulink. In order to investigate the effect of feed flow rate changes, three simulation runs were carried out by varying the feed flow rate from 60,000 bbl/day to 50,000, 55,000, and 65,000 bbl/day. For each flow rate level, the prediction results of LIV-based soft sensors and Aspen inferential quality (IQ) were recorded when steady-state conditions were reached. The results show that difference values between LIV-based soft sensors and Aspen inferential quality (IQ) change either with the feed flow rate or with the byproduct type. Lookup tables were developed based on the feed flow rate and difference values and augmented with LIV-based soft sensor models in the PIP control structure. The results present improvement in the predictions of LIV-based soft sensors as well as acceptable control performance in feed flow rate variations. Therefore, the proposed update term using lookup tables is suitable for implementation in the advanced monitoring scheme due to simplicity and low computational time. It is important to emphasize that soft sensing models need not be retrained in feed flow rate variations using the lookup table method. Accordingly, this method can be easily combined with different soft sensing algorithms, including the effect of changes in influencing process variables.

ACKNOWLEDGMENT

Technical support from Shiraz Refinery, Shiraz, Iran is gratefully acknowledged.

DECLARATION OF COMPETING INTEREST

The authors declare that they have no known competing financial interests or personal relationships that could have appeared to influence the work reported in this paper.

A MATLAB-Simulink implementation file is available on request.

REFERENCES

[1] V. Kumar, A. Sharma, I. R. Chowdhury, S. Ganguly, and D. N. Saraf, "A crude distillation unit model suitable for online applications," *Fuel Processing Technology*, Vol. 73, No. 1, pp. 1-21, 2001.

[2] *ASTM D86: standard test method for distillation of petroleum products at atmospheric pressure*, 2010.

[3] T. Chatterjee and D. N. Saraf, "On-line estimation of product properties for crude distillation units," *Journal of Process Control*, vol. 14, No. 1, pp. 61–77, 2004.

[4] D. Wang, J. Liu, and R. Srinivasan, "Data-driven soft sensor approach for quality prediction in a refining process," *IEEE TRANSACTIONS ON INDUSTRIAL INFORMATICS*, vol. 6, No. 1, pp. 11-17, 2010.

[5] A. C. Serfidan, F. Uzman, and M. Turkay, "Optimal estimation of physical properties of the products of an atmospheric distillation column using support vector regression," *Computers and Chemical Engineering*, Vol. 134, p. 106711, 2020.

[6] C. M. Pappalardo and D. Guida, "System identification algorithm for computing the modal parameters of linear mechanical systems," *Machines* Vol. 6, No. 2, p. 12, 2018.

[7] B. Roset and H. Nijmeijer, "Observer-based model predictive control," *International Journal of Control*, Vol. 77, No. 17, pp. 1452-1462, 2006.

[8] P. Kadlec, B. Gabrys, and S. Strandt, "Data-driven soft sensors in the process industry," *Computers and Chemical Engineering*, Vol. 33, No. 4, pp. 795–814, 2009.

[9] H. Singh, A. K. Pani, and H. K. Mohanta, "Quality monitoring in petroleum refinery with regression neural network: Improving prediction accuracy with appropriate design of training set," *Measurement*, Vol. 134, pp. 698-709, 2019.

[10] H. A. Behrooz, "Robust set-point optimization of inferential control system of crude oil distillation units," *ISA Transactions*, Vol. In Press, Corrected Proof, 2019.

[11] F. Griesing-Scheiwe, Y. A. W. Shardt, G. Pérez-Zuñiga, and X. Yang, "Soft sensor design for variable time delay and variable sampling time," *Journal of Process Control*, Vol. 92, pp. 310-318, 2020.

[12] L. Fortuna, S. Graziani, A. Rizzo, and M. G. Xibilia, *Soft sensors for monitoring and control of industrial processes*. New York: Springer, 2007.

[13] H. J. Galicia, Q. P. He, and J. Wang, "A reduced order soft sensor approach and its application to a continuous digester," *Journal of Process Control*, Vol. 21, No. 4, pp. 489–500, 2011.

[14] J. Liu, "Developing a soft sensor based on sparse partial least squares with variable selection," *Journal of Process Control*, Vol. 24, No. 7, pp. 1046-1056, 2014.

[15] K. Zheng and K. Funatsu, "Partial constrained least squares (PCLS) and application in soft sensor," *Chemometrics and Intelligent Laboratory Systems*, Vol. 177, pp. 64-73, 2018.

[16] Z. Ge, "Mixture Bayesian Regularization of PCR Model and Soft Sensing Application," *IEEE Transactions on Industrial Electronics*, Vol. 62, No. 7, pp. 4336-4343, 2015.

[17] Z. Ge, C. Yang, and Z. Song, "Improved kernel PCA-based monitoring approach for nonlinear processes," *Chemical Engineering Science*, Vol. 64, No. 9, pp. 2245–2255, 2009.

[18] X. Shi and W. Xiong, "LWS based PCA subspace ensemble model for soft sensor development," *IFAC-PapersOnLine*, Vol. 51, No. 18, pp. 649-654, 2018.

[19] L. Fortuna, P. Giannone, S. Graziani, and M. G. Xibilia, "Virtual instruments based on stacked neural networks to improve product quality monitoring in a refinery," *IEEE Transactions on Instrumentation and Measurement*, Vol. 56, No. 1, pp. 95-101, 2007.

[20] J. C. B. Gonzaga, L. A. C. Meleiro, C. Kiang, and R. M. Filho, "ANN-based soft-sensor for real-time process monitoring and control of an industrial polymerization process," *Computers & Chemical Engineering*, Vol. 33, No. 1, pp. 43-49, 2009.

[21] K. Sun, S.-h. Huang, S.-S. Jang, and D. S.-H. Wong, "Development of soft sensor with neural network and nonlinear variable selection for crude distillation unit process," *Computer Aided Chemical Engineering*, Vol. 38, pp. 337-342, 2016.

[22] N. Bakhtadze, E. M. Maximov, and R. T. Valiakhmetov, "Fuzzy soft sensors for chemical and oil refining processes," *IFAC Proceedings Volumes*, Vol. 41, No. 2, pp. 46-50, 2008.

[23] E. AbdulJalee and K. Aparna, "Neuro-fuzzy Soft Sensor Estimator for Benzene Toluene Distillation Column," *Procedia Technology*, Vol. 25, pp. 92-99, 2016.

[24] T. Zhao, P. Li, and J. Cao, "Soft sensor modeling of chemical process based on self-organizing recurrent interval type-2 fuzzy neural network," *ISA Transactions*, Vol. 84, pp. 237-246, 2019.

[25] P. V. C. Souza, "Fuzzy neural networks and neuro-fuzzy networks: A review the main techniques and applications used in the literature," *Applied Soft Computing*, Vol. 92, p. 106275, 2020.

[26] P. Jain, I. Rahman, and B. D. Kulkarni, "Development of a soft sensor for a batch distillation column using support vector regression techniques," *Chemical Engineering Research and Design*, Vol. 85, No. 2, pp. 283–287, 2007.

[27] Y. Liu and J. Chen, "Integrated soft sensor using just-in-time support vector regression and probabilistic analysis for quality prediction of multi-grade processes," *Journal of Process Control*, Vol. 23, No. 6, pp. 793–804, 2013.

[28] S. Herceg, Ž. U. Andrijić, and N. Bolf, "Development of soft sensors for isomerization process based on support vector machine regression and dynamic polynomial models," *Chemical Engineering Research and Design*, Vol. 149, pp. 95-103, 2019.

[29] Q. Li, Q. Du, W. Ba, and C. Shao, "Multiple-input multiple-output soft sensors based on KPCA and MKLS-SVM for quality prediction in atmospheric distillation column," *International Journal of Innovative Computing, Information and Control*, Vol. 8, No. 12, pp. 8215-8230, 2012.

[30] Q. Jiang and X. Yan, "Weighted kernel principal component analysis based on probability density estimation and moving window and its application in nonlinear chemical process monitoring," *Chemometrics and Intelligent Laboratory Systems*, Vol. 127, pp. 121–131, 2013.

[31] X. Zhang, Q. Zhu, Z.-Y. Jiang, Y. He, and Y. Xu, "A novel ensemble model using PLSR integrated with multiple activation functions based ELM: Applications to soft sensor development," *Chemometrics and Intelligent Laboratory Systems*, Vol. 183, pp. 147-157, 2018.

[32] H. Liu, C. Yang, M. Huang, and C. Yoo, "Soft sensor modeling of industrial process data using kernel latent variables-based relevance vector machine," *Applied Soft Computing*, Vol. 90, p. 106149, 2020.

[33] P. C. Young, "The data-based mechanistic approach to the modelling, forecasting and control of environmental

systems," *Annual Reviews in Control*, Vol. 30, No. 2, pp. 169–182, 2006.
[34] H. Gharehbaghi and J. Sadeghi, "A novel approach for prediction of industrial catalyst deactivation using soft sensor modeling," *Catalysts*, Vol. 6, No. 7, pp. 93-109, 2016.
[35] B. Bidar, J. Sadeghi, F. Shahraki, and M. M. Khalilipour, "Data-driven soft sensor approach for online quality prediction using state dependent parameter models," *Chemometrics and Intelligent Laboratory Systems*, Vol. 162, pp. 130–141, 2017.
[36] P. C. Young, *Recursive estimation and time-series analysis*, Second ed. New York: Springer, 2011.
[37] B. Bidar, M. M. Khalilipour, F. Shahraki, and J. Sadeghi, "A data-driven soft-sensor for monitoring ASTM-D86 of CDU side products using local instrumental variable (LIV) technique," *Journal of the Taiwan Institute of Chemical Engineers*, Vol. 84, pp. 49-59, 2018.
[38] M. M. Khalilipour, J. Sadeghi, F. Shahraki, and K. Razzaghi, "Nonsquare multivariable non-minimal statespace-proportional integral plus (NMSS-PIP) controlfor atmospheric crude oil distillation column," *Chemical Engineering Research and Design*, Vol. 113, pp. 140-150, 2016.
[39] M. M. Khalilipour, F. Shahraki, J. Sadeghi, and k. Razzaghi, "Control Structure Design and Dynamic Modeling for Atmospheric Distillation Column: Effect of Increase Capacity," *International Journal of Industrial Electronics, Control and Optimization*, Vol. 1, No. 2, pp. 103-113, 2018.
[40] J. Sadeghi, "Modelling and control of non-linear systems using State-Dependent Parameter (SDP) models and Proportional-Integral-Plus (PIP) control method," Doctor of Philosophy, Centre for Research on Environmental System and Statistics, Lancaster University, United Kingdom, 2006.
[41] B. Bidar, F. Shahraki, J. Sadeghi, and M. M. Khalilipour, "Soft Sensor Modeling Based on Multi-State-Dependent Parameter Models and Application for Quality Monitoring in Industrial Sulfur Recovery Process," *IEEE Sensors Journal*, Vol. 18, No. 11, 2018.
[42] A. B. Hocking, M. A. Aiello, J. C. Knight, S. Shiraishi, M. Yamaura, and N. Arechiga, "Proving Properties of Simulink Models that Include Discrete Valued Functions," *SAE World Congress and Exhibition*, 2016.
[43] J. J. Macias, P. Angelov, and X. Zhou, "A method for predicting quality of the crude oil distillation," in *International Symposium on Evolving Fuzzy Systems*, Ambleside, UK, IEEE, pp. 214–220, 2006.
[44] W. Zhang, X. Chen, K. Cui, T. Xie, and N. Yuan, "DOA Estimation for Coprime Linear Array Based on MI-ESPRIT and Lookup Table," *Sensors*, Vol. 18, No. 9, pp. 1-11, 2018.

Bahareh Bidar received her bachelor's degree in chemical engineering from the Ferdowsi University of Mashhad, Iran, in 2007 and her master's and Ph.D. degrees in chemical engineering process design from the University of Sistan and Baluchistan, Iran in 2012 and 2018, respectively. Her main areas of research interest are process modeling and simulation, especially in soft sensor design for chemical process, process identification and control. She is currently an assistant professor in the chemical engineering department at the University of Sistan and Baluchestan.

Mir Mohammad Khalilipour received his bachelor's degree in chemical engineering from Quchan University in 2004 and his master's and Ph.D. degrees in chemical engineering process design from the University of Sistan and Baluchistan, Iran in 2008 and 2016, respectively. He has been involved in safety management industrial projects for many Iranian oil and gas refineries from 2008 to 2011. He is currently an assistant professor at the Chemical Engineering Department, the University of Sistan and Baluchestan. His research interests are chemical safety, control, and process simulation especially with a focus on practical interesting of control, and soft sensors in chemical processes.

Farhad Shahraki received his B.S. degree in chemical engineering from the University of Sistan and Baluchestan, Zahedan, Iran in 1989, his M.S. degree in chemical engineering from Tarbiat Modares University, Tehran, Iran in 1992, and his Ph.D. degree in chemical engineering from The University of Manchester, Manchester, the U.K. in 2001. He is currently a professor of chemical engineering at the University of Sistan and Baluchestan. His research interests include process integration, process modeling, and optimization.

Jafar Sadeghi received his B.S. in chemical engineering from the Isfahan University of Technology, Isfahan, Iran, his M.S. degree in chemical engineering from the Sharif University of Technology, Tehran, Iran and his Ph.D. degree in chemical engineering from University of Lancaster, the U.K. in 1991, 1995, and 2007, respectively. He is currently an associate professor at the University of Sistan and Baluchestan, Zahedan, Iran. His research interests cover process modeling and simulation, process control, process identification, process intensification, automation, and instrumentation.

International Journal of Industrial Electronics, Control and Optimization © 2021 IECO
Vol. 4, No. 2, pp. 221-234, April (2021)

Woodpecker Mating Algorithm for Optimal Economic Load Dispatch in a Power System with Conventional Generators

Morteza Karimzadeh Parizi[1, †], Farshid Keynia[2], Amid Khatibi Bardsiri[3]

[1,3] Department of Computer Engineering, Kerman Branch, Islamic Azad University, Kerman, Iran.
[2] Department of Energy Management and Optimization, Institute of Science and High Technology and Environmental Sciences, Graduate University of Advanced Technology, Kerman, Iran.

ABSTRACT

Economic Dispatch (ED) is one of the most important optimization problems in power systems. The ultimate goal of ED is to minimize the cost of power generation operations. In this paper, the Woodpecker Mating Algorithm (WMA) is used to solve the ED problem considering the nonlinear properties of generators such as valve point effects (VPE), prohibited operating zones (POZ), ramp rate limits, multiple fuel options, and transmission loss. The WMA algorithm is a novel metaheuristic algorithm inspired by the mating behavior of woodpeckers and sound intensity (a physical quantity). The WMA is implemented on six test systems of different operational dimensions and characteristics to show its capacity for solving the ED problem. The results are compared with the latest and most efficient methods introduced in the literature. Proving the efficiency of the WMA to solve the ED problem, simulation results are promising and offer the optimal fuel cost of production.

Article Info

Keywords:
Economic Dispatch, Nonlinear Optimization, Valve Point Effects, Woodpecker Mating Algorithm.

Article History:
Received 2020-07-21
Accepted 2020-12-10

I. INTRODUCTION

Today, with the increasing demand for electricity, we are facing an increase in the price of fuel produced. Therefore, it is essential to bring down power production costs and develop a reliable operating system for electric generators [1]. The Economic Dispatch is one of the most important optimization problems in electric power systems, which aims to determine the optimal allocation for all generating units located in the circuit, meet the required power demand with the lowest possible operating costs and production fuel, and eliminate all restrictions on the operation of power systems [2].

The ultimate goal of the ED problem is to minimize the cost of operations in a power generation system while supplying the power requirements [3]. Optimal load distribution can help maximize the capacity of thermal units, reduce production costs, and improve system reliability and stability [1, 4, 5].

The ED problem has become a constrained and distributed optimization problem with a nonlinear, discontinuous, non-convex, non-smooth, non-differential, and multi-modal cost function, despite the presence of valve point effects (VPE), prohibited operating zones (POZ), ramp rate limits, multiple fuel options, power balance constraint, and transmission loss [2, 6-8]. Therefore, it is challenging for classical optimization methods to obtain the global optimum for solving the ED problem [4]. These challenges include falling trapped in a local optimum, slow convergence, sensitivity, dependence on the initial starting point, and low accuracy due to linearity [2, 9-11].

[†]**Corresponding Author**: Mkarimzadeh313@gmail.com
Tel: 09135860688, Department of Computer Engineering, Kerman Branch, Islamic Azad University, Kerman, Iran.

TABLE I
NOMENCLATURE

ED problem	
a_i, b_i, c_i	Fuel cost coefficients of unit *i*
e_i, f_i	Fuel cost coefficients of unit *i* considering valve-point effects
a_{ij}, b_{ij}, c_{ij}	Fuel cost coefficients for fuel type *j* of unit *i*
e_{ij}, f_{ij}	Fuel cost coefficients for fuel type *j* of unit *i* considering valve-point effects
B_{ij}, B_{0i}, B_{00}	B-matrix coefficients for transmission power loss
d	The total number of generating units
P_D	The total system load demand
P_L	The total transmission loss
P_i	The output power of unit *i*
P_i^{max}	The maximum output power of unit *i*
P_i^{min}	The minimum output power of unit *i*
$P_{i,z}^{l}$	The lower bound for prohibited zone z of unit *i*
$P_{i,z-1}^{u}$	The upper bound for prohibited zone z of unit *i*
$F_i(P_i)$	Fuel cost function of generator *i*
DR_i	The rise border values of the ramp rate limits
UR_i	The fall border values of the ramp rate limits
WMA algorithm	
P_S	Sound wave energy at the sound source
r	Euclidean distance to the sound source.
x_i^t	Current position of the *i*th woodpecker in iteration *t*
r_1, r_2, r_3, R	The random numbers
δ_i^t	The random factor for the *i*th woodpecker in iteration t
α_{gpop}	The step size of a female woodpecker toward gpop
α_{mj}	The step size of a female woodpecker toward *m*th male
x_{gpop}^t	Position of the best member of the population in iteration *t*
x_{mj}^t	The *j*th male woodpecker population in iteration *t*
t	Current iteration
t_{max}	The maximum number of iterations
$Tansig$	Tangent sigmoid function
RA	Running away function
RRA	Random Running away
GRA	Gpop Running away
$H\alpha$	The highest level α
N	Population size of woodpeckers
x_{RRA}^i	The position of a new element obtained from RRA on the *i*th woodpecker
lb	Lower bound of the variables
ub	Upper bound variables
x_{GRA}^i	The position of a new element obtained from GRA on the ith woodpecker
GRA_{bit}	Binary vector as long as the problem dimensions.
x_r	The position of the random woodpecker

Given the above-mentioned issues, metaheuristic optimization algorithms have attracted many researchers due to their high flexibility and efficiency for solving a wide range of ED problems [7, 9]. For instance, particle swarm optimization (PSO) [12, 13], grey wolf optimization (GWO) [14], modified crow search algorithm (MCSA) [15], charged system search algorithm (CSS), adaptive charged system search algorithm (ACSS) [16], improved bird swarm algorithm (IBSA) [17], dual-population adaptive differential evolution (DPADE) [18], two-stage artificial bee colony (TSABC) [19], chaotic improved harmony search algorithm (CIHSA) [20], distance-based firefly algorithm (DFA) [21], island bat algorithm (IBA) [22], chaotic bat algorithm (CBA) [23], backtracking search algorithm (BSA) [24], moth flame optimizer (MFO) [25], water cycle algorithm (WCA) [26], orthogonal learning competitive swarm optimizer (OLCSO) [27], improved fireworks algorithm with chaotic sequence operator (IFWA-CSO) [28], krill herd algorithm (KHA) and opposition-based krill herd algorithm (OKHA) [29], improved differential evolution (IDE) [30], exchange market algorithm (EMA) [11], chaotic teaching-learning-based optimization (CTLBO) [2], genetic algorithm (GA) [31], ant lion optimizer (ALO) [32], and root tree optimization algorithm (RTO) [33] have been employed to solve the ED problem.

Besides, drawing on the advantages of the evolutionary process, an artificial cooperative search algorithm (ACS) [34] has been developed to estimate the global optimum accurately for different types of complex ED problems. In [35], a novel metaheuristic algorithm named TFLWO, inspired by whirlpools created in turbulent water flows, was proposed to solve the ED problem. In [1], AGWO was proposed as the augmented version of the GWO algorithm by adding random local search mechanisms, opposite based learning (OBL), and random global exploration to solve the ED problem. In [36], the ED problem was solved by using the modified version of PSO. This algorithm includes the mutation operator, self-adaptive regulation of social parameters, and control of the inertia weight parameter (ω) by using fuzzy rules. The improved version of PSO, known as IPSO, benefits from sequences of chaos mixed with the linear reduction of parameter (ω) and the crossover operator [37]. Moreover, another method of solving the ED problem by metaheuristic algorithms is PPSO in which the PSO parameters are tuned with $phasor(\theta)$ [38]. In the recent decade, many researchers have been interested in combining metaheuristic optimization algorithms to increase efficiency and improve proposed solutions to the ED problem. For instance, the DE algorithm was combined with the quantum PSO to develop the DE-CQPSO method [39], and HPSO-MVO algorithm hybridized PSO and Multi-Verse Optimizer (MVO) [40]. The MPSO-GA algorithm combined PSO with the GA algorithm [41] and the HAAA [42], algorithm hybridized artificial algae algorithm (AAA) and simplex search method (SSM) to solve the ED problem.

This paper proposes a novel metaheuristic algorithm, named the WMA, to solve the ED problem. The WMA is inspired by the mating behavior of woodpeckers and the concept of sound intensity [43]. This algorithm has many mechanisms to effectively implement exploration and exploitation phases and strike a balance between these two phases. Since the parameters of this algorithm are regulated self-adaptively, it has the potential to solve engineering design optimization and real-world problems. The WMA is employed in this study to solve a wide range of system tests in the ED problem with a high level of nonlinearity and complexity assessment in the presence of operational constraints and limitations on

generators. The results are then compared with a series of the latest and most efficient methods introduced in the research literature.

The rest of this paper consists of different sections. Section II presents the ED problem formulation. Section III introduces the WMA algorithm. In Section IV, the WMA implementation is explained to solve the ED problem. Section V reports the results of solving the evaluated test systems. Finally, conclusions are made in Section VI. In addition, Table I lists the nomenclatures of this paper.

II. ED PROBLEM MATHEMATICAL FORMULATION

A. Two types of fuel costs function for ED problem

The fuel costs of the thermal units are obtained from Eq. (1).

$$F_t = \sum_{i-1}^{d} F_i(P_i) = \sum_{i-1}^{d} (\alpha_i P_i^2 + b_i P_i + c_i) \quad (1)$$

where P_i is the production power of the *i*th power generator, F_i (p) is the fuel cost of the *i*th power generator, and *d* shows the number of power plants. Moreover, the coefficients of the *i*th power generator units are indicated by α_i, b_i, and c_i. In ED, the production powers of the power plants are changed to minimize the cost function proposed as Eq. (1) (fuel consumption cost). Also, the cost function is not quadratic in the ED. Real generators are affected as long as steam valves are open, and the cost function is transformed into Eq. (2) by considering the valve point effect.

$$F_t = \sum_{i-1}^{d} (\alpha_i P_i^2 + b_i P_i + c_i + e_i * \left| sin\left(f_i * \left(P_i^{min} - P_i\right)\right)\right|) \quad (2)$$

where e_i and f_i are the valve point loading coefficients of the *i*th power generator and p_i^{min} is the possible lowest production power of the *i*th generator.

B. Multiple fuel options

Since fuels of many thermal generators are supplied from different fuel sources such as coal, oil, and natural gas, the most profitable type of fuel should be selected within a specific area of work [6]. In this case, Eq. (1) and (2) will be transformed into Eq. (3) and (4).

$$F_i(P_i) = \begin{cases} \alpha_{i1}(P_i)^2 + b_{i1}(P_i) + c_{i1} \; if \; P_i^{min} \le P_i \le P_{i1} \\ \alpha_{i2}(P_i)^2 + b_{i2}(P_i) + c_{i2} \quad if \; P_{i1} \le P_i \le P_{i2} \\ \alpha_{ik}(P_i)^2 + b_{ik}(P_i) + c_{ik} \; if \; P_{ik-1} \le P_i \le P_i^{max} \end{cases} \quad (3)$$

$$F_i(P_i): \begin{cases} if \; P_i^{min} \le P_i \le P_{i1} \\ \alpha_{i1}(P_i)^2 + b_{i1}(P_i) + c_{i1} + \left| e_{i1} \times sin\left(f_{i1} \times \left(P_i^{min} - P_i\right)\right)\right| \\ if \; P_{i1} \le P_i \le P_{i2} \\ \alpha_{i2}(P_i)^2 + b_{i2}(P_i) + c_{i2} + \left| e_{i2} \times sin\left(f_{i2} \times (P_{i2} - P_i)\right)\right| \\ if \; P_{ik-1} \le P_i \le P_i^{max} \\ \alpha_{ik}(P_i)^2 + b_{ik}(P_i) + c_{ik} + \left| e_{ik} \times sin\left(f_{ik} \times (P_{ik} - P_i)\right)\right| \end{cases} \quad (4)$$

where $a_{i,k}, b_{i,k}, c_{i,k}, e_{i,k}, f_{i,k}$ are the cost coefficients of the *i*th generator by using the *k*th type of fuel.

C. Transmission loss function

In an extensive interconnected network for long-distance power transmission across areas with low-load densities, the transmission loss is an essential factor affecting the optimal distribution of power. The loss is usually expressed as a quadratic function of the production power of a generator. The transmission loss is obtained by Eq. (5).

$$P_L = \sum_{i=1}^{d} \sum_{j=1}^{d} (P_i B_{ij} P_j) + \sum_{i=1}^{d} B_{0i} P_i + B_{00} \quad (5)$$

where P_L is the power loss of a network and B_{0i}, B_{ij}, and B_{00} are the loss coefficients.

D. Power balance constraint

The total production power is equal to the summation of total power demanded and total transmission loss (Eq. (6)).

$$\sum_{i=1}^{d} P_i = P_D + P_L \quad (6)$$

where $\sum_{i=1}^{d} P_i$ is the total power (T_P) generated by all of the generators, and P_D and P_L are the demanded network power and the loss network power, respectively.

E. The value of power generation constraint

The active power generation output of each thermal power unit should vary within its minimum power permitted and maximum power permitted. The value of the power generation constraint is expressed as Eq. (7).

$$P_i^{min} \le P_i \le P_i^{max} \quad (7)$$

where p_i^{min} and p_i^{max} are the potential minimum and maximum power production of the *i*th generator, respectively.

F. Prohibited operating zone (POZ)

Due to work constraints in some cases, power plants are unable to generate power in all ranges between the minimum and maximum powers. These areas, in which production is impossible, are called the prohibited operating zone (POZ) and can be shown as Eq. (8).

$$P_i \in \begin{cases} P_i^{min} \le P_i \le P_{j,1}^{l} \\ P_{i,z-1}^{u} \le P_i \le P_{i,z}^{l} \;\; z = 2,3, \ldots, pz_i \\ P_{i,pz_i}^{u} \le P_i \le P_i^{max} \end{cases} \quad (8)$$

where $P_{i,z-1}^{u}$ and $P_{i,z}^{l}$ show the upper and lower limits of the *z*th POZ for the *i*th power generation unit, respectively and pz_i is the number of POZs for the *i*th power generation unit.

G. Ramp rate limits

The physical limitation on and off of the generators limits the rate of change in production, as shown below. Increasing production is limited to the values obtained from Eq. (9).

$$P_i - P_i^0 \le UR_i \quad (9)$$

Similarly, the reduction constraint is defined as Eq. (10).

$$P_i^0 - P_i \le DR_i \quad (10)$$

where P_i^0 refers to the power in the previous stage and DR_i and UR_i shows ofare the down-ramp limit and up-ramp rate limit of the *i*th generating unit, respectively. Eq. (9) and (10) can be combined to express the power production range of a unit in the form of Eq. (11).

$$P_i - P_i^0 \le UR_i \; and \; P_i^0 - P_i \le DR_i \quad (11)$$

III. WOODPECKER MATING ALGORITHM (WMA)

Recently, the metaheuristic WMA proposed here has been inspired by the mating behavior of red-bellied woodpeckers [43, 44]. The main metaphor in the algorithm is the drumming sound of male woodpeckers made to attract female ones. The WMA has also been inspired by the notion of sound wave intensity in physics. It is a cross algorithm that includes two groups, *i.e.*, male and female woodpeckers. The female woodpeckers are the main search factors, whereas the male ones are the best positions already explored by them. In fact, the female woodpeckers are attracted by the drumming sounds made by the male ones. The level of attraction depends on the quality of the received sound in proportion to sound intensity. This quantity is expressed by Eq. (12).

$$I = \frac{P_S}{4\pi r^2} \quad (12)$$

where P_S is the sound wave energy at the sound source and r is the hearer's Euclidean distance to the sound source.

In the WMA, each female woodpecker updates its position according to Eq. (13).

$$x_i^{t+1} = x_i^t + r_1 * \frac{\delta_i^t * \left(\alpha_{gpop} * (x_{gpop}^t - x_i^t) + \alpha_{mj} * (x_{mj}^t - x_i^t)\right)}{2} \quad (13)$$

where x_i^t represents the current position of the *i*th woodpecker in iteration t, x_{gpop}^t indicates the position of the best member of the population, x_{mj}^t denotes the *j*th male woodpecker, r_1 shows a random number from a normal distribution in the range [0, 1], and δ_i^t is a random factor for the *i*th woodpecker in iteration *t*, the value of which is self-tuned during the iteration cycle using Eq. (14). The parameter α (α_{gpop}, α_{mj}) is obtained by Eq. (15). In WMA, each female woodpecker may update its position as affected by drumming from the best member of the population and the male woodpecker at the shortest distance from it. That is what x_{mj}^t refers to in this Eq.

$$\delta_i^t = r_2 * Tansig\left(1 - \frac{t}{t_{max}}\right) \quad (14)$$

where r_2 is a random number of a normal distribution in [0, 3], Tansig represents the tangent sigmoid function, *t* indicates the number of the current iteration, and t_{max} is the maximum number of iterations. If $\delta > 1$, the search factors diverge from the target point, which leads to exploration. If $\delta \le 1$, the female woodpeckers converge toward the male ones, which leads to exploitation.

$$\alpha = \frac{1}{1 + SI_j^i} \quad (15)$$

where α represents the attractiveness of the *j*th male woodpecker to the *i*th female woodpecker, and SI_j^i indicates the sound intensity of the target (*j*th) woodpecker heard by the female (*i*th) one. In addition, α is the step size of a female woodpecker, specifying how close it can reach the corresponding male woodpecker

In the WMA, the RA function has been considered for stochastic moves of the factors when the drumming sounds are overloaded, the woodpecker is attacked, etc. The function includes the two operators RRA and GRA, only one of which is run for each woodpecker in each generation proportionately to the corresponding value of α, based on Eq. (16). The value of Hα is calculated using Eq. (17) in the first iteration.

$$RA = \begin{cases} RRA & if \; \alpha \ge H\alpha \\ GRA & else \end{cases} \quad (16)$$

$$H\alpha = 0.8 * \frac{\sum_1^{n-1} \alpha_{gpop}^i}{N-1} \quad (17)$$

where N is the population size of woodpeckers and $H\alpha$ is the highest level α.

RRA is a totally stochastic move across the search space that is focused directly on exploration. It is implemented using Eq. (18).

$$x_{RRA}^i = lb - (lb - ub) * r_3 \quad (18)$$

where x_{RRA}^i is the position of a new element obtained from RRA on the *i*th woodpecker, lb represents the lower bound of the variables, ub indicates their upper bound, and r_3 is a random number from a normal distribution in the range [0, 1].

The GRA operator causes stochastic changes in some of the variables concerning the female woodpeckers based on the best male one and the position of another random woodpecker. The operator is applied based on Eq. (19).

$$x_{GRA}^i = x_i^t + GRA_{bit} * \left\{\left(x_{gpop}^t - x_r\right) * R\right\} \quad (19)$$

where x_{GRA}^i is the position of a new element obtained from GRA on the *i*th woodpecker, R is random numbers from a random distribution in the range [-1, 1], x_r is the position of the random woodpecker, x_i^t is that of the *i*th female woodpecker, and x_{gpop}^t is the position of the best woodpecker throughout the population. Also, GRA_{bit} is a binary vector as long as the problem dimensions.

IV. WMA ALGORITHM APPLIED TO ED

In this section, the steps of the proposed model for solving the ED problem are provided. In other words, we would explain how to adapt WMA for ED problems. Also, Fig. 1 shows the flowchart of the proposed model.

Step 1: The population of woodpeckers is initialized randomly based on the lower and upper bounds of the production power of each active generator. In fact, each woodpecker is a potential solution in the form of a vector and each item of this algorithm is considered the proposed production power for a corresponding active generator. The magnitude of this vector is equal to the number of active generators in the studied power system. In this step, if a woodpecker does not comply with the terms of the operational and production restrictions of the ED problem and the proposed answer has a violation, it will be reinitialized. With this strategy, the initial population of woodpeckers will be inside a favorable area.

Step 2: The fitness (the generation fuel cost) is calculated

for each candidate solution in the population of woodpeckers using Eq. (3) and (4). The fitness value reflects the distance of each female woodpecker to the male woodpecker.

Step 3: The population of woodpeckers is sorted based on the generation fuel cost and divided into two categories of male and female woodpeckers. In each generation, the fittest search agents are chosen to be marked as male woodpeckers.

Step 4: In the population of woodpeckers, each member updates its position based on Eq. (13) and/or RA function. In fact, the position of the search agents is a potential power generation plan for the generators.

Step 5: In this step, the feasibility of the candidate solutions regarding the equality and inequality constraints of POZ, ramp rate limits, minimum and maximum generation limit, and the load balance equality constraint (Eq. (6)) are investigated. In cases of upper and lower limits of power generation, as well as ramp rate limits, if the recommended power is less than the acceptable power generation range, the value is shifted to the minimum acceptable value. Conversely, if the power generation of an agent is more than the acceptable range, this value is shifted to the maximum acceptable value.

In this paper, the penalty function is used to handle the equality constraint of the load balance (Eq. (20)). In fact, adding the penalty term to the cost function turns the constraint into an inequality constraint, which can then be handled. In this case, if a solution does not satisfy the equality constraint, the cost would be non-zero and the added penalty term would increase the cost function, which woul lead to its elimination. Conversely, in cases where the equality constraint is satisfied, violation (V) would be zero. Therefore, the optimal generation cost stays the same.

$$F_i(P_i)_{penalty} = F_i(P_i) \times (1 + \varphi \times \mathrm{V}) \quad (20)$$

where $F_i(P_i)_{penalty}$ is the fuel cost defined based on the penalty function and $F_i(P_i)$ is the fuel cost. φ, the penalty coefficient, is a relatively large positive real number that is defined as the penalty of an infeasible solution. Its value depends on the complexity of the search space and the optimization problem and is determined via trial and error. V indicates the degree to which a solution violates the constraints of the problem, which is a number in the range [0,1]. The larger the error is, the greater the penalty of the infeasible solution would be. The value V is determined using Eq. (21).

$$\mathrm{V} = max\left(\left\{1 - \frac{T_P - P_L}{P_D}\right\}, 0\right) \quad (21)$$

where max is the maximum operator, and T_P, P_L, and P_D are the total generated power, transmission loss, and the load demand of the network, respectively.

Steps 3 and 5 will be repeated until the termination conditions are met for the WMA. Finally, the best solution with the least fuel cost would be chosen as the most optimal power generation plan for the generators and the output of the algorithm.

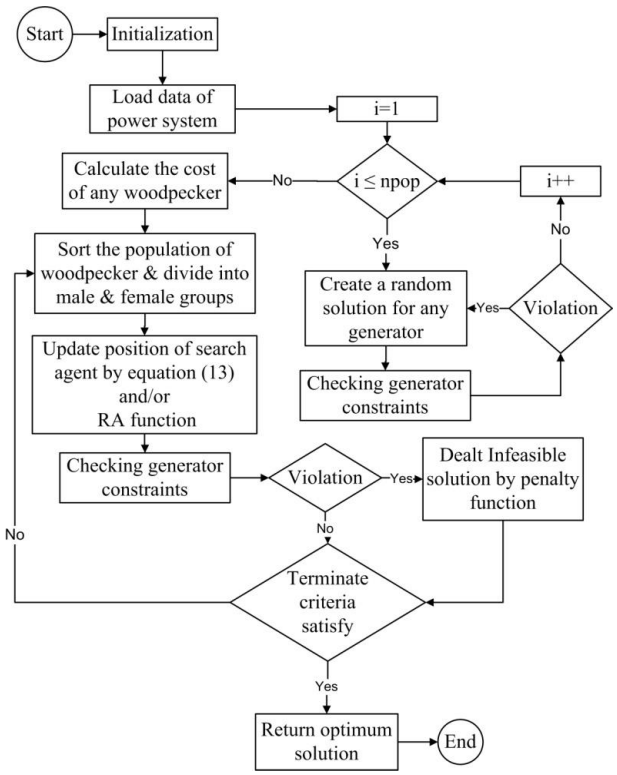

Fig. 1. The flowchart of the proposed model.

V. CASE STUDIES AND EXPERIMENTAL RESULTS

In this section, the WMA is implemented and evaluated on six different real-world test systems for electrical power engineering design. In all the tests, there were 50 woodpeckers with 200 possible iterations. The WMA was executed 50 times separately on each test system to report the average (avg), best (B), and worst (W) solutions. All tests were performed on a system with a processor Intel Core™ i7–7500U 2.7 GHz and an 8GB RAM DDR4. All tests were run in MATLAB 2017a. The characteristics of the power test systems are summarized in Table II and the details of the generator unit data are given in the appendix.

TABLE II
CHARACTERISTICS OF SIX DIFFERENT TEST SYSTEMS

Characteristics	Case 1	Case 2	Case 3	Case4	Case 5	Case 6
VPE					❖	❖
Transmission lost	❖	❖	❖			
POZ	❖	❖			❖	
Ramp rate limits	❖	❖			❖	
multiple fuel options					❖	❖
Unit number	6	15	20	38	140	10
P_D	1263	2630	2500	6000	49342	2700

A. *Test System 1*

This test was conducted to analyze a real system including six thermal generators by considering POZ and ramp rate limits, as well as the transmission loss and a quadratic cost

function. The total load demand is considered $P_D = 1263$ MW. The operational characteristics of this test system including fuel cost coefficients and generator capacities are listed in [45]. Table III compares the statistical results of WMA with a series of methods introduced in the literature. Accordingly, the WMA algorithm produced the lowest production fuel cost of all of the evaluated methods by outperforming other compared algorithms. The optimum and feasible dispatch of generators and transmission loss obtained by the WMA in this power system are tabulated in Table IV.

TABLE III
COMPARISON OF STATISTICAL RESULTS OF THE OPTIMIZATION METHODS FOR THE TEST SYSTEM 1

Methods	B ($/h)	Ave ($/h)	W ($/h)	Time
WMA	15443.0796	15443.0796	15443.0799	0.103
PSO [36]	15450.0000	15454.0000	15450.0000	NA
MCSA [15]	15449.1672	15449.2358	15449.3854	NA
NAPSO[36]	15443.7657	15443.7657	15443.7657	NA
FAPSO[36]	15445.2440	15448.0520	15451.6300	NA
CSS [16]	15448.3972	15557.8899	16616.3788	1.04
ACSS [16]	15443.5562	15458.2023	15490.6899	1.08
HBB [46]	15444.2600	15446.4600	15448.8900	5.6554
IDPSO[12]	15449.8900	15450.7000	NA	0.727

* Time is the average time (s) of simulation and NA is not available.

B. *Test System 2*

This section evaluates a system composed of 15 generators. This test system includes POZ, ramp rate limits, and transmission loss. The physical properties of these generators are presented in [6]. This power system had a quadratic cost function with total load demand $P_D = 2630$ MW. Table V presents the statistical results of testing Test System 2 through the WMA. Moreover, Table 5 draws a comparison between the WMA results and those of other methods proposed to solve the ED problem. Accordingly, the WMA algorithm yielded much more optimal and better results at lower fuel costs. These results prove the ability of the WMA to solve complex ED problems. The optimum and feasible dispatch of the generators and transmission loss obtained by the WMA in Test System 2 are tabulated in Table VI.

TABLE IV
OPTIMAL DISPATCH RESULTS OF THE WMA ALGORITHM FOR TEST SYSTEM 1

Generators						
P1-P6	447.34	173.28	263.38	138.90	165.42	87.12
T_P (MW)	1275.45	P_L(MW)	12.45	Violation: 0.0		

C. *Test System 3*

Test System 3 includes 20 thermal generators with quadratic cost functions and total load demand $P_D = 2500$ MW. This test system considers the transmission loss. the operational properties of thermal generators and the information on the transfer network loss are mentioned in [6]. Table VII shows the statistical results of Test System 3 with the WMA algorithm and draws a comparison between the WMA results and those of ADE-MMS [6], FMLP [7], HOSMEPO [47], IEAM-R[48], IA_EDP [49], and CBA [23]. Accordingly, the WMA yielded a lower fuel cost than other methods. As a result, the WMA outperformed all of the other compared algorithms. The optimum dispatch of the generators and transmission loss obtained by the WMA in this power system are presented in Table VIII.

TABLE V
COMPARISON OF STATISTICAL RESULTS OF THE OPTIMIZATION METHODS FOR TEST SYSTEM 2

Methods	B ($/h)	Ave ($/h)	W ($/h)	Time
WMA	32679.0	32679.1	32679.3	0.127
CS-CLM [50]	32704.5	32704.5	32704.5	0.225
C-MIMO-CSO [51]	32701.2	32701.2	32701.2	2. 72
IODPSO-G [52]	32692.4	32692.4	32692.4	NA
IODPSO-l [52]	32692.4	32692.4	32692.4	NA
WCA [26]	32704.4	32704.5	32704.5	NA
OLCSO [27]	32692.4	32692.4	32692.4	3.5
CSS [16]	32693.3	32798.4	32971.1	2.5
IBSA [17]	32703.7	32703.8	32704.1	NA
ICA [53]	32715.4	NA	NA	NA

TABLE VI
OPTIMAL DISPATCH RESULTS OF THE WMA ALGORITHM FOR TEST SYSTEM 2

Generators					
P1-P5	455	455	130	130	240.107
P6-P10	460	465	60	25	25.0036
P11-P15	77.2848	79.9977	25	15	15
T_P (MW): 2657.3931		P_L (MW): 27.3931		Violation: 0.0	

TABLE VII
COMPARISON OF STATISTICAL RESULTS OF THE OPTIMIZATION METHODS FOR THE TEST SYSTEM 3

Methods	B($/h)	Ave($/h)	W ($/h)	Time
WMA	62448.141	62448.748	62450.731	0.453
ADE-MMS	62456.507	62456.638	62457.061	NA
FMLP	62456.633	NA	NA	3.154
HOSMEPO	62453.490	NA	NA	NA
IEAM-R	62452.861	NA	NA	NA
IA_EDP	62466.804	62487.511	62528.987	1.928
CBA	62456.6328	62456.6348	62501.6714	1.16

TABLE VIII
OPTIMAL DISPATCH RESULTS OF THE WMA ALGORITHM FOR TEST SYSTEM 3

Generators					
P1-P5	512.005	170.009	126.325	102.596	113.783
P6-P10	74.5664	115.068	116.257	99.5265	105.952
P11-P15	150.473	292.617	120.657	31.0146	115.195
P16-P20	36.2376	66.7766	88.7096	99.0573	54.7075
T_P (MW): 2591.5331		P_L: 91.5331		Violation: 0.0	

D. *Test System 4*

This section evaluates a power system with 38 thermal generators and a quadratic cost function. The total load demand of this test system is $P_D = 6000$ MW, and the transfer line loss was disregarded. The operational properties of this test system are mentioned in [1]. Table IX presents the statistical results of the WMA on Test System 4 and compares

the performance of the WMA with that of the ADE-MMS [6], AGWO [1], GWO [3], MHS [54], and IDE [30]. Accordingly, the WMA managed to have a lower fuel cost than other methods by outperforming them significantly. As a result, the WMA can solve complex ED problems. The optimum dispatch of the generators obtained by the WMA in this power system is tabulated in Table X.

TABLE IX
COMPARISON OF STATISTICAL RESULTS OF THE OPTIMIZATION METHODS FOR TEST SYSTEM 4

Methods	B($/h)	Ave($/h)	W($/h)	Time
WMA	9025100.059	9025103.675	9025110.682	1.178
ADE-MMS	9417235.787	9417235.789	9417235.793	NA
AGWO	9417226.000	9417229.000	9417231.000	NA
GWO	9419270.188	9419978.978	9421100.000	9.457
EP-EPSO	9387925.497	NA	NA	NA
IDE	9417235.786	9417235.786	9417235.786	9.149

TABLE X
OPTIMAL DISPATCH RESULTS OF THE WMA ALGORITHM FOR TEST SYSTEM 4

Generators					
P1-P5	435.451	418.073	388.040	499.999	423.757
P6-P10	439.917	400.778	414.469	114.051	114.115
P11-P15	144.912	119.063	110	90.1284	82
P16-P20	120.008	159.679	65.690	65.030	271.986
P21-P25	271.991	259.382	125.012	10.5565	108.278
P26-P30	84.109	39.487	26.5991	20.0002	20
P31-P35	20.6661	20.115	25.499	18	8
P36-P38	25.149	20	20.006		
T_P (MW): 6000			Violation: 0.0		

E. *Test System 5*

The most extensive and complicated test system, evaluated in this paper, is a large-scale power system including 140 power generators named the Korean system. This system includes VPE, POZ, ramp rate limits, and multiple fuel options with total load demand P_D =49342 MW. The transfer network loss is disregarded in this test system. It is a fossil fuel-based power system, comprising 40 thermal generating units, 51 gas units, 20 nuclear units, and 29 oil units. Out of the 140 units, 6 thermal units, 4 gas units, and 2 oil units have non-convex fuel cost function addressing valve loading effects, and some units having prohibited operating zones. The operational properties of this test system are mentioned in [6]. Table XI shows the statistical results of the WMA in solving Test System 5 and draws a comparison between the best results of the WMA and the other methods proposed in the research literature. Accordingly, the WMA managed to obtain the lowest fuel cost. The more optimal solution provided by the WMA algorithm proves its superiority and efficiency in comparison with all of the other evaluated algorithms. The optimum dispatch of the generators obtained by the WMA in this power system is tabulated in Table XII.

TABLE XI
COMPARISON OF STATISTICAL RESULTS OF THE OPTIMIZATION METHODS FOR TEST SYSTEM 5

Methods	B($/h)	Ave($/h)	W ($/h)	Time
WMA	1559682.1	1559684.0	1559688.1	2.44
AGWO [1]	1559708.0	1559708.0	1559709.0	NA
CS-CLM [50]	1559848.4	1559908.5	1559993.2	11.9
CL_CLM [50]	1559708.4	1559708.4	1559708.4	9 .25
AAA [42]	1559909.0	1560060.8	1560303.0	166
HAAA [42]	1559710.0	1559712.9	1559731.0	112
C- CSO [51]	1559712.0	1559715.7	1559734.0	32.3
OGWO [14]	1559709.9	1559713.2	1559743.5	41.8
GWO[14]	1559953.2	1560132.9	1560228.4	45.5
KHA [29]	1560173.9	1560176.7	1560177.9	30.5
OKHA [29]	1560146.9	1560148.9	1560149.9	25.7

TABLE XII
OPTIMAL DISPATCH RESULTS OF THE WMA ALGORITHM FOR TEST SYSTEM 5

Generators					
P1-5	115	188.99	190	190	168.55
P6- 10	190	490	490	496	496
P11- 15	496	496	506	509	506
P16- 20	505	506	506	505	505
P21- 25	505	505	505	505	536.9
P26- 30	536.9	549	549	501	501
P31-35	506	505.9	505.98	505.98	500
P36-40	499.97	241	241	774	768.98
P41-45	3	3	250	245.9	250
P46-50	250	240.95	249.98	249.98	250
P51-55	165	165	165	165	180
P56-60	180	103	198	311.98	281.17
P61-65	163	95	160	160	490
P66-70	197	490	489.99	130	234.80
P71-75	137	325.44	195	175	175.00
P76-80	175	175	330	530.96	530.99
P81-85	397	56	115.01	115.03	115
P86-90	207	207.00	175	175.00	175.00
P91-95	175	579.24	647	984	977.99
P96-100	681.89	720	717.58	719.9	964
P101-105	957.86	1006.79	1005.5	1013	1019.99
P106-110	954	951.99	1006	1012.99	1020.97
P111-115	1014	95	95	94	244
P116-120	244.00	244	95.00	95.00	116
P121-125	175	2	4	15	9
P126-130	12	10	112	4	5
P131-135	5	50.00	5	42	42
P136-140	41	17	7	7	26
T_P: 49342		Violation: 0.0			

F. *Test System 5*

This power system includes 10 generators with the effects of valve point effect, multiple fuel options, and disregarding the transfer line loss. The load demand of this test system P_D = 2700 MW. The physical properties of the generators and multiple fuel options information of the thermal units are mentioned in [31]. The optimum dispatch of the generators, fuel type, and fuel cost obtained by the WMA in this power system are tabulated in Table XIII. Table XIV shows the statistical results of executing Test System 6 through the WMA and compares the results of the WMA algorithm with the other methods proposed to solve the ED problem. Accordingly, the WMA yielded much more optimal and better results at the lowest fuel cost. These results prove that the

WMA can solve complex ED problems.

TABLE XIII
OPTIMAL DISPATCH RESULTS OF THE WMA ALGORITHM FOR TEST SYSTEM 6

Generators					
P1-P5	215.52	214.25	281.45	242.39	276.9
Fuel type	2	1	1	3	1
P6-P10	237.25	292.94	239.3	424.68	275.3
Fuel type	3	1	3	3	1
T_P (MW): 2700			Violation : 0.0		

TABLE XIV
COMPARISON OF STATISTICAL RESULTS OF THE OPTIMIZATION METHODS FOR TEST SYSTEM 6

Methods	B($/h)	Ave($/h)	W ($/h)	Time
WMA	623.544	623.56	623.58	0.868
PPSO [9]	623.83	623.84	623.85	NA
M2 [55]	623.81	623.81	NA	0.59
TFWO [35]	623.83	623.84	623.85	NA
CTPSO [37]	623.83	623.88	623.83	3.2
NAPSO [36]	623.62	623.63	623.68	2.8
FAPSO [36]	624.22	624.28	624.30	5.9
DPADE [18]	623.82	623.82	623.82	10.34
C-CSO [51]	623.83	623.83	623.83	9.261
MCSA [15]	623.83	623.83	623.85	NA
SDP [56]	623.81	NA	NA	NA
IPSO-G [52]	623.83	623.84	623.83	NA
IPSO-l [52]	623.83	623.83	623.83	NA
TSABC [19]	623.83	623.85	623.87	2.32

Fig. 2 in the Appendix shows the convergence diagram of the WMA algorithm of all evaluated systems. As can be seen, in all evaluated systems, the WMA showed a fast, smooth, and steady convergence.

VI. CONCLUSION

The ED problem is one of the most fundamental optimization problems in power engineering. Optimizing this problem can reduce the production cost and increase the reliability of power generators. In this paper, the WMA algorithm is employed to solve the ED problem by considering the operational conditions and production constraints of different generators such as valve point effect, multiple fuel options, ramp rate limits, prohibited operating zone, and power balance constraint, as well as the loss over the power transmission line. The WMA algorithm is inspired by the mating behavior of woodpeckers and the physics law of sound intensity. The WMA is evaluated on six real-world test systems and then compared with a series of novel and efficient methods proposed in the research literature. The WMA managed to yield promising results at the lowest fuel cost among all other methods. The simulation results prove the ability and efficiency of the WMA in solving the complex ED problem. This algorithm can solve other real-world optimization and power engineering design problems as well.

Appendix

TABLE XV
DATA FOR TEST SYSTEM 1

$Unit_i$	P_i^{min}	P_i^{max}	a_i	b_i	c_i	UR_i	DR_i	P_i^0	POZ
1	100	500	240	7	0.0070	80	120	440	[210,240] [350,380]
2	50	200	200	10	0.0095	50	90	170	[90,110][140,160]
3	80	300	220	8.5	0.0090	65	100	200	[150,170][210,240]
4	50	150	200	11	0.0090	50	90	150	[80,90][110,120]
5	50	200	220	10.5	0.0080	50	90	190	[90,110][140,150]
6	50	120	190	12	0.0075	50	90	110	[75,85][100,105]

TABLE XVI
DATA FOR TEST SYSTEM 2

$Unit_i$	P_i^{min}	P_i^{max}	a_i	b_i	c_i	UR_i	DR_i	P_i^0	POZ
1	150	455	671	10.1	0.000299	80	120	400	
2	150	455	574	10.2	0.000183	80	120	300	[185,225][305,335][420,450]
3	20	130	374	8.80	0.001126	130	130	105	
4	20	130	374	8.80	0.001126	130	130	100	
5	150	470	461	10.40	0.000205	80	120	90	[180,200][305,335][390,420]
6	135	460	630	10.10	0.000301	80	120	400	[230,255][365,395][430,455]
8	60	300	227	11.2	0.000338	65	100	95	
9	25	162	173	11.2	0.000807	60	100	105	
10	25	160	175	10.7	0.001203	60	100	110	
11	20	80	186	10.2	0.003586	80	80	60	
12	20	80	230	9.90	0.005513	80	80	40	[30,40][55,65]
13	25	85	225	13.1	0.000371	80	80	30	
14	15	55	309	12.1	0.001929	55	55	20	
15	15	55	323	12.4	0.004447	55	55	20	

TABLE XVII
DATA FOR TEST SYSTEM 3

$Unit_i$	P_i^{min}	P_i^{max}	a_i	b_i	c_i	$Unit_i$	P_i^{min}	P_i^{max}	a_i	b_i	c_i
1	150	600	0.00068	18.2	1000	11	100	300	0.005	16.69	800
2	50	200	0.00071	19.3	970	12	150	500	0.003	16.76	970
3	50	200	0.0065	19.8	600	13	40	160	0.009	17.36	900
4	50	200	0.005	19.1	700	14	20	130	0.005	18.7	700
5	50	160	0.00738	18.1	420	15	25	185	0.004	18.7	450
6	20	100	0.00612	19.3	360	16	20	80	0.071	14.26	370
7	25	125	0.0079	17.1	490	17	30	85	0.009	19.14	480
8	50	150	0.00813	18.9	660	18	30	120	0.007	18.92	680
9	50	200	0.00522	18.3	765	19	40	120	0.006	18.47	700
10	30	150	0.00573	18.9	770	20	30	100	0.008	19.79	850

TABLE XVIII
DATA FOR TEST SYSTEM 4

$Unit_i$	P_i^{min}	P_i^{max}	a_i	b_i	c_i	$Unit_i$	P_i^{min}	P_i^{max}	a_i	b_i	c_i
1	220	550	0.3133	797	64782	20	120	272	0.492	696.1	39197
2	220	550	0.3133	797	64782	21	120	272	0.573	660.2	45576
3	200	500	0.3127	796	64670	22	110	260	0.357	803.2	28770
4	200	500	0.3127	796	64670	23	80	190	0.942	818.2	36902
5	200	500	0.3127	796	64670	24	10	150	52.12	33.5	105510
6	200	500	0.3127	796	64670	25	60	125	1.142	805.4	22233
7	200	500	0.3127	796	64670	26	55	110	2.028	707.1	30953
8	200	500	0.3127	796	64670	27	35	75	3.074	833.6	17044
9	114	500	0.7075	916	172832	28	20	70	16.77	2188.7	81079
10	114	500	0.7075	916	172832	29	20	70	26.36	1024.4	124767
11	114	500	0.7515	884	176003	30	20	70	30.58	837.1	121915
12	114	500	0.7083	884	173028	31	20	70	25.1	1305.2	120780
13	110	500	0.4211	1250	91340	32	20	60	33.72	716.6	104441
14	90	365	0.5145	1299	63440	33	25	60	23.92	1633.9	83224
15	82	365	0.5691	1299	65468	34	18	60	32.56	969.6	111281
16	120	325	0.5691	1291	77282	35	8	60	18.36	2625.8	64142
17	65	315	2.5881	238	190928	36	25	60	23.92	1633.9	103519
18	65	315	3.8734	1150	285372	37	20	38	8.482	694.7	13547
19	65	315	3.6842	1269	271676	38	20	38	9.693	655.9	13518

TABLE XIX
DATA FOR TEST SYSTEM 5 (C: COAL, O: OIL, N: NUCLEAR, L: LNG)

$Unit_i$	a_i	b_i,	c_i	P_i^{min}	P_i^{max}	UR_i	DR_i	P_i^0	$Unit_i$	a_i	b_i,	c_i	P_i^{min}	P_i^{max}	UR_i	DR_i	P_i^0
C01	0.032888	61.242	1220.645	71	119	30	120	98.4	L44	0.014382	93.966	3174.939	207	307	120	180	252.0
C02	0.008280	41.095	1315.118	120	189	30	120	134.	L45	0.013161	94.723	3218.359	207	307	120	180	221.
C03	0.003849	46.310	874.288	125	190	60	60	141.5	L46	0.016033	66.919	3723.822	175	345	318	318	245.9
C04	0.003849	46.310	874.288	125	190	60	60	183.3	L47	0.013653	68.185	3551.405	175	345	318	318	247.9
C05	0.042468	54.242	1976.469	90	190	150	150	125.0	L48	0.028148	60.821	4322.615	175	345	318	318	183.6
C06	0.014992	61.215	1338.087	90	190	150	150	91.3	L49	0.013470	68.551	3493.739	175	345	318	318	288.0
C07	0.007039	11.791	1818.299	280	490	180	300	401.1	C01	0.000064	2.842	226.799	360	580	18	18	557.4
C08	0.003079	15.055	1133.978	280	490	180	300	329.5	N02	0.000252	2.946	382.932	415	645	18	18	529.5
C09	0.005063	13.226	1320.636	260	496	300	510	386.1	N03	0.000022	3.096	156.987	795	984	36	36	800.8
C10	0.005063	13.226	1320.636	260	496	300	510	427.3	N04	0.000022	3.040	154.484	795	978	36	36	801.5
C11	0.005063	13.226	1320.636	260	496	300	510	412.2	N05	0.000203	1.709	332.834	578	682	138	204	582.7
C12	0.003552	14.498	1106.539	260	496	300	510	370.1	N06	0.000198	1.668	326.599	615	720	144	216	680.7
C13	0.003901	14.651	1176.504	260	506	600	600	301.8	N07	0.000215	1.789	345.306	612	718	144	216	670.7
C14	0.003901	14.651	1176.504	260	509	600	600	368.0	N08	0.000218	1.815	350.372	612	720	144	216	651.7
C15	0.003901	14.651	1176.504	260	506	600	600	301.9	N09	0.000193	2.726	370.377	758	964	48	48	921.0
C16	0.003901	14.651	1176.504	260	505	600	600	476.4	N10	0.000197	2.732	367.067	755	958	48	48	916.8
C17	0.002393	15.669	1017.406	260	506	600	600	283.1	N11	0.000324	2.651	124.875	750	1007	36	54	911.9
C18	0.002393	15.669	1017.406	260	506	600	600	414.1	O05	0.030266	64.125	4965.124	244	379	480	480	318.4
C19	0.003684	14.656	1229.131	260	505	600	600	328.0	O06	0.030266	64.125	4965.124	244	379	480	480	335.8
C20	0.003684	14.656	1229.131	260	505	600	600	389.4	O07	0.024027	76.129	2243.185	95	190	240	240	151.0
C21	0.003684	14.656	1229.131	260	505	600	600	354.7	O08	0.001580	81.805	2290.381	95	189	240	240	129.5
C22	0.003684	14.656	1229.131	260	505	600	600	262.0	O09	0.022095	81.140	1681.533	116	194	120	120	130.0
C23	0.004004	14.378	1267.894	260	505	600	600	461.5	O10	0.076810	46.665	6743.302	175	321	180	180	218.9
C24	0.003684	14.656	1229.131	260	505	600	600	371.6	O11	0.953443	78.412	394.398	2	19	90	90	5.4
C25	0.001619	16.261	975.926	280	537	300	300	462.6	O12	0.000044	112.09	1243.165	4	59	90	90	45.0
C26	0.005093	13.362	1532.093	280	537	300	300	379.2	O13	0.072468	90.871	1454.740	15	83	300	300	20.0
C27	0.000993	17.203	641.989	280	549	360	360	530.8	O14	0.000448	97.116	1011.051	9	53	162	162	16.3
C28	0.000993	17.203	641.989	280	549	360	360	391.9	O15	0.599112	83.244	909.269	12	37	114	114	20.0
C29	0.002473	15.274	911.533	260	501	180	180	480.1	O16	0.244706	95.665	689.378	10	34	120	120	22.1
C30	0.002547	15.212	910.533	260	501	180	180	319.0	O17	0.000042	91.202	1443.792	112	373	**1080**	**1080**	125.0
C31	0.003542	15.033	1074.810	260	506	600	600	329.5	O18	0.085145	104.50	535.553	4	20	60	60	10.0
C32	0.003542	15.033	1074.810	260	506	600	600	333.8	O19	0.524718	83.015	617.734	5	38	66	66	13.0
C33	0.003542	15.033	1074.810	260	506	600	600	390.0	O20	0.176515	127.79	90.966	5	19	12	6	7.5
C34	0.003542	15.033	1074.810	260	506	600	600	432.0	O21	0.063414	77.929	974.447	50	98	300	300	53.2
C35	0.003132	13.992	1278.460	260	500	660	660	402.0	O22	2.740485	92.779	263.810	5	10	6	6	6.4
C36	0.001323	15.679	861.742	260	500	900	900	428.0	O23	0.112438	80.950	1335.594	42	74	60	60	69.1

Table XIX (CONTINUED)

$Unit_i$	a_i	b_i,	c_i	P_i^{min}	P_i^{max}	UR_i	DR_i	P_i^0	$Unit_i$	a_i	b_i,	c_i	P_i^{min}	P_i^{max}	UR_i	DR_i	P_i^0
C37	0.002950	16.542	408.834	120	241	180	180	178.4	O24	0.041529	89.073	1033.871	42	74	60	60	49.9
C38	0.002950	16.542	408.834	120	241	180	180	194.1	O25	0.000911	161.29	1391.325	41	105	528	528	91.0
C39	0.000991	16.518	1288.815	423	774	600	600	474.0	O26	0.005245	161.83	4477.110	17	51	300	300	41.0
C40	0.001581	15.815	1436.251	423	769	600	600	609.8	O27	0.234787	84.972	57.794	7	19	18	30	13.7
L01	0.902360	75.464	669.988	3	19	210	210	17.8	O28	0.234787	84.972	57.794	7	19	18	30	7.4
L02	0.110295	129.544	134.544	3	28	366	366	6.9	O29	1.111878	16.087	1258.437	26	40	72	120	28.
L01	0.024493	56.613	3427.912	160	250	702	702	224.3	L44	0.014382	93.966	3174.939	207	307	120	180	252.0
L02	0.029156	54.451	3751.772	160	250	702	702	210.0	L45	0.013161	94.723	3218.359	207	307	120	180	221.0
L03	0.024667	54.736	3918.780	160	250	702	702	212.0	L46	0.016033	66.919	3723.822	175	345	318	318	245.9
L04	0.016517	58.034	3379.580	160	250	702	702	200.8	L47	0.013653	68.185	3551.405	175	345	318	318	247.9
L05	0.026584	55.981	3345.296	160	250	702	702	220.0	L48	0.028148	60.821	4322.615	175	345	318	318	183.6
L06	0.007540	61.520	3138.754	160	250	702	702	232.9	L49	0.013470	68.551	3493.739	175	345	318	318	288.0
L07	0.016430	58.635	3453.050	160	250	702	702	168.0	C01	0.000064	2.842	226.799	360	580	18	18	557.4
L08	0.045934	44.647	5119.300	160	250	702	702	208.4	N02	0.000252	2.946	382.932	415	645	18	18	529.5
L09	0.000044	71.584	1898.415	165	504	1350	1350	443.9	N03	0.000022	3.096	156.987	795	984	36	36	800.8
L10	0.000044	71.584	1898.415	165	504	1350	1350	426.0	N04	0.000022	3.040	154.484	795	978	36	36	801.5
L11	0.000044	71.584	1898.415	165	504	1350	1350	434.1	N05	0.000203	1.709	332.834	578	682	138	204	582.7
L12	0.000044	71.584	1898.415	165	504	1350	1350	402.5	N06	0.000198	1.668	326.599	615	720	144	216	680.7
L13	0.002528	85.120	2473.390	180	471	1350	1350	357.4	N07	0.000215	1.789	345.306	612	718	144	216	670.7
L14	0.000131	87.682	2781.705	180	561	720	720	423.0	N08	0.000218	1.815	350.372	612	720	144	216	651.7
L15	0.010372	69.532	5515.508	103	341	720	720	220.0	N09	0.000193	2.726	370.377	758	964	48	48	921.0
L16	0.007627	78.339	3478.300	198	617	2700	2700	369.4	N10	0.000197	2.732	367.067	755	958	48	48	916.8
L17	0.012464	58.172	6240.909	100	312	1500	1500	273.5	N11	0.000324	2.651	124.875	750	1007	36	54	911.9
L18	0.039441	46.636	9960.110	153	471	1656	1656	336.0	N12	0.000344	2.798	130.785	750	1006	36	54	898.0
L19	0.007278	76.947	3671.997	163	500	2160	2160	432.0	N13	0.000690	1.595	878.746	713	1013	30	30	905.0
L20	0.000044	80.761	1837.383	95	302	900	900	220.0	N14	0.000650	1.503	827.959	718	1020	30	30	846.5
L21	0.000044	70.136	3108.395	160	511	1200	1200	410.6	N15	0.000233	2.425	432.007	791	954	30	30	850.9
L22	0.000044	70.136	3108.395	160	511	1200	1200	422.7	N16	0.000239	2.499	445.606	786	952	30	30	843.7
L23	0.018827	49.840	7095.484	196	490	1014	1014	351.0	N17	0.000261	2.674	467.223	795	1006	36	36	841.4
L24	0.010852	65.404	3392.732	196	490	1014	1014	296.0	N18	0.000259	2.692	475.940	795	1013	36	36	835.7
L25	0.018827	49.840	7095.484	196	490	1014	1014	411.1	N19	0.000707	1.633	899.462	795	1021	36	36	828.8
L26	0.018827	49.840	7095.484	196	490	1014	1014	263.2	N20	0.000786	1.816	1000.367	795	1015	36	36	846.0
L27	0.034560	66.465	4288.320	130	432	1350	1350	370.3	O01	0.014355	89.830	1269.132	94	203	120	120	179.0
L28	0.081540	22.941	13813.001	130	432	1350	1350	418.7	O02	0.014355	89.830	1269.132	94	203	120	120	120.8
L29	0.023534	64.314	4435.493	137	455	1350	1350	409.6	O03	0.014355	89.830	1269.132	94	203	120	120	121.0
L30	0.035475	45.017	9750.750	137	455	1350	1350	412.0	O04	0.030266	64.125	4965.124	244	379	480	480	317.4
L31	0.000915	70.644	1042.366	195	541	780	780	423.2	O05	0.030266	64.125	4965.124	244	379	480	480	318.4
L32	0.000044	70.959	1159.895	175	536	1650	1650	428.0	O06	0.030266	64.125	4965.124	244	379	480	480	335.8
L33	0.000044	70.959	1159.895	175	540	1650	1650	436.0	O07	0.024027	76.129	2243.185	95	190	240	240	151.0
L34	0.001307	70.302	1303.990	175	538	1650	1650	428.0	O08	0.001580	81.805	2290.381	95	189	240	240	129.5
L35	0.000392	70.662	1156.193	175	540	1650	1650	425.0	O09	0.022095	81.140	1681.533	116	194	120	120	130.0
L36	0.000087	71.101	2118.968	330	574	1620	1620	497.2	O10	0.076810	46.665	6743.302	175	321	180	180	218.9
L37	0.000521	37.854	779.519	160	531	1482	1482	510.0	O11	0.953443	78.412	394.398	2	19	90	90	5.4
L38	0.000498	37.768	829.888	160	531	1482	1482	470.0	O12	0.000044	112.09	1243.165	4	59	90	90	45.0
L39	0.001046	67.983	2333.690	200	542	1668	1668	464.1	O13	0.072468	90.871	1454.740	15	83	300	300	20.0
L40	0.132050	77.838	2028.945	56	132	120	120	118.1	O14	0.000448	97.116	1011.051	9	53	162	162	16.3
L41	0.096968	63.671	4412.017	115	245	180	180	141.3	O15	0.599112	83.244	909.269	12	37	114	114	20.0
L42	0.054868	79.458	2982.219	115	245	120	180	132.0	O16	0.244706	95.665	689.378	10	34	120	120	22.1
L43	0.054868	79.458	2982.219	115	245	120	180	135.0	O17	0.000042	91.202	1443.792	112	373	**1080**	**1080**	125.0
N12	0.000344	2.798	130.785	750	1006	36	54	898.0	O18	0.085145	104.50	535.553	4	20	60	60	10.0
N13	0.000690	1.595	878.746	713	1013	30	30	905.0	O19	0.524718	83.015	617.734	5	38	66	66	13.0
N14	0.000650	1.503	827.959	718	1020	30	30	846.5	O20	0.176515	127.79	90.966	5	19	12	6	7.5
N15	0.000233	2.425	432.007	791	954	30	30	850.9	O21	0.063414	77.929	974.447	50	98	300	300	53.2
N16	0.000239	2.499	445.606	786	952	30	30	843.7	O22	2.740485	92.779	263.810	5	10	6	6	6.4
N17	0.000261	2.674	467.223	795	1006	36	36	841.4	O23	0.112438	80.950	1335.594	42	74	60	60	69.1
N18	0.000259	2.692	475.940	795	1013	36	36	835.7	O24	0.041529	89.073	1033.871	42	74	60	60	49.9
N19	0.000707	1.633	899.462	795	1021	36	36	828.8	O25	0.000911	161.29	1391.325	41	105	528	528	91.0
N20	0.000786	1.816	1000.367	795	1015	36	36	846.0	O26	0.005245	161.83	4477.110	17	51	300	300	41.0
O01	0.014355	89.830	1269.132	94	203	120	120	179.0	O27	0.234787	84.972	57.794	7	19	18	30	13.7
O02	0.014355	89.830	1269.132	94	203	120	120	120.8	O28	0.234787	84.972	57.794	7	19	18	30	7.4
O03	0.014355	89.830	1269.132	94	203	120	120	121.0	O29	1.111878	16.087	1258.437	26	40	72	120	28.
O04	0.030266	64.125	4965.124	244	379	480	480	317.4									

TABLE XX

GENERATOR DATA WITH VALVE POINT EFFECTS OF TEST SYSTEM 5

$Unit_i$	a_i	b_i	c_i	e_i	f_i
C05	0.042468	54.242	1976.469	700	0.080
C10	0.005063	13.226	1320.636	600	0.055
C15	0.003901	14.651	1176.504	800	0.060
C22	0.003684	14.656	1229.131	600	0.050
C33	0.003542	15.033	1074.810	600	0.043
C40	0.001581	15.815	1436.251	600	0.043
L10	0.000044	71.584	1898.415	1100	0.043
L28	0.081540	22.941	13813.001	1200	0.030
L30	0.035475	45.017	9750.750	1000	0.050
L42	0.054868	79.458	2982.219	1000	0.050
O08	0.001580	81.805	2290.381	600	0.070
O10	0.076810	46.665	6743.302	1200	0.043

TABLE XXI

PROHIBIT ZONES OF UNITS OF TEST SYSTEM 5

Generator	Zone 1	Zone 2	Zone 3
C08	[250, 280]	[305, 335]	[420, 450]
C32	[220, 250]	[320, 350]	[390, 420]
L32	[230, 255]	[365, 395]	[430, 455]
O25	[50,74]	[84, 95]	

TABLE XXII
DATA FOR TEST SYSTEM 6

$Unit_i$	P_i^{min}	F1	P1	F2	P3	F3	P_i^{max}	Fuel type	a_i	b_i	c_i	e_i	f_i
1	100			196			250	1 & 2	0.0019	-0.3059	21.1300	0.0211	-3.0590
		1				2							
2	50		114		157		230	1 & 2 & 3	0.0042	-1.2690	118.4000	0.1184	-12.6900
		2		3		1							
3	200		332		388		500	1 & 2 & 3	0.0015	-0.3116	39.7900	0.0398	-3.1160
		1		3		2							
4	99		138		200		265	1 & 2 & 3	0.0059	-2.3380	266.8000	0.2668	-23.3800
		1		2		3							
5	190		338		407		490	1 & 2 & 3	0.0011	-0.0873	13.9200	0.0139	-0.8733
		1		2		3							
6	85		138		200		265	1 & 2 & 3	0.0059	-2.3380	266.8000	0.2668	-23.3800
		2		1		3							
7	200		331		391		500	1 & 2 & 3	0.0011	-0.1325	18.9300	0.0189	-1.3250
		1		2		3							
8	99		138		200		265	1 & 2 & 3	0.0059	-2.3380	266.8000	0.2668	-23.3800
		1		2		3							
9	130		213		370		440	1 & 2 & 3	0.0006	-0.0182	14.2300	0.0142	-0.1817
		3		1		3							
10	200		362		407		490	1 & 2 & 3	0.0011	-0.0994	13.9700	0.0140	-0.9938
		1		3		2							

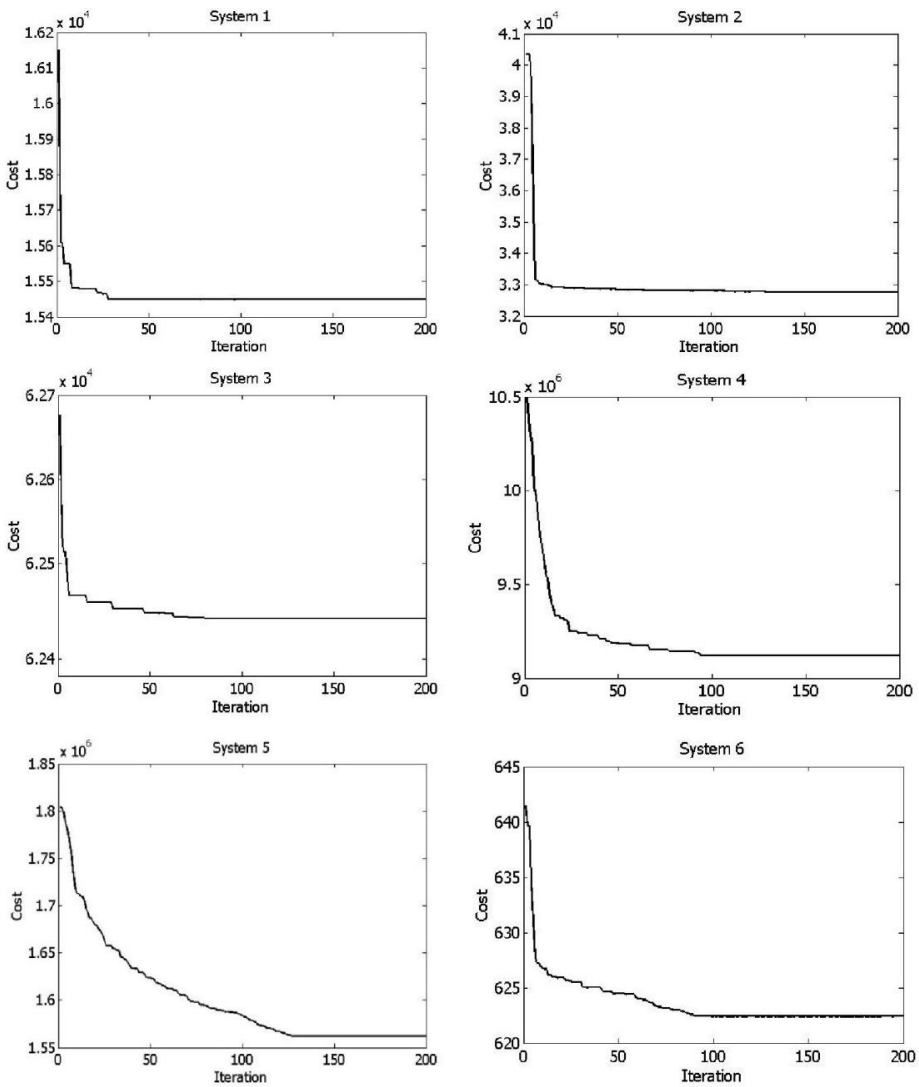

Fig. 2. Convergence diagram for six power test systems

REFERENCES

[1] D. Singh and J. Dhillon, "Ameliorated grey wolf optimization for economic load dispatch problem," *Energy*, vol. 169, pp. 398-419, 2019.

[2] X. He, Y. Rao, and J. Huang, "A novel algorithm for economic load dispatch of power systems," *Neurocomputing*, vol. 171, pp. 1454-1461, 2016.

[3] V. K. Kamboj, S. Bath, and J. Dhillon, "Solution of non-convex economic load dispatch problem using Grey Wolf Optimizer," *Neural Computing and Applications*, vol. 27, pp. 1301-1316, 2016.

[4] J. X. V. Neto, G. Reynoso-Meza, T. H. Ruppel, V. C. Mariani, and L. dos Santos Coelho, "Solving non-smooth economic dispatch by a new combination of continuous GRASP algorithm and differential evolution," *International Journal of Electrical Power & Energy Systems*, vol. 84, pp. 13-24, 2017.

[5] M. Pradhan, P. K. Roy, and T. Pal, "Grey wolf optimization applied to economic load dispatch problems," *International Journal of Electrical Power & Energy Systems*, vol. 83, pp. 325-334, 2016.

[6] Q. Zhang, D. Zou, N. Duan, and X. Shen, "An adaptive differential evolutionary algorithm incorporating multiple mutation strategies for the economic load dispatch problem," *Applied Soft Computing*, vol. 78, pp. 641-669, 2019.

[7] S. Pan, J. Jian, H. Chen, and L. Yang, "A full mixed-integer linear programming formulation for economic dispatch with valve-point effects, transmission loss and prohibited operating zones," *Electric Power Systems Research*, vol. 180, p. 106061, 2020.

[8] H. Sharifzadeh, "Solving economic load dispatch by a new hybrid optimization method," *International Journal of Industrial Electronics, Control and Optimization*, 2020.

[9] M. Gholamghasemi, E. Akbari, M. B. Asadpoor, and M. Ghasemi, "A new solution to the non-convex economic load dispatch problems using phasor particle swarm optimization," *Applied Soft Computing*, vol. 79, pp. 111-124, 2019.

[10] M. A. Al-Betar, M. A. Awadallah, A. T. Khader, A. L. a. Bolaji, and A. Almomani, "Economic load dispatch problems with valve-point loading using natural updated harmony search," *Neural Computing and Applications*, vol. 29, pp. 767-781, 2018.

[11] N. Ghorbani and E. Babaei, "Exchange market algorithm for economic load dispatch," *International Journal of Electrical Power & Energy Systems*, vol. 75, pp. 19-27, 2016.

[12] W. T. Elsayed, Y. G. Hegazy, M. S. El-bages, and F. M. Bendary, "Improved random drift particle swarm optimization with self-adaptive mechanism for solving the power economic dispatch problem," *IEEE Transactions on Industrial Informatics*, vol. 13, pp. 1017-1026, 2017.

[13] B. Taheri, G. Aghajani, and M. Sedaghat, "Economic dispatch in a power system considering environmental pollution using a multi-objective particle swarm optimization algorithm based on the Pareto criterion and fuzzy logic," *International Journal of Energy and Environmental Engineering*, vol. 8, pp. 99-107, 2017.

[14] M. Pradhan, P. K. Roy, and T. Pal, "Oppositional based grey wolf optimization algorithm for economic dispatch problem of power system," *Ain Shams Engineering Journal*, vol. 9, pp. 2015-2025, 2018.

[15] F. Mohammadi and H. Abdi, "A modified crow search algorithm (MCSA) for solving economic load dispatch problem," *Applied Soft Computing*, vol. 71, pp. 51-65, 2018.

[16] P. Zakian and A. Kaveh, "Economic dispatch of power systems using an adaptive charged system search algorithm," *Applied Soft Computing*, vol. 73, pp. 607-622, 2018.

[17] C. Fu, S. Zhang, and K.-H. Chao, "Energy Management of a Power System for Economic Load Dispatch Using the Artificial Intelligent Algorithm," *Electronics*, vol. 9, p. 108, 2020.

[18] X. Chen, "Novel dual-population adaptive differential evolution algorithm for large-scale multi-fuel economic dispatch with valve-point effects," *Energy*, p. 117874, 2020.

[19] X.-l. Chen, P.-h. Wang, Q. Wang, and Y.-h. Dong, "A Two-Stage strategy to handle equality constraints in ABC-based power economic dispatch problems," *Soft Computing*, vol. 23, pp. 6679-6696, 2019.

[20] H. Rezaie, M. Kazemi-Rahbar, B. Vahidi, and H. Rastegar, "Solution of combined economic and emission dispatch problem using a novel chaotic improved harmony search algorithm," *Journal of Computational Design and Engineering*, vol. 6, pp. 447-467, 2019.

[21] G. Chen and X. Ding, "Optimal economic dispatch with valve loading effect using self-adaptive firefly algorithm," *Applied Intelligence*, vol. 42, pp. 276-288, 2015.

[22] M. A. Al-Betar and M. A. Awadallah, "Island bat algorithm for optimization," *Expert Systems with Applications*, vol. 107, pp. 126-145, 2018.

[23] B. Adarsh, T. Raghunathan, T. Jayabarathi, and X.-S. Yang, "Economic dispatch using chaotic bat algorithm," *Energy*, vol. 96, pp. 666-675, 2016.

[24] M. Modiri-Delshad, S. H. A. Kaboli, E. Taslimi-Renani, and N. Abd Rahim, "Backtracking search algorithm for solving economic dispatch problems with valve-point effects and multiple fuel options," *Energy*, vol. 116, pp. 637-649, 2016.

[25] A. Bhadoria, V. K. Kamboj, M. Sharma, and S. Bath, "A solution to non-convex/convex and dynamic economic load dispatch problem using moth flame optimizer," *INAE Letters*, vol. 3, pp. 65-86, 2018.

[26] M. Elhameed and A. A. El-Fergany, "Water cycle algorithm-based economic dispatcher for sequential and simultaneous objectives including practical constraints," *Applied Soft Computing*, vol. 58, pp. 145-154, 2017.

[27] G. Xiong and D. Shi, "Orthogonal learning competitive swarm optimizer for economic dispatch problems," *Applied Soft Computing*, vol. 66, pp. 134-148, 2018.

[28] V. C. Pandey, V. K. Jadoun, N. Gupta, K. Niazi, and A. Swarnkar, "Improved fireworks algorithm with chaotic sequence operator for large-scale non-convex economic load dispatch problem," *Arabian Journal for Science and Engineering*, vol. 43, pp. 2919-2929, 2018.

[29] S. M. A. Bulbul, M. Pradhan, P. K. Roy, and T. Pal, "Opposition-based krill herd algorithm applied to economic load dispatch problem," *Ain Shams Engineering Journal*, vol. 9, pp. 423-440, 2018.

[30] D. Zou, S. Li, G.-G. Wang, Z. Li, and H. Ouyang, "An improved differential evolution algorithm for the economic load dispatch problems with or without valve-point effects," *Applied Energy*, vol. 181, pp. 375-390, 2016.

[31] C.-L. Chiang, "Improved genetic algorithm for power economic dispatch of units with valve-point effects and multiple fuels," *IEEE transactions on power systems*, vol. 20, pp. 1690-1699, 2005.

[32] V. K. Kamboj, A. Bhadoria, and S. Bath, "Solution of non-convex economic load dispatch problem for small-scale power systems using ant lion optimizer," *Neural Computing and Applications*, vol. 28, pp. 2181-2192, 2017.

[33] Y. Labbi, D. B. Attous, H. A. Gabbar, B. Mahdad, and A. Zidan, "A new rooted tree optimization algorithm for economic dispatch with valve-point effect," *International Journal of Electrical Power & Energy Systems*, vol. 79, pp. 298-311, 2016.

[34] S. H. A. Kaboli and A. K. Alqallaf, "Solving non-convex economic load dispatch problem via artificial cooperative search algorithm," *Expert Systems with Applications*, vol. 128, pp. 14-27, 2019.

[35] M. Ghasemi, I. F. Davoudkhani, E. Akbari, A. Rahimnejad, S. Ghavidel, and L. Li, "A novel and effective optimization algorithm for global optimization and its engineering applications: Turbulent Flow of Water-based Optimization (TFWO)," *Engineering Applications of Artificial Intelligence*, vol. 92, p. 103666, 2020.

[36] T. Niknam, H. D. Mojarrad, and H. Z. Meymand, "Non-smooth economic dispatch computation by fuzzy and self adaptive particle swarm optimization," *Applied Soft Computing*, vol. 11, pp. 2805-2817, 2011.

[37] J.-B. Park, Y.-W. Jeong, J.-R. Shin, and K. Y. Lee, "An improved particle swarm optimization for nonconvex economic dispatch problems," *IEEE Transactions on power systems*, vol. 25, pp. 156-166, 2009.

[38] M. Ghasemi, E. Akbari, A. Rahimnejad, S. E. Razavi, S. Ghavidel, and L. Li, "Phasor particle swarm optimization: a simple and efficient variant of PSO," *Soft Computing*, vol. 23, pp. 9701-9718, 2019.

[39] Z. Xin-gang, L. Ji, M. Jin, and Z. Ying, "An improved quantum particle swarm optimization algorithm for environmental economic dispatch," *Expert Systems with Applications*, p. 113370, 2020.

[40] P. Jangir, S. A. Parmar, I. N. Trivedi, and R. Bhesdadiya, "A novel hybrid particle swarm optimizer with multi verse optimizer for global numerical optimization and optimal reactive power dispatch problem," *Engineering Science and Technology, an International Journal*, vol. 20, pp. 570-586, 2017.

[41] H. Barati and M. Sadeghi, "An efficient hybrid MPSO-GA algorithm for solving non-smooth/non-convex economic dispatch problem with practical constraints," *Ain Shams Engineering Journal*, vol. 9, pp. 1279-1287, 2018.

[42] M. Kumar and J. Dhillon, "Hybrid artificial algae algorithm for economic load dispatch," *Applied Soft Computing*, vol. 71, pp. 89-109, 2018.

[43] M. Karimzadeh Parizi, F. Keynia, and A. Khatibi Bardsiri, "Woodpecker Mating Algorithm (WMA): a nature-inspired algorithm for solving optimization problems," *International Journal of Nonlinear Analysis and Applications*, vol. 11, pp. 137-157, 2020.

[44] M. Karimzadeh Parizi and F. Keynia, "OWMA: An improved self-regulatory woodpecker mating algorithm using opposition-based learning and allocation of local memory for solving optimization problems," *Journal of Intelligent & Fuzzy Systems*, pp. 1-28.

[45] Z.-L. Gaing, "Particle swarm optimization to solving the economic dispatch considering the generator constraints," *IEEE transactions on power systems*, vol. 18, pp. 1187-1195, 2003.

[46] Y. Labbi and D. B. Attous, "A Hybrid Big Bang–Big Crunch optimization algorithm for solving the different economic load dispatch problems," *International Journal of System Assurance Engineering and Management*, vol. 8, pp. 275-286, 2017.

[47] G. Dhiman, "MOSHEPO: a hybrid multi-objective approach to solve economic load dispatch and micro grid problems," *Applied Intelligence*, vol. 50, pp. 119-137, 2020.

[48] B. Sharma, R. Prakash, S. Tiwari, and K. Mishra, "A variant of environmental adaptation method with real parameter encoding and its application in economic load dispatch problem," *Applied Intelligence*, vol. 47, pp. 409-429, 2017.

[49] V. S. Aragón, S. C. Esquivel, and C. C. Coello, "An immune algorithm with power redistribution for solving economic dispatch problems," *Information Sciences*, vol. 295, pp. 609-632, 2015.

[50] Z. Huang, J. Zhao, L. Qi, Z. Gao, and H. Duan, "Comprehensive learning cuckoo search with chaos-lambda method for solving economic dispatch problems," *Applied Intelligence*, pp. 1-21, 2020.

[51] M. Kumar and J. Dhillon, "A conglomerated ion-motion and crisscross search optimizer for electric power load dispatch," *Applied Soft Computing*, vol. 83, p. 105641, 2019.

[52] Q. Qin, S. Cheng, X. Chu, X. Lei, and Y. Shi, "Solving non-convex/non-smooth economic load dispatch problems via an enhanced particle swarm optimization," *Applied Soft Computing*, vol. 59, pp. 229-242, 2017.

[53] E. Bijami, M. Jadidoleslam, A. Ebrahimi, J. Askari, and M. M. Farsangi, "Implementation of imperialist competitive algorithm to solve non-convex economic dispatch problem," *Journal of the Chinese Institute of Engineers*, vol. 37, pp. 232-242, 2014.

[54] D. C. SECUI, G. Bendea, and H. Cristina, "A modified harmony search algorithm for the economic dispatch problem," *Studies in Informatics and Control*, vol. 23, p. 144, 2014.

[55] W. T. El-Sayed, E. F. El-Saadany, H. H. Zeineldin, and A. S. Al-Sumaiti, "Fast initialization methods for the nonconvex economic dispatch problem," *Energy*, p. 117635, 2020.

[56] K. Alawode, A. Jubril, L. Kehinde, and P. O. Ogunbona, "Semidefinite programming solution of economic dispatch problem with non-smooth, non-convex cost functions," *Electric Power Systems Research*, vol. 164, pp. 178-187, 2018.

Morteza Karimzadeh Parizi received his B.S. degree in computer software engineering from Vali-asr University, Rafsanjan, Iran in 2006, and his M.S. and Ph.D. degree in software engineering from Islamic Azad University, Kerman, Iran in 2020. He published about 15 research papers in international journals and conference proceedings. His areas of research interests include optimization, metaheuristic algorithm, swarm intelligence, hybrid algorithm, and neural network. E-mail: Mkarimzadeh313@gmail.com

Farshid Keynia received Associated Professor at the Department of Energy Management and Optimization Graduate University of Advanced Technology, Kerman, Iran. He received his Ph.D. in electrical engineering from Semnan University. His M.Sc. in electrical engineering from Shahid Bahonar University, Kerman, Iran, and his B.Sc. in electrical engineering from Shahid Bahonar University, Kerman, Iran. E-mail: fkeynia@gmail.com

Amid Khatibi Bardsiri received his B.Sc. degree in computer software engineering from Shahid Bahonar University, Kerman, Iran in 2008 and his M.Sc. and Ph.D. degrees in software engineering from Islamic Azad University, Tehran, Iran in 2014. He published about 45 research papers in international journals and conference proceedings. His areas of research interests include information systems engineering, software development, software metrics, grid computing, and cloud computing. E-mail: a.khatibi@srbiau.ac.ir

International Journal of Industrial Electronics, Control and Optimization © 2021 IECO
Vol. 4, No. 2, pp. 235-244, April (2021)

Optimal Design of a Brushless DC Motor Aiming at Decreasing Cogging Torque

Mina Salarian [1], Milad Niaz Azari [2,†], Mostafa Hajiaghaei- Keshteli [3]

[1,2] Department of Electrical Engineering, University of Science and Technology of Mazandaran, Behshahr, Iran
[3] Department of Industrial Engineering, University of Science and Technology of Mazandaran, Behshahr, Iran

ABSTRACT

One of the important issues in designing high-performance brushless direct current (BLDC) motors is reducing the cogging torque since it results in mechanical vibration, audible noises, and torque ripples, which adversely impact the performance of the motor, which is awkward high-accuracy applications. This paper proposes an optimum design for BLDC motors aimed at reducing the cogging torque based on the capability of metaheuristics algorithms in finding the optimal solution. For this purpose, a simplified cogging torque equation is used as the objective function whose design variables include air gap length, magnet height, slot height, slot opening, and motor axial length. These are the five most influential parameters of cogging torque. On the other hand, we employ not only the old metaheuristics algorithms like the Genetic Algorithm (GA) and Simulated Annealing (SA) but also more recent algorithms such as Keshtel Algorithm (KA) along with the hybrid ones to benefit from their strength. The simulation is performed in the Matlab package. First, five selected optimization algorithms are applied and the results are investigated. The results of all the algorithms show a significant reduction in the cogging torque. Eventually, the proposed algorithms are compared to one another in terms of their value of cogging torque. The results show the superiority of the KASA algorithm in comparison with the others.

Article Info

Keywords:
Brushless DC motors, Cogging torque, Design, Metaheuristics algorithms, Optimization, Reduction.

Article History:
Received 2020-07-21
Accepted 2020-09-24

NOMENCLATURE

$w'(\theta)$: air gap co-energy
N: order of cogging torque harmonics
T_{CN}: amplitude of the *n*th harmonic component of cogging frequency
g: air gap length
L: motor axial length
D: stator inner diameter
k_c: carter's coefficient of the air gap that takes into account slot openings
B_g: flux density
t_1: stator slot pitch
l_m: magnet height
h_s: magnet height
k_{ok}: factor of stator slot opening
k_{sk}: factor of stator skew
w_s: slot opening
θ: rotor position angle
Q: number of slots
μ_0: magnetic permeability of free space
α: pole arc to pole pitch ratio
φ_g: air-gap flux

[†]**Corresponding Author**: miladniazazari@mazust.ac.ir
Tel: +98-01134556000, Fax: +98-01134556004,
Faculty of Electrical and Computer Engineering, University of Science and Technology of Mazandaran, Behshahr, Iran

I. INTRODUCTION

BLDC motors are widely used in various fields from domestic appliances to industrial machinery and speed and position control systems due to their high efficiency, high-density power, and easy speed control. One of the important and inherent drawbacks of BLDC motors is the cogging torque, which results from the interaction of the stator teeth, slots, and permanent magnets (PM) in all PM machines. The cogging torque prevents the rotor to rotate smoothly, so it is a major source of undesirable mechanical vibrations and noises in PM machines. Besides, it is one of the most important factors in torque ripple and can affect the control accuracy. Hence, in high performance and accuracy applications of BLDC motors, it is imperative to reduce cogging torque [1]-[4].

There are different methods for cogging torque reduction, such as physical methods and changing the geometry of the stator and rotor. They include using certain number of auxiliary slots in particular position [5], selecting an optimal number for poles and stator's pitch, optimizing the rotor's pole geometry by experimental results, skewing the stator or the magnetic pole [6], modifying the shape of stator teeth by changing the stator teeth tang span [1], using the eccentric structure of stator teeth [7], and a new manufacturing method with respect to the influence of the stator and rotor stacks' tolerance [2].

Some analytical methods, e.g. computing cogging torque [8],[9], study alterations of cogging torque according to slots number of the pole of the rotor [10] and also making $N_s/GCD(N_s,N_P)$ ≥4 (GCD: great common divisor, N_s: slot number, N_P: pole number) [11]. The sine-shaped PMs can be used to cancel the cogging torque. On the other hand, if the number of slots /pole /phase is equal to 0.25, 0.5, and 1, respectively, the amplitude of the cogging torque can increase in three-phase SPM machines with the Sine+3rd-shaped PM [12].

Due to the nature of the problem, optimization techniques can be very useful in minimizing the cogging torque. For this purpose, the particle swarm optimization (PSO), genetic algorithms, and modified particle swarm optimization are used to find the optimal design [13],[14].

Changing the geometry of the stator and rotor may cause other problems in PM machines. For example, the slanting of PM, which is the most common approach to decreasing the cogging torque, can reduce the flux linkage and increase the unbalanced emf [13]. On the other hand, analytical methods have been used in the literature for cogging torque-related computations. However, analytical methods should be used along with other methods, such as optimization or FEA, for mitigating the cogging torque. In the optimization method used in this paper, the cogging torque's influential parameters are changed over a specified range. Not only does this change lower the cogging torque as much as possible but it also does not lead to manufacturing problems in machines. In this method, previous studies have applied two or three design variables. But, the objective function in this paper contains five influential parameters of cogging torque and uses them as design variables.

The use of an objective function, which includes the five most influential parameters of the cogging torque, along with the use of new and hybrid algorithms, as well as comparing the results with well-known algorithms such as GA and SA, is a new work that has not been done before. This paper presents an optimal design of BLDC motors with the objective of minimizing the cogging torque by employing metaheuristics algorithms such as Genetic Algorithm (GA), Simulated Annealing (SA), Keshtel Algorithm (KA), and a hybrid of these algorithms. The algorithms are used in the Matlab package. Every algorithm is run individually and after all parameters are investigated, the results are compared. The analysis shows that the cogging torque can be minimized to a certain level and the KASA algorithm provides a more optimal solution than others.

For clarity, the paper is organized as follows. Section 2 describes the problem and objective function. Section 3 presents the proposed metaheuristics algorithms for optimizing the cogging torque and how they are implemented. Section 4 discusses the parameters setting used for optimizing, the design variables, and the constraints. Section 5 examined the results of the simulation of the algorithms and compares them. Also the obtained result were compared with the result of other similar methods. Finally, the concluding points and the recommendations for future studies are presented in Section 6.

II. COGGING TORQUE EXPLANATION AND THE OBJECTIVE FUNCTION

The BLDC motor is one of the most fascinating choices for industrial drives because of its attractive properties such as high torque density, reliable structure, and low maintenance requirements. But, the cogging torque components affect the BLDC motor's output. Hence, the reduction of cogging torque is an important issue in designing a BLDC motor [1]. This section

defines the cogging torque equation and expresses the objective function aimed to minimize this torque. The design variable is introduced at the end of this section.

A. Cogging Torque Explanation

Cogging torque is a kind of reluctance torque that is generated due to the tendency to reduce the reluctance between the rotor PMs and the stator teeth. The cogging torque can be minimized by reducing the change in air gap reluctance or decreasing the flux of the air gap [1],[15]. Reluctance R is given by Equ. (1).

$$R = \frac{l}{\mu A} \tag{1}$$

To determine the flux path length l, in addition to the length of the air gap g, the hieght of the stator slots h_s should be considered too because h_s is the length of the flux that enters the slot opening. So, the flux path length is considered in the range of $g < l < g + h_s$

Based on changes in the reluctance, the cogging torque can be defined by Equ. (2) as below [1],[16].

$$T_{cog} = -\frac{1}{2}\varphi_g^2 \frac{dR}{d\theta} \tag{2}$$

B. The Objective Function

Equ. (3) is a simplified cogging torque equation of PM machines, which is used as the objective function in this paper [17].

$$T_{cog} \approx -\frac{Lg}{2\mu_0}\frac{D}{2}K_1(X) \tag{3}$$

In which $K_1(X)$ is obtained by Equ. (4) and is a function of the distance X. In addition, Equ. (5) is used to express A.

$$k_1(x) = -\frac{4}{k_c}AB_g^2 \sin[\alpha(X + \frac{a+b}{2})] \sin\left(\alpha\frac{a-b}{2}\right) \tag{4}$$

$$\mathrm{A} = 2\gamma\frac{g}{t_1}{k_{ok=1}}^2{k_{sk=1}}^2 \tag{5}$$

In which α can be defined by Equ. (6) as follows.

$$\alpha = \frac{2\pi}{t_1} \tag{6}$$

Equs. (7) and (8) determine a and b, respectively, but to express b it is necessary to define c_t by Eq. (9).

$$a = 0.5t_1 \tag{7}$$

$$b = 0.5\,w_s + c_t \tag{8}$$

$$c_t = t_1 - w_s \tag{9}$$

In which γ can be defined by Equ. (10) as below [17].

$$\gamma = \frac{4}{\pi}\left[\frac{w_s}{2g}\tan^{-1}(\frac{w_s}{2g}) - \ln\sqrt{1+\frac{w_s}{2g}^2}\right] \tag{10}$$

C. Design Variables

The cogging torque can be minimized by selecting the most suitable value for the motor design parameters. Thus, selecting design variables to optimize is an important part of cogging torque reduction. Because of the transfer of the main energy in the air gap, not only are air gap and slot opening important variables but magnet length is also an important design variable to be optimized for cogging torque reduction [13]. Here, α, l_m, w_s, h_s and g are selected as the motor design variables. For better understanding, the geometric representation is shown in Fig. 1 [16].

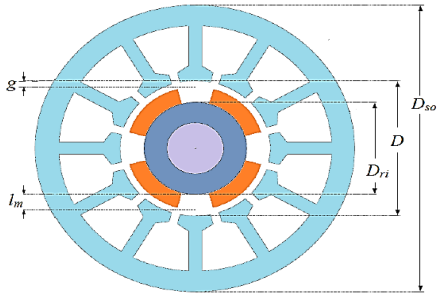

(a)

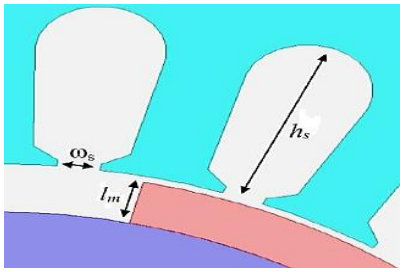

(b)

Fig. 1. Motor geometry: (a) parameters of the motor and (b) slot view.

III. SOLUTION APPROACH

A. Genetic Algorithm (GA)

GA is a population-based technique and a famous evolutionary algorithm. In general, GA has four main steps, i.e. reproduction, selection mechanism, mutation, and crossover. Mutation and crossover are two search operators of GA that not only produce a new generation but also search for the potential area of problems.

Moreover, their focus is on intensification and diversification, respectively. Due to the nature of chromosomes, GA chromosomes is used as an array of variables. On the other hand, mutation and crossover alter chromosomes to create a set of new solutions and solve the huge and complex problems [18],[19]. The main parameters of GA to determine the general behavior are expressed as follows: the number of population is 10, the probability of crossover is 0.3, and the probability of mutation is 0.3.

B. *Simulated Annealing (SA)*

SA is based on the process of annealing metals, which is a kind of local search optimization techniques. Besides, SA is one of the well-known single solution algorithms. The SA process is as follows. The first step is choosing a solution randomly which is presented as the best solution. At the next step, an initial temperature must be fixed. Then, a neighbor solution with a near close position to the best solution is generated during a process and it is evaluated. If it is conclusively or by a probability better than the best solution, the new solution replaces the previous one. Afterward, the best solution and the temperature are updated. This cycle is continued until the updated temperature becomes greater than the threshold [20]. The main parameters of SA to determine the general behavior are that the initial temperature is 50 and α is 0.97.

C. *Keshtel Algorithm (KA)*

KA was introduced by Hajiaghaei-Keshteli and Aminnayeri [21] inspired by how a dabbling duck whose common name is Keshtel in the north of Iran is fed. Generally, Keshtels work together as a group while feeding and when a Keshtel finds a rich source of food, the side Keshtels approach it and seek food by swirling in a circle. As soon as Keshtel finds food, it sinks its head under water and rotates its body around its beak like a moving circle. The other nearby Keshtels approach it and rotate in the same direction of the first Keshtel while it is in the center of the circle. They continue to rotate until no food remains. Again when a Keshtel finds a good source of food, this process is repeated. An important result of this algorithm is a solution with higher quality; a result that satisfies us to use it for our problem.

In order to identify the counterpart of the proposed algorithm, initial Keshtels are divided into three categories (i.e. N1, N2, and N3) to search the feasible space. N1 includes lucky Keshtels – the ones that have found good foods in their first try. In contrary to N1, N3 contains the worst solutions, which are generated randomly in each iteration. If better food is found for each lucky Keshtel, a new lucky will be replaced. Otherwise swirling will be continued. For N2 type Keshtels, they move between two lucky Keshtels [22]. The flowchart of the KA algorithm is shown in Fig. 2.

D. *Hybrid of KA and SA (KASA)*

Hybridization is considered as combining two search algorithms to find the best solution for a given problem. The KASA algorithm is based on KA. Thus, KA is the main loop and the role of SA is to help the algorithm for an intelligent probe.

Furthermore, the properties of the exploration step are investigated by the SA loop. Generally, this algorithm is used to enhance the strength of intensification and diversification steps. Using SA as a sub-loop in per iteration can modify the randomization of the procedure. Accordingly, in KA, each Keshtel is evaluated and compared with the previous one and the better Keshtel replaces but the opposite of KA in SA uses a temperature rate controller to accept the rejected solutions during the iterations. The flowchart of the KASA algorithm is shown in Fig. 3. Also, more details of this metaheuristic KASA pseudo-code are displayed in Fig. 4 [23].

E. *Hybrid of GA and SA (GASA)*

GASA is a hybrid optimization strategy created by combining the GA and the SA. Two weaknesses of the SA algorithm are the limiting behavior of convergence and computation time. The hybrid approach is an efficient way to overcome these problems. In addition, it can help improve SA performance. Adding this sampling to the GA not only can help avoid the search getting stuck in a local optimum solution but it can also extend the search scope [24]. SA can locally optimize each individual solution. On the other hand, GA works on the optimal solution in a global sense. These two powerful properties are the motivation for the combination of GA and SA.

The GASA algorithm has two phases. The first phase is performed by GA, which is a global search. The second phase is named the local search phase, which is applied by SA. The pseudo-code of GASA is explained in Fig. 5. Also, the flowchart of the GASA algorithm is depicted in Fig. 6 [25].

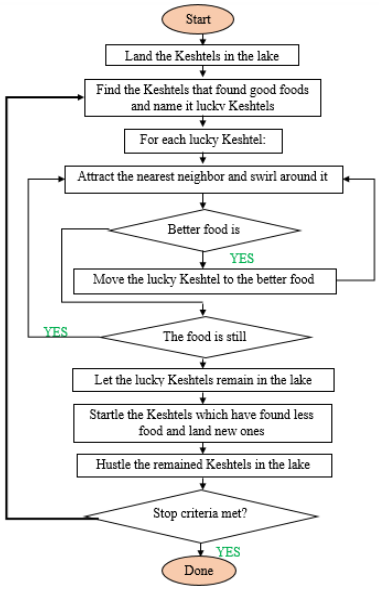

Fig. 2. The flowchart of the KA algorithm

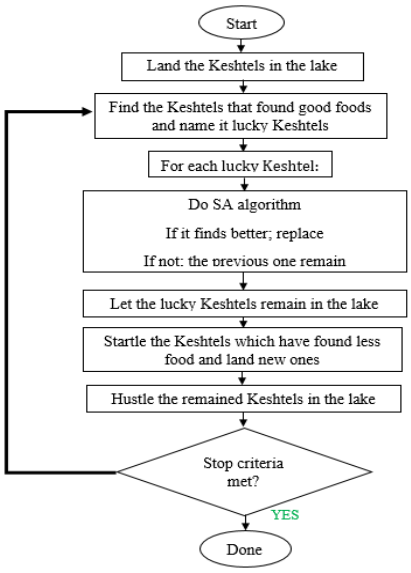

Fig. 3. The flowchart of the KASA algorithm

IV. PARAMETERS SETTING

A notable section in implementing all algorithms is the parameter-setting. The model of the motor used in this paper is a 4 pole, 220 v, and 550 w motor. The characteristics of the BLDC motor that we require to optimize are presented in Table I.

The constraints considered as ranges of design variables are defined in Table II.

Initialize Keshtels population.
Calculate the fitness and sort them in three types: M_1, M_2 and M_3
Y*=the best solution.
while (z< maximum number of iteration)
  for each M_1
  Calculate the distance between this lucky Keshtel and all Keshtels.
Select the closest neighbor.
  while (S< maximum number of swirling)
  Do the swirling.
  if the fitness of this new position is better than prior
  Update this lucky Keshtel.
    break
 endif
 S=S+1
 endwhile
endfor
for each M_2
  Move the Keshtel between the two lucky Keshtels.
endfor
for each M_3
  Create a neighbor from the one of luck Keshtels randomly.
  if the function value of the new solution is better than prior
    Replace the new solution as old solution.
 else
 Calculate δ, $\delta = |f_{old} - f_{new}|$.
      if rand< $\exp(-\delta/T)$
        Replace the new solution.
      endif
    endif
  endfor
  Merge the M_1, M_2 and M_3
Sort the Keshtels and form M_1, M_2 and M_3 for next iteration and Update Pareto optimal solutions.
  Update the Y* if there is better solution.
  z=z+1
end while
return Y*

Fig 4. The pseudo-code of KASA

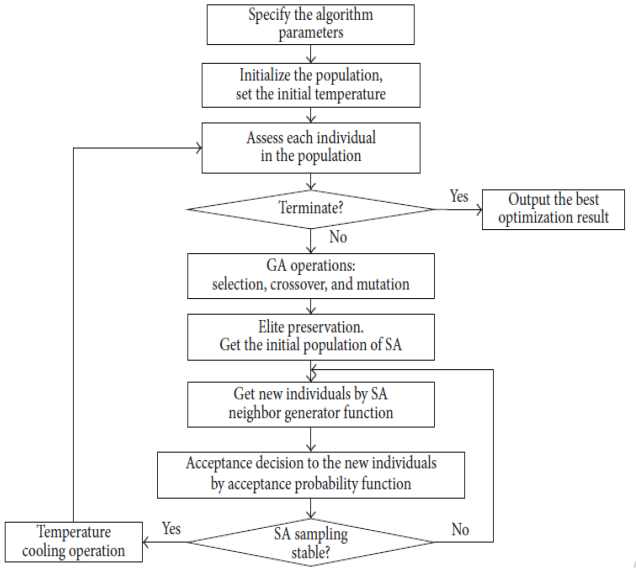

Fig. 5. The flowchart of the GASA algorithm

V. SIMULATION

Using the MATLAB software, the GA, SA, KA, KASA, and GASA algorithms are applied to optimize the objective function according to the specifications and constraints. In all algorithms, the iteration is set on 200.

```
MAX_GENS: max number of generations
NUM_GENES: number of genes, POP_SIZE: population size
RANDOM: decimal between 0 and 1, T: temperature
Pnew: new placement, Pold: old placement, Pcrossover: probability of
crossover rate
Pmutation: probability of mutation rate, Plocal: probability of local
improvement rate
Preserve: the percent of population reserved in the generation
e: constant of 2.732
begin
        initialize_population ()
        while (generation < MAX_GENS) do
            evaluate_population_fitness ();
            reproduce_population (Preserve);
            for i = 1 to POP_SIZE/2 do
                crossover (Pcrossover);
            for j = 1 to NUM_GENES do
                mutate (Pmutation);
            for i = 1 to POP_SIZE do
                local_improvement (Plocal);
            elitism();
        end while
        select_the_best_one();
        T = set_temperature();
/* following algorithm is pseudo-code of SA*/
        while (exit_criterion() == FALSE) do
            while (inner_criterion() == FALSE) do
                Pnew = generate_movement ()
                ΔC = C (Pnew)−C (Pold);
                RANDOM = generate_number();
                if (RANDOM < e exp (−ΔC/T))
                    Pold = Pnew;
            end while
        end while
end algorithm
```

Fig. 6. The pseudo-code of GASA

TABLE I
The Specifications of a Sample BLDC Motor

Parameter	Value	Definition
T_C	719.1 mN.m	Cogging torque
P	4	Number of pole
S	24	Number of slot
D	75 mm	Stator inner diameter
D_{ri}	26 mm	Rotor inner diameter
D_{so}	120 mm	Stator outer diameter
D_{ro}	74 mm	Rotor outer diameter
G	1 mm	Air gap length
L	65 mm	Axial length
L_m	3.5 mm	Magnet height
α	0.7	Pole arc to pole pitch ratio
φ	3 mwb	Magnetic flux under pole
h_s	8.2 mm	Slot height
w_s	2.5 mm	Slot opening

Due to the random nature of metaheuristic algorithms, the values of the parameters and cogging torque show the average value of each of them after 20 times of the algorithm implementation. Table III, IV and V present the design parameters required to implement the SA, GA and KA algorithms, respectively.

TABLE II
The Ranges of the Design Variable

Variable	Min	Max
α	0.65	0.85
l_m (mm)	2	5
g (mm)	0.5	2
w_s (mm)	2	4
h_s (mm)	7	10

TABLE III
Design Parameter for SA

Parameters	Value
T_0	50
Alpha	0.97
Iterations	200

TABLE IV
Design Parameter for GA

Parameters	Value
No of variables	5
Population	10
Iterations	200
Probability of crossover (P_c)	0.3
Probability of mutation (P_m)	0.3

TABLE V
Design Parameter for KA

Parameters	Value
No of variables	5
Population	150
Iterations	200
Condition stop swirling	1
No of swirling	40
Percentage of N_1 population	0.5
Percentage of N_2 population	0.5

A. Simulation Results

The optimized values for parameters are shown in Table VI. According to Table VI, all algorithms able to reduce the cogging torque compared to the cogging torque of sample motor. However the best solution is presented by the KASA algorithm that has the minimum value of the cogging torque.

TABLE VI
The Optimized Values of the Algorithms' Parameters

Parameter	GA	SA	KA	KASA	GASA	Sample motor
α	0.8194	0.7071	0.8474	0.8470	0.7810	0.7
l_m (mm)	4.2078	4.3757	4.2303	4.2358	4.0550	3.5
g (mm)	1.9616	1.6757	1.9389	1.9859	1.8970	1
w_s (mm)	2.0609	2.0604	2.0620	2.0261	2.0352	2.5
h_s (mm)	9.1328	9.3536	9.7590	9.9384	9.7935	8.2
T_C N.m	0.2737	0.3334	0.2097	0.1957	0.2979	0.7191

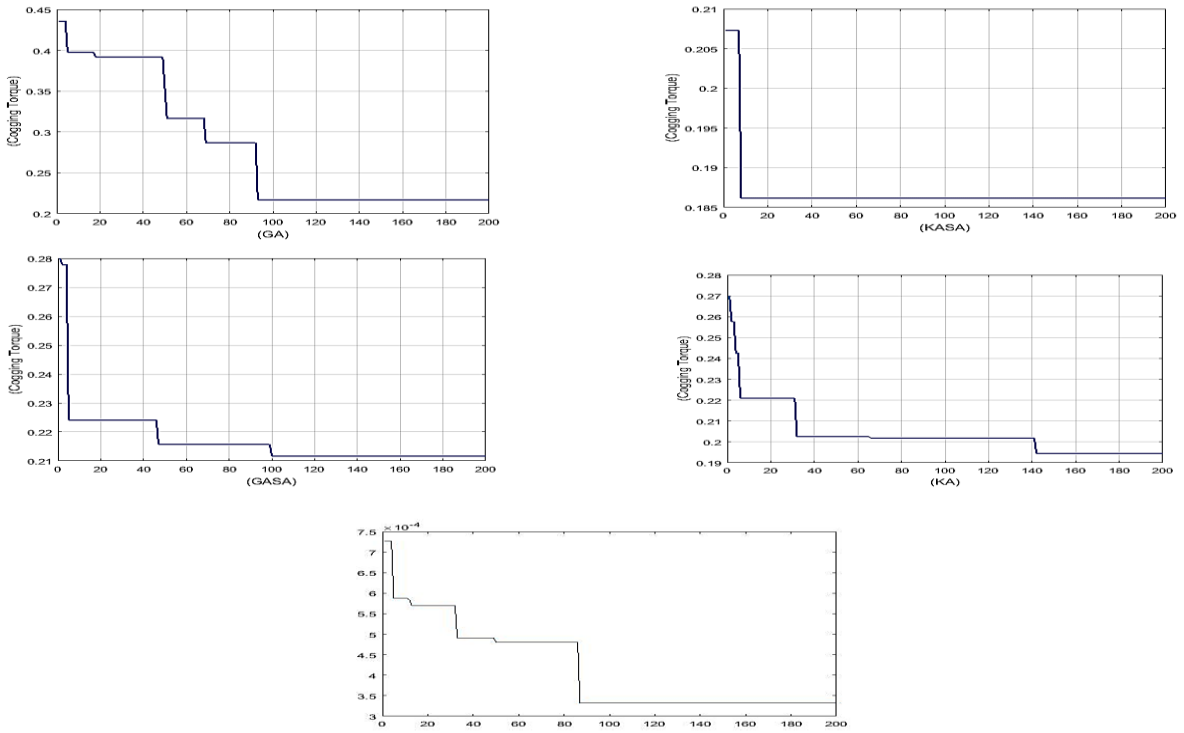

Fig. 7. Graph of cogging torque changes during 200 iteration for GA, SA, KA, GASA and KASA algorithms

Besides, all variable parameters are in their specific range. Also, the maximum value belongs to the SA algorithm. As shown in Table VI, the cogging torque is not completely eliminated, but it can be reduced significantly. Fig. 7 displays graph of the cogging torque changes during 200 iteration for GA, SA, KA, GASA and KASA algorithms and it can be seen that the KASA algorithm converges to best solution faster than the others. The cogging torque can be minimized in the design of the BLDC motor by using the optimal values of the parameters obtained. For more explanation, the results of optimization are compared in Fig. 8, and Fig. 9 shows the results of the design variables by the optimization algorithms. The computational time of the proposed algorithms presents in Table VII that KASA and SA have maximum and minimum time. This result was predictable.

B. Comparison with Some Similar Methods

In Ref. [13] PSO and GA are applied to optimize a BLDC motor with the aim of minimizing the cogging torque.

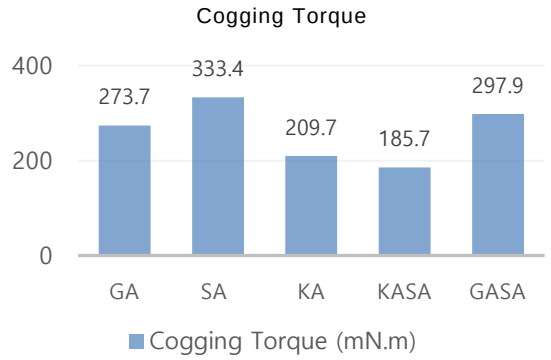

Fig. 8. The comparison of the cogging torque optimization results by the GA, SA and KA, GASA and KASA algorithms.

TABLE VII
The Computational Time of the Proposed Algorithms

	GA	SA	KA	GASA	KASA
Elapsed Time (Second)	1.442	0.285	13.253	5.180	135. 557

In this procedure, slot opening, air gap length and magnet length are chosen as design variables. The result shows reduction of cogging torque from 0.0510 to 0.025 using PSO and 0.0510 Nm to 0.04 Nm using GA.

Ref. [26] uses GA as an optimization tool to decrease the cogging torque in permanent magnet synchronous motor. Pole span, magnet thickness and shape of the magnets are design variables. In this method the cogging torque reduces from 0.368 Nm to 0.0169 Nm.

In this paper, the results show the superiority of the KASA algorithm in comparison with the other algorithms. Here pole arc to pole pitch ratio, slot height, air gap length, slot opening and magnet length are selected as the motor design variables. KASA reduces the cogging torque from 0.7191 Nm to 0.1957 Nm.

For comparison these three methods, the value of cogging torque reduction is defined as indice and it can be obtained by subtraction of the optimized motor cogging torque from the sample motor cogging torque. Table VIII shows this comparison and according to Table VIII KASA has maximum reduction of the cogging torque.

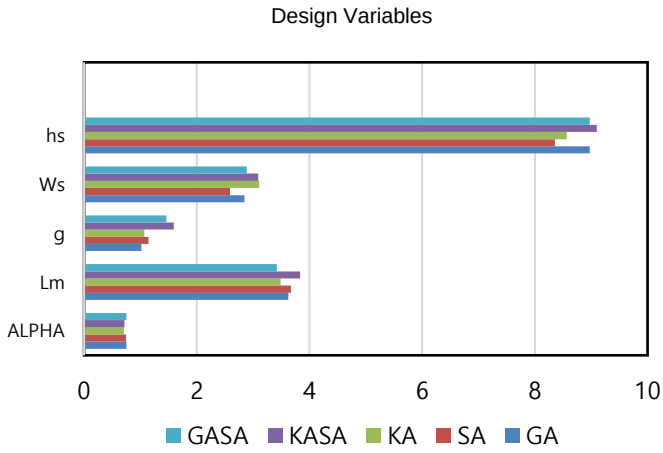

Fig. 9. The results of the design variables by the GA, SA, KA, GASA, and KASA algorithms

TABLE VIII
Comparison of Three Methods through Reduction of Cogging Torque Value

		Ref [13]	Ref [27]	This paper
Reduction of Cogging Torque (N.m)	PSO	0.026		
	GA	0.011	0.3518	
	KASA			0.5234

VI. CONCLUSION

The cogging torque has a detrimental effect on the performance of the PM machines, so the reduction of the cogging torque is an important issue in BLDC motors to gain high performance.

This paper proposed an optimum design of the BLDC motors with the aim of reducing the cogging torque by employing metaheuristics algorithms such as GA, SA, KA, KASA, and GASA. The analysis shows:

- All selected algorithms able to decrease the cogging torque value
- All variable parameters are in their specific range for all algorithms so they can be used for manufacturing.
- The KASA algorithm presents the minimum cogging torque value
- The SA algorithm presents the maximum cogging torque value in comparison with the other algorithms.

In the future works, the authors will offer an optimal solution for the BLDC motor that, in addition to reducing the cogging torque, will also consider the value of the output torque.

REFRENCES

[1] Kamal, D. Amudhavalli and T. Thyagarajan, "Reformed Stator Design of BLDC Motor for Cogging Torque Minimization Using Finite Element Analysis," *In 2018 4th International Conference Electrical Energy Systems (ICEES), IEEE,* Chennai, pp.481-484, 2018.

[2] J. Ou, Y. Liu, R. Qu and M. Doppelbauer, "Experimental and theoretical research on cogging torque of PM synchronous motors considering manufacturing tolerances," *IEEE Trans. Industrial Electronics,* Vol. 65, No. 5, pp. 3772-3783, 2017.

[3] M.N. Azari, M. Samami and S.A. Pahnehkolaei. "Optimal Design of a Brushless DC Motor, by Cuckoo Optimization Algorithm (research note)," *IJE Trans. Applications*, Vol. 30, No. 5, pp. 668-677, 2017.

[4] Hajiaghaei-Keshteli. "An Improved Red Deer Algorithm to Address a Direct Current Brushless Motor Design Problem," *Scientia iranica*, 2019.

[5] D.U. Xiao-bin, H.U.A.N.G. Kai-sheng and H.U.A.N.G. Xin, "Reduction of Cogging Torque of Permanent Magnet Machines Based on Harmonic Analysis," *Small & Special Electrical Machines*, Vol. 47, No. 1, p. 37, 2019.

[6] M. POPESCU, E. TUDOR, S. NICOLAIE, C.I. ILIE, , L. POPOVICI and C. DUMITRU, "Experimental Results Regarding Cogging Torque Reduction for the Permanent Magnet Synchronous Motors PMSM," *In 2019 11th International Symposium on Advanced Topics in Electrical Engineering (ATEE), IEEE,* pp. 1-4, 2019.

[7] K. Wang, Y. Liang, D. Wang and C. Wang, "Cogging torque reduction by eccentric structure of teeth in external rotor permanent magnet synchronous motors," *IET Electric Power Applications,* Vol.13, No. 1, pp. 57-63, 2018.

[8] Ebadi, M. Mardaneh, A. Rahideh and N. Bianchi, "Analytical Energy-Based Approaches for Cogging Torque Calculation in Surface-Mounted PM Motors," *IEEE Transactions on Magnetics,* Vol. 55, No. 5, pp. 1-10, 2019.

[9] L. Jing, J. Chen, Z. Huang and J. Gong "Exact Analytical Method for Air-Gap Main Magnetic Field Computation and Cogging Torque of SMPM Motors," *Progress In Electromagnetics Research,* Vol. 81, pp. 75-84 2019.

[10] L. Jing, J. Gong and Y. Lin, "Analysis and Reduction of Cogging Torque of Line-Start Permanent Magnet Motors," *Progress In Electromagnetics Research,* Vol. 78, pp. 115-124, 2019.

[11] H.Y. Sun and K. Wang, "Effect of Third Harmonic Flux Density on Cogging Torque in Surface-Mounted Permanent Magnet Machines," *IEEE Trans, Industrial Electronics,* Vol. 66, No. 8, pp. 6150-6158, 2018.

[12] K. Wang, and Z.Q. Zhu, "Analysis of Cogging Torque in Surface-Mounted Permanent Magnet Machines with Shaped Magnets," *In Third Harmonic Utilization in Permanent Magnet Machines, Springer, Singapore,* pp. 121-141, 2019.

[13] Kamal, T. Thyagarajan, M. Selvakumari and D. Kalpana "Cogging torque minimization in brushless DC motor using PSO and GA based optimization," *In 2017 Trends in Industrial Measurement and Automation (TIMA), IEEE, Chennai,* pp. 1-5, 2017.

[14] Z. Xue, H. Li, Y. Zhou, N. Ren and W. Wen, "Analytical prediction and optimization of cogging torque in surface-mounted permanent magnet machines with modified particle swarm optimization," *IEEE Trans. Industrial Electronics,* Vol. 64, No. 12, pp. 9795-9805, 2017.

[15] C.Y. Hsiao, S.N. Yeh and J.C. Hwang, "A novel cogging torque simulation method for permanent-magnet synchronous machines," *Energies,* Vol.4, No. 12, pp. 2166–2179, 2011.

[16] R. Ilka, Y. Alinejad-Beromi and H. Yaghobi, "Cogging torque reduction of permanent magnet synchronous motor using multi-objective optimization," *Elsevier B.V. Mathematics and Computers in Simulation,* Vol. 153, pp. 83-95, 2018.

[17] J.F. Gieras, "Analytical approach to cogging torque calculation of PM brushless motors," *IEEE Trans, Industry Applications,* Vol. 40, No.5, pp. 1310-1316, 2004.

[18] Abdi, A.M. Fathollahi-Fard and M. Hajiaghaei-Keshteli, "A set of calibrated metaheuristics to address a closed-loop supply chain network design problem under uncertainty," *International Journal of Systems Science: Operations & Logistics,* pp. 1-18 2019.

[19] H. Moradi CheshmehBeigi and A. Mohamadi, "Torque Ripple Minimization in SRM Based on Advanced Torque Sharing Function Modified by Genetic Algorithm Combined with Fuzzy PSO," *International Journal of Industrial Electronics, Control and Optimization,* Vol. 1, No. 1, pp. 71-80, 2018.

[20] S. Sadeghi-Moghaddam, M. Hajiaghaei-Keshteli and M. Mahmoodjanloo, "New approaches in metaheuristics to solve the fixed charge transportation problem in a fuzzy environment," *Neural Computing and Applications*, Vol. 31, No. 1, pp. 477-497, 2019.

[21] M. Hajaghaei-Keshteli, M. Aminnayeri, M.J.A.S.C., "Solving the integrated scheduling of production and rail transportation problem by Keshtel algorithm," *Elsevier B.V. Applied Soft Computing*, Vol. 25, pp.184-203, 2014.

[22] A.M.F. Fard and M. Hajaghaei-Keshteli, "A tri-level location-allocation model for forward/reverse supply chain," *Elsevier B.V. Applied Soft Computing*, Vol. 62, pp. 328-346,

[23] M. Hajiaghaei-Keshteli and A.M. Fathollahi-Fard, "A set of efficient heuristics and metaheuristics to solve a two-stage stochastic bi-level decision-making model for the distribution network problem*," Elsevier Ltd. Computers & Industrial Engineering,* Vol. 123, pp. 378-395, 2018.

[24] Han, M., Li, P. and Sun, J. "The algorithm for berth scheduling problem by the hybrid optimization strategy GASA", *In 2006 9th International Conference on Control,*

Automation, Robotics and Vision, IEEE, Singapore, pp. 1-4, 2006.

[25] M. Yang, A.E.A. Almaini and P. Wang, "FPGA placement optimization by two-step unified genetic algorithm and simulated annealing algorithm*," Journal of Electronics (China)*, Vol. 23, No. 4, pp. 632-636, 2006.

[26] V. Sarac, "Performance optimization of permanent magnet synchronous motor by cogging torque reduction*," Journal of Electrical Engineering*, Vol. 70, No. 3, pp. 218-226, 2019.

Mina Salarian was born in Nur, Mazandaran, Iran in 1992. She completed her B.Sc. in Electrical Engineering from University of Gilan: Rasht, Iran in 2015. She is currently studying her M.Sc. in Electrical Engineering in field of Power Electronics and Electric Machines at University of Science and Technology of Mazandaran**:** Behshahr, Iran.
Email: minasalaryan@gmail.com

Milad Niaz Azari was born in Babol, Iran, in 1984. He received his B.S degree in electrical engineering from Noshirvani University of Technology, Babol, Iran in 2007. He Graduated in M.S degree in the department of Electrical Engineering, Amir Kabir University of Technology, Tehran, Iran in 2009. Also he graduated in PhD degree in Amirkabir University of Technology, Tehran, Iran in 2013. Since 2014, he has been at University of Science and Technology of Mazandaran, Behshahr, Iran, as an assistant Professor in the department of Electrical Engineering. His areas of interest are electrical machines design and power electronics.
Email: miladniazazari@mazust.ac.ir

Mostafa Hajiaghaei-Keshteli was born raised in Babol, Iran. He earned his B.Sc. from Iran University of Science & Technology, Tehran, Iran (2004); M.Sc. from Iran University of Science & Technology, Tehran, Iran (2006); and Ph.D. from Amirkabir University of Technology (Tehran- Polytechnic) Tehran, Iran (2012); all in Industrial Engineering. He is currently Industrial Engineering an Assistant Professor at University of Science & Technology of Mazandaran, Iran. He has over 10 years of experiences in Business Development, System Analysis, Inventory and Project Magnet. Mostafa also has worked for many corporations in Iran and has held the positions of consulter, planning and project manager and VP. The main focus of his research is in the area of Inventory Control, Supply Chain Network, Transportation and Meta-heuristics.
Email: mostafahaji@mazust.ac.ir

International Journal of Industrial Electronics, Control and Optimization © 2021 IECO
Vol. 4, No. 2, pp. 245-255, April (2021)

Efficient Networked Microgrid Management Considering Plug-in Electric Vehicles and Storage Units

Mahdi Vosoogh[1], Masoud Rashidinejad[1,2,†], Amir Abdollahi[1,2], Morteza Ghaseminezhad[3]

[1]Department of Electrical Engineering, Sirjan Branch, Islamic Azad University, Sirjan, Iran.
[2]Department of Electrical Engineering, Shahid Bahonar University of Kerman, Kerman, Iran.
[3]Department of Electrical Engineering, Sirjan University of Technology, Sirjan, Iran.

ABSTRACT

This article addresses the optimal energy management and operation of networked microgrids considering different types of dispatchable units like fuelcell and microturbine and non-dispatchable units such as wind turbine and solar units. To change the just-consuming role of vehicles into an active role with the ability to make a profit, the vehicle-to-grid technology (V2G) is deployed here. Due to the complex and nonlinear structure of the problem, an effective optimization energy management framework based on the bat algorithm (with a modification) and unscented transform is devised to find the most optimal operation point of the devices from the economic point of view. Due to the high uncertainties injected by electric vehicles pattern behavior in addition to the renewable sources output power variations, the unscented transform is proposed to make the analysis more realistic. The simulation results on an IEEE networked microgrid test system advocate the high capability and proper performance of the proposed method. The results show that the total system operation cost is 53897.004$ and 53711.704$ in the 1st and 2nd scenarios, respectively. Moreover, it is seen that considering uncertainty in the problem has added 0.586% and 0.762% to the cost function value in the first and second scenarios, compared to the deterministic framework.

Article Info

Keywords:
Electric Vehicle, Fuel Cell, Micro-Turbine, Networked Microgrid, Smart Grid, Storages, Uncertainty.

Article History:
Received 2020-09-22
Accepted 2020-11-26

I. INTRODUCTION

The traditional electric grid structure is experiencing a fast change due to the high share of distributed generations (DGs) in the form of either dispatchable generators including fuelcell (FC) and microturbine (MT) or snon-dispatchable units including wind turbine (WT) and photovoltaics (PVs). This has created a great opportunity for the last-longing idea of microgrids which can not only support their loads based on the self-supply sources of DGs, but can also benefit the main grid at peak-load hours when the heavy loading bothers the utilities [1, 2]. Due to this great opportunity, different types of AC and DC microgrids are emerging among which the networked microgrids could provide the most interesting and charming features for both the microgrid owners and the power grid utilities. Some of the main rewards of networked microgrids can say as progressed reliability, better voltage profile, more economic power supply, better electrical services, and more support of renewable energy sources and electric vehicles [3, 4]. While these benefits could stabilize the position of microgrid concept in the power system more than before, there are new challenges emerging in the grid which are partly due to the renewable energy sources (RESs) unstable power supply and the much uncertainty they inject and partly due to the electric vehicles high penetration with random charging behaviors [5, 6]. Therefore, in the previous years, many researches were done to check different aspects

†Corresponding Author: mrashidi@uk.ac.ir,mas.rashidinejad@gmail.com Tel: +98-9133414044, Fax: +98-9133414044, Shahid Bahonar University of Kerman. Department of Electrical Engineering, Shahid Bahonar university of kerman, Kerman, Iran.

of this new emerging technology and find solution for the potential problems of their future.

In [7], a distributed energy management framework for the networked microgrids is proposed which uses a wireless protocol for data transaction and getting to a consensus point. The diffusion based procedure is compatible with the very wide area covered by the networked microgrid and so makes it possible for an economic power dispatch. In [8], a two-stage stochastic bi-level structure is proposed for the energy management of a high voltage networked microgrid. The proposed bi-level model is deployed for facilitating the interaction between the distribution system and main grid. In [9], the confident consequence of networked microgrids in progressing the hardening of the main grid is investigated. It also explains some of the main experiments in growing DGs at networked microgrids and provides an answer for the broad resiliency enhancement in contradiction of extreme occasions. In [10], a financial dispatch exemplary is presented in the shape of mixed-integer cone programming to guarantee the safety and efficacy of a networked microgrid. It utilizes innovative control techniques for instance tap-changing transformers, switching, etc to energize the microgrid. In [11], authors propose a new management model for scheduling of a multi-carrier energy hub considering (DGs), storage devices with a practical degradation model and heating/cooling. In [12], a centralized architecture is employed for the optimal operation of a networked microgrid. It provides a situation that microgrids can sell/purchase power to/from the utility through a linear quadratic preparation. In [13], authors propose a managing scheme for the networked microgrids which can include different renewable energy sources and handle the power trade happening between the microgrid and the main grid. In [14], a deep neural network model is combined with the reinforcement learning to learn the energy management pattern in a networked microgrid. The objective function is to reduce the demand-side peak load when increasing the selling profit at the same time. In [15], demand response program is used to operate an active distribution grid with a structure of networked microgrid. It evaluates the technical indices of supply-adequacy and voltage profile when improving the reliability at the same time. In [16], an advanced control protocol based on wireless communication is proposed to manage the reactive power sharing between networked microgrids. Therefore, first the amount of reactive power which is needed for the microgrid is predicted and then genetic algorithm tries to minimize the power division error in the microgrid. In [17, 18], a distributed outline is devised for energy managing of multiple microgrids within themselves and with each other.

Based on these explanations, the optimal energy management of networked microgrids has attracted the attention of engineers and power researchers in recent years. Although there are significant works published in the previous years, still the research in this area is at the beginning of the way and there are many unforeseen challenges which need to be studies carefully. Accordingly, this research article aims to assess the interacting behavior of microgrids with each other in a networked microgrid and with the main grid when facing the high penetration of renewable energy sources such as WTs, PVs and non-dispatchable units such as FCs and MTs. In addition, with the very rapid growth of the electric vehicle market, the necessity of studying and then managing these high tech components in the networked microgrids is more than before. To this end, a novel framework based on the vehicle-to-grid technology is suggested which makes it possible for the networked microgrid to make use of the electric vehicles as active power sources. This reduces their costs and improves the power quality to the electric consumers. A stochastic energy management framework based on unscented transform is devised which captures the uncertainties associated with the departure and arrival times of the electric vehicles for scheduling concerns, wind power oscillations, solar radiations, and the forecast error in the hourly load demands of the microgrids' consumers. The objective function incorporates the cost of power supply for DGs, cost of power bought from the neighboring connected microgrid, cost of power trading with the power grid and cost of shut-down or starts-up of the units. Moreover, in order to make the analysis more practical, the V2G cost as a battery degradation issue is modeled in the cost function to reflect the amount of life damage which is received by the battery. Due to the high complexity and very nonlinear formulation of the problem, a new optimization algorithm based on bat algorithm (BA) is devised. In addition, a novel modification method is used to enhance the search ability of the algorithm and help it to get directly to the optimal global solution. The performance of the suggested approach is examined on an IEEE test networked microgrid with several DGs, RESs, and electric vehicles.

II. NETWORKED MICROGRID FORMULATION WITH RESS AND ELECTRIC VEHICLES

A. Technologies in the Microgrid

Networked microgrids which simultaneously incorporate several DGs and RESs can provide vital benefits to the utilities and the power consumers including but not limited to more reliable power supply, higher security, improved voltage profile, more economic scheduling and planning schemes, less power losses and more power balance. In the eyes of the main grid operators, the networked microgrid is a quite controllable unit which can be a big help for the utility to get into its main purposes. In fact, networked microgrid idea brings a new concept to the smart grid technology for higher support of the fine idea of RESs and electric vehicles

for a cleaner future. From the consumers' points of view, the networked microgrid is a set of microgrids which are ringed to provide a more stable and reliable power source which probably can benefit them by lower price and higher power quality services. This is a special situation which can benefit both sides of a deal, i.e. the consumers and the utility, simultaneously. Fig. 1 shows the structure a regular networked microgrid. According to this figure, although the networked microgrid concept shows a more complex idea for the microgrids, but the supporting role of microgrids for supplying power through exchange is the key point of its success. With the advent of electric vehicles and RESs, the necessity of studying the optimal operation and management of networked microgrids is felt more than before. Therefore, the next part provides a holistic model to formulate the networked microgrid operation problem in a real environment with high penetration of DGs, RESs, and electric vehicles.

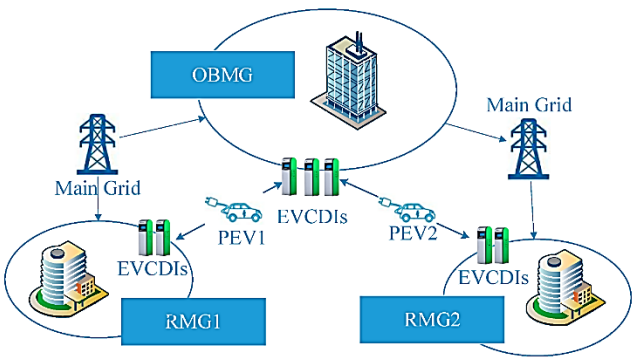

Fig. 1. The idea of multi-microgrids in the structure and technology

B. Problem Formulation

The proposed problem formulation is a single-objective constraint optimization problem which aims to minimize the total cost of the networked microgrid incorporating the cost of power purchasing from internal DGs, cost of power purchasing from the other grids (either main grid or other microgrids and), cost of shut-down and start-up units and cost of V2G due to the repeating charging/discharging of the electric vehicle battery as follows [2]:

$$Min\ \ E(f(X)) = Cost^{DG} + Cost^{sd/st} + Cost^{bat} + Cost^{exch} + Cost^{V2G} \quad (1)$$

$$Cost^{DG} = \sum_{k=1}^{N_{MG}} \sum_{t=1}^{T} \left(\sum_{i=1}^{N_{DG}} [u_{itk}\ E(p_{itk}^{G}) B_{ik}^{G} \right) \quad (2)$$

$$Cost^{sd/st} = \sum_{k=1}^{N_{MG}} \sum_{t=1}^{T} \begin{pmatrix} S_{ik}^{G-off} \max\{0, u_{i(t-1)k} - u_{itk}\} + \\ S_{ik}^{G-on} \max\{0, u_{itk} - u_{i(t-1)k}\} \end{pmatrix} \quad (3)$$

$$Cost^{bat} = \sum_{k=1}^{N_{MG}} \sum_{t=1}^{T} \left(\sum_{j=1}^{N_S} [u_{jtk} E(p_{jtk}^{s}) B_{sk} \right) \quad (4)$$

$$Cost^{exch} = \sum_{k=1}^{N_{MG}} \sum_{t=1}^{T} \left(E(p_{tk}^{grid}) B_{tk}^{grid} \right) \quad (5)$$

$$Cost^{V2G} = \sum_{k=1}^{N_{MG}} \sum_{t=1}^{T} \left(\sum_{t=1}^{T} \sum_{v=1}^{N_v} c_{vtk}^{PEV} P_{vtk}^{PEV} + \sum_{z=1}^{N_{dis}} C_{zk}^{d}(\gamma^{I}, \gamma^{F}) \right) \quad (6)$$

where X is the problem variables, N_{DG} shows the number of generators, T is the number of operation hours, N_{MG} shows the quantity of microgrids, N_S shows the quantity of batteries, N_v shows the number of vehicle fleets, C_{vtk}^{PEV} is charging/discharging cost of electric vehicles, $C_{zk}^{d}(\gamma^{I}, \gamma^{F})$ is the battery degradation cost from initial status of γI to γf, N_{dis} shows the quantity of charge/discharge cycles per the operation time horizon, u_{itk} is the On/Off for i^{th} DG, p^{G}_{itk} is the power generation of i^{th} DG, B^{G}_{ik} is the electricity price offer by i^{th} DG, S_{ik}^{G-on} shows start-up price by i^{th} DG, S_{ik}^{G-off} shows the shut-down price by i^{th} DG, u_{jtk} is the On/Off for j^{th} battery, p^{s}_{jtk} shows the offer of j^{th} battery, B^{S}_{ik} is the electricity price offer of the i^{th} battery, S_{ik}^{S-on} represents the start-up price by i^{th} battery, S_{ik}^{S-off} represents the shut-down price by i^{th} battery, p_{tk}^{grid} is the power generation of the grid, B_{tk}^{grid} is the electricity price offer of the main grid to microgrid k. It worth noting that here we have used the operator $E(.)$ to show the expectation operator.

The battery degradation cost is calculated as a function of the number of cycles (charging and discharging together) that an electric vehicle experiences during its operation. This can be shown as (7). In this equation, the cost of battery degradation from the initial SoC of γ^{I} to the final SoC of γ^{F} is calculated. In (8), the expected cost of battery at a specific SoC value γ^{s} is shown based on the maximum number of cycles which it can experience over its life based on the Wöhler curve which is explained later [5].

$$\sum_{z=1}^{N_{dis}} C_z^{d}(\gamma^{I}, \gamma^{F}) = \sum_{z=1}^{N_{dis}} C_z^{d}(0, \gamma^{F}) - C_z^{d}(0, \gamma^{I}) \quad (7)$$

$$C_z^{d}(0, \gamma^{s}) = \frac{C^{bat} \times \gamma^{s} \times E^{bat}}{N^{c}(\gamma^{s})} \quad (8)$$

where E^{bat} is the battery energy and C^{bat} is the cost battery.

As that is seen in (8), in order to calculate the battery degradation cost, the Wöhler curve is needed. As per definition, the Wöhler curve calculates the number of cycles a battery can experience before getting damaged. Fig. 2 shows the Wöhler curve for a typical battery [5]. Wöhler curve is formulated in a math format which is shown as $Nc(\gamma)=a.\gamma^{b}$ [16] where parameters a and b are found based on the battery type.

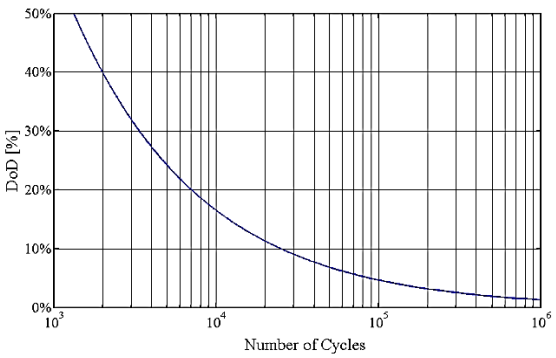

Fig. 2. Wöhler curve for a typical battery [5]

The above cost function (1) is optimized meeting several equality and practical inequality constraints which are explained in the rest:

The generation and demand balance can be met by converging the AC power flow in the microgrids as follows [9]:

$$E(P_{mtk}^{Inj}) = \sum_{n=1}^{N_B} E(V_{tmk})E(V_{tnk})Y_{mnk}\cos\left(\theta_{mnk} + E(\delta_{mtk}) - E(\delta_{ntk})\right) \quad (9)$$

$$E(Q_{mtk}^{Inj}) = \sum_{n=1}^{N_B} E(V_{tmk})E(V_{tnk})Y_{mnk}\sin\left(\theta_{mnk} + E(\delta_{mtk}) - E(\delta_{ntk})\right) \quad (10)$$

where V_{tmk} is bus voltage number m at hour t in microgrid k, Y_{mnk} is feeder admittance linking buses m to n, θ_{mnk} is the admittance phase between busses m to n, δ_{mtk} is bus voltage angle. As it can be seen from the above equation, it is quite nonlinear so it will be solved using the backward-forward sweep approach.

There are limitations due to the capacity for DGs power generation as follows [9]:

$$p_i^{G,\min} \le E(p_{itk}^G) \le p_i^{G,\max} \quad (11)$$

where $p_i^{G,\min}$ / $p_i^{G,\max}$ displays the lower/upper power capacity of unit i.

For the main grid and storage battery, the rule is the same. The maximum and minimum power capacity is as follows [9]:

$$p_j^{s,\min} \le E(p_{jtk}^s) \le p_j^{s,\max} \quad (12)$$

$$p^{grid,\min} \le E(p_t^{grid}) \le p^{grid,\max} \quad (13)$$

where $p_j^{s,\min}$ / $p_j^{s,\max}$ is the lower/upper charge/discharge limit and $p^{grid,\min}$ / $p^{grid,\max}$ is the lower/upper limit of the utility. For the battery storage, the maximum energy storage capacity is calculated according to its initial state of charge (SoC) and the hours it is charging/discharging as follows [9]:

$$E(W_t^{ess}) = E(W_{t-1}^t) + \eta^{charge}E(P_{charge})\Delta t - \frac{1}{\eta^{discharge}}E(P_{\text{discharge}})\Delta t \quad (14)$$

$$\begin{cases} W^{ess,\min} \le E(W_t^{ess}) \le W^{ess,\max} \\ E(P_t^{charge}) \le P^{charge,\max} \\ E(P_t^{discharge}) \le P^{discharge,\max} \end{cases} \quad (15)$$

where W_t^{ess} is the energy stored, η^{charge} and $\eta^{discharge}$ are the charge/discharge efficacy.

According to its materials and diameter, each feeder is capable of transferring a specific amount of power which is shown as follows [9]:

$$|E(P_{lt}^{Line})| < P_l^{Line,\max} \quad (16)$$

where P_{lt}^{Line} is the value of the power flow in line l at time t and $P_l^{Line,\max}$ is the maximum allowed power limit in line l.

Technically, the microgrid voltage should be preserved in the safe zone as follows [9]:

$$V_m^{\min} \le E(V_{mt}) \le V_m^{\max} \quad (17)$$

Regarding the electric vehicle, some constraints need to be considered. When connected to the charger, the electric vehicle may experience three different modes of operation including idle mode U_{vt}^I =1, charging model U_{vt}^c =1,and discharging mode U_{vt}^d =1. Therefore, the electric vehicle may be in only one mode of operation at each time as (18) [5, 11]:

$$U_{vt}^c + U_{vt}^d + U_{vt}^I = U_{vt} \quad (18)$$

There is a limit on the maximum power charging/discharging by the electric vehicle as follows [5, 11]:

$$P_v^{c,\min} \le P_{vt}^c \le P_v^{c,\max} \quad (19)$$

$$P_v^{d,\min} \le P_{vt}^d \le P_v^{d,\max}$$

The sum of energy stored in the electric vehicle is calculated as (20). This energy should not exceed the total capacity of the electric vehicle as in (21) [5]:

$$E_{vt} = E_v^{ini} + \sum_{l=1}^{t}(U_{vt}^c P_{vl}^c \eta_v^c - U_{vt}^d P_{vl}^d \eta_v^d) - \sum_{l=1}^{t}(1-U_{vl})E_{vl}^D \quad (20)$$

$$E_v^{\min} \le E_{vt} \le E_v^{\max} \quad (21)$$

where η_v^c / η_v^d are the charging/discharging efficiency of the electric vehicle and E^D is the energy for PEVs in a fleet to drive.

The electric vehicle is supposed to keep the same amount of energy at the end of the day as the amount of energy it had at the beginning of the day [5]:

$$E_v^{fin} = E_v^{ini} \quad (22)$$

Also, it is supposed that the electric vehicle battery is charged

to its maximum capacity when leaving the home in the morning [5]:

$$E_v^{t'} = E_v^{\max} \tag{23}$$

where *t'* shows the time of the first travel in the morning.

III. Stochastic Framework Based on Unscented Transform

As it was mentioned in the previous sections, the proposed problem contains much uncertainty mainly arising from the RESs such as WT and PV as well the electric vehicles traveling pattern for example departure time and arrival time and the number of vehicles available. More than that, the prediction error in the hourly load demand in the microgrid is a serious issue which due to its low voltage level should be modeled, precisely. Therefore, this paper makes use of unscented transform [19] to construct a strong and reliable stochastic framework for modeling the uncertainties of the above problem. In contrast to the Monte Carlo method which uses a very high number of samples to converge, unscented transform only uses $2p+1$ points, wherein p is the number of uncertain parameters. In order to better perceive the unscented transform, let's consider the whole nonlinear format of our problem as $V_O=F(V_I)$ in which V_I is the output vector of the stochastic input vector V_O. Let's also assume that r is the uncertain parameter with a normal distribution, mean value and standard deviation of $\bar{m}$ and D, respectively. The unscented transform requires to extract $2p+1$ points to model the uncertainty effects through some recursive steps as follows:

Step 1: Find $2p+1$ samples as follows:

$$V_I^{\,0} = \bar{m} \tag{24}$$

$$V_I^{\,\kappa} = \bar{m} + \left(\sqrt{\frac{r}{1-W^0}}\,Q_{VI}\right)_\kappa \qquad \forall \kappa \in \Omega^\kappa \tag{25}$$

$$V_I^{\,\kappa+p} = \bar{m} - \left(\sqrt{\frac{r}{1-W^0}}\,Q_{VI}\right)_\kappa \qquad \forall \kappa \in \Omega^\kappa \tag{26}$$

where Q_{VI} represents the input covariance matrix and also W^0 is the initial weigh corresponding to $\bar{V}_I = \bar{m}$.

Step 2: find the weights associated with each sample point as follows:

$$\omega^0 = \omega^0 \tag{27}$$

$$\omega^\kappa = \frac{1-\omega^0}{2p} \qquad \forall \kappa \in \Omega^\kappa, \kappa = 1,2,...,p \tag{28}$$

$$\omega^{\kappa+p} = \frac{1-\omega^0}{2p} \qquad \forall \kappa \in \Omega^\kappa, \kappa+p = p+1,...,2p \tag{29}$$

It should be noted that the sum of the weights must equal 1.

Step 3: find the mean output vector $\bar{V}_O$ and the output covariance matrix Q_{VO} by running some equations as below:

$$\bar{V}_O = \sum_{l\in\Omega^l} \omega^l V_O^l \qquad \forall l \in \Omega^l, l = 1,2,...,2p \tag{29}$$

$$Q_{VO} = \sum_{l\in\Omega^l} W^l (V_O^l - \bar{V}_O)\left(V_O^l - \bar{V}_O\right)^T \qquad \forall l \in \Omega^l, l = 1,2,...,2p \tag{30}$$

Fig. 3 shows the concept of the unscented transform used in this paper for modeling the uncertainty effects.

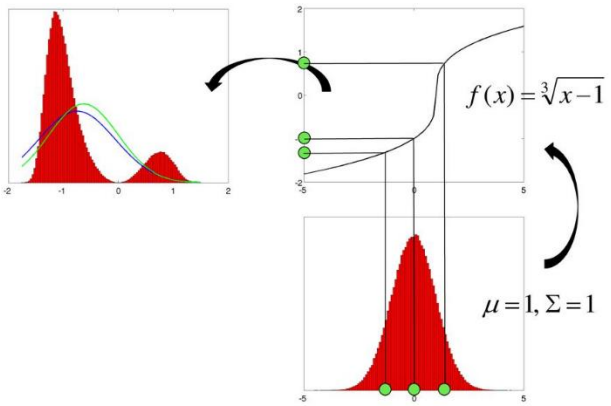

Fig. 3. The nonlinear mapping happening the unscented transform

IV. Modified Bat Optimization Algorithm

As it can be inferred from the problem formulation in section II, the problem structure is a kind of hard one which if not solved by a global search algorithm may fell in the local optima. In order to deal with this issue, this paper proposes a fresh optimization approach, called BA, to solve the problem. In addition, a new modification method is proposed to help the algorithm to improve its shortcoming and escape from the premature convergence. BA was initially developed in 2010 by Xin-She Yang [20] as an evolutionary algorithm mimicking the foraging behavior of bats in nature. Being among the top algorithms in those days, BA was constructed based on the echolocation process of bats in distinguishing between a food and prey. In fact, these mammals send a signal to the air and wait to hear its echolocation. This process is repeated several times so making them capable of routing even in a dark space. This idea brings a nice concept in the mind for making a powerful optimization algorithm, called BA. In the principal body, the BA is constructed based on four ideas: a bat X_b flies with a speed of V_b in the dark space and generates a signal of the frequency f_b with magnitude A_b. 2) the signal power (represented by its magnitude A_b) reduces as time is spent from high to a low level. 3) the echo assistances the bat to differentiate between a food and a prey. 4) the frequency f_b and rate r_b change in an unconscious course.

Initially, a set of bats are generated randomly in the feasible region of the problem. Each bat contains some numbers

showing the optimal value of the control variables of the problem. After calculating the cost function value for any bat, the dominant bat X_g is saved and the remained bats need to get progressed as follows:

$$\begin{aligned} \mathbf{V}_b^{Iter+1} &= \mathbf{V}_b^{Iter} + f_b(X_g - X_b) \qquad ;b=1,\ldots,N_{Bat} \\ X_b^{Iter+1} &= X_b^{Iter} + \mathbf{V}_b^{Iter} \qquad ;b=1,\ldots,N_{Bat} \\ f_b &= f_b^{\min} + \varphi_1(f_b^{\max} - f_b^{\min}) \qquad ;b=1,\ldots,N_{Bat} \end{aligned} \tag{31}$$

Where N_{Bat} is the size of bat population; $f_b^{\max}$ / $f_b^{\min}$ are the lower/upper limits for the frequency of b^{th} bat. Also, φ_1 to φ_6 are random parameters in the range (0,1] in this article.

In addition to the above movement, bat algorithm is equipped with a random search as well. After generating a random value β, it is compared with the signal rate r_b. In the case that it is bigger than the signal rate, then the bat will fix its position in the near surrounding as follows:

$$X_b^{Iter+1} = X_b^{Iter} + \varepsilon A_{mean}^{Iter} \qquad ;i=1,\ldots,N_{Bat} \tag{32}$$

Where ε is a random value in the range of [-1,1] and A_{mean}^{old} is the average value of the bats' frequency loudness. If β is smaller than r_i, a bat X_b^{rand} is generated, randomly. This new bat is verified only if the following two conditions are guarantied:

$$\begin{aligned} &\beta < A_b \\ &f(X_b) < f(Gbest) \end{aligned} \tag{33}$$

Based on the fourth rule of BA, the signal features are updated in an unconscious course:

$$\begin{aligned} A_b^{Iter+1} &= \alpha A_b^{Iter} \\ r_b^{Iter+1} &= r_b^0[1-exp(-\gamma \times Iter)] \end{aligned} \tag{34}$$

Where α and γ are adjusting parameters.

Some special characteristics of the BA are simple concept, high searching ability, few adjusting parameters, no need to differentiation, compatible with mixed integer nonlinear programming, etc. But it still suffers from the premature convergence when facing complex and multi-modal optimization problems. Therefore, this article suggests a new modification method to help BA improve its performance and find the global solution with high probability. These modifications are explained in the following.

Sub-modification method 1**:** Since X_g is the best bat in the population, it can be a good guide for the other bats to accelerate their improvisation process. Therefore, (35) is proposed to improve the population in each iteration. Here the population mean value M_{bat} is evaluated as a scale for the acceleration:

$$X_b^{Iter+1} = X_b^{Iter} + T_F \times \phi_4 \times \left(X_g - M_{bat}\right) \tag{35}$$

Where T_F is a random integer value. Based on (35), the BA can increase its convergence rate using a very good guide of its best bat in every iteration.

Sub-modification method 2**:** This modification method exchanges the control variables between bats to simulate a kind of interaction between them. This is like a knowledge sharing process which helps bats to make use of the others' experiences in finding food. Such an idea can be simulated by the crossover operator as follows:

$$X^{Test1} = \begin{cases} x_{b,j} & ;\ \varphi_4 < \varphi_5 \\ x_{g\,j} & ;\ \varphi_4 \geq \varphi_5 \end{cases} \tag{36}$$

$$X_b = [x_{b,1}, x_{b,2}, \ldots, x_{b,n}]$$

$$X_g = [x_{g1}, x_{g2}, \ldots, x_{gn}]$$

V. Simulation Results

In this section, the performance and capabilities of the proposed stochastic method for optimal operation and management of a networked microgrid are examined. The test system is shown in Fig. 4. It consists of four microgrids connecting with each other and exchanging power with either each other or the main grid. The voltage level is 12.66 (kV). There are several DGs installed in the networked microgrid so that microgrids can supply their own power. Therefore, a PV is installed in bus 10 of microgrid one, a battery unit is installed in bus 36 of microgrid one, an MT is installed in bus 63 of microgrid one. There is one WT installed in bus 10 in the microgrid two. There is a wind turbine in bus 18 of microgrid 3. Finally, microgrid number 4 has an FC installed on bus 43 and an MT on bus 53. According to the figure, the networked microgrid is capable of power exchange with the main grid. There are three electric vehicles fleets considered in the networked microgrid traveling on different paths. The travel pass of the electric vehicle fleets number one is all inside the microgrid number one, between the buses 4 and 37. Electric vehicle fleet number two travels between the first and the second microgrids, though the buses 13 and 42. Finally, the electric vehicle fleet number three travels between the third and the fourth microgrid. Tables I and II show the specifications of the electric vehicle fleets including their charging/discharging capacity and departure and arrival time and location. According to Table II, each electric vehicle experiences two travels in a day one from home to the work office and then a second one from the work office heading to the home. Therefore, during the hours that they are in the parking (either the office parking or home parking), the vehicles are unused and can attend the V2G plan to earn money and reduce the microgrid costs.

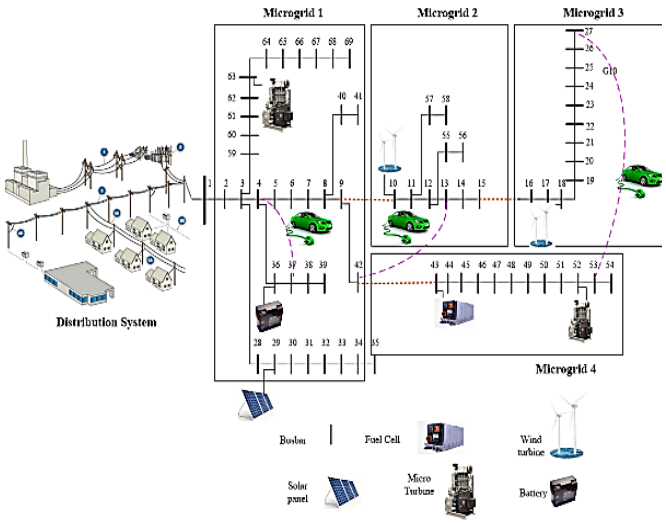

Fig. 4. Networked MG system incorporating RESs, DGs and electric vehicles

TABLE I
PEV FLEET TRAVEL CHARACTERISTICS

Fleet Number	First Trip				Second Trip			
	Departure		Arrival		Departure		Arrival	
	Time	Bus	Time	Bus	Time	Bus	Time	Bus
One	6	5	8	35	15:00	35	17:00	5
Two	8	52	9	29	18:00	29	19:00	52
Three	8	15	9	41	13:00	41	14:00	15

TABLE II
FEATURES OF THE ELECTRIC VEHICLE FLEETS

Fleet Number	Capacity (kWh)		Charge/Discharge rate (kW)	
	Min	Max	Min	Max
One	263	1973	7.3	496
Two	219	1644	7.3	292
	210	1812	7.3	313

Regarding the DGs, their characteristics are shown in Table III. For the storage unit, the charging/discharging rate is 200 kW/hour and the maximum storage capacity is 2000 kWh. Some data in Table III (such as prices) are borrowed from [21]. The problem is solved for 24 hours. For non-dispatchable units such as WT and PV, their forecast power is plotted in figures 5 and 6. It is well accepted that RESs due to their non-dispatchable nature may generate as much power as they can. Also figures 7 and 8 show the load power factor of the grid and the market price, respectively.

TABLE III
Features of the Distributed Units Deployed In The Microgrid

Unit	Type	Cost Coefficient ($/kWh)	Min-Max Capacity (kW)	Start-up Or shut-down Cost
WindUnit1	ND	1.0734	0, 1600	0
WindUnit 2	ND	1.073	0, 1920	0
SolarUnit	ND	2.584	0, 2300	0
Fuelcell	D	0.294	90, 1400	0.96
MicroTurbine1	D	0.457	120, 1500	1.65
MicroTurbine2	D	0.457	120, 1700	1.65
Utility	-	-	500, 2500	-

D: Dispatchable, ND: nondispatchable

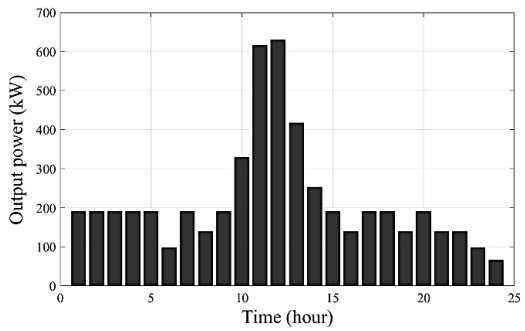

Fig. 5. Forecast wind turbine output power pattern

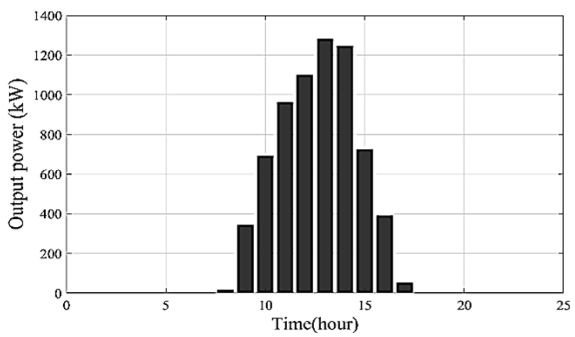

Fig. 6. Forecast photovoltaic unit output power generation

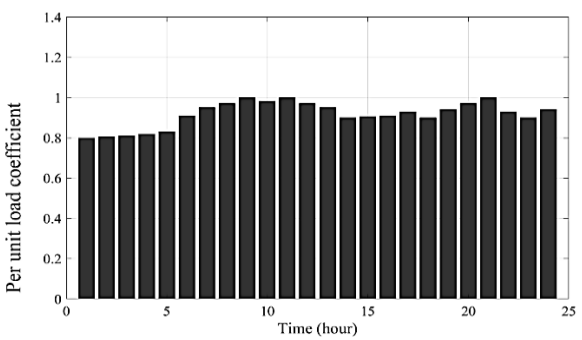

Fig. 7. System load factor over 24 hours based on the IEEE peak load value

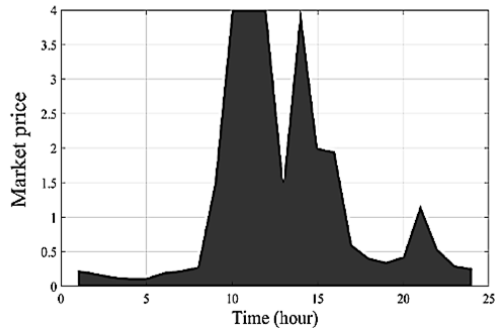

Fig. 8. Electricity market price offered by the main grid

Two different scenarios are simulated in this paper to reveal the capabilities of the proposed method. In the first scenario, electric vehicles are ignored and DGs and batteries are only considered. DGs can also switch On or Off depending on their preferences. In the second scenario, electric vehicles charging and possible discharging demands are considered in the microgrid. Table IV and V show the optimal power dispatch of the networked microgrid in the first and second scenario. According to these results, the microgrids number two and three have to purchase their extra power needs from the first microgrid since they only have RESs of WT and PV as DGs inside their areas. This reveals the significant role of microgrid number one in bridging between the main grid and other microgrids which can increase its profits. The situation is different for microgrid number four since it has dispatchable DGs of FC and MT and thus can only rely on internal productions for the power supply. This provides a more economic position for this microgrid to reduce its cost and attend the power trade when benefits. For microgrid number one, it has both adequate internal power generation capacity and a direct connection to the main grid. Therefore, this makes it the most stable microgrid which can reduce its costs by optimal managing of its units and the main grid. For the battery, it is seen that the battery is charged at the beginning of the day to get discharged later at the peak-load times. This is a very economic plan for making the maximum advantage of the storage units.

TABLE IV
Optimal Power Dispatch Of Units In Scenario One

Time (h)	Wind turbine 1 (kW)	Wind turbine 2 (kW)	Photovoltaics (kW)	Fuel cell (kW)	Micro Turbine 1 (kW)	Micro Turbine 2 (kW)	Storage Unit (kW)
1	190.4000	228.4800	0	0	0	0	0
2	190.4000	228.4800	0	0	0	0	-29.8166
3	190.4000	228.4800	0	0	0	0	-61.6241
4	190.4000	228.4800	0	0	0	0	-96.5816
5	190.4000	228.4800	0	0	0	0	-78.3473
6	97.6000	117.1200	0	0	0	0	-32.0543
7	190.4000	228.4800	0	0	0	0	-120.1656
8	139.2000	167.0400	18.4	0	0	0	-22.8289
9	190.4000	228.4800	345.0	1226.5	1079.1	548.3	184.3805
10	329.6000	395.5200	692.3	1035.9	1237.7	226.4	-191.2522

Table IV continued

11	616.0000	739.2000	961.4	472.1	126.7	916.0	-29.2607
12	630.4000	756.4800	1099.4	372.3	232.1	469.1	128.4086
13	417.6000	501.1200	1278.8	770.8	363.7	411.8	-131.7213
14	252.8000	303.3600	1246.6	979.3	4381	243.6	-41.7469
15	190.4000	228.4800	724.5	1201.0	1203.7	0	-107.0821
16	139.2000	167.0400	388.7	1290.3	722.0	601.1	151.6652
17	190.4000	228.4800	50.6	1052.5	1500.0	442.6	71.4839
18	190.4000	228.4800	0	1400.0	1222.2	0	137.0802
19	138.8800	166.6560	0	1129.5	0	1700.0	127.1509
20	190.4000	228.4800	0	1093.9	603.1	1700.0	-127.8503
21	138.7200	166.4640	0	1378.4	831.3	1212.1	75.1165
22	138.7200	166.4640	0	1399.9	741.8	894.1	195.0461
23	97.6000	117.1200	0	1336.0	0	0	0
24	65.6000	78.7200	0	0	0	0	0

TABLE V
Optimal Power Dispatch of Units in Scenario Two

Time (h)	Wind turbine 1 (kW)	Wind turbine 2 (kW)	Photovoltaics (kW)	Fuel cell (kW)	Micro Turbine 1 (kW)	Micro Turbine 2 (kW)	Storage Unit (kW)
1	190.4	228.48	0	0	411.1801	0	-0.0137
2	190.4	228.48	0	0	264.2646	0	-2.6450
3	190.4	228.48	0	223.7159	0	0	-17.6346
4	190.4	228.48	0	0	0	0	-85.1593
5	190.4	228.48	0	0	0	0	-1.4869
6	97.6	117.12	0	0	0	243.9681	10.9565
7	190.4	228.48	0	0	0	244.5895	9.9259
8	139.2	167.04	18.4	0	0	0	20.7859
9	190.4	228.48	345.0	792.5566	1053.9803	363.5021	37.8371
10	329.6	395.52	692.3	721.9271	571.0821	392.4715	-82.7094
11	616.0	739.20	961.4	467.8826	0	422.9153	55.9942
12	630.4	756.48	1099.4	0	884.4738	357.0653	-79.4686
13	417.6	501.12	1278.8	0	760.7829	666.2651	-34.7672
14	252.8	303.36	1246.6	378.7729	0	656.9597	-90.9020
15	190.4	228.48	724.5	1014.6598	638.2393	781.7054	50.4240
16	139.2	167.04	388.7	1025.3934	720.9894	1340.4373	-54.6269
17	190.4	228.48	50.6	1399.7238	561.0359	637.0073	-14.5553
18	190.4	228.48	0	1400	0	437.5930	74.7302
19	138.88	166.656	0	0	0	0	93.0087
20	190.4	228.48	0	0	0	382.9724	83.6701
21	138.72	166.464	0	436.2503	1500	1028.4159	26.6084
22	138.72	166.464	0	719.7058	1040.1948	1036.9315	-0.1097
23	97.6	117.12	0	275.4172	634.9327	0	-0.02351
24	65.6	78.72	0	0	0	0	0.05193

Table VI shows the optimal operating point of electric vehicle fleets in the second scenario. According to this table, the electric vehicles are neither in charging mode nor discharging mode when they are on the road. Owing to the V2G technology, now the vehicles are changing their role from just-consuming components into active players which could discharge at heavy loading condition. It is seen that vehicles could actively attend the V2G plan when parked in the parking and are unused. This is a wise strategy for making the maximum advantage of these devices for benefiting the microgrid. For sure it has some unwanted costs which is modeled as the battery degradation cost in the objective function.

TABLE VI
Electric Vehicle Fleets Performance for 24 Hours

Time (h)	Electric Vehicle Fleet Number 1	Electric Vehicle Fleet Number 2	Electric Vehicle Fleet Number 3
1	139.41601	192.9079	0
2	480.38419	174.7460	1.8396
3	-308.6526	-291.9977	0
4	275.2524	292	288.4197
5	496	292	311.7763
6	0	292	247.3129
7	0	0	287.0541
8	-153	-180	0
9	-331.0259	-279.4162	-180
10	-301.8570	-128.5881	-275.5103
11	-90.9377	-226.1966	-221.6559
12	332.8514	-108.1917	-264.4336
13	-248.7874	0	169.8892
14	-338.8346	-155.5431	-180
15	259.2956	53.4450	-125.3398
16	-85.5866	91.43379	261.2915
17	0	-107.2613	-274.8871
18	0	0	162.6318
19	-153	-180	311.6599
20	400.1334	63.7333	-147.2028
21	-189.5206	-155.9086	-160.3014
22	-270.9295	155.6934	-312.9647
23	0	-20.48481	-211.3681
24	0	-216.1296	-1.4083

The convergence characteristics of the proposed MBA for a hundred and fifty iterations considering electric vehicles and RESs (second scenario) are shown in Fig. 9. As it can be seen from this figure, the proposed algorithm shows a robust convergence in optimizing the cost objective function. Also, it is seen that it could converge before a hundred iteration which is a very good performance.

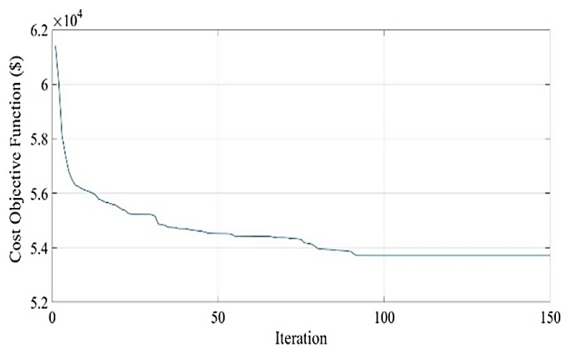

Fig. 9. Convergence characteristics of the algorithm over a hundred iteration in the second scenario

In order to better perceive the appropriate capability of the proposed stochastic framework, Fig. 10 shows the comparative cost function value plots in the first and second scenarios with and without considering the uncertainty effects. Here, the stochastic framework uses unscented transform to model the uncertainties of the WT, PV, load demand and vehicle behaviors. The first conclusion from this figure is that the electric vehicles can help to reduce the cost function if designed well by the V2G technology. This is a quite great result since it was expected that the vehicles appearance in the networked microgrid will increase its cost. But on the contrary, the cost was reduced since they can now play the role of a mobile storage to reduce the heavy loading effects on the microgrids. The second conclusion comes around the uncertainty effects. It is seen that modeling the uncertainty has increased the cost values. This could be expected since with uncertainty, the analysis is now more realistic and thus it is assumed to pay money for remaining in the safe zone. In overall, the results advocate the appropriate and reliable presentation of the proposed stochastic framework.

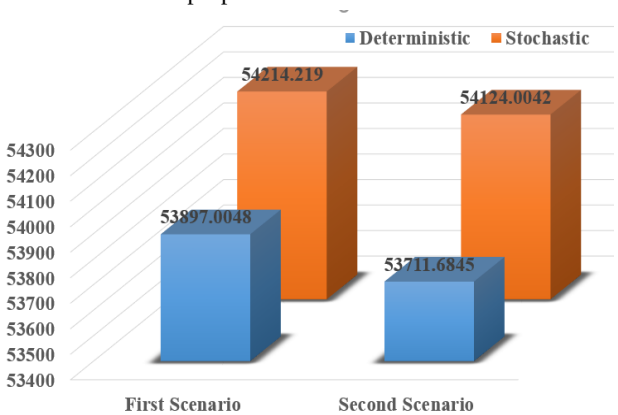

Fig. 10. Stochastic framework and the deterministic optimizing cost function in the networked microgrid.

VI. CONCLUSION

Networked microgrid idea include many returns not only to the customers but also to the power grids and the single microgrids. This article tries to investigate the optimal energy management in a networked microgrid considering the most advanced technologies of DGs such as WT, PV, FC and MT as well as electric vehicles and storage units. We used a stochastic framework to not only solve the optimal economic dispatch of the units but also capture the uncertainty effects of RESs, electric vehicle and load demand. The new framework is constructed based on unscented transform and MBA to provide a very good tool for managing a networked microgrid. The main paper outcomes can be summarized as below:

- The simulation results on a test networked grid with four interconnected microgrids through two different scenarios show that the model developed in this paper is capable to provide appropriate performance for the microgrids. It was seen that storage unit attends the economic program of the networked microgrid and can mitigate the total costs

by charging the cheap load hours and discharge at peak-load hours. All renewable sources attended the power dispatch plan as forecasted.

- It is seen that V2G technology may have some degradation cost but can change the passive role of electric vehicles from just-consumers into the active role of mobile storages. This could reduce the networked microgrid costs by letting the vehicles attend the V2G plans when parked in the parking of office or home.
- From the optimization point of view, the proposed MBA shows robust performance in optimizing the cost function. The total cost of operation of the networked microgrid in the first and second scenarios (incorporating uncertainty effects) 54214.219$ are 54124.0042$ respectively.
- From the uncertainty point of view, modeling the uncertainty increased the operating costs but will provide a safe zone for the reliable operating of the microgrids. Although the stochastic framework based on UT added 0.586% and 0.762% to the cost function value in the first and second scenarios, the new results are more realistic and trustable for the test system.

References

[1] L. Che, M. Shahidehpour, A. Alabdulwahab, Y. Al-Turki, "Hierarchical Coordination of a Community Microgrid With AC and DC Microgrids", *IEEE Trans. Smart Grid*, Vol. 6, No. 6, pp. 13-27, 2015.

[2] B Wang, M Dabbaghj, A Kavousi-Fard, S Mehraeen, "Cybersecurity Enhancement of Power Trading Within the Networked Microgrids Based on Blockchain and Directed Acylic Graph Approach", *IEEE Trans. Indus. Applications* Vol. 55, No. 6, pp. 7300 – 7309, 2020.

[3] R Sedaghati, A Kavousi-Fard, "A hybrid fuzzy-PEM stochastic framework to solve the optimal operation management of distribution feeder reconfiguration considering wind turbines", *Journal of Intelligent & Fuzzy Systems* Vol. 26, No. 4, pp. 1711-1721, 2014.

[4] Md. Rasheduzzaman, Jacob A. Mueller, Jonathan W. Kimball, "Reduced-Order Small-Signal Model of Microgrid Systems", *IEEE Trans. Sustainable Energy*, Vol. 6, No. 4, pp. 33-49, 2015.

[5] A Kavousi-Fard, T Niknam, M Fotuhi-Firuzabad, "Stochastic Reconfiguration and Optimal Coordination of V2G Plug-in Electric Vehicles Considering Correlated Wind Power Generation", *IEEE Trans. Sustainable Energy* Vol. 6 , No. 3, pp. 822-830, 2015.

[6] Z. Zhao, P. Yang, J.M. Guerrero, Z. Xu, T.C. Green, "Multiple-Time-Scales Hierarchical Frequency Stability Control Strategy of Medium-Voltage Isolated Microgrid", *IEEE Trans. Power Electronics*, Vol. 31, No. 8, pp. 443-455, 2016.

[7] K. Moharm, "State of the art in big data applications in microgrid: A review", *Advanced Engineering Informatics*, Vol. 42 No. 1, pp. 134-142, October 2019.

[8] A. Naebi Toutounchi, S. Seyedshenava, J. Contreras, A. Akbarimajd, " Stochastic Bilevel Model to Manage Active Distribution Networks With Multi-Microgrids", *IEEE Systems Journal*, Vol. 1, No. 99, pp. 1-12, 2019.

[9] A Kavousi-Fard, A Zare, Amin Khodaei, "Effective Dynamic Scheduling of Reconfigurable Microgrids", *IEEE Trans. Power Systems*, Vol. 23, No. 5, pp. 5519 - 5530, 2018.

[10] R. Zhang, K. Yan, G. Li, T. Jiang, H. Chen, "Privacy-preserving decentralized power system economic dispatch considering carbon capture power plants and carbon emission trading scheme via over-relaxed ADMM", *International Journal of Electrical Power & Energy Systems*, Vol. 121, pp. 543-561, October 2020.

[11] M. S. Javadi; A. Anvari-Moghaddam; J. M. Guerrero, "Optimal scheduling of a multi-carrier energy hub supplemented by battery energy storage systems", 2017 IEEE International Conference on Environment and Electrical Engineering and 2017 IEEE Industrial and Commercial Power Systems Europe (EEEIC / I&CPS Europe), 6-9 June 2017, Milan, Italy.

[12] A. Ouammi, H. Dagdougui, R. Sacile, "Optimal Control of Power Flows and Energy Local Storages in a Network of Microgrids Modeled as a System of Systems", IEEE Trans. Control Systems Technology, Vol. 23 , No. 1, pp. 128 – 138, 2015.

[13] M. R. Sandani, S. Sirousour, "Priority-Based Microgrid Energy Management in a Network Environment, IEEE Trans. Sustainable Energy, Vol.9 , No. 2, pp. 980 – 990, 2018.

[14] Y. Du, F. Li, "Intelligent Multi-microgrid Energy Management based on Deep Neural Network and Model-free Reinforcement Learning", IEEE Trans. Smart Grid, Vol. 99, No. 1, pp. 1-11, 2019.

[15] H. Haddadian, R. Noroozian, "Multi-Microgrid-based Operation of Active Distribution Networks Considering Demand Response Programs", IEEE Trans. Sustainable Energy, Vol. 99, No. 1, pp. 346-354, 2019.

[16] Y. Zhu, F. Zhuo, F.Wang, B.Liu, R. Gou, Y. Zhao, "A Virtual Impedance Optimization Method for Reactive Power Sharing in Networked Microgrid", *IEEE Trans. Power Electronics*, Vol. 31, No. 4, pp. 2890 – 2904, 2016.

[17] D. Gregoratti, J.Matamoros, "Distributed Energy Trading: The Multiple-Microgrid Case", *IEEE Transactions Indus, Electronics*, Vol. 62, No. 4, pp. 2551 – 2559, 2015.

[18] L. Yung-Tang Liao, L. Chan-Nan Lu, "Dispatch of EV Charging Station Energy Resources for Sustainable Mobility", *IEEE Trans. Transportation Electrification*, Vol. 1, No. 2, pp. 86 – 93, 2015.

[19] S. Tabatabaee, S. Saeedallah Mortazavi, T. Niknam, "Stochastic energy management of renewable micro-grids in the correlated environment using unscented transformation", *Energy*, Vol. 109, pp. 365-377, 2016.

[20] M.A. Al-Betar, M.A. Awadallah, "Island bat algorithm for optimization", *Expert Systems with Applications*, Vol. 107, pp.126-145, 2018.

[21] A Baziar, A Kavousi-Fard, "Considering uncertainty in the optimal energy management of renewable micro-grids including storage devices", *Renewable Energy* Vol. 59, pp. 158-166, 2013.

Mahdi Vosoogh was born in Kermand and received the B.Sc. degree in electrical engineering from Yazd Azad University in 2009; M.Sc. degree in power system engineering from the Science and Research Branch, Sirjan Azad University in 2013. He is currently a PhD candidate at Sirjan Azad Universirty since 2014. His research interests include smart grids, microgrids, power system optimization, renewable energy sources, electric vehicles, machine learning application in power system and energy management in smart grids.

Masoud Rashidinejad (M'10–SM'14) received the B.Sc. degree in electrical engineering and M.Sc. degree in systems engineering from the Isfahan University of Technology, Khomeyni Shahr, Iran, and the Ph.D. degree in electrical engineering from Brunel University, London, U.K., in 2000.

Prof. Rashidinejad is a professor with the department of the electrical engineering, Shahid Bahonar university of Kerman, Kerman, Iran. His research interests include power system optimization, power system planning, electricity restructuring, energy efficiency, and energy management in smart electricity grids.

Amir Abdollahi received the B.Sc. degree in electrical engineering from the Shahid Bahonar University of Kerman, Kerman, Iran, in 2007, the M.Sc. degree in electrical engineering from Sharif University of Technology, Tehran, Iran, in 2009, and the Ph.D. degree in electrical engineering from Tarbiat Modares University, Tehran, in 2012. Dr. Abdollahi is currently an Associate Professor with the Department of Electrical Engineering, Shahid Bahonar University of Kerman. His current research interests include demand-side management, planning, reliability, and economics in smart electricity grids.

Morteza Ghaseminezhad was born in Bardsir, Iran, in 1985. He received the B.Sc. degree from Electrical Engineering Department of Shahid Bahonar University, Kerman, Iran, in 2007 and the M.Sc. and Ph.D. Degree in electrical engineering from Shahed University, Tehran, Iran, in 2010, and 2017, respectively. At the present, he is the assistant professor of electrical engineering department in Sirjan University of Technology. His especial fields of interest include transient in power systems, power quality and electrical machines.

IECO
This page intentionally left blank.

International Journal of Industrial Electronics, Control and Optimization © 2021 IECO
Vol. 4, No. 2, pp. 257-266, April (2021)

An Improved Sliding Mode Controller for DC/DC Boost Converters Used in EV Battery Chargers with Robustness against the Input Voltage Variations

Gholamreza Mohebalizadeh [1], Hasan Alipour [†,2], Leila Mohammadian[3], Mehran Sabahi[4]

[1, 2, 3] Department of Electrical Engineering, Islamic Azad University, Shabestar Branch, Shabestar, Iran.
[4] Department of Electrical and Computer Engineering, University of Tabriz, Tabriz, Iran.

ABSTRACT

An Electric Vehicle Battery Charger (EVBC) faces serious challenges such as continuous charging voltage ripple, charging speed, input voltage level variations, and its ability to adapt to the Battery State of Charge (BSOC). A proper controller has an important role to play in preparing for all mentioned above. A nonlinear controller such as a Sliding Mode Controller (SMC) is eminently suitable for solving these problems. Therefore, this work presents an improved SMC for taking the control of a DC/DC boost converter such as an EVBC. The proposed controller has a more robust structure when exposed to significant variations of input voltage than the other SMCs. Therefore, this allows the application of various power supplies as input voltages in EVBC stations. The EVBC power and battery voltage/capacity in this converter are assumed to be 14 kW and 400V/60Ah, respectively. The simulation results in Matlab Simulink verify the controller's high performance compared with other SMCs.

Article Info

Keywords:
Battery State of Charge (BSOC), Electric Vehicle Battery Charger (EVBC), Mean Displacement Error (MDE), Renewable Energy Source (RES), Sliding Mode Controller (SMC)

Article History:
Received 2020-05-31
Accepted 2020-11-09

I. INTRODUCTION

An increase in oil prices and concerns over air pollution are prompting the introduction of electric vehicles (EVs) and plug-in hybrid EVs (PHEVs). Nowadays and in the immediate future, considerable regards to establishing stations fully equipped with EVBC are required. On-board and off-board are two classifications of EVBC [1]. On-board EVBCs are installed in EVs. Therefore, their application is faced with main constraints such as weight, volume, and power limitations. Off-board EVBCs, which do not have those constraints, are installed in EVBC stations [2]. Moreover, these EVBCs can be supplied by 3-phase electric grid, ancillary batteries, and Renewable Energy Sources (RESs) such as Photovoltaic Cells (PVCs) and wind turbines [3]. Therefore, a perfect match must occur with these input power supplies. Moreover, the charging current and voltage should be in accordance with the BSOC [4].

These can be fully implemented by applying an SMC. SMCs face serious challenges such as eminently suitable designation of sliding surface and state reference values [5-7]. The output voltage level of EVBC gradually varies in accordance with the SOC. Therefore, the input current also varies and a proper consideration of input reference current requires a considerable degree of flexibility for the controller [8]. Because of using fuel cells as the input voltage and limitation of voltage gain of the boost converter, it is possible to reach the reference voltage level (400V) by considering a large number of cells. So, this consideration increases the number of fuel cells. The constant input voltage and reference

[†] Corresponding Author: hasan.alipour2006@gmail.com
Tel: +98-9141090533, Department of Electrical Engineering, Islamic Azad University, Shabestar Branch, Shabestar, Iran.

current's assumption are the defects of this controller.

In [9], the sliding mode controller for a single-switch cascade converter is proposed. The constant input reference current assumption is the main defect of this controller. In [10], a 3-stage controller with a Dual Active Bridge (DAB) is proposed. The first stage has the Power Factor Correction (PFC) function, and the controller strategy is based on the status of DC link voltage proportional with the instantaneous SOC. Therefore, the controller is complicated and cannot be used in the other input power supplies. In [11], an on-board EVBC is proposed with a compensator consisting of zeta and boost converters cascaded with the Cuk converter. The compensator is used to decrease current and voltage ripples to descend the filter capacitor size resulting in the complication of the controller. In [12], a non-PWM sliding mode controller for a Sheppard-Taylor converter in presented. The reference current proportional with the voltage error is considered. Because of using the non-PWM sliding mode controller, the switching frequency is variable. A cascade buck and boost are applied in [13] in which different duty cycles with variable phase shift structures are considered. The efficiency and power factor are increased. Moreover, the total harmonic distortion is decreased, but the control system is highly complex. A current control in a buck DC/DC converter by means of a PWM-based sliding mode technique is presented in [14]. The output voltage/input current errors as state variables are applied in sliding surface consideration in this work. Moreover, the input reference current is considered a constant quantity. Therefore, the negative effect of input voltage variations in the converter cannot be controlled. A multi-input EVBC using SMC is presented in [15]. The converter's structure is well designed, but the applied state variables in the sliding surface are considered unsuitable and insufficient. More state variables should be applied in complex structures such as these certain types of converters.

This paper proposes an improved SMC to control a DC/DC boost converter as an EVBC. The integral function of the charging voltage error is considered as the input reference current. Therefore, a more robust structure in the input power supply voltage variations is made by this controller, and this distinctive characteristic allows flexibility in the input voltage level variations. Moreover, a minimal amount of charging voltage error, ripple, and mean displacement percentage can be attained in the proposed controller compared to the other SMCs.

This paper consists of seven sections. In section II, a DC/DC boost converter as an EV battery charger is introduced. Section III reviews common sliding mode control approaches. Section IV introduces the proposed controller. In section V, the proposed PWM sliding mode controller simulation results in MATLAB Simulink environment are presented and compared with the other SMCs. Finally, Section VI presents the concluding points.

II. DC/DC BOOST CONVERTER AS AN EVBC

A general battery charger is designed and constructed by a DC/DC converter in a simple structure. The DC input voltage can be prepared by different kinds of RESs. An AC/DC converter is required to supply the grid-line/wind turbine power to its input. The possible variations in these AC powers may cause trouble in the battery charger.

Hint1:

General battery chargers have a fixed-level input voltage related to their application, but an EVBC can be supplied by some different types of input power supplies in an EVBC station. Therefore, an EVBC with robustness against input voltage variations can also be used as a general battery charger.

Hint2:

An AC/DC converter is required in an EVBC station whenever a one-(or three-)phase grid power or a wind turbine is used. Moreover, the input DC voltage variation ranges of EVBC are considered about ten volts in the proposed controller. It is important to mention that the input voltage variation is a cause for the variation of wind/line power. A multi-input DC/DC converter is also required whenever the PV cells are applied to use ancillary batteries beside those cells. The output voltage variation that is applied as an input of the EVBC will be low enough whenever this multi-input converter is well designed.

Fig. 1 shows the DC/DC boost EV battery charger's structure with its controller. The voltage and current gain and the duty cycle equations are presented as (1).

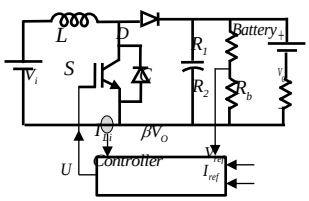

Fig.1. A schematic diagram of the DC/DC Boost Converter

$$D = \frac{T_{on}}{T_S}; G_V = \frac{V_o}{V_i} = \frac{1}{1-D}; G_I = \frac{I_b}{I_L} = 1 - D; \quad (1)$$

where D, V_o, V_i, I_b, I_L, G_I, G_v, T_{on}, and T_s are the duty cycle, the output and input voltage, the output and input current, the current and voltage gain, the ON time of the IGBT function duration, and the switching period, respectively. The output

voltage is instantaneously compared with the reference voltage. The IGBT gate gets no pulses when the output voltage reaches the reference voltage. By applying the equation of Kirchhoff's law, the main boost converter's equation is obtained as (2).

$$\left\{\begin{matrix} V_L = V_i - V_o \times (1-D) \\ i_c = i_L \times (1-D) - i_b \end{matrix}\right\} \Rightarrow \left\{\begin{matrix} \frac{di_L}{dt} = \frac{v_i}{L} - \frac{v_o}{L} \times \bar{D} \\ \frac{dv_o}{dt} = \frac{i_L}{C} \times \bar{D} - \frac{v_o}{R_L C} \end{matrix}\right\} \quad (\bar{D} = 1 - D) \tag{2}$$

where L, C, i_C, and R_L are inductance, capacitance, the capacitor's current, and the output resistance, respectively.

III. Common SMC Approaches

A. Mathematical Formulation

Consider a nonlinear time-dependent switching system defined by the following equation [18]:

$$\dot{x}(t) = g(x(t)) + \Phi(x(t)).u(t)$$

where $x(t)$ is the state variable vector in an n-dimensional space R_n, $g(0)$ and $\phi(0)$ are the smooth vector fields in the same space, and $u(t)$ is the discontinuous control action expressed as:

$$u(t) = \begin{Bmatrix} U^+ ....if, S(x,t) > 0 \\ U^- ....if, S(x,t) < 0 \end{Bmatrix} \tag{3}$$

where U^+ and U^- are either scalar values or scalar functions of $x(t)$ and $S(x, t)$ is the instantaneous feedback-tracking trajectory of the system and is a predetermined function of the state variables. Typically, for the ease of design and implementation, $S(x, t)$ is chosen as a linear combination of the weighted values of the state variables and is given as

$$S(x,t) = \sum_{i=1}^{m} \alpha_i x_i(t) \tag{4}$$

where α_i for i = 1 to m denotes the set of the control parameters known as sliding coefficients and $x_i(t) \in x(t)$. A system with this description is said to exhibit SM property when all the required conditions, namely hitting, existence, and stability conditions, are met.

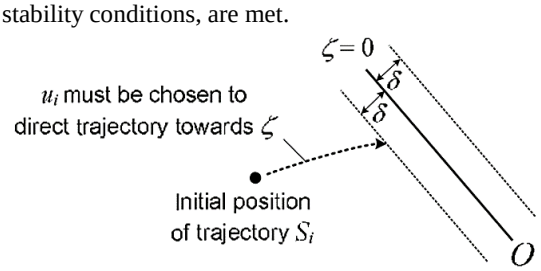

Fig.2. Trajectory S converging to the sliding manifold in the SM control process when the hitting condition is fulfilled.

1) Hitting Condition

The objective of the hitting condition is to ensure that regardless of the location of the initial condition, the corresponding control decision will direct the trajectory of the system to approach and eventually reach, within a vicinity of δ, the sliding manifold (see Fig. 2). Assume that the system is at an initial state with vector $x_i=x(t=0)$ and a trajectory $S_i=S(t=0)$, which is located at a distance away from the sliding manifold ζ = 0. The necessary and sufficient condition for the system to satisfy the hitting condition is that the resulting controls $u_i=u(t>0)$ produces a state-variable vector $x(t>0)$ and consequently a controlled trajectory $S(t>0)$, which satisfies the following inequality:

$$S\frac{dS}{dt} < 0....(for, t > 0, and, that, |S| \geq \delta) \tag{5}$$

The inequality (5) is a partial result of the Lyapunov second theorem on stability, of which the Lyapunov function candidate is

$$V(s) = \frac{1}{2}S^2 \tag{6}$$

The compliance of (5) signifies that at a position not within the vicinity of the sliding manifold, the state trajectory S is continuously being attracted and is always converging to the sliding manifold ζ = 0 for t > 0, and that the choice of $u_i = u(t) > 0$ is supporting this attraction. Hence, one important and fundamental aspect of designing an SM control is to first determine, for a desired set of control parameters (sliding coefficients), the suitable discontinuous control action for the system, as described in (3). In other words, the design of U^+ and U^- would have to ensure that the hitting condition is always satisfied for a given system.

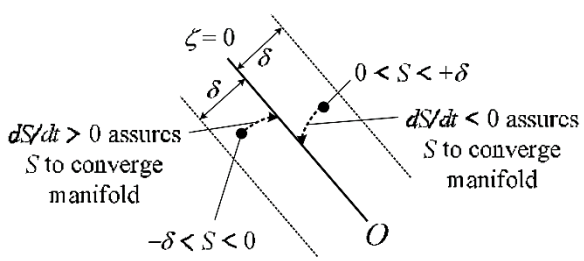

Fig. 3. Trajectory S at a location within the vicinity of sliding manifold 0 < |S| < δ converging to the sliding manifold in SM control process when the existence condition is fulfilled.

2) Existence Condition

Having the system already designed to fulfil the hitting condition, it is then necessary to check if the system also

complies with the existence condition, which ensures that once the trajectory is at locations within the vicinity of the sliding manifold such that 0 < |S| < δ, it is still always directed toward the sliding manifold, as illustrated in Fig. 3. The existence condition of the SM operation can be determined by inspecting only the local reachability condition of S.dS/dt<0 such that in the domain of 0 < |S| < δ, the condition

$$\lim_{S \to 0} S.\frac{dS}{dt} < 0 \tag{7}$$

must be satisfied. This can be expressed as:

$$\left\{ \lim_{S \to 0^+} S.\frac{dS}{dt} < 0 \right\}; \left\{ \lim_{S \to 0^-} S.\frac{dS}{dt} > 0 \right\} \tag{8}$$

In a physical sense, the existence condition can be understood as being a requirement for the controlled trajectory and its time derivative to have opposite signs in the vicinity of a discontinuous surface

3) Stability Condition

In addition to the existence condition, the control action and sliding coefficients must be designed to comply with the stability condition. This is to ensure that in the event of operating in the sliding phase, the desired sliding manifold will always direct the trajectory toward a stable equilibrium point. Failure to achieve this will lead to an unstable SM system. Fig. 4(a) shows the trajectory of a system under SM operation stabilizing at the desired point of equilibrium O when stability condition is fulfilled, and Fig. 4(b) shows the same trajectory moving pass O when stability condition is not fulfilled.

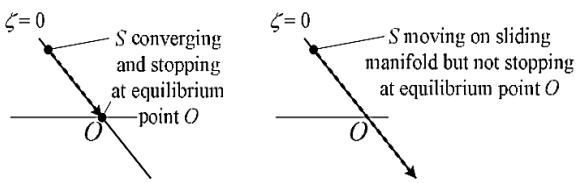

(a) Stable (b) Unstable

Fig.4. Trajectory S moving on the sliding manifold and (a) converging to the desired point of equilibrium O when stability condition is fulfilled, and (b) passing through and not stopping at the desired point of equilibrium O when stability condition is not fulfilled.

In general, the stability of a system is obtained by ensuring that the eigenvalues of the Jacobian of the system at the steady-state region have negative real parts. In the following, we will consider how the stability condition of the SM operation can be found for a system with a linear sliding manifold and a system with a nonlinear sliding manifold.

To define the problem and determine the objectives of the proposed method, it is required to explain some conventional sliding mode controllers used in EV battery chargers.

B. Sliding mode voltage control (SMVC)

This control method only considers the output voltage as a reference, which is more suitable for the buck converters [16]. The sliding surface and the converter's duty cycle as the control input are presented as (9) and (10), respectively.

$$\begin{aligned} S &= a_1 X_1 + a_2 X_2 + a_3 X_3 \\ &= a_1(V_{ref} - \beta V_o) + a_2(-\frac{\beta}{C} i_C) + a_3 \int (V_{ref} - \beta V_o) dt \end{aligned} \tag{9}$$

where S, X_n, α_n (n = 1, 2, 3), V_{ref}, and β are the sliding surface, the state and coefficient variables, the reference voltage, and the output voltage sampling percent, respectively. The controller's output equation as the switch's duty cycle is obtained as (10).

$$U_{eq} = \frac{-K_{p_1} i_c + \beta(V_o - V_i) + K_{p_2}(V_{ref} - \beta V_o)}{\beta(V_o - V_i)} \tag{10}$$

where Kp_1 and Kp_2 are calculated according to [17].

C. Indirect Sliding Mode Current Control (ISMC)

In this method, the output voltage and the input current references are simultaneously considered. The input current reference is considered in form of a coefficient of the output voltage error [18]. The sliding surface and the duty cycle equations are presented as (11) and (12), respectively.

$$\begin{aligned} S &= a_1 X_1 + a_2 X_2 + a_3 X_3 \\ &= a_1 i_{Lref} - a_1 i_L + a_2(V_{ref} - \beta V_o) \\ &+ a_3 \int \left[(1+K)(V_{ref} - \beta V_o) - i_L \right] dt \\ &\Rightarrow i_{Lref} = K(V_{ref} - \beta V_o) \end{aligned} \tag{11}$$

where X_1, X_2, X_3, and i_{Lref} are the current/voltage error, the integral summation of the voltage, and current errors, respectively. The input reference current is a proportion of the output voltage error. Moreover, the coefficient K is considered sufficiently large.

$$U_{eq} = \frac{-\beta(V_i - V_o) + \beta K_2 i_c + \beta K_1(V_{ref} - \beta V_o) - \beta K_3 i_L}{\beta V_o} \tag{12}$$

The calculation steps of the coefficients K_1, K_2, and K_3 are

given in [17].

D. Double Integral Sliding Mode Control (DISMC)

By considering an additional integral variable at the sliding surface, the ISMC controller's steady-state error is improved in this strategy. The sliding surface and the duty cycle equations are presented as (13) and (14), respectively [17].

$$S = a_1\left[K(V_{ref} - \beta V_o) - i_L\right] + a_2(V_{ref} - \beta V_o) + a_3\int\left[K(V_{ref} - \beta V_o) - i_L + V_{ref} - \beta V_o\right]dt + a_4\iiint\left[K(V_{ref} - \beta V_o) - i_L + V_{ref} - \beta V_o\right]dtdt \quad (13)$$

$$U_{eq} = \frac{(1 + K_1 / R_L)V_o - V_i + KK_2(V_{ref} - \beta V_o) - (K_1 + K_2)i_L + KK_3\int(V_{ref} - \beta V_o)dt - K_3\int i_L dt}{V_o - K_1 i_L}$$

$$K_1 = \frac{L\beta}{C}(K + \frac{a_2}{a_1}); K_2 = L\frac{a_3}{a_1}; K_3 = L\frac{a_4}{a_1} \quad (14)$$

where K_n (n = 1, 2, 3) is calculated according to the steps presented in [18].

IV. Proposed Integral SMC (PISMC)

In the proposed method, the reference current is considered proportional to the integral of the output voltage error. The sliding surface variables in the proposed controller are considered as (15).

$$\begin{aligned} X_1 &= i_{ref} - i_L; i_{ref} = K\int(V_{ref} - \beta V_o)dt \\ X_2 &= V_{ref} - \beta V_o \\ X_3 &= \int X_1 dt \end{aligned} \quad (15)$$

The sliding surface is presented as (16).

$$\begin{aligned} S &= a_1X_1 + a_2X_2 + a_3X_3 \\ S &= a_1(K\int(V_{ref} - \beta V_o)dt - i_L) + \\ &a_2(V_{ref} - \beta V_o) + a_3\int(K\int(V_{ref} - \beta V_o)dt - i_L)dt \end{aligned} \quad (16)$$

The 4th part of the sliding surface used in the DISMC method is not necessary. Moreover, the sliding surface must reach zero (or close to zero) at infinity to maintain asymptotic stability so as (17):

$$\dot{S} = a_1K(V_{ref} - \beta V_o) - a_1\frac{di_L}{dt} - a_2\beta\frac{dV_o}{dt} + a_3K\int(V_{ref} - \beta V_o)dt - a_3i_L = 0 \quad (17)$$

As: $V_L = L\frac{di_L}{dt}; V_L = V_i - V_o(1 - U_{eq})$ So:

$$a_1K(V_{ref} - \beta V_o) - \frac{a_1}{L}\left[V_i - V_o(1 - U_{eq})\right] - \frac{a_2\beta}{C}i_c + a_3K\int(V_{ref} - \beta V_o)dt - a_3i_L = 0 \quad (18)$$

By putting the ic and according to (19), (20) is attained.

$$i_c = (1 - U_{eq})i_L - \frac{V_o}{R_L} \quad (19)$$

$$a_1K(V_{ref} - \beta V_o) - \frac{a_1}{L}\left[V_i - V_o(1 - U_{eq})\right] - \frac{a_2\beta}{C}\left[(1 - U_{eq})i_L - \frac{V_o}{R_L}\right] + a_3K\int(V_{ref} - \beta V_o)dt - a_3i_L = 0 \quad (20)$$

where R_L is the internal battery resistance and varies with the battery temperature. By multiplying (20) in L/α_1, (21) is attained.

$$LK(V_{ref} - \beta V_o) - V_i + V_o - V_oU_{eq} - \frac{La_2\beta}{Ca_1}i_L + \frac{La_2\beta}{Ca_1}U_{eq}i_L + \frac{La_2\beta}{Ca_1} \times \frac{V_o}{r_L} + \frac{La_3K}{a_1}\int(V_{ref} - \beta V_o)dt - \frac{La_3}{a_1}i_L = 0 \quad (21)$$

By simplification of (21), (22) is attained.

$$\begin{aligned} &LK(V_{ref} - \beta V_o) - V_i + V_o - K_1i_L - K_2i_L + K_1\frac{V_o}{r_L} + \\ &+K_2K\int(V_{ref} - \beta V_o)dt = U_{eq}(V_o - K_1i_L) \end{aligned} \quad (22)$$

$$K_1 = \frac{La_2\beta}{Ca_1}; K_2 = \frac{La_3}{a_1}$$

Finally, the main controller's output as the duty cycle is obtained as (23)

$$U_{eq} = 1 - \frac{-K_1\frac{V_o}{R_L} - LK(V_{ref} - \beta V_o) + V_i + K_2i_L - K_2K\int(V_{ref} - \beta V_o)dt}{V_o - K_1i_L} \quad (23)$$

The coefficients α_n (n = 1, 2, 3), K, and K_n (n = 1, 2) are unknown in (23). The system's stability condition is guaranteed (the positioning of the system's poles on the left side of the imaginary axis) [18].

In the boost converter as Eq. (2):

$$\left\{\begin{array}{l} \frac{di_L}{dt} = \frac{v_i}{L} - \frac{v_o}{L}\frac{-K_1\frac{V_o}{R_L} - LK(V_{ref} - \beta V_o) + V_i + K_2i_L - K_2K\int(V_{ref} - \beta V_o)dt}{V_o - K_1i_L} \\ \frac{dv_o}{dt} = \frac{i_L}{C}\frac{-K_1\frac{V_o}{R_L} - LK(V_{ref} - \beta V_o) + V_i + K_2i_L - K_2K\int(V_{ref} - \beta V_o)dt}{V_o - K_1i_L} - \frac{v_o}{R_LC} \end{array}\right\} \quad (24)$$

Given the nonlinearity (23), the Laplace method cannot be used to solve it. Using the small-signal method for variables around the point of equilibrium in small variations is considered. By applying the energy conservation law around the equilibrium point as (25), (26) is attained

$$\begin{aligned} &I_L = \frac{V_o^2}{V_iR_L}; v_o = V_o + \tilde{v}_o; i_L = I_L + \tilde{i}_L; v_i = V_i; V_{ref} - \beta V_o = 0 \\ &I_{ref} = I_L; K \gg 1; V_o \gg \tilde{v}_o; I_L \gg \tilde{i}_L \end{aligned} \quad (25)$$

$$\begin{cases} \frac{d(I_L+\tilde{i}_L)}{dt}=\frac{v_i}{L}-(\frac{V_o+\tilde{v}_o}{L})* \\ \frac{-K_1\frac{(V_o+\tilde{v}_o)}{R_L}-LK\left[V_{ref}-\beta(V_o+\tilde{v}_o)\right]+V_i+K_2(I_L+\tilde{i}_L)-K_2K\int\left[V_{ref}-\beta(V_o+\tilde{v}_o)\right]dt}{V_o-K_1\frac{V_o^2}{V_iR_L}} \\ \frac{d(V_o+\tilde{v}_o)}{dt}=\frac{(I_L+\tilde{i}_L)}{C}* \\ \frac{-K_1\frac{V_o+\tilde{v}_o}{R_L}-LK\left[V_{ref}-\beta(V_o+\tilde{v}_o)\right]+V_i+K_2(I_L+\tilde{i}_L)-K_2K\int\left[V_{ref}-\beta(V_o+\tilde{v}_o)\right]dt}{V_o-K_1\frac{V_o^2}{V_iR_L}}-\frac{V_o+\tilde{v}_o}{R_LC} \end{cases} \quad (26)$$

V_o and I_L are fixed values and their derivatives are equal to zero, and (27) is obtained by solving (26).

$$\begin{cases} \frac{d\tilde{i}_L}{dt}=a_{11}\tilde{i}_L+a_{12}\tilde{v}_o+a_{13}\int\tilde{v}_o dt \\ \frac{d\tilde{v}_o}{dt}=a_{21}\tilde{i}_L+a_{22}\tilde{v}_o+a_{23}\int\tilde{v}_o dt \\ \frac{d\int\tilde{v}_o dt}{dt}=a_{31}\tilde{i}_L+a_{32}\tilde{v}_o+a_{33}\int\tilde{v}_o dt \end{cases} \quad (27)$$

$$a_{11}=\frac{K_2V_iR_L}{L(K_1V_o-V_iR_L)};a_{12}=\frac{LK\beta V_iR_L-2K_1V_i+K_2V_o}{L(K_1V_o-V_iR_L)};a_{13}=\frac{K_2K\beta V_iR_L}{L(K_1V_o-V_iR_L)}$$

$$a_{21}=\frac{2K_2V_o-K_1V_i}{C(K_1V_o-V_iR_L)};a_{22}=\frac{-LK\beta V_o+V_i}{C(K_1V_o-V_iR_L)};a_{23}=\frac{-K_2K\beta V_o}{C(K_1V_o-V_iR_L)}$$

$$a_{31}=a_{33}=0;a_{32}=1$$

Equation (27) is the linear system equation around the equilibrium point that is transformed in the form of standard state equations as follows:

$$Determinant\,[\mathrm{SI}-\mathrm{A}]=0 \quad (28)$$

where I and A are the 3x3 identity matrix and the coefficients matrix, respectively.

$$\mathrm{SI}-\mathrm{A}=\begin{pmatrix} S-a_{11} & -a_{12} & -a_{13} \\ -a_{21} & S-a_{22} & -a_{23} \\ 0 & -1 & S \end{pmatrix} \quad (29)$$

where a_{ij} is obtained as follows:

$$S(S-a_{11})(S-a_{22})-a_{13}a_{21}-a_{23}(S-a_{11})-a_{12}a_{21}S=0$$

$$S^3+P_1S^2+P_2S+P_3=0$$

$$P_1=-a_{11}-a_{22};P_2=a_{11}a_{22}-a_{12}a_{21}-a_{23};P_3=a_{11}a_{23}-a_{13}a_{21}$$

$$P_1\geq 0;P_2\geq\frac{P_3}{P_1};P_3\geq 0 \quad (30)$$

Conditions (30) must be satisfied. By applying the conditions specified in these relations, the range for the unknown coefficients K_1 and K_2 will be obtained as long as the poles remain on the left side of the imaginary axis. For having the maximum range of variations for R_L and V_i, the mean points of coefficients K_1 and K_2 are considered. The proposed control circuit is shown in Fig. 5.

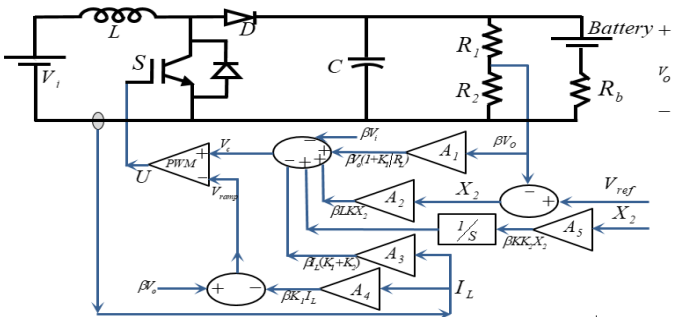

Fig. 5. A schematic diagram of the proposed integral sliding mode control to be used in EVBC

V. SIMULATION RESULTS

Simulations were performed in Matlab Simulink at three SOC levels of 20%, 50%, and 80% to have a comprehensive survey of the proposed controller's performance

Table1. The parameter values used in the simulation

Parameters		Quantities	Parameters	Quantities
Vo		400 V	L	2 mH
Vi	0 s < t < 3.5 s	160 V	K	100
	3.5 s < t < 7 s	170 V	K1	2.5
	t > 7 s	160 V	K2	35
Fs		50 kHZ	Simulation duration	7 sec (0 -7)
β		1	SOC	%20,%50,%80
C		680 μF	RL	0.5 Ω

Tables 1 and II and Fig. 6 present all parameters' quantities and battery charging current/voltage parameters in an example for more clearness, respectively. Moreover, all parameters of battery charging voltage such as Error, Ripple, %Ripple, and %Mean Displacement are distinctly considered in all SOCs in Figs. 7(a), 7(c), and 7(e). Similarly, Ripple and %Ripple of battery charging current in all SOCs are distinctly considered as well in Figs. 7(b), 7(d), and 7(f). The proposed controller demonstrates how well it controls those parameters in comparison with the other SMCs in all mentioned Figures.

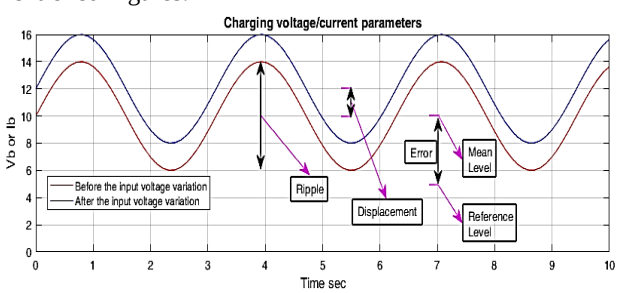

Fig. 6. The presentation of battery charging current/voltage parameters in an example diagram for more clearness

Table II. The definitions of the voltage/current parameters

Parameters	Explanations	Equations
%Mean Displacement	The output displacement directly affected by input variation	$\%Mean.Displacement = \frac{Displacement}{V_{before.input.variation}(I_{before.input.variation}) + Displacement/2} x\,100$
Error	Difference between the output and its reference	$Error = V_{o\cdot Mean}(I_{o\cdot Mean}) - V_{ref}(I_{ref})$
Ripple	The output peak to peak	$Ripple = V_{peak^+}(I_{peak^+}) - V_{peak^-}(I_{peak^-})$
%Ripple	Multiplying the output peak to peak divide by its mean by 100	$\%Ripple = 100 \cdot \frac{V_{peak^+}(I_{peak^+}) - V_{peak^-}(I_{peak^-})}{V_{mean}(I_{mean})}$

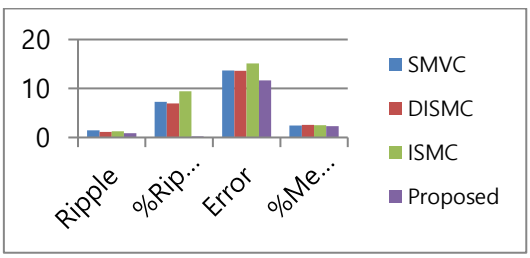

a. SOC: %20

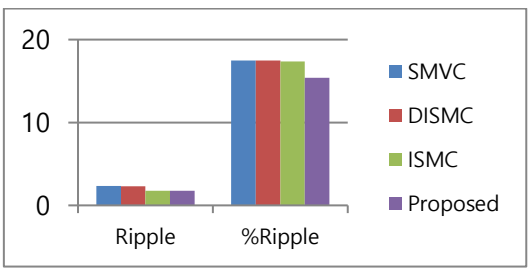

b. SOC: %20

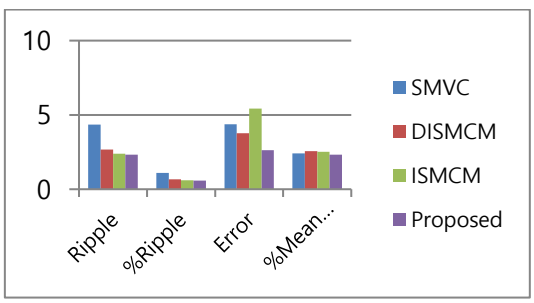

c. SOC: %50

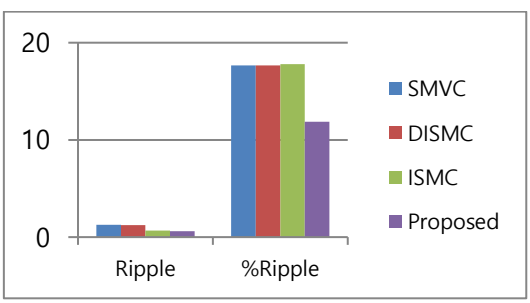

d. SOC: %50

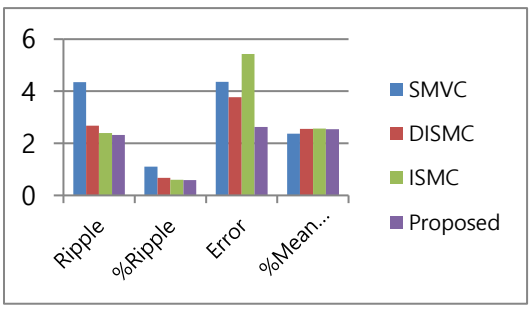

e. SOC: %80

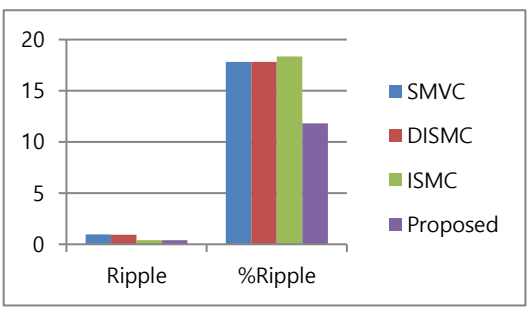

f. SOC: %80

Fig.7. The proposed controller charging voltage and current parameters in comparison with the other SMCs.

Fig. 8 depicts the charging battery voltage for the proposed controller compared to the other SMCs on the three SOCs specified in Table I. According to all parts of Fig. 8, the battery charging voltage is close to its reference on SOC 80%. Therefore, the voltage error of its reference lessens by an increase in SOC's amount. Moreover, this parameter in the proposed controller has the lowest amount in comparison with the other SMCs.

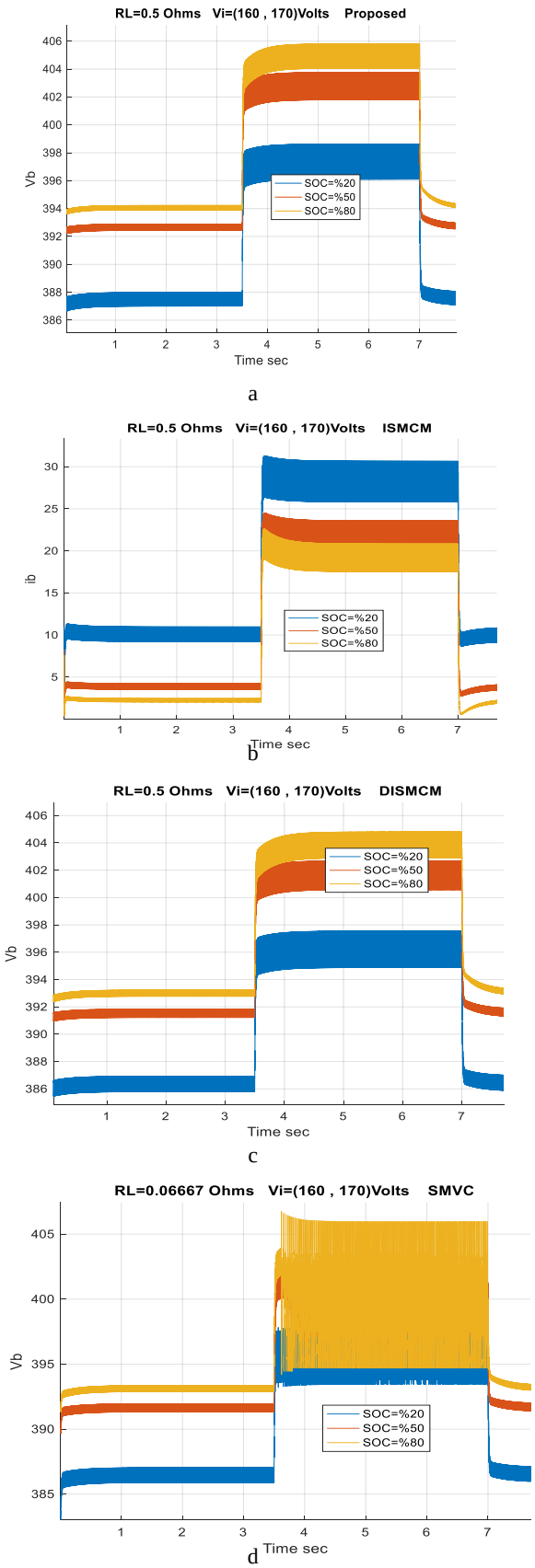

Fig.8. Battery charging voltage-time characteristics for the proposed controller and the other SMCs.

Fig. 9 depicts the charging battery current for the proposed controller compared to the other SMCs on the three SOCs specified in Table I. An extensive charging current ripple is clearly seen by input variations in Fig. 9(d).

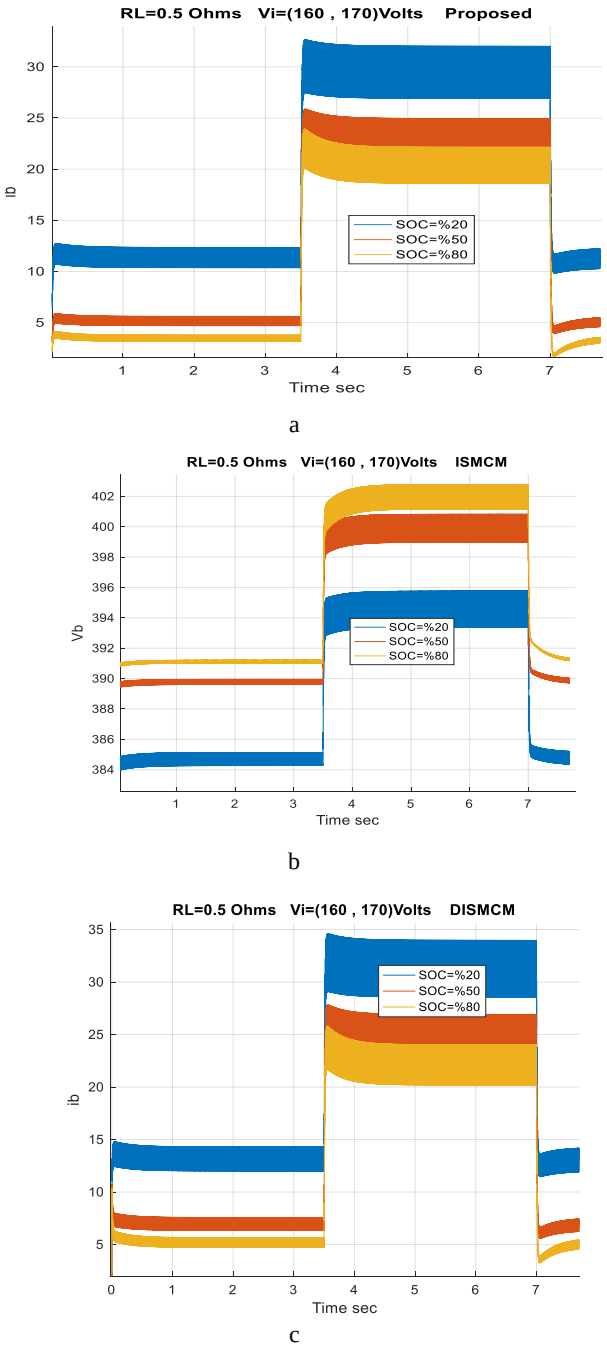

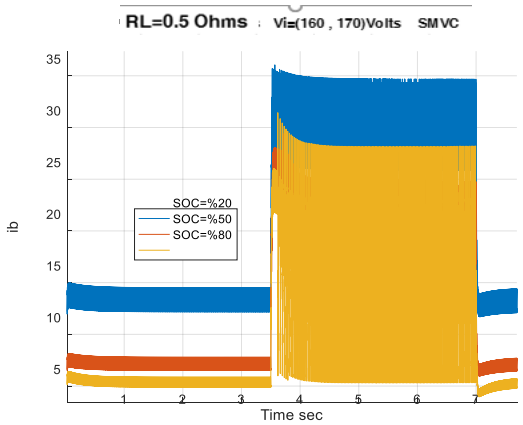

d

Fig.9. Battery charging current time characteristics for the proposed controller and the other SMCs.

VI. CONCLUSIONS

An improved SMC applicable in a DC/DC boost converter as an EVBC is presented in this paper. Based on the simulation results, all charging voltage and input current parameters demonstrate how the proposed controller keeps those to a minimum based on the comparisons with the other SMCs. Ripple, error, mean displacement, and their percentages were considered as the parameters mentioned above. A more robust structure in the input power supply voltage variations is another distinctive characteristic of the proposed controller. This property is attained by making a comparison between the input current and integral function of the charging voltage error parameter. Moreover, this allows flexibility in the input voltage level variations. Therefore, this controller makes it possible to use various kinds of input power supplies such as RESs, PVCs, wind turbines, and ancillary batteries for EVBCs.

REFERENCES

[1] A.V. J. S. Praneeth, and Sh. S Williamson, "A Review of Front End AC-DC Topologies in Universal Battery Charger for Electric Transportation," *2018 IEEE Transportation Electrification Conference and Expo (ITEC)*, DOI: 10.1109/ITEC.2018.845018630, August 2018.

[2] M. Y. Metwly, M. S. Abdel-Majeed, A. S. Abdel-Khalik, R .A Hamedy, and M. S. Hamad, "A Review of Integrated On-Board EV Battery Chargers Advanced Topologies Recent Developments and Optimal Selection of FSCW Slot Pole Combination," *IEEE Access*, pp. 85216 – 8524206, DOI: 10.1109/ACCESS.2020.2992741, May 2020.

[3] S. Kumar, and A. Usman, "A Review of Converter Topologies for Battery Charging Applications in Plug-in Hybrid Electric Vehicles," *2018 IEEE Industry Application Society Annual Meeting (IAS)*, DOI: 10.1109/IAS.2018.8544609, 29 November 2018.

[4] A. Taheri, and N. Asghari, "Sliding Mode Control of LLC Resonant DC-DC Converter for Wide output voltage Range in Battery Charging Applications," *2019 International Journal of Industrial Electronics (IECO)*, pp. 127-136, DOI: 10.22111/IECO.2018.27333.1096, April 2019.

[5] M. R. Shokoohinia, and M. M. Fateh, "Model-free tracking control via adaptive dynamic sliding mode control with application to robotic systems," *2020 International Journal of Industrial Electronics (IECO)*, DOI: 10.22111/ieco.2020. 31596.1207, 2020.

[6] J. Keighobadi, and M. M. Fateh, "Adaptive Robust Tracking Control Based on Back stepping Method for Uncertain Robotic Manipulators Including Motor Dynamics," *2020 International Journal of Industrial Electronics (IECO)*, DOI: 10.22111/ ieco.2020.31792.1213, 2020.

[7] A. Noori, M. A. Sadrnia, and M. B. Naghibi-Sistani, "Fault Tolerant Control of Blood Glucose Concentration Using Reinforcement Learning," *2020 International Journal of Industrial Electronics (IECO)*, pp. 353-364 DOI: 10.22111/ ieco.2020.31719.1217, July 2020.

[8] A. Tiwari, O. Jaga, and Sh. Singh Soni, "Sliding mode controller based interleaved boost converter for fuel cell," *2017 Recent Developments in Control, Automation & Power Engineering (RDCAPE)*, DOI: 10.1109/RDCAPE. 2017. 8358325, 14 May 2018.

[9] F. Z. Belhaj, H. El Fadil, A. Tahri, K. Gaouzi, A. Rachid, and F. Giri "Sliding mode control of cascade boost converter for fuel cell energy generation system," *2017 International Conference on Electrical and Information Technologies (ICEIT)*, DOI: 10.1109/EITech.2017.8255239, 15 January 2018.

[10] V. M. Iyer, S. Gulur, and S. Bhattacharya, "Variable dc bus control for a bidirectional on-board EV charger," *2017 IEEE 6th International Conference on Renewable Energy Research and Applications (ICRERA)*, DOI: 10.1109/ICRERA.2017. 8191216, 14 December 2017.

[11] D. Patil, and V. Agarwal, "Compact on-board single-phase EV battery charger with novel low frequency ripple compensator and optimum filter design," *IEEE Transactions on Vehicular Technology*, Vol. 65, No. 4, DOI: 10.1109 / TVT. 2015. 2424927, 21 April 2015.

[12] A. Karaarslan, "The analysis of average sliding control method applied on Sheppard-Taylor power factor correction converter," *Electronics Engineering (2013)* 95:255–265 DOI 10.1007/s00202-012-0257-3, 23 September 2012.

[13] A. Mallik, J. Lu, and A. Khaligh, "Sliding mode control of single phase interleaved totem-pole PFC for electric vehicle on-board chargers," *2018 IEEE Transactions on Vehicular Technology*, Vol. 67, No. 9, pp. 8100-8109, DOI: 10. 1109/ TVT.2018.2848238, 18 June 2018.

[14] P. Guerriero, M. Coppola, D. Lauria, and S. Daliento, " PWM Based Sliding Mode Control of a fast charger for super capacitors," *2020 International Symposium on Power Electronics, Electrical Drives, Automation and Motion (SPEEDAM)*, DOI**:** 10.1109/SPEEDAM48782.2020.9161872, 7 August 2020.

[15] A. Verma, B. Singh, A. Chandra, and K. Al-Haddad, "An Implementation of Solar PV Array Based Multifunctional EV Charger," *2018 IEEE Transportation Electrification Conference and Expo (ITEC)*, DOI**:** 10.1109 / ITEC. 2018. 8450191, 30 August 2018.

[16] J. Ackermann, and V. Utkin, "Sliding mode control design based on Ackermann's formula," *IEEE Transactions on Automatic Control* Vol. 43, No. 2, pp. 234–237, DOI: 10.1109/9.661072, , Feb 1998.

[17] R. Redl, N. O. Sokal, "Current-mode control, five different types, used with the three basic classes of power converter: Small-signal AC and large-signal DC characterization, stability requirements, and implementation of practical

circuits," *1985 IEEE Power Electronics Specialists Conference*, DOI: 10.1109/PESC.1985.7071020, 30 March 2015.

[18] Siew-Chong Tan&Yuk-Ming Lai&Chi Kong Tse, "Sliding Mode Control of Switching Power Converters-Techniques and Implementation," *Boca Raton, FL 33487-2742© 2012 by Taylor & Francis Group*, 2012.

Gholamreza Mohebalizadeh was born in Tehran, Iran, in 1967. He received a B.Sc. degree in electronic engineering from the University of Shiraz, Shiraz, in 1991, an M.Sc. degree in nuclear engineering from Tehran Azad University, Tehran, Iran, in 2000, and he is a Ph.D. candidate in electrical engineering from Islamic Azad University, Shabestar Branch. His current research interests include power electronic converters and renewable energy systems.

Hasan Alipour received his B.Sc., M.Sc., and Ph.D. degrees in power electrical engineering from Iran University of Science and Technology (IUST), Tehran, Iran, in 2008, the University of Tehran, Tehran, Iran, in 2011, and the University of Tabriz, Tabriz, Iran, in 2015, respectively. Currently, he is an assistant professor in the engineering faculty of Islamic Azad University, Shabestar Branch. His research interest focuses on electric and hybrid electric vehicles, electric machines drive, linear electric motors, renewable energies, and distributed generation.

Leila Mohammadian was born in Tabriz, Iran in 1984. She received her B.Sc., M.Sc., and Ph.D. degrees in Electrical Engineering from the Department of Electrical and Computer Engineering, University of Tabriz, Tabriz, Iran, in 2007, 2011, and 2015, respectively. She has been with Shabestar Branch, Islamic Azad University, Shabestar, Iran since 2011. She has been an assistant professor since 2015. Her current research interests include the analysis and control of power electronic converters and their applications.

Mehran Sabahi was born in Tabriz, Iran, in 1968. He received his B.Sc. degree in electronic engineering from the University of Tabriz, Tabriz, in 1991, his M.Sc. degree in electrical engineering from Tehran University, Tehran, Iran, in 1994, and his Ph.D. degree in electrical engineering from the University of Tabriz, in 2009. In 2009, he joined the Faculty of Electrical and Computer Engineering, University of Tabriz, where he has been an associate professor since 2014. His current research interests include power electronic converters and renewable energy systems.